

## University of Southampton Research Repository

Copyright © and Moral Rights for this thesis and, where applicable, any accompanying data are retained by the author and/or other copyright owners. A copy can be downloaded for personal non-commercial research or study, without prior permission or charge. This thesis and the accompanying data cannot be reproduced or quoted extensively from without first obtaining permission in writing from the copyright holder/s. The content of the thesis and accompanying research data (where applicable) must not be changed in any way or sold commercially in any format or medium without the formal permission of the copyright holder/s.

When referring to this thesis and any accompanying data, full bibliographic details must be given, e.g.

Thesis: Kash Saddul (2025) "Mission Analysis for NanoSats using a Printed Micro-Thrust Distributed Propulsion System", University of Southampton, Faculty of Engineering and Physical Sciences, PhD Thesis.

# Mission Analysis for NanoSats using a Printed Micro-Thrust Distributed Propulsion System

by

Kash Saddul

**ORCiD**: 0000-0003-4876-7510



This thesis is submitted in partial fulfillment of requirements for the degree of

Doctor of Philosophy

June 2025

University of Southampton

Aeronautics, Astronautics & Computational Engineering

## **Abstract**

While the miniaturisation of satellites has made space more accessible, traditional propulsion systems struggle with size, power and mass constraints. Many small satellites launch without propulsion, limiting their orbital and attitude capabilities. This leads to most miniature satellites being constrained in a given altitude range to guarantee a practical operational lifetime. This thesis focuses on the operational analysis of small satellites using a novel propulsion system called the Distributed micro-Propulsion System (D $\mu$ PS), a novel technology developed as part of a joint research project between two teams at the University of Southampton, to enable miniaturised satellites to operate at orbital altitudes beyond what is currently possible. When fired, the unique distributed architecture of the D $\mu$ PS leads to torque generation, creating complex operational and modelling challenges. This thesis details the approach to these problems by introducing two novel mission concepts demonstrating the practical application of the D $\mu$ PS on miniaturised satellites.

The thesis first reviews the literature on the state-of-the-art miniaturised propulsion system and highlights existing potential thrust generation principles for the  $D\mu PS$ . After presenting standard orbital and attitude dynamics modeling techniques, the limitations of existing software solutions are discussed. While there are numerous commercial software packages and published routines available to model attitude and orbital dynamics, none offer the flexibility required to model distributed propulsion systems at the necessary fidelity. Therefore, a bespoke coupled orbit-attitude simulator, the Comprehensive High-fidelity Attitude and Orbit Simulator (CHAOS), is developed to analyse the dynamics of spacecraft equipped with the  $D\mu PS$ .

The second part of this research analyses the potential of the  $D\mu PS$  as a de-orbiting device for 1U CubeSats. This chapter specialises the  $D\mu PS$  concept into the CubeSat De-orbiting All-Printed Propulsion System (Cube-de-ALPS), by adding required components, such as sensors and necessary control laws, thus fully defining the propulsion system. The attitude and orbit simulations components are also updated to better model Cube-de-ALPS distributed architecture. Its operation is outlined, and preliminary estimates of its performance in various configurations are performed before using CHAOS to confirm the concept's viability. As a result, I show that Cube-de-ALPS can de-orbit 1U CubeSats from altitudes twice as high as naturally possible while remaining compliant with debris mitigation guidelines.

The last part of this thesis examines the D $\mu$ PS's performance in Very Low Earth Orbit (VLEO). The HexSat, a 2.5 cm thick flat hexagonal satellite architecture designed for efficient packing inside rocket fairings, is introduced. For actuation, HexSats use the D $\mu$ PS,

embedded in the satellite frame, which produces thrust on the order of micro-Newtons. This research investigates the D $\mu$ PS's capability to operate on HexSats at 250 km altitude in VLEO with available power exceeding 100 W. Compared to the Cube-de-ALPS system, the D $\mu$ PS provides less altitude change due to the exponentially increased drag forces at lower altitudes. The angular acceleration, drag profiles, and expected performance are determined for different mission scenarios. The results show the  $D\mu PS$  enables HexSats to operate at 250 km whilst actively tracking up to 8 ground targets per orbit and providing over 100 W of average payload power.

## **Contents**

Abstract	ii
List of Figures	ix
List of Tables	x
<b>Definitions and abbreviations</b>	xi
List of Acronyms	xi
Greek Symbols	xii
Roman Symbols	xii
Vectors	xiii
<b>Declaration</b>	xv
Acknowledgements	xvii
1 Introduction	4
2 Manoeuvrability of nanoSats	11
2.1 Orbital actuation	
2.2 Attitude actuation	
2.3 Conclusion	29
3 Distributed micro ( $\mu$ )-Propulsion System	30
4 Fundamentals of satellite dynamics	35
4.1 Orbital motion	
4.2 Attitude motion	
4.3 Perturbations	41
4.4 Existing software	45
4.5 Review of tools used in literature	48
4.6 Conclusion	49
5 Comprehensive High-fidelity Attitude and Orbit S	
5.1 Equations of motion	
5.2 Geometry of the satellite	

CONTENTS	Kash Saddul v
----------	---------------

	5.3	Perturbation modelling	57
	5 4	Validation	74
	5.5	Code structure	88
	5.6	Conclusion	91
	5.0	Conclusion	71
6	App	lication: CubeSat post-mission disposal	92
	6.1	CubeSat de-orbiting All-Printed Propulsion System	93
	6.2	Semi-analytical propagator	99
	6.3	System performance analysis	102
	6.4	Numerical results	107
	6.5	Conclusion	113
7	App	lication: A hexagonal flat nanosatellite in VLEO	114
	7.1	<u>DiskSats</u>	115
	7.2	Hexagons are the bestagons	117
	7.3	HexSat performance	122
	7.4	Operational mode & orbit geometries	130
	7.5	HexSat power analysis	137
	7.6	Conclusion	142
8	Con	clusion	144
Bi	bliogi	-aphy	148

# **List of Figures**

	1.1	Illustration of different CubeSat configurations.	5
	2.1	Cold Gas Thruster thrust generation principle.	12
	2.2	Liquid monopropellant thruster thrust generation principle	13
	2.3	Solid propellant thruster thrust generation principle.	14
	2.4	Gridded Ion Thrusters thrust generation principle.	15
	2.5	Hall Effect Thrusters thrust generation principle.	16
	2.6	Electrosprays thrust generation principle.	19
	2.7	Vacuum Arc Thruster thrust generation principle.	20
	2.8	Example shuttlecock configuration of a 3U CubeSat.	24
	2.9	Schematic of a magnetorquer.	26
	2.10	Reaction wheel applied torque against operational time to saturation.	27
	2.11	Reaction wheels in a 3-axis configuration.	27
	0.1		
_	3.1	A nanosatellite with the D $\mu$ PS. The flexible architecture allows for any layout desired	31
	3.2	Picture of a Distributed micro ( $\mu$ )-Propulsion System (D $\mu$ PS) prototype and	<i>J</i> 1
	5.2	a pixel cross-section. Images taken and adapted from $\boxed{\square}$	32
	4.1	Representation of the classical Keplerian elements.	36
_	4.2	Sketch of the RSW frame. $R$ is along the radial direction, $S$ is along the	
누		orbital path and in the velocity direction, and $\hat{W}$ completes the right-hand	38
_	4.3	Aerodynamic forces acting on a satellite.	42
	4.4	Solar radiation pressure forces acting on a satellite.	43
	4.5	Geopotential forces acting on a satellite.	44
	4.6	NI 1 1 7 7 4 W	45
	7.0	N-body acceleration acting on a satellite.	73
	5.1	A body-fixed frame $xyz$ rotated relative to an inertial frame $XYZ$	52
	5.2	Visualisation of satellite facets.	55
	5.3	Ideal conical shadow model.	59
	5.4	Types of eclipse.	60

LIST OF FIGURES Kash Saddul vii

	5.5	Error in keplerian elements variation over 400 days in a Keplerian orbit for	
		CHAOS, HPOP, GMAT and REBOUND relative to the analytical solution.	
		In the first five plots, CHAOS is not visible on the logarithmic scale as its	
		error is too low. Due to fast oscillations, the lines can appear as solid blocks	
		which are overlapping as the different propagators present similar behaviour.	76
	5.6	Orbital energy variation over 400 days in a Keplerian orbit for CHAOS,	
		HPOP, GMAT and REBOUND.	77
	5.7	Keplerian elements error of CHAOS relative to HPOP and GMAT over 400	
Г		days under gravitational perturbations. Due to fast oscillations, the lines can	
F		appear as solid blocks which are overlapping as the different propagators	
F		present similar behaviour.	79
	5.8	Keplerian elements error of CHAOS relative to HPOP and GMAT over 400	
г		days under Luni-Solar perturbations. Due to fast oscillations, the lines can	
F		appear as solid blocks which are overlapping as the different propagators	
F		present similar behaviour.	80
	5.9	Keplerian elements error of CHAOS relative to HPOP and GMAT over 400	
	0.5	days under solar radiation pressure perturbations. Due to fast oscillations,	
늗		the lines can appear as solid blocks which are overlapping as the different	
늗		propagators present similar behaviour.	82
	5 10	Keplerian elements error of CHAOS relative to HPOP and GMAT over 400	
г	5.10	days under aerodynamic perturbations.	84
	5.11	Decay times between simulators using the Jacchia-Roberts and Jacchia-77	
	J.11	atmospheric models.	85
	5 12	Error between CHAOS and STK quaternion in torque-free motion	86
		Error between CHAOS and STK angular velocity vector in torque-free motion	
			. 67
_	5.14	A 3U CubeSat with deployable panels arranged in a shuttlecock configura-	87
L	C 1 C	tion for passive aerodynamic stabilisation.	
		Passive aerodynamic stabilisation of a 3U CubeSat at different altitudes.	89
	5.16	<u> </u>	
느		elling Language. For visualisation, the arrows denoting the inheritance re-	0.0
L		lationship are coloured in brown.	90
	6.1	Drawing of the thruster pixels of CubeSat de-orbiting All-Printed Propul-	
Г	0.1	sion System (Cube-de-ALPS), with a Faraday cup in the centre. The differ-	
늗		ent colours correspond to the quadrant division.	94
	6.2	Sketch of the Faraday cup.	96
		<u> </u>	90
_	6.3	Unit sphere of all possible spacecraft orientations with the thrusting cone defined by $\alpha$ . The highlighted sphere cap enclosed by the thrusting cone	
늗		indicates all orientations in which Cube-de-ALPS fires	100
	C 1		100
_	6.4	Decay time with respect to altitude for Copper (Cu), aluminium (Al), Tung-	
늗		sten (W), and printed silver (Ag). The plot presents the semi-analytical re-	
늗		sults and a baseline, corresponding to HUMSAT-D naturally decaying with-	104
_	C =	out Cube-de-ALPS	104
_	6.5	Decay time with respect to altitude for Copper (Cu), using signal-to-noise	107
1		ratios of 10, 9, 7, 1, 3 and 5 for the 1-F and 2-F configurations	105

Kash Saddul viii LIST OF FIGURES

	6.6	Operational zone of Cube-de-ALPS. The green area ( ) highlights the al-	
		titudes for which HUMSAT-D would naturally decay. The blue shades de-	
		fine the zones where the 1-F ( ) and the 2-F ( ) can provide de-orbiting.	
		The maximum altitude from which Cube-de-ALPS can provide de-orbiting	
		is marked for the 1-F ( $\bigcirc$ ) and the 2-F ( $\nabla$ ). For each initial altitude, the $SN$	
		leading to the fastest de-orbiting is also shown (). The dotted area de-	
Ē		fines the heights and $SN$ where de-orbiting within 25 years is impossible,	
〒		even with Cube-de-ALPS. Dashed contour lines () mark the maximum	
F		thrusting cone half-angle $\alpha$ detectable, with the red line (—) bounding a	
$\equiv$		region where no cone is perceived.	107
	6.7	Example of the angular velocity of a 1U CubeSat equipped with Cube-de-	
г		ALPS using the closed-loop control law.	109
	6.8	High-fidelity numerical decay time predictions compared to the semi-analytica	1
		estimation The altitude of the HUMSAT-D satellite is marked for the 1-F	
$\overline{}$		(a) and the 2-F (b) configurations. Dotted lines mark the one and two year	
干		decay times, which corresponds to the lifetime of HumSat-D when equipped	
		with Cube-de-ALPS	110
	7.1	Comparison of base units for a CubeSat (1U), a PocketQube (1P), and a	
		DiskSat (not to scale).	115
	7.2	Render of a DiskSat with the D $\mu$ PS concept	116
	7.3	HexSat concept: A flat hexagonal satellite using the D $\mu$ PS for orbital and	
		attitude actuation	117
	7.4	DiskSats stacked vertically inside a launch vehicle fairing	118
	7.5	Packing configurations of DiskSats, SquareSats and HexSats inside a launcher	
Г		fairing. The configurations proven to be optimal are highlighted in green	
F		while the best-known configurations are in orange. Configurations that are	
		conjectured for this work are highlighted in blue.	119
	7.6	Individual satellite sizes for different numbers of satellite columns in the	
Г		Electron, Vega and Falcon 9 launchers. If the surface area of is greater than	
〒		the DiskSat demonstration mission, then it is highlighted in green. If not	
		then the shape is highlighted in red.	120
	7.7	Maximum thrust misalignments for HexSats, SquareSats and DiskSats	121
	7.8	Orbit-average power as a function of inclination and RAAN, which change	
Г		the orbit orientation relative to the Sun. Plot generated for an altitude of 250	
		<u>km</u>	124
	7.9	Measurement of inclination (INC) and RAAN relative to the Sun	125
		Orbit-average power of a HexSat as a function of side-length, assuming a	
Г	7.72.5	circular orbit at 250 km with the Sun vector in the orbital plane.	125
	7.11	Forces generated by the $D\mu PS$ on a HexSat. The red and orange arrows rep-	
	, . 1 1	resent the forces generating torques around the $\hat{z}$ axis, while torques around	
H		the $\hat{x}$ and $\hat{y}$ axes will be created by the forces illustrated with $\otimes$ . The analysis	
$\vdash$		is simplified thanks to the symmetry of the HexSat.	127
	7.12	Deliverable angular velocity around the $\hat{x}$ , $\hat{y}$ and $\hat{z}$ axes, assuming a circular	14/
_	1.12	orbit at 250 km with the Sun vector in the orbital plane.	129
		ANDREAL 4.7V KIII WILLI LIIV DULI VEVIUL III LIIV DEDILAI DIAIIV	1 4 7

7.13 HexSat agility as a function of its side-length for the $\hat{x}$ , $\hat{y}$ and $\hat{z}$ axes, as-	
suming a circular orbit at 250 km with the Sun vector in the orbital plane.	
	30
7.14 Geometry of the drag forces affecting a HexSat in VLEO	31
7.15 Constant Nadir-pointing mode: the spacecraft's instruments are always aligned	
towards the centre of the Earth	33
7.16 Required acceleration profile and flight path angle to perform Nadir pointing	
in low-eccentricity orbits with varying apogee altitudes. The perigee is fixed	
at 250 km for all orbits, and the legend represents the varying apogee altitudes. 1.	34
7.17 Sketch of a full Active Ground Tracking cycle, including preparation, track-	
ing, and streamlining	34
7.18 Active ground tracking mode: the spacecraft's instrument briefly point at a	
target on its ground track	35
7.19 Angular acceleration profile and flight path angle to perform AGT in a 250	
	37
7.20 Excess power based on HexSat size and apogee height, with contour lines	
indicating 100 W, 50 W and 10 W levels. The perigee is fixed at 250 km 1.	39
7.21 Excess power based on HexSat size and duty cycle $\zeta$ for a 250 km circular	
orbit. The blue line represents the optimal HexSat size for maximum power	
at a given duty cycle	40
7.22 Excess power based on HexSat size, duty cycle $\zeta$ and orbit height. The blue	
line represents the optimal HexSat size for maximum power at a given duty	
cycle	41
7.23 Orbital lifetime based on HexSat size and duty cycle $\zeta$ for a 250 km circular	
orbit	43

# **List of Tables**

1.1	Satellite class names based on mass, according to NASA [2]	4
2.1	Summary of example thrusters for nanosatellites.	21
5.1	Summary of the models and techniques used in Comprehensive High-fidelity	
	Attitude and Orbit Simulator (CHAOS).	73
5.2	Low Earth Orbit (LEO) orbit taken from Curtis for the validation of CHAOS	
	<u> [3].</u>	75
5.3	1U CubeSat properties for validation.	75
5.4	Initial conditions for validation of torque-free motion	85
C 1		0.0
6.1	Summary of Cube-de-ALPS sensors and properties	98
6.2	HUMSAT-D satellite properties.	102
6.3	Fuel materials for Cube-de-ALPS. The nominal thrust and firing time are	
	taken from [4] and scaled to the operational power of 1.5 W. The number of	
	pulses correspond to firing at 100 Hz.	103
7.1	Control characteristics of DiskSats, SquareSats, and HexSats. The con-	
	trolled axes, worst-case thrust vector misalignment, and associated required	
	thrust magnitude are illustrated for each satellite architecture. I assumed	
	100 pixels are mounted on the thickness of the DiskSat for this example	122
7.2	Summary of $D\mu PS$ and HexSat properties.	123

## **Definitions and abbreviations**

## **List of Acronyms**

**GITs** 

**GMAT** 

Abbreviation	Description
ADCS	Attitude Determination and Control System
AGI STK	Analytical Graphics Incorporated System Tool Kit
AGT	Active Ground Tracking
AOP	Argument of Perigee
<b>ASTERIA</b>	Arcsecond Space Telescope Enabling Research in Astrophysics
BRITE	Bright Target Explorer
CHAOS	Comprehensive High-fidelity Attitude and Orbit Simulator
CNES	Centre National d'Études Spatiales
COTS	Commercial-Off-The-Shelf
CPOD	CubeSat Proximity Operations Demonstration
CSSWE	Colorado Student Space Weather Experiment
Cube-de-ALPS	CubeSat de-orbiting All-Printed Propulsion System
$\mathbf{D}\mu\mathbf{PS}$	Distributed micro ( $\mu$ )-Propulsion System
DART	Double Asteroid Redirection Test
ECI	Earth Centred Inertial
EP	Electric Propulsion
ESA	European Space Agency
FEEP	Field Emission Electric Propulsion
FOV	Field Of View
GGM	GRACE Gravity Model

**Gridded Ion Thrusters** 

General Mission Analysis Tool

Kash Saddul xii Greek Symbols

Abbreviation	Description
GOCE	Gravity field and steady state Ocean Circulation Explorer
GRACE	Gravity Recovery and Climate Experiment
GSI	Gas-Surface Interaction
HETs	Hall Effect Thrusters
HPOP	High-Precision Orbital Propagator
IADC	Inter-Agency Space Debris Coordination Committee
JPL	Jet Propulsion Laboratory
LEO	Low Earth Orbit
MRP	Modified Rodrigues Parameter
NASA	National Aeronautics and Space Administration
NOAA	National Oceanic and Atmospheric Administration
ODE	Ordinary Differential Equation
Orekit	Orbit Extrapolation Kit
<b>PMACS</b>	Passive Magnetic Attitude Control System
Q-PACE	CubeSat Particle Aggregation Collision Experiement
RAAN	Right Ascension of the Ascending Node
SRP	Solar Radiation Pressure
SSO	Sun Synchronous Orbit
STL	Stereolithography
VATs	Vacuum Arc Thrusters
VLEO	Very Low Earth Orbit

## **Greek Symbols**

Symbol	Description
$\mu_E$	Earth gravitational parameter
$\omega_p$	Argument of Perigee
$ ho_{atm}$	Atmospheric density
$\sigma$	Shadow function
$ au_t$	Ratio of firing time to total mission time
$ au_{orbit}$	Orbital period
$ heta_{TA}$	True Anomaly
$\varphi$	Angle of attack

Roman Symbols Kash Saddul xiii

## **Roman Symbols**

Symbol	Description
$A_{\hat{p}}$	Projected area in the direction $\hat{p}$
$A_{\hat{v}}$	Projected area in the velocity direction
$C_D$	Drag coefficient
$C_L$	Lift coefficient
$C_R$	Satellite coefficient of reflectivity
$F_{10.7}$	Solar flux index at 10.7 cm wavelength
$I_{sp}$	Specific impulse
$R_E$	Nominal Earth radius
$R_{Sun}$	Nominal Sun radius
$T_p$	Thrust-to-power ratio
$\Omega$	Right Ascension of Ascending Node
$\bar{F}_{10.7}$	81-day running average of $F_{10.7}$
A	Direction Cosine Matrix
I	Satellite inertia matrix
$\vec{ au}_{peak}$	Peak torque vector
a	Semi-major axis
$a_r$	Perturbing acceleration in the radial direction
$a_s$	Perturbing acceleration in the tangential direction
$a_w$	Perturbing acceleration in the normal direction
c	Speed of light
e	Eccentricity
$h_{orb}$	Orbital angular momentum
i	Inclination
$m_{sat}$	Satellite mass
n	Mean motion
p	Semi parameter
s	HexSat side-length
t	Time
$t_{hex}$	HexSat thickness
u	Argument of Lattitude

## Vectors

Kash Saddul xiv Vectors

Symbol	Description
$\ddot{\vec{r}}_{sat}$	Satellite orbital acceleration vector
$\hat{n}_i$	Normal vector of an STL facet
$ec{D}$	Drag force vector
$ec{L}$	Lift force vector
$\vec{\omega}$	Satellite angular velocity vector
$ec{ au}_p$	External torques
$\vec{a}_p$	Perturbing acceleration vector
$\vec{a}_{rsw}$	Perturbing acceleration in the RTW frame
$ec{q}$	Attitude quaternion
$\vec{r}_{sat}$	Satellite orbital position vector
$\vec{v}_{sat}$	Satellite orbital velocity vector

## **Declaration of Authorship**

- I, Kash Saddul, declare that this dissertation and the work presented in it are my own and have been generated by me as the result of my own original research. I confirm that:
  - 1. This work was done wholly or mainly while in candidature for a degree at this University;
  - 2. Where any part of this thesis has previously been submitted for any other qualification at this University or any other institution, this is always clearly attributed;
  - 3. Where I have consulted the published work of others, this is always clearly attributed;
  - 4. Where I have quoted from the work of others, the source is always given. With the exception of such quotations, this thesis is entirely my own work;
  - 5. I have acknowledged all main sources of help;
  - 6. Where the thesis is based on work done by myself jointly with others, I have made clear exactly what was done by others and what I have contributed myself;
  - 7. Either none of this work has been published before submission, or parts of this work have been published as:
    - Journal papers:
      - K. Saddul, J. Saletes, M. Kim, and A. Wittig, "Mission analysis of a 1U CubeSat post-mission disposal using a thin-film vacuum arc thruster," *Acta Astronautica*, vol. 219, pp. 318–328, 6 2024.
      - K. Saddul, J. Saletes, M. Kim, and A. Wittig, "HexSats: A novel flat hexagonal nanosatellite for high-power applications," *Acta Astronautica*, vol. 225, pp. 27–40, 12 2024.
      - J. Saletes, K. Saddul, A. Wittig, and M. Kim, "Implementation of direct battery driven discharge in triggerless operation of vacuum arc thrusters," *Journal of Electric Propulsion*, vol. 3, p. 4, 1 2024.
    - Conference Proceedings:

Kash Saddul xvi Vectors

 K. Saddul, A. Wittig, J. Saletes, and M. Kim, "End-Of-Life Disposal of Sub-3U CubeSat with a printed thin-film Vacuum Arc Thruster," in *Proceedings of the International Astronautical Congress*, 2022.

 J. Saletes, M. Kim, K. Saddul, A. Wittig, K. Honda, and P. Katila, "Development of a novel CubeSat de-orbiting all printed propulsion system," Space Propulsion, 2022.

#### • Technical Reports:

 J. Saletes, K. Saddul, M. K. Kim, and A. Wittig, "Innovative propulsion systems for CubeSats and MicroSats-EXPRO+: CubeSat de-orbit ALlprinted Propulsion System Final Report," tech. rep., 2022.

## Acknowledgements

Reflecting upon my experience, many people have helped me complete this thesis. At the front of this list, I would like to express my most sincere gratitude to my lead supervisor, Dr. Alexander Wittig, for his support and guidance. He provided invaluable mentorship throughout my academic journey. His insights, feedback, and tireless commitment to precision have been instrumental for my professional development, shaping me into a better engineer.

Additionally, I am also grateful to my co-supervisor, Dr. Minkwan Kim, whose visionary ideas led to this exciting project in collaboration with the European Space Agency.

I would also like to thank James Saletes, a colleague and dear friend, whose presence made the challenges of the lockdown and other difficult times more bearable.

I extend my gratitude to all my colleagues and friends in the Boldrewood office, who have kept me motivated and made the long office hours more enjoyable. Last but not least, I am forever grateful to my family and friends for their unconditional support, patience and understanding.

Kash Saddul 2 Vectors

"It has often proved true that the dream of yesterday is the hope of today, and the reality of tomorrow."

—Robert Goddard

Vectors Kash Saddul 3

"It all starts with an idea."

-Ralitsa Stoyanova

# 1

## Introduction

In November 1971, the world's first microprocessor, the Intel 4004 was released [5]. This 4-bit processor paved the way for modern technology, sparking a global trend towards miniaturisation. The development of smaller and more powerful microprocessors rippled across the supply chain, enabling newer electronics to be increasingly small and more performant. Many fields have leapt forward, enabling downsized and enhanced technologies. Nowadays, a typical smartphone has more computing power than the Launch Vehicle Digital Computer, the onboard computer for the Saturn V rocket, which landed the first humans on the Moon [6]. The camera from those hand-held devices also provides much better resolution than the 3 kg camera used for the Apollo 11 mission.

Group name	Mass [kg]		
Large	> 1000		
Medium	501 to 1000		
Mini	101 to 500		
Micro	11 to 100		
Nano	1.1 to 10		
Pico	0.1 to 1		
Femto	< 0.1		

Table 1.1: Satellite class names based on mass, according to NASA [2].

The ripple effects of this miniaturisation trend have since reached the space industry, revolutionising how satellites are designed and manufactured. With the use of miniaturised

electronics, satellite instruments have become ever smaller and cheaper. Downsized satellites can now provide the performance of large, heavy spacecraft. Beyond being cheaper to launch, a smaller, lighter satellite is faster to design and manufacture [7]. The lower overall cost has contributed to their popularity and led to many different satellite groups with different masses. The names of each group, with their corresponding masses, are shown in Table [1.1].

A particularly popular satellite group is the nanosatellite, which has a mass in the range of 1.1 to 10 kg. Its popularity is due to the existence of standardised form factors for nanosatellites, which minimise design and manufacturing efforts. The standards ensure a uniform interface with the launch vehicle, which lowers the efforts required during the design phase. On top of this, thanks to their low-cost philosophy, nanosatellite operators do not typically design all parts of the spacecraft themselves. Instead, they commonly use commercially available devices, called Commercial-Off-The-Shelf (COTS) components, enabling operators to further minimise costs and accelerate the development time of a spacecraft. Typically, large-scale Earth observation satellites cost in the tens to hundreds of millions of dollars, while CubeSats cost in the hundreds of thousands [8, 9].

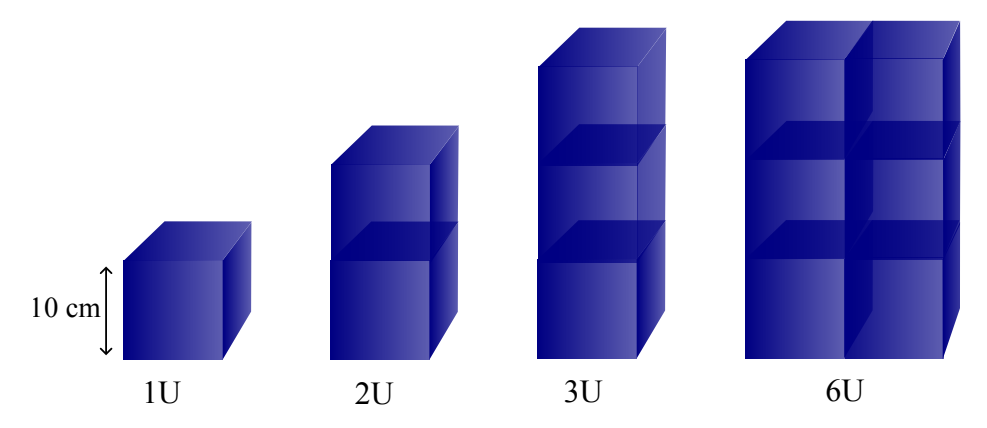


Figure 1.1: Illustration of different CubeSat configurations.

According to the National Aeronautics and Space Administration (NASA) s report on small satellite technology, the state-of-the-art of standardised nanosatellite architectures are Cube-Sats and PocketCubes [10]. A CubeSat is a miniaturised, scalable satellite developed in 1999 by Jordi Puig-Suari which has a base unit of a 10 cm cube, called a 1U [11]. Typically, a 1U has a mass of 1.33 kg, although a recent version of the CubeSat standard allows it to go up to 2 kg [12]. Larger CubeSats can be built by stacking multiple units together in different configurations, as shown in Figure [1.1]. PocketQubes are similar to CubeSats, but have a base unit of a 5 cm cube (1P). Although they present a similar form factor, CubeSats have remained significantly more popular than PocketQubes. As of 2023, PocketQubes accounted for 3.2% of all nanosatellite launches, while CubeSats made up 92.8% [13]. The

most popular CubeSat class, the 3U, accounted for 40.9% of all launched nanosatellites.

However, the standardisation of nanosatellite to a box-like structure has also come with its own challenges. The restricted surface area makes power generation difficult for many CubeSats, especially in the smaller range, below 3U (sub-3U). Typically, a 1U will generate up to 2.3 W of orbit-average power assuming all six faces are covered in solar panels, while a 3U can generate up to 15 W without deployable solar panels [14]. Using highly efficient solar arrays, 6U CubeSats can generate around 25 W of peak power. However, the restricted surface area must accommodate many subsystems, such as thermal control, communication antennas and payload instruments. Fitting all these subsystems on a Cube-Sat's surface while meeting the power requirement has proved challenging, and thus, many nanosatellites are equipped with deployable solar arrays to meet their mission requirements. Yet, even with deployable arrays, the exacting mass and volume requirement of CubeSats tends to prohibit many COTS components from being placed onboard, especially for sub-3U. Significant trade-offs have been necessary to fit mission-critical subsystems into Cube-Sats, with all non-essential equipment being usually excluded. For example, 1U CubeSats commonly dismiss COTS Attitude Determination and Control System (ADCS), as they tend to be too power-intensive. The CubeADCS, a commercially available ADCS package from CubeSPACE, consumes on its own an average of 1.9 W, which would leave 0.4 W for the payload and other subsystems [15]. While the power consumption alone is enough to dismiss the CubeADCS, it not the only limiting factor, as a standard version of the CubeADCS requires a 0.5U volume, and weighs over 400 grams. Priority is therefore frequently given to the instruments or other critical subsystems.

Such concessions mean many CubeSats are limited compared to larger satellites, despite the high performance of their miniaturised instruments. In particular, CubeSats rarely include both active attitude and orbit actuation subsystems in their design, as they are heavy, voluminous, and power-intensive components [16, 17]. Passive attitude stabilisation methods, such as aerodynamic stabilisation, gravity gradient or Passive Magnetic Attitude Control System (PMACS), can be used but have limited performance because they depend on environmental conditions [18, 19]. Passive aerodynamic stabilisation requires aerodynamic surfaces interacting with the air to generate torques that orient the CubeSat with the velocity direction, while PMACS uses permeable magnetic materials and a permanent magnet to align the CubeSat with the local magnetic field. Gravity gradient uses the Earth's gravitational field to induce a torque on an elongated satellite to align its axis along the local vertical passively. However, in the case of 1U CubeSats, this is difficult to achieve due to the symmetry of their box-like structure [3]. While they require no power, these methods only provide stabilisation around two axes.

If a CubeSat has no onboard actuation or uses passive stabilisation methods, it often remains under-actuated, severely affecting its operation. Under-actuation typically results in a CubeSat tumbling uncontrollably around at least one axis. Unlike active actuation systems, passive stabilisation is inflexible and does not allow a CubeSat to re-orient itself once deployed in space. In this scenario, the CubeSat cannot perform any manoeuvres to change its orientation or actively control its angular velocity.

Since most missions require at least modest pointing accuracy to transmit the collected data to Earth, smaller CubeSats frequently dismiss their orbital actuation system to enable pointing control, although larger CubeSats can accommodate both. Earth observation and remote sensing missions, which account for 46% of CubeSat launches [20], will also require monitoring specific regions of the Earth and possibly tracking targets on the ground. Astronomy and astrophysics missions typically have much more rigorous pointing requirements and therefore require more capable actuation systems. For example, the Bright Target Explorer [BRITE] and Arcsecond Space Telescope Enabling Research in Astrophysics (ASTERIA) missions were 10 kg 8Us and 6Us respectively, equipped with reaction wheels and magnetorquers [21], [22]. The attitude control system was mission-critical and could not be excluded, so both CubeSats were without propulsion systems.

The CubeSat's operation is limited when the orbit actuation system is omitted, as it cannot change its trajectory. This leaves the CubeSat unable to avoid a collision, compensate for perturbations, or provide early de-orbiting. The exclusion of orbital manoeuvres also limits nanosatellites' range of operation altitudes. Without thrusters, a satellite orbiting at low altitudes will experience high drag forces, which will de-orbit the spacecraft quickly. However, a satellite orbiting at very high altitudes will experience a negligible drag force and could take hundreds to thousands of years to de-orbit, contributing to the growing space debris population. Without a propulsion system to compensate for drag or accelerate de-orbiting, nanosatellites typically stay above 400 km to avoid de-orbiting prematurely and below 650 km to de-orbit within a time specified by international guidelines.

This limited operational range, which corresponds to a maximum of 3% change in the orbit's semi-major axis, a measure of an orbit's size, significantly limits the use of nanosatellites. Many orbits above 650 km are interesting for both scientific and commercial purposes. At higher altitudes, spacecraft instruments benefit from a wider Field Of View (FOV), allowing them to observe a greater area. This is particularly useful for global weather monitoring or communication missions which require wide coverage. Satellites also orbit slower relative to the Earth at higher altitudes, allowing spacecraft to monitor a given target for longer.

Unfortunately, operating at higher altitudes presents challenges. The most densely popu-

lated region of space is the 650 -1000 km band, with the highest density at 800 km [23]. Spacecraft operating in this zone have a higher risk of collision and should minimise the chances of generating space debris. Many space agencies, such as European Space Agency (ESA) or the Inter-Agency Space Debris Coordination Committee (IADC) provide guidelines for reducing the growth of the space debris population. One such measure, called post-mission disposal, recommends that once spacecraft in LEO are no longer operational, they should be de-orbited quickly. Many studies on the impact of post-mission disposal regulations have shown the importance of disposing defunct satellites [24]. This has led the ADC to recommend that a non-operational satellite should be de-orbited within 25 years of its end-of-life. This guideline, colloquially known as the 25-year rule, was adopted by many agencies. More recently, ESA committed to a zero-debris approach and changed the recommendation to a 5-year rule. However, above 650 km, the thin atmospheric density has a very weak effect on the orbital trajectory. CubeSats just above 650 km will take more than 30 years to de-orbit, which is much longer than even the ADC suggests. Therefore, without an orbital propulsion system to actively de-orbit, nanosatellites have been generally contained to lower altitudes, to guarantee passive orbital decay. This reliance on the environment can be problematic, as environmental conditions are hard to predict, and can lead to significant changes in the de-orbiting time at a given altitude. This variation could also mean that an operational satellite will de-orbit before it is defunct [25]. An actuation system would then provide nanosatellites with greatly needed flexibility in their operation, whether it allows them to operate at higher altitudes and de-orbit quickly, or to extend the mission lifetime at lower altitudes.

Alternatively, operating below 400 km would allow nanosatellites to access an orbital regime that is much closer to the Earth, the Very Low Earth Orbit (VLEO) No universal definition of VLEO has been agreed upon [26]. However, the upper bounds of 300 km, 450 km, and 500 km are commonly used [27], [28], [29]]. For the purposes of this work, I consider an orbit in the VLEO regime if it is below 400 km. The proximity of the VLEO regime to the Earth's surface provides many benefits, as outlined in the work of Crisp et al. [30]. The shorter distance to the ground allows for increased data resolution and lower latency, improving performance for the same instruments. Alternatively, operating closer to the Earth enables lower-grade instruments to perform as well as high-quality equipment used at higher altitudes. This capability can potentially allow operators to save up to 75% on the system mass compared to an equivalent mission at a higher altitude [28]. The low altitude of VLEO also makes it more cost-effective to deploy satellites into orbit. As the satellites do not need to be launched far away, operators can either save on fuel, or increase the mass of the spacecraft. All these benefits have led to an interest in using this regime for commercial applications [27]. An additional benefit for satellites operating in VLEO is the higher resilience to the

proliferation of space debris. Thanks to the high atmospheric density of VLEO, most debris will rapidly re-enter the Earth's atmosphere, thus limiting the risk of collision.

However, the high atmospheric density in VLEO also presents challenges for active spacecraft. Whilst operational, satellites must compensate for the drag, which requires regularly operating onboard thrusters. For example, the Gravity field and steady state Ocean Circulation Explorer (GOCE) mission, which was launched in a 224 km orbit to measure the Earth's gravity field in with high resolution, was equipped with an ion engine to maintain its orbit [31], 32]. The thrust level required directly depends on the drag experienced, which is affected by the altitude and spacecraft geometry. Satellites in VLEO also can spend more time in the Earth's shadow, affecting the satellite's power generation. Being closer to the Earth's surface also typically results in a narrower field of view for most instruments. This impacts the number of satellites needed, based on the coverage requirements. For instance, SpaceX's Starlink constellation projects to use 4408 satellites operating in the 500 km to 600 km region but predicts 7518 satellites to operate in the 300 - 350 km band [33]. This 70% increase in the number of satellites not only inflates the cost of manufacturing, launching, and operating the constellation but also raises sustainability concerns [34]. The greater number of spacecraft increases the risk of collisions, which in turn generates undesired space debris.

For many operators, the incentive to operate nanosatellites outside their current operational range is greater than the associated disadvantages. To achieve this, a small, low-power and versatile actuation system is needed to provide orbit and attitude actuation to all nanosatellites, including the smaller range of CubeSats. To address this need, the University of Southampton is developing the  $D\mu PS$ , a novel flat, distributed propulsion system designed for small CubeSats, which is composed of many individual thrusters mounted on the satellite structure [35] II. This thesis focuses on the mission analysis and design applications of this propulsion system, contributing two novel mission concepts to expand the operational envelope of nanosatellites. The first mission, a deorbiting mission using the D $\mu$ PS on a 1U CubeSat, was developed as part of an ESA project led by Dr. Min Kwan Kim, and demonstrates operation at higher altitudes [36]. The second mission introduces a highpower VLEO mission using the D $\mu$ PS on HexSat, a novel flat satellite architecture based on the DiskSat concept, and developed during this work.

The thesis is structured as follows: Chapter presents a review of the current state-of-the-art propulsion systems for nanosatellites, to show the lack of existing adequate systems. The development of a new propulsion system for use on nanosatellites, the  $D\mu PS_{ij}$  is summarised from Saletes et al. in Chapter 3 [II] 35, 36]. Due to the distributed architecture of the  $D\mu PS$ , a bespoke spacecraft dynamics simulator is required to accurately model the effect of the thrust and associated control laws on orbital and attitude dynamics. The fundamentals of satellite motion are thus outlined in Chapter 4, and the design of the Comprehensive Attitude and Orbital Simulator is then detailed in Chapter 5. For the first novel application, I apply the distributed propulsion system to the problem of de-orbiting a 1U CubeSat in Chapter 6 and extend their operational ceiling to 1400 km. Then, the operation of nanosatellites with the distributed propulsion system in VLEO is considered in Chapter 7 through the introduction of HexSats, a novel flat satellite form factor orbiting at 250 km of altitude while providing over 100 W of power.

## Manoeuvrability of nanoSats

This chapter examines the current state-of-the-art actuation systems for providing orbital and attitude control to nanosatellites, establishing the technological context for the distributed micro-propulsion system proposed in this thesis. Traditional chemical propulsion systems face significant miniaturization challenges due to their reliance on pressurized tanks, propellant feed systems, and combustion chambers, making them suboptimal for nanosatellite applications. Electric propulsion technologies like Gridded Ion Thrusters and Hall Effect Thrusters offer high efficiency but resist effective downsizing due to increasing erosion rates and prohibitive power demands. Similarly, reaction wheels and magnetorquers, commonly used for attitude control, encounter performance limitations when scaled down. Through systematic evaluation of existing technologies, electrospray thrusters and vacuum arc thrusters emerge as the most promising candidates for miniaturized propulsion on nanosatellites—laying the foundation for the novel  $D\mu PS$  system introduced in Chapter 3 that addresses these identified limitations.

#### 2.1 Orbital actuation

Orbital actuation devices refer to systems capable of actively changing the orbital trajectory of a satellite. They are typically used to deploy the spacecraft into a different orbit or to compensate for natural perturbations to maintain the spacecraft's current orbit. This capability is crucial to allow nanosatellites to perform outside their current operational range. I review

different thrust generation principles and discuss their limitations regarding miniaturisation for nanosatellites.

#### **Chemical propulsion**

Chemical propulsion systems offer an attractive option for spacecraft because they deliver high thrust, perform impulsive manoeuvres, and leverage an extensive flight heritage. However, the CubeSat design standard imposes a limitation of 100 Wh on the onboard chemical energy storage [12]. It is equivalent to 19 g of hydrazine, one of the most popular propellants, restricting the widespread adoption of such systems for nanosatellite missions [37]. Nonetheless, chemical thruster technologies have successfully flown on CubeSat platforms.

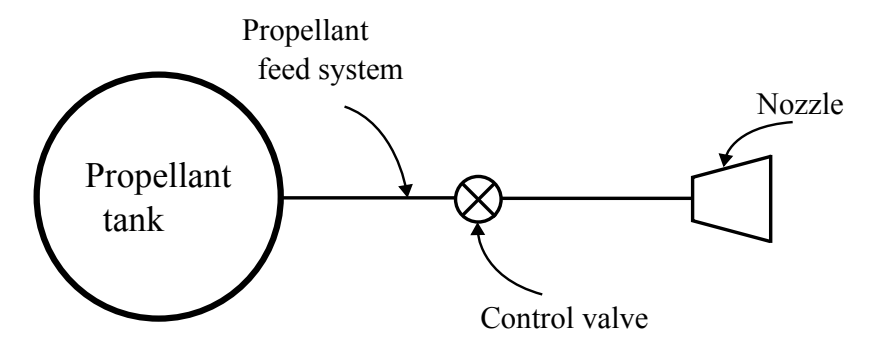


Figure 2.1: Cold Gas Thruster thrust generation principle.

The cold gas thruster represents the simplest form of chemical propulsion system. It stores a compressed gas propellant and relies solely on its pressure to generate thrust, as depicted on Figure [2.1] This design offers advantages such as low cost, robustness, and ease of integration [38]. Nonetheless, they require a pressurised tank and a propellant feed system, significantly increasing their mass and volume. They are characterised by the specific impulse ( $I_{sp}$ ), a measure of propellant efficiency, typically in the 30-150 s range and their thrust reduces as the propellant is depleted. While adding heaters can help maintain the thrust by increasing the propellant temperature, this solution adds complexity and power consumption. Cold gas thrusters are thus best suited for low-impulse manoeuvres, such as attitude control and drag compensation [37]. Despite their limitations, they have flight heritage on CubeSats, as demonstrated by the Tyvak Nanosatellite Systems' CubeSat Proximity Operations Demonstration (CPOD) mission, which used a cold gas thruster to achieve docking of 3U CubeSats [39, 40]. This thruster has a mass of 1.3 kg and fits in a 0.8U volume [41], making it inadequate for small nanosatellites, such as CubeSats under 3U.

Liquid monopropellant thrusters have been popular for spacecraft with high mass. Similarly to cold gas thrusters, they operate using pressurised propellant but achieve higher thrust lev-

els and propellant efficiency through an exothermic decomposition process catalysed by a reactive agent [38], as shown in Figure 2.2. This chemical reaction releases thermal energy, enhancing the performance compared to cold gas systems, with the  $I_{sp}$  typically around 200-250 s. Hydrazine's high fuel efficiency has historically made it an attractive option. An example of a miniaturised monopropellant thruster using hydrazine is Aerojet Rocketdyne's MPS-120. However, the thruster weighs 1.48 kg, takes the entire volume of a 1U CubeSat and requires at least 10 W of power, making it unsuitable for smaller CubeSats. Hydrazine is also highly toxic and requires specialised storage, making it expensive and impractical for many nanosatellites [37], [42]. Even ESA have considered moving away from this propellant due to safety concerns [43]. Hydrazine can also self-combust accidentally at room temperature, raising safety risks and associated costs to mitigate this effect. The limitations

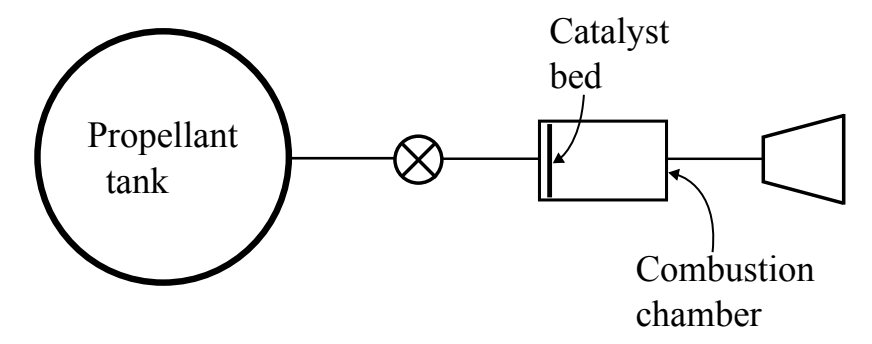


Figure 2.2: Liquid monopropellant thruster thrust generation principle.

associated with hydrazine have driven the development of "green" propellants with lower toxicity and simpler storage needs. These propellants, such as Ammonium Dinitramide (ADN), offer advantages including higher density and easier storage but require significant preheating [38] [37]. This adds to the complexity and can triple the power requirement of the thruster. As a result, liquid monopropellant thrusters are not frequently considered for nanosatellites.

While solid propellant thrusters offer more straightforward storage and handling than liquid propellant systems, they are unsuitable for nanosatellite applications. These thrusters consist of a solid propellant material housed within a robust casing. The propellant material is a premixed combination of fuel and oxidiser, eliminating the need for separate tanks and complex propellant feed systems. The ignition process triggers a rapid, self-sustaining combustion reaction within the propellant material. The reaction's hot, high-pressure gases are then channelled through a precisely designed nozzle, generating the thrust. A depiction of the thrust generation principle is illustrated in Figure 2.3. However, a notable limitation of solid propellant thrusters is their inability to be deactivated once ignited, and they offer limited thrust control capabilities [44]. This drawback means solid propellant thrusters are not used when precise impulse delivery is needed, such as in attitude control. The requirement for a

nozzle also leads them to be typically voluminous and heavy, leading them to be inadequate for nanosatellites. The lack of data on their use in CubeSat applications also shows that solid propellant thrusters are not used for nanosatellite missions [38] [45].

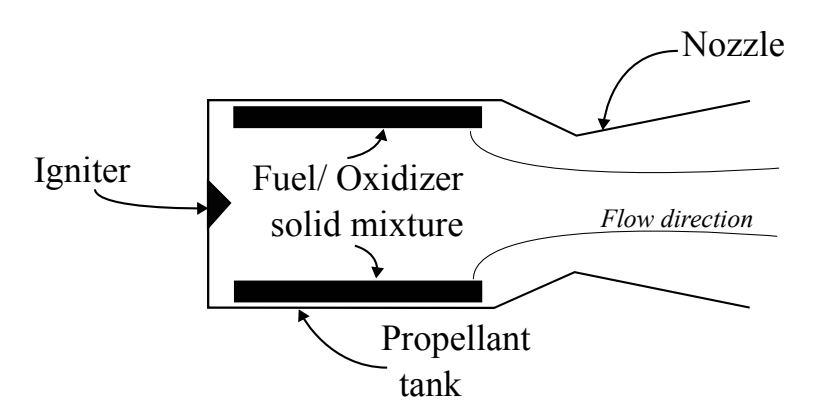


Figure 2.3: Solid propellant thruster thrust generation principle.

In conclusion, chemical propulsion systems typically offer a high thrust and strong flight heritage but face miniaturisation and propellant limitations for CubeSats. Cold gas thrusters are the most common option due to their simplicity, but they suffer from low efficiency and thrust degradation over time. Liquid and solid options perform better but introduce drawbacks like size constraints, safety concerns, and limited controllability. While offering potential, the miniaturisation challenges and associated costs necessitate careful consideration. The cost associated with the rigorous testing required often makes these complex systems prohibitive for the smaller range of CubeSats. As a result, one can turn to electric propulsion systems to provide appreciable impulse at small dimensions.

#### **Electric propulsion**

Electric Propulsion (EP) systems are particularly interesting for CubeSats, as they typically present high fuel efficiency [46], leading to a smaller amount of fuel required, which could save mass and volume on the spacecraft. However, their implementation is not straightforward, as EP systems tend to come with heavy electronic components and high power requirements [45]. Still, research has been ongoing in miniaturising the most popular EP technologies to fit them on nanosatellites. The thrust generation principle of Gridded Ion [Thrusters (GITs), Hall Effect Thrusters (HETs)], Field Emission Electric Propulsion (FEEP) and Vacuum Arc Thrusters (VATs) are outlined below. The current state of miniaturisation efforts and associated limitations for these respective electric propulsion technologies are also discussed.

#### **Gridded Ion Thrusters**

GITs are electric propulsion systems that achieve high specific impulse by expelling ionised particles at very high velocities. These thrusters use an inert gaseous propellant, commonly Xenon, which undergoes an ionisation process facilitated by microwaves, radio frequencies, or an electron beam. Then, a series of charged grids accelerate the ionised propellant to generate thrust, typically in the milli-Newtons. Figure 2.4 illustrates the thrust generation principle. However, gridded ion thrusters are difficult to miniaturise. One major challenge is grid erosion. Due to the attraction between ions and the charged grids, a small portion of the ions collide with the grid structure, causing erosion damage. Over long operational periods, this erosion can reach critical levels, leading to thruster failure. As the thruster's size diminishes for miniaturisation, the erosion rate increases, leading to shorter operational lifetimes. An additional challenge with GITs is the necessity for a neutraliser. This component releases electrons into the thruster plume, neutralising the ions' positive charge. This neutralisation step prevents the build-up of positive charge on the spacecraft's surface, which could disrupt its electrical systems.

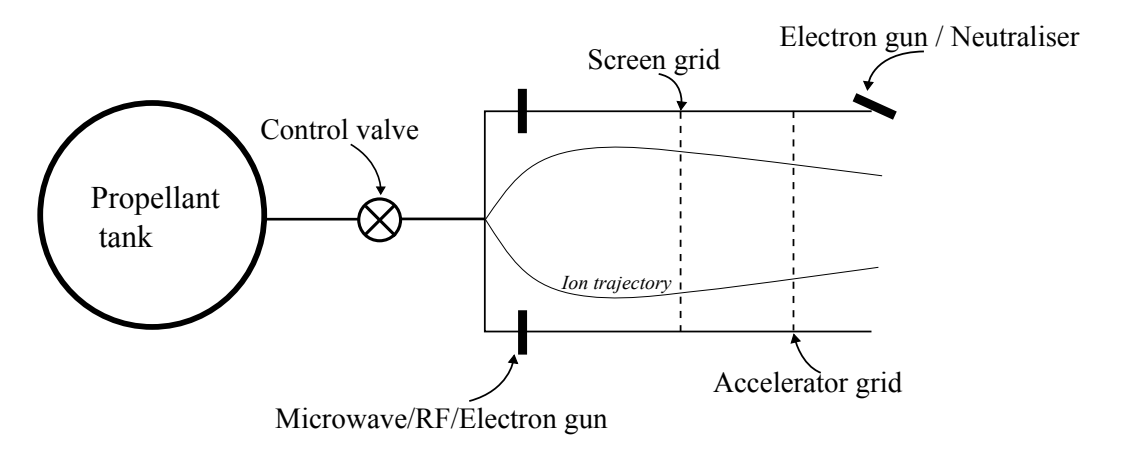


Figure 2.4: Gridded Ion Thrusters thrust generation principle.

The need for an ionisation process, a charged grid, and a neutraliser mean that GITs are typically heavy, voluminous, and power-intensive. NASA's state-of-the-art report on GITs [10] for small satellites lists seven GITs, with only one that could be fitted on a 1U, the Ariane Group RIT- $\mu$ X. Indeed, the other GITs presented in the report have a mass greater than 1.33 kg, the maximum mass of a typical 1U CubeSat [12]. The Ariane Group RIT- $\mu$ X is also the least power-consuming of all the GITs shown and typically uses up to 50 W of power. An experimental, miniaturised version of the RIT- $\mu$ X, known as the RIT-2.5, was developed with a diameter of 25 mm [47]. This downsized thruster provides 575  $\mu$ N of thrust at 34.4 W of power. Pennsylvania State University also studied a 25 mm gridded ion thruster capable of operating at 8W and producing 217  $\mu$ N of thrust, called the Miniature

Microwave Frequency Ion Thruster (MMIT) [48]. Another thruster developed at the same university is the Miniature Radio Frequency Ion Thruster (MRIT), a 1 cm thruster capable of delivering 59  $\mu$ N of thrust at 13 W of power, with an  $I_{sp}$  of 5480 s [49]. However, as previously stated, 1U CubeSats typically cannot generate more than 2 W of power, and 3U can generally produce up to 15 W of peak power, assuming highly efficient solar panels on all six faces [14, 50]. While CubeSats of the 3U class or larger could accommodate the miniaturised GITs, they would also require a fuel tank, and the associated propellant feed system, which can be prohibitively heavy, voluminous, and expensive for nanosatellites. These constraints mean that current GITs are unlikely to be used on the smaller range of CubeSats, as they meet neither the mass, volume or power budget required.

#### **Hall Effect Thrusters**

Hall Effect Thrusters are the most popular type of EP and have reasonable flight heritage on CubeSats [7]. Unlike gridded ion thrusters, HETs employ a magnetic field instead of charged grids. A primary propellant, typically Xenon again, is injected into the thruster and undergoes ionisation. A strong radial magnetic field then traps the freed electrons, preventing them from exiting. The electron cloud, acting like a 'virtual' charged grid, attracts the ionised propellant towards the exhaust, generating thrust as depicted on Figure 2.5 Efforts to downsize HETs have been challenging due to the higher surface-to-volume ratios in the ionisation chamber, and the resulting increased erosion rates have limited their operational lifetime [51]. Attempts to mitigate this issue often involve implementing magnetic shielding of the wall. However, this solution comes at the cost of complicating the magnetic circuitry, an already power-intensive subsystem [52].

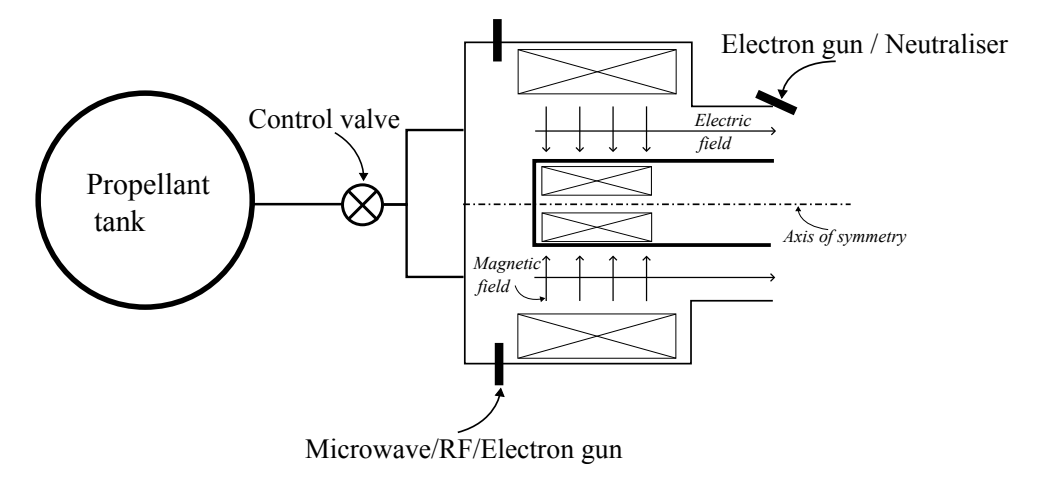


Figure 2.5: Hall Effect Thrusters thrust generation principle.

Many experimental miniature thrusters have been developed, with few that could be consid-

ered for use on CubeSats. The Space Flight Laboratory in Canada has developed a HET with a 26 mm head capable of operating within the 50-200 W range [53]. An even lower power HET, presenting a 24 mm diameter and operating on 25 W, was developed by the Plasma Sources and Applications Centre/Space Propulsion Centre in Singapore [54]. Similarly, the TCHT-4, developed at the Osaka Institute of Technology in Japan, is a 7 x 14 mm cylindrical thruster that has a power range as low as 10 W, providing a specific impulse of 350 s [55]. Its peak efficiency occurs at 66 W with an Isp of 1580 s. According to Yeo et al. [52], only one miniature HET has successfully flown in Earth orbit, the ExoMG-nano [56]. Developed by Exotrail, it features an external tank measuring 3.5 cm, producing a thrust of 2 mN at a power of 53 W. Similarly to GITs, the size of the HETs thruster themselves can be miniaturised to fit on nanosatellites. However, while the demanding power requirements of HETs could fit on larger CubeSats, they are prohibitive to the smaller range. A propellant tank and propellant feed system must also be incorporated, similarly to GITs. Again, this leads HETs to be currently unsuitable for the smaller range of CubeSats.

#### **VLEO-specific propulsion**

For operations in VLEO, air-breathing electric propulsion represents an area of ongoing research [29]. It enables long-duration missions at altitudes traditionally limited by high atmospheric drag. Air-breathing systems collect the atmospheric particles along the orbital path —primarily oxygen and nitrogen, which are then ionised and accelerated to produce thrust similarly to HETs or GITs [29, 57]. This allows spacecraft to remain in VLEO with little to no onboard propellant. Multiple studies and initiatives reinforce the concept's potential, particularly at altitudes below 350 km, where conventional electric propulsion becomes less viable due to high drag and orbital decay. For example, the AETHER project, funded under the EU's Horizon 2020 programme, has tested an air-breathing thruster capable of compensating drag under variable atmospheric conditions [58]. The project highlighted two parallel acceleration technologies: one using crossed electric and magnetic fields -similar to HETs, and another relying on electrostatic charge separation -closer to the thrust generation principle of GITs.

Complementing this, Crandall and Wirz analysed air-breathing propulsion systems for Cube-Sats, showing that for spacecraft below 220 km, it is the only propulsion solution capable of supporting mission durations of three years or longer [59]. The work emphasised the importance of non-dimensional coefficients, such as spacecraft length-to-width ratio, and the critical influence of inlet efficiency, thrust-to-power ratio, and drag reduction on the system's overall performance. However, the proposed Super Low Perigee Orbit (SuLPO)

concept is still beyond the reach of CubeSats due to a high required operational power of 200 W. Despite this limitation, research is ongoing to develop air-breathing propulsion solutions for VLEO applications [29, 57, 60].

#### **Electrospray thrusters**

Electrospray thrusters are a form of EP suitable for the smaller end of CubeSats [7] 38], as some have low mass, volume, and power requirements. Their operating principle relies on a strong electrostatic field to extract and accelerate ions directly from an emitter which stores conductive liquid propellant [7], as shown in Figure 2.6. This process generates a beam of charged particles, positive or negative ions, depending on the propellant, which, in some cases, eliminates the need for a neutralizer due to the inherent charge balance within the plume. Ionic propellants are often preferred for electrospray thrusters due to their favourable properties, such as high conductivity and the absence of preheating reguirements [45]. However, the emitters themselves can be expensive to manufacture [61]. The high cost stems from their small size and need for precise features. These tiny nozzles, often with microscopic holes or sharp edges, require specialised manufacturing techniques like micro-machining or chemical etching. These processes can be slow, labour-intensive, or require expensive equipment and materials. The relatively low thrust generated by electrospray thrusters, typically on the micro-Newton range, leads to using multiple emitter arrays rather than a single thruster [38], increasing the overall costs. These emitter arrays are often arranged in a grid or similar formation to achieve the desired overall thrust for spacecraft manoeuvres. Unlike HETs and GITs, they become more efficient as their size decreases and have low power and size requirements [7].

For example, the Accion Systems TILE-2 Electrospray thruster weighs 0.45 kg and requires roughly 4 W of power [62]. As it takes only 0.5U in volume, a 3U CubeSat could potentially incorporate it as an actuator. However, the mass and power requirements are still unfeasible for smaller CubeSats. To cater for Sub-3U, one could look at the NanoFEEP thruster, which was flown on the UWE-4 satellite [63], or examine experimental works. One such system, an electrospray thruster measuring 3.8 x 3.8 x 1.5 cm, was developed in the work of Natisin et al. [64]. This thruster, equipped with multiple emitters, demonstrates stable performance from 0.6 mW to 1.3 W with an observed thrust-to-power ratio of  $30\mu$ N/W. Another more compact thruster, the NanoFEEP emitter, was developed by TU Dresden [65] [66]. With a size fitting in a 3 cm³ volume, this emitter provides a thrust of 8  $\mu$ N for power in the range of 50 to 150 mW. Electrospray thrusters are thus a form of EP that present low mass, volume, and power requirements. This potential for miniaturisation makes them a good fit

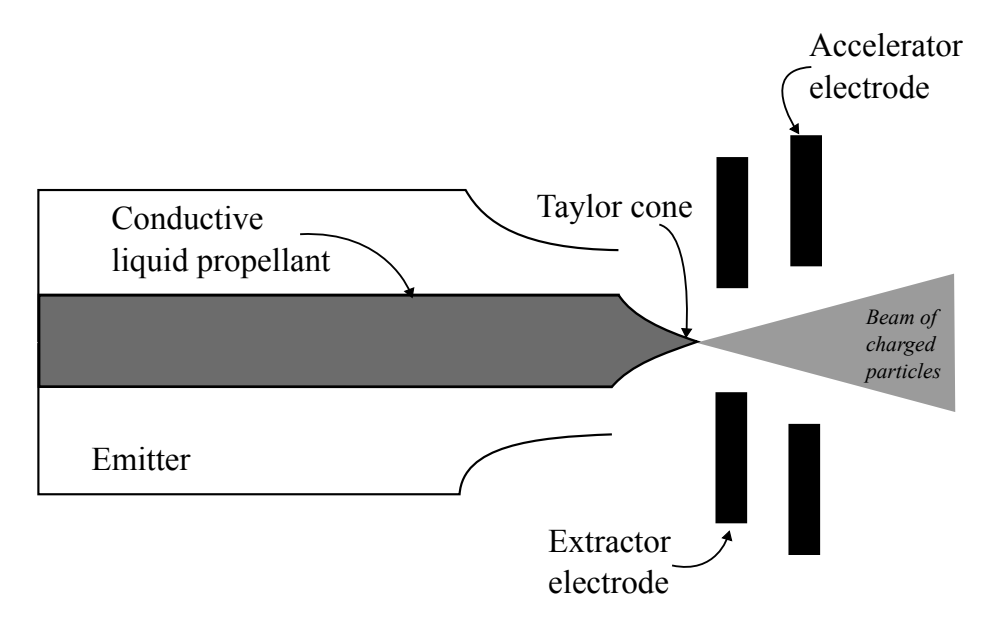


Figure 2.6: Electrosprays thrust generation principle.

for application on nanosatellites, even the smaller range of CubeSats.

#### Vacuum Arc Thrusters

VATs are an alternative that also provides easy miniaturisation, operation at low power, and use of solid propellant. They generate thrust by creating an electric arc across a solid propellant surface, as shown on Figure 2.7. This electric arc vaporises and ionises the propellant material, transforming it into a gaseous plasma state. Then, a self-induced magnetic field inherent to the electric arc accelerates the ionised particles, producing the thrust force. The simplicity of this thrust generation principle is the core reason for their easy miniaturisation and leads to their broad range of thrust and thrust-to-power ratios - up to mN-level of thrust and tens of  $\mu N/W$  of thrust-to-power ratios [67]. Combined with their power requirements, as low as 0.3 W [68, 69], VATs are very suitable for both orbital and attitude control of smaller CubeSats [70].

One example of a miniaturised thruster is the  $\mu$ CAT used onboard the BRICSat-P 1.5U CubeSat [71]. Developed by the United States Naval Academy, it is characterised by a specific impulse up to 3000 s and can operate at very low power levels. Another notable example is the Pulsed Plasma Thruster for CubeSat Propulsion (PPTCUP), jointly developed by the University of Southampton and Mars Space Ltd [68, 69]. This VAT can operate with power levels as low as 0.3 W and has a miniaturised design, fitting within a 33 mm box. The University of Illinois also developed a miniature VAT with dimensions of 4x4x4 cm. With an operational power range of 1-100 W and a thrust-to-power ratio of 10  $\mu$ N/W, this

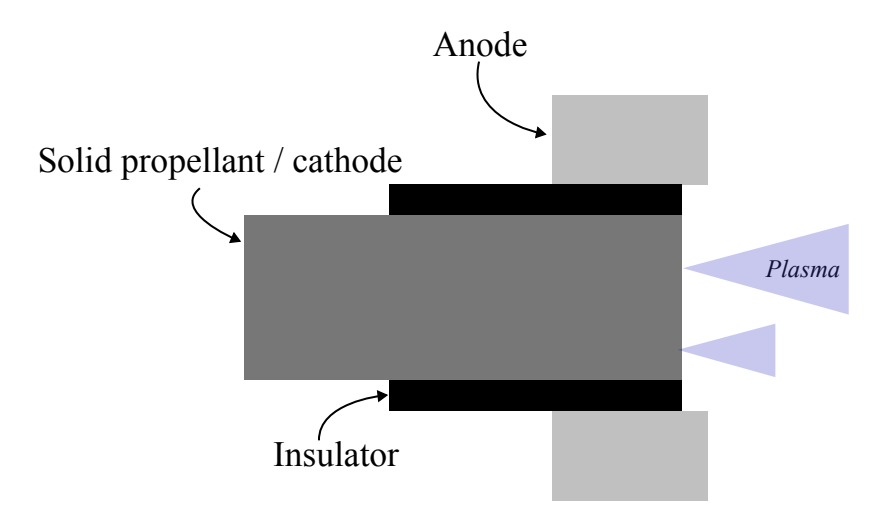


Figure 2.7: Vacuum Arc Thruster thrust generation principle.

system demonstrates that miniature VATs can still produce highly scalable thrust levels [72]. VATs are viable for use on nanosatellites, as they present low power requirements and small volume and mass. Their use of solid propellant makes for easier integration and makes them cheaper than electrospray thrusters [38].

Name	Type	Mass	Volume	Thrust	$\begin{array}{ccc} \textbf{Specific} & \textbf{im-} \\ \textbf{pulse} \ (I_{sp}) & \end{array}$	Power
C-POD	Cold gas	1.3 kg	0.8U	0.25 mN	40 s	5 W
Aerojet Rocket- dyne's MPS-120	Hydrazine monoprop.	1.48 kg	1U	25- 125 mN	206- 217 s	10 W
RIT- $\mu$ X	GIT	0.44 kg	7.8 × 7.8 × 7.6 cm	0.5 mN	-	50 W
RIT-2.5	GIT	-	-	0.575 mN	-	34.4 W
MMIT	GIT	-	-	0.217 mN		8 W
MRIT	GIT	-	-	0.59 mN	5480 s	13 W
TCHT-4	HET	-	$0.7 \times 1.4$ cm cylinder	-	350 s	10 W
ExoMG-nano	HET	-	-	2 mN	-	53 W
BHT-100	HET	1.2 kg	$275 \text{ cm}^3$	6.3 mN	1086 s	105 W
TILE-2	Electrospray	0.45 kg	0.5U	-	-	4 W
NanoFEEP	Electrospray	-	$3 \text{ cm}^3$	0.008  mN	-	0.5- 1.5 W
Illinois University VAT	VAT	-	$4 \times 4 \times 4$ cm	0.01 mN/W	-	1- 100 W
PPTCUP	VAT	-	33 mm box	-	-	0.3 W
AIS-VAT1-PQ	VAT	0.056 kg	$37 \text{ cm}^3$	0.26 mN	87 s	5 W

Table 2.1: Summary of example thrusters for nanosatellites.

Given the limitations associated with traditional propulsion systems, VATs and electrospray thrusters emerge as promising candidates for nanosatellites due to their potential for miniaturisation and low power requirements. However, precise control over the thrust direction is essential to use these actuation systems effectively [73]. The following section will review the state-of-the-art actuation systems employed for attitude control in nanosatellite applications.

While all the previously mentioned thrust generation principles and thrusters can change the course of a spacecraft, expanding the current operational range requires more than just orbital actuation devices. A thruster must provide adequate thrust in the correct direction to achieve a precise trajectory or orbit change. This creates a fundamental requirement for attitude actuation systems in spacecraft design. An orbital actuation system without attitude control would be ineffective, as the spacecraft would have no means to direct its thrust vector. The success of orbital manoeuvres then depends on accurate attitude control - the spacecraft must maintain precise orientation to apply thrust effectively. Without reliable attitude control, even a well-designed propulsion system would waste propellant and would likely move the spacecraft off-course. This relationship between attitude and orbital control means that whenever an orbital actuation system is discussed, an associated attitude actuation system must also be reviewed. Therefore, I will review attitude actuation systems commonly used onboard nanosatellites in the next section.

#### 2.2 Attitude actuation

Attitude actuation devices refer to systems capable of changing a satellite's pointing or rotational motion. They are typically used to reorient the spacecraft, provide it with tracking capabilities, or prevent uncontrolled tumbling. They are an important subsystem that allows nanosatellites to perform tasks such as accurately pointing a camera or a thruster in the correct direction. In this section, I review different popular actuation systems and discuss their limitations regarding miniaturisation for nanosatellites.

#### Passive attitude stabilisation

Due to their simplicity and minimal resource requirements, PMACS are frequently employed for attitude control in smaller CubeSat missions [16]. These systems combine permanent magnets and rods made of a permeable magnetic material called hysteresis rods [74].

They are lightweight, typically weighing less than 100 g, require minimal space, and operate passively without consuming power. PMACS leverage the Earth's magnetic field for stabilisation. The permanent magnet aligns the CubeSat with the local magnetic field line, while the hysteresis rods dissipate angular momentum. However, this alignment introduces a constraint, as the CubeSat will point along the magnetic field line throughout its orbit. Careful positioning of the permanent magnet and the hysteresis rods is crucial for the Cube-Sat. The magnet's location dictates the CubeSat's preferred orientation, while the rods, to ensure stability, must be placed perpendicular to each other. Hysteresis rods are made from soft ferromagnetic materials, which get magnetised by an external magnetic field, leading them to act as magnets. If the rods are rotating in a magnetic field, the induced magnetic field creates a torque which dampens their motion. The size of the hysteresis rods is particularly critical. Undersized rods lack the necessary strength to effectively dampen unwanted angular motion, while oversized rods can introduce destabilising torques. The case of QuakeSat exemplifies this challenge, where its oversized rods led to uncontrolled motion after launch [75]. If the hysteresis rods are perpendicular to the local Earth magnetic field, then they are not magnetised and produce no dampening torques. This drawback renders them ineffective in dissipating angular motion around the axis of the permanent magnet, leading to a residual angular velocity remaining around that axis, which induces a slight motion in the other axes. While the changing orientation of the magnetic field along the orbit trajectory can introduce some corrective torque, a small amount of rotation around the permanent magnet axis is typically expected throughout the CubeSat's mission. Nonetheless, PMACS have allowed for successful CubeSat missions, such as the CubeSat Particle Aggregation Collision Experiement (Q-PACE), Colorado Student Space Weather Experiment (CSSWE) and the SLUCUBE-2 [76, 74, 77].

Passive aerodynamic attitude stabilisation is an alternative to PMACS, also offering a simple, resource-efficient approach to attitude control. This method uses drag from the thin atmosphere to align the satellite with the velocity direction [78, 19]. The satellite's geometry is modified to create restoring torques that dampen unwanted rotation. Aerodynamic surfaces, placed far from the centre of mass, give the satellite a shuttlecock-like appearance [79, 80], as shown in Figure 2.8. Typically, these aerodynamic surfaces are covered in solar arrays, which can provide additional power to the nanosatellite. Like PMACS, passive aerodynamic attitude stabilisation constrains the attitude of the nanosatellite and does not control all axes. The rotation around the velocity direction remains unchecked, and the motion around the other axes is never completely dampened. Careful sizing of the aerodynamic surfaces is crucial to ensure effective attitude stabilisation. Too small surfaces may not generate sufficient restoring torques, and substantial surfaces could introduce overly strong torques, preventing proper attitude stabilisation.

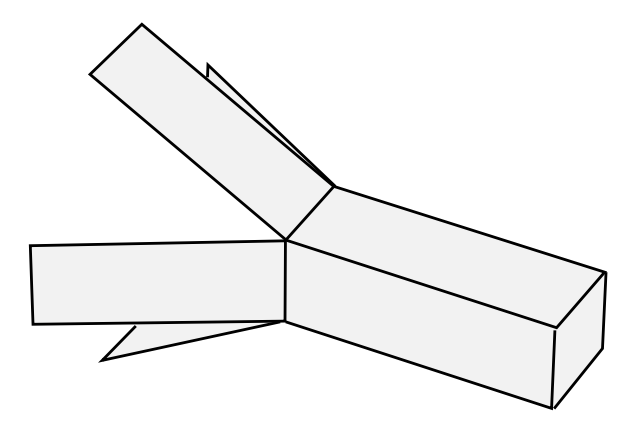


Figure 2.8: Example shuttlecock configuration of a 3U CubeSat.

Neither passive aerodynamic and/or magnetic systems can operate outside of LEO. The air density is so low at high altitudes that the required aerodynamic surfaces become impractically large, limiting their use to roughly 400-500 km. Similarly, the Earth's magnetic field weakens at higher altitudes, and torques become too weak to provide useful stabilisation. Therefore, while passive aerodynamic and magnetic stabilisation provide attitude stabilisation at low mass and no power cost, they stabilise only two axes, constrain the nanosatellite in an unchangeable attitude configuration, and can be used only up to 500 km.

Solar sail passive stabilisation offers another resource-efficient approach to attitude control, utilising solar radiation pressure instead of aerodynamic or magnetic forces. This method exploits the momentum transfer from solar photons to create restoring torques that align the spacecraft relative to the Sun vector [81] [82] [83]. The satellite requires large, lightweight reflective surfaces mounted in a pyramidal fashion away from the centre of mass, creating a stabilising effect towards the Sun. However, unlike aerodynamic stabilisation, which works against the velocity vector, or magnetic stabilisation, which aligns the spacecraft with the local magnetic field, solar sail stabilisation can operate at orbital altitudes where solar radiation pressure is significant, which extends well beyond LEO.

Like other passive methods, solar sail stabilisation cannot provide complete three-axis control. While it can maintain Sun-pointing, the rotation around the Sun vector remains underactuated. The effectiveness of the stabilisation also varies with the satellite's position in orbit, as the solar pressure changes with the angle between the sail and the Sun and disappears completely in Earth's shadow. A homogeneous operation, where the Sun vector always comes from the same direction, is then only possible in Sun-Synchronous orbits [84]. The sizing of the sail surfaces presents similar trade-offs to aerodynamic stabilisation. Insufficient area results in weak restoring torques, while oversized sails can lead to excessive disturbance torques. While solar sail stabilisation and passive aerodynamic both use control surfaces in a "flow" to control the attitude of a spacecraft, the relative weakness of

solar radiation pressure leads solar sails to have a much greater surface area than their aerodynamic counterparts. This means that at lower altitudes, they will also experience greater drag forces, which will shorten the spacecraft's lifetime and disrupt the stabilisation with respect to the Sun vector.

As passive aerodynamic and magnetic stabilisation systems cannot be used at altitudes higher than the current operational range of nanosatellites, they are not considered suitable for the aims of this thesis. Reversedly, solar sail stabilisation is only viable for operation at high altitudes and cannot operate closer to the Earth, and is therefore also not considered suitable for the aims of this thesis. Therefore, active attitude actuation systems are now examined.

#### Magnetorquers

A natural progression from PMACS is using electromagnets instead of permanent magnets and hysteresis rods. Electromagnets consist of coils of wire that produce a magnetic field when an electric current flows through them, as depicted on Figure 2.9 [19]. The strength of this magnetic field can be controlled by adjusting the current, allowing tailored torques for attitude control. Electromagnets are also lightweight, low-power, and compact. The NASA report on the state-of-the-art for small satellites shows several electromagnets for attitude control, called magnetorquers, which weigh less than 100 grams and have a nominal power consumption below 1 watt [62]. These characteristics make them attractive for CubeSat applications, where they are commonly used for detumbling [85]. However, magnetorquer performance still depends on the environment. In order to provide the desired torque, a magnetometer is required to measure the local magnetic field. They can compensate for a weaker Earth magnetic field at higher altitudes by increasing the current, but this leads to higher power consumption, which can cause overheating and potentially damage electronics onboard the spacecraft. In practice, the operational ceiling of magnetorquers is determined by the peak magnetic field they can generate, which is limited by their design. Another limitation is that magnetorquers cannot generate a torque along the axis aligned with the local magnetic field. Rotation around the magnetic field line is then never controllable with magnetorquers. This constraint means magnetorquers are typically combined with another control mechanism to achieve complete 3-axis stabilisation of a CubeSat.

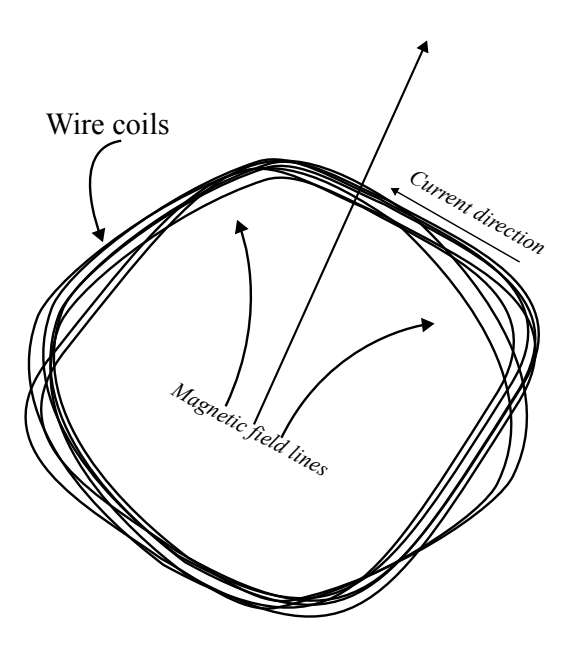


Figure 2.9: Schematic of a magnetorquer.

#### **Reaction wheels**

Reaction wheels are a popular choice for achieving precise attitude control in spacecraft [41], [62]. Their operation relies on the principle of conservation of angular momentum. By spinning up a reaction wheel onboard the satellite, an equal and opposite angular momentum is imparted to the spacecraft, causing it to rotate in the opposite direction. Complete attitude control can be achieved by placing three reaction wheels orthogonal to each other, although a pyramidal configuration involving a fourth wheel can be preferred for redundancy [19]. Reaction wheels have extensive flight heritage on CubeSats. For example, the CPOD and ASTERIA CubeSats both used three reaction wheels to provide pointing accuracy below 0.25 degrees and 0.003 degrees respectively [40], 86], 87].

However, reaction wheels operate within certain limitations. Each wheel has a maximum achievable spin rate, which translates to a finite storage capacity for angular momentum, known as the saturation point [19]. Once a wheel reaches saturation, it can no longer generate additional torque, limiting the maximum angular velocity the satellite can achieve. Due to their increased inertia, larger wheels have a greater capacity for storing angular momentum. However, this benefit comes at the cost of increased mass, volume, and power consumption. As a consequence, nanosatellites typically use smaller reaction wheels. While these offer advantages in size and power consumption, they saturate faster. Figure 2.10 shows COTS reaction wheels for different spacecraft classes. For smaller spacecraft, a lower torque is available, and the wheels will saturate faster. A reaction wheel can be de-saturated by de-spinning and transferring the angular momentum to the spacecraft. Then, an external

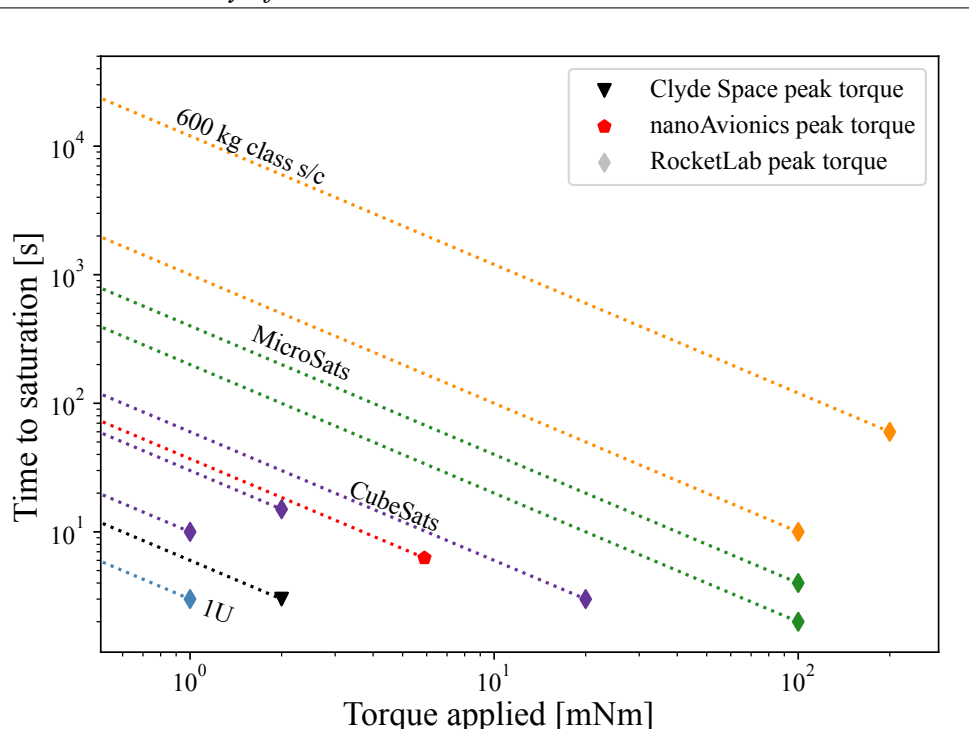


Figure 2.10: Reaction wheel applied torque against operational time to saturation.

torque is required to dampen the satellite's rotation. Magnetorquers provide one potential approach, but they necessitate complex control algorithms for de-saturation and cannot alter motion around the local magnetic field line [88]. The resulting torque then still depends on the local magnetic field strength.

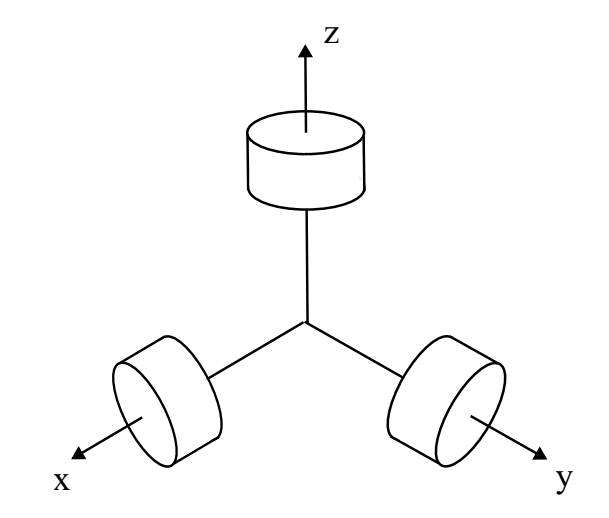


Figure 2.11: Reaction wheels in a 3-axis configuration.

As all wheels eventually saturate, they are rarely seen on their own. Instead, commercial companies offer pre-integrated ADCS solutions. These packages typically include reaction wheels for precise manoeuvring, magnetorquers for de-saturation, and attitude determination instruments. While these COTS packages boast impressive capabilities, with most

achieving sub-degree pointing accuracy, they can be prohibitively heavy and voluminous. NASA's report on the state-of-the-art of integrated ADCS shows the lightest system, the CubeADCS by CubeSPACE, which weighs only 300 grams and fits in a 0.5U volume [62]. However, this low mass comes at the expense of pointing accuracy, as the CubeADCS offers control with a 5-degree error [15]. Further miniaturisation requires smaller wheels, which in turn leads to reduced performance. The state-of-the-art of integrated ADCS shows a reaction wheel weighing only 12 g, but it saturates after applying a torque of 0.0001 Nm for one second, corresponding to a rotational speed of 2.1 deg/s for a typical 1U CubeSat.

Integrated units are mainly popular with the larger class of nanosatellites, which can easily accommodate them. However their mass, volume, and power budget must be considered along with the onboard orbital propulsion system. As a result, they tend to be unsuitable for the smaller range of CubeSat despite their high performance.

#### **Thrusters**

The same thruster systems reviewed in Section 2.1 can be adapted for attitude control. Thrusters can generate torque by producing a force not aligned with the satellite's centre of mass [19]. Since the ability to precisely control the direction of the thrust, called thrust vectoring, is not common in spacecraft propulsion, secondary thrusters are typically placed on the satellite. To achieve complete control over all three axes, a minimum of six thrusters is required, with two thrusters controlling each axis. If two thrusters placed diametrically opposite each other are fired simultaneously, they generate pure rotation without unwanted translational motion by cancelling the net force while generating a torque.

A significant advantage of using thrusters as attitude control systems is that they can also be used for orbital manoeuvres or combined attitude-orbit manoeuvres [89, 90, 91], which can remove the need for a dedicated orbital actuation system. Unlike reaction wheels, they are also not limited by a maximum angular velocity, although the onboard fuel limits the total angular momentum deliverable. The choice of thruster will directly impact the generated torque. While cold gas thrusters offer reasonable torques, they are inefficient in terms of propellant usage. They also require a dedicated propellant feed system, which adds to the system's overall mass. Electric propulsion, on the other hand, has superior efficiency but generates significantly lower torques. The use of thrusters for attitude control is not a novel concept. Large spacecraft often employ dedicated secondary thrusters for attitude control and reaction wheel de-saturation [92]. Electric thrusters have also been explored for attitude control applications due to their capacity to achieve precise pointing with low

thrust levels [93, 70, 94]. However, integrating a single thruster into a nanosatellite design can be challenging and expensive, but a minimum of six would be needed for attitude control. Therefore, a lightweight, low-power system is required to allow the smaller range of nanosatellites to use active propulsion without significantly sacrificing their mission objectives

#### **Conclusion** 2.3

reviewSThis chapter has critically examined the state-of-the-art actuation systems for nanosatellites and identified the fundamental challenges of miniaturisation that motivate this thesis. While traditional chemical thrusters provide high thrust, their heavy pressurised tanks, propellant feed systems, and combustion chambers render them impractical for nanosatellite applications. Similarly, HETs and GITs, although highly efficient, resist effective miniaturisation and maintain prohibitive power requirements. Conventional attitude control systems also present limitations: reaction wheels lose effectiveness as they downsize and require external torque for desaturation, while magnetorquers, though commonly paired with reaction wheels, cannot apply torque around the local magnetic field line. From this comprehensive analysis, electrospray and VATs technologies emerge as the most viable candidates for both orbital and attitude actuation in nanosatellites—a finding that directly informs the development of the Distributed micro-Propulsion System (D $\mu\mu$ PS) detailed in the following chapter. This gap in existing propulsion technology establishes the foundation for the novel contributions presented throughout this thesis.

# 3

### Distributed micro ( $\mu$ )-Propulsion System

Among the discussed methods for orbital and attitude control of spacecraft, electrospray and VATs offer the highest potential for miniaturisation while providing complete actuation. With their easy downscaling and high performance at small sizes, even a small 1U CubeSat could accommodate more than six miniaturised thrusters. However, with only six thrusters, a single thruster failure would cause the spacecraft to become underactuated [95]. Underactuation significantly impacts spacecraft operations, as the spacecraft might be unable to maintain its nominal attitude, compensate for environmental disturbances, or execute planned orbital manoeuvres. While underactuation due to thruster failure can affect any spacecraft using thrusters for attitude control, this is rarely a concern for satellites which rely on reaction wheels or magnetorquers, such as nanosatellites. Nevertheless, underactuation remains common in nanosatellites due to their mass, volume and power restrictions [16, 96]. Many larger CubeSats employ complex algorithms to operate with only two working reaction wheels, either due to in-operation failure or by design [97]. While literature shows that it is possible to control the CubeSat and achieve some mission objectives under these conditions, the feasibility of operation becomes increasingly challenging as attitude requirements become more stringent [98, 99]. For some high-precision pointing missions, underactuation can make operations impossible [100]. Complete three-axis actuation is therefore always preferred to allow easy operation of nanosatellites. To address potential underactuation in thruster-based systems, mounting more thrusters can provide useful redundancy. This redundancy ensures continued full actuation capability in case of individual thruster failures and enhances the satellite's manoeuvrability by allowing torque generation in multiple directions. The attitude control of nanosatellites using low-thrust electric propulsion systems has been shown to be feasible [94, 92, 93]. Multiple thrusters can be fired simultaneously to generate larger forces in specific directions, or different combinations can be used to create pure torques around desired axes, providing more flexible and robust attitude control. Furthermore, by keeping the total fuel mass constant, each thruster would hold less propellant, potentially enabling further miniaturisation. If significant miniaturisation is achieved, then the downsized propulsion systems can be placed anywhere convenient on the satellite. This provides flexibility to the thrusters to be placed anywhere while minimising disruption to the other spacecraft subsystems.

As part of a joint research project between two teams at the University of Southampton and ESA, a nanosatellite design with multiple miniature thrusters distributed along its structure was proposed [36, 35]. In this scenario, each individual thruster head, also called a pixel, would be individually addressable and provide a thrust-to-power ratio at the micro-Newton per Watt level. While each pixel is fixed on the structure and cannot provide thrust vectoring, positioning them across multiple faces enables complete three-axis actuation of the spacecraft. The satellite can then be precisely controlled by keeping the pixels re-ignitable and the thrust level scalable. In this thesis, I call such a thruster concept a Distributed micro  $(\mu)$ -Propulsion System ( $D\mu PS$ ). The term "distributed" indicates many thruster heads are spread across the satellite, while "micro-propulsion" refers to both the low thrust level and the small dimensions of the pixels. Figure 3.1 illustrates a nanosatellite with the  $D\mu PS$ . The pixels provide thrust for orbital actuation and torques for attitude control.

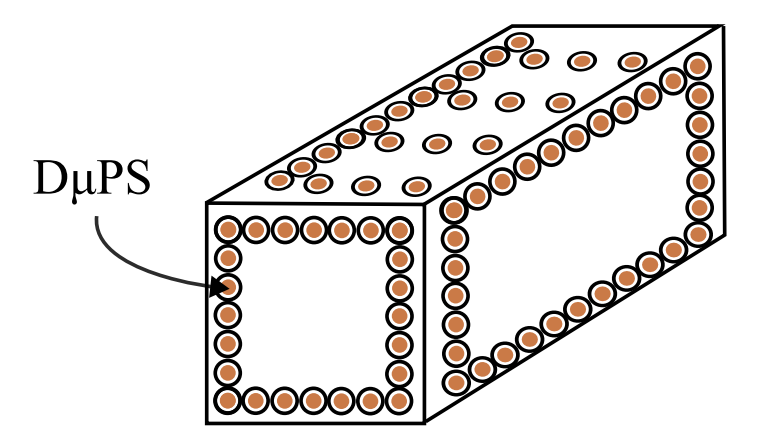


Figure 3.1: A nanosatellite with the D $\mu$ PS. The flexible architecture allows for any layout desired.

The  $D\mu PS$  necessitates a thruster system with a flexible architecture that can operate in a distributed configuration on nanosatellites. This requires the use of the lightest and most miniaturised thruster technology available. Despite their improved performance at smaller scales, electrospray thrusters also pose challenges due to their reliance on liquid propellants

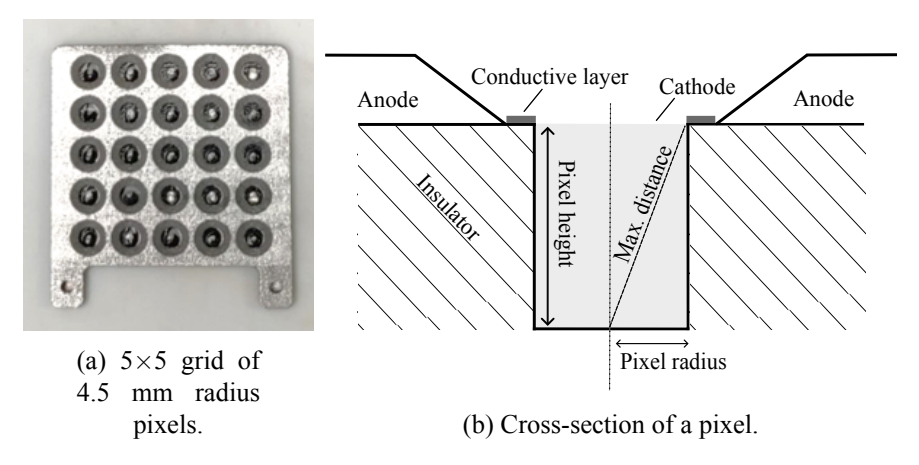


Figure 3.2: Picture of a  $\boxed{D\mu PS}$  prototype and a pixel cross-section. Images taken and adapted from  $\boxed{\square}$ .

and power-intensive preheating requirements. This leaves  $\overline{VATs}$  as the most promising candidate for the  $\overline{D\mu PS}$  concept. Their ease of miniaturisation and use of solid propellant make them viable for operation on constrained nanosatellites.

Their simple design and thrust generation principle allows them to be produced as a flat thruster. By combining this with 3D-printing techniques, VATs can also have the modular and flexible architecture required to operate as the  $D\mu PS$ . This thesis uses the performance parameters of a thin-film VAT prototyped in Saletes et al. [35], although the  $D\mu PS$  concept is agnostic towards the specific thrust generation principle. The thin-film VAT is a flat thruster comprising multiple individual pixels of tunable diameter. Each pixel consists of a circular anode surrounding a cathode material, which vaporises upon ignition, effectively acting as fuel. A prototype of this  $D\mu PS$ , including a cross-section of a single pixel, is depicted in Figure 3.2. It has radius of 4.5 mm and uses solid metal as fuel, providing a thrust-to-power ratio approximately in the micro-Newton per Watt [4].

The VAT operates on a pulsed-mode system. When ignited, a short electrical signal is sent to the chosen pixel at 100 Hz, corresponding to the frequency of the pulsed electrical signal. At each pulse, the pixel vaporises some propellant and produces thrust normally distributed around a nominal value dependent on the fuel material. This is caused by different plasma plume distributions, are current amplitudes, and effective pulse durations, which are natural and uncontrollable variations between each pulse. The pulse standard deviation is taken to be 10% [101]. While each pulse produces a different thrust level, the average thrust over a given firing time has a much smaller deviation due to the high pulsing frequency of 100 Hz. The frequency can be adjusted to modulate the average thrust, providing a wide variety of thrust performances. Changes in operational frequency also affect fuel consumption rate. Higher thrust results in a lower operational lifetime, although the exact fuel consumption

rate and thruster lifetime depend on the specific fuel material used.

Pixels can be ignited individually or in groups. If the pixels are spread across multiple faces, igniting multiple thruster heads can create tailored thrust and torque vectors, from rotational to translational motion. However, if the pixels are all grouped on one face, pure translational motion is only achievable through specific configurations: igniting a single pixel above the satellite's centre of mass or igniting symmetrically opposite thruster heads to cancel out torque components. In this configuration, pure rotational motion becomes impossible, as no pixel can be ignited to cancel the translational motion. Instead, the D $\mu$ PS can ignite one or multiple pixels simultaneously to control the direction and magnitude of the thrust and torque vectors applied to the satellite. Although the exact control law overseeing the ignition depends on the mission objectives, pixel layout, and available power on-board, an interesting parallel can be drawn with electrochromic control for solar sails. Electrochromic materials change their optical properties when current is applied, allowing solar sails to modulate the reflectivity of different sections of their surface, as demonstrated by the Ikaros mission [102]. By controlling optical properties across the sail, thrust and torque can be generated in different directions, providing the spacecraft with additional manoeuvrability [103, 104, 105]. This approach shares conceptual similarities with a D $\mu$ PS configuration if all pixels are mounted on a single spacecraft face. In both cases, specific areas (pixels or electrochromic sections) can be activated to produce the desired thrust or torque. While these systems seem similar in control representation and dynamics, they differ fundamentally in their thrust generation principles. A notable example of electrochromic control in space is the IKAROS mission, which implemented variable electrochromic material on the tips of the sail membrane to achieve attitude control. Applying an electric current can switch these materials between an "on" state, where solar radiation is reflected specularly—and an "off" state, where radiation is reflected diffusely. Unlike traditional solar sailing, which adjusts the sail's angle of incidence to control the direction of acceleration due to solar radiation pressure, electrochromic orbit control modifies the reflectivity coefficient of the sail surface. This method allows thrust vectoring without precise attitude control or complex deployment mechanisms. The discrete nature of the thrust generation on each electrochromic cell is also similar to the D $\mu$ PS pixels, and thus, the control implementations in such systems are inherently tied to the spatial distribution and number of controllable elements across the membrane or satellite. With a limited number of sections, as in the original IKAROS configuration, only coarse attitude control is achievable, typically restricted to a small number of torque vectors. However, increasing the number of individually addressable electrochromic cells makes it possible to exert distributed and directional thrust across multiple axes, significantly enhancing control capabilities and flexibility in the torque response. This approach would make the IKAROS controls align more closely with the D $\mu$ PS

system. However, a D $\mu$ PS pixel produces comparatively higher thrust magnitudes, resulting in faster response times.

Given the  $\boxed{D\mu PS}$ 's unconventional architecture and its reliance on low-thrust propulsion systems, its impact on nanosatellite dynamics need to be fully understood. The following chapter will review the fundamental principles governing satellite motion around the Earth, and detail the natural perturbations experienced in such orbits. Then, a review of available tools for simulating nanosatellite dynamics with the D $\mu PS$  will be presented.

4

### Fundamentals of satellite dynamics

reviews This chapter establishes the theoretical and computational foundation necessary for accurately simulating the  $\boxed{D\mu PS}$ 's unique distributed architecture. Beginning with the fundamentals of orbital dynamics, it develops the mathematical framework and common equations essential for numerical orbit propagation. The chapter then addresses the inherent challenges of attitude representation, evaluating alternative formulations and their associated mathematical expressions to identify elegant approaches for modelling the complex attitude dynamics of nanosatellites equipped with the  $\boxed{D\mu PS}$ . Particular attention is given to relevant perturbations in Low Earth Orbit (LEO), with detailed analysis of thrust modelling, atmospheric drag effects, and gravitational disturbances—factors that significantly influence spacecraft behaviour in this orbital regime. The effects of solar radiation pressure and third-body gravitational influences are also examined for comprehensive modelling fidelity. The chapter concludes with a systematic evaluation of existing software packages against the specific requirements of this research, demonstrating the necessity for the bespoke Comprehensive Attitude and Orbital Simulator (CHAOS) developed in Chapter  $\boxed{5}$  to accurately capture the unique dynamics of the  $\boxed{D\mu PS}$  system in various mission scenarios.

#### 4.1 Orbital motion

In order to understand the impact of the  $\boxed{D\mu PS}$  on nanosatellite trajectories, it is essential to investigate the orbital dynamics of satellites. This investigation will inform the selection of an appropriate simulation tool for the  $\boxed{D\mu PS}$ . The most straightforward approach

to orbital analysis is to assume an unperturbed environment, which provides a fundamental understanding of satellite motion. However, this idealised scenario must be built upon to accurately model the complex motion of spacecraft and the various perturbations encountered in real-world orbital environments.

Several simplifying assumptions are made for the unperturbed orbital motion [3]: the central body and spacecraft are treated as point masses, with the central body's mass significantly greater than the satellite's. Only the gravitational acceleration from the central body is considered, with no other forces applied. Under these conditions, the properties defining its trajectory are constants, except for the variable denoting the spacecraft's position along the orbit. These constants are called Orbital Elements. The most intuitive Orbital Elements are called Keplerian elements, which are illustrated in Figure [4.1] It consists of the semi-major axis [a], the eccentricity [c], the inclination [i], the Right Ascension of the Ascending Node [RAAN]  $\Omega$ , the Argument of Perigee (AOP)  $\omega_p$ , and the True anomaly  $\theta_{TA}$ . This idealised, unperturbed scenario is known as a Keplerian orbit [3]. However, satellites orbiting

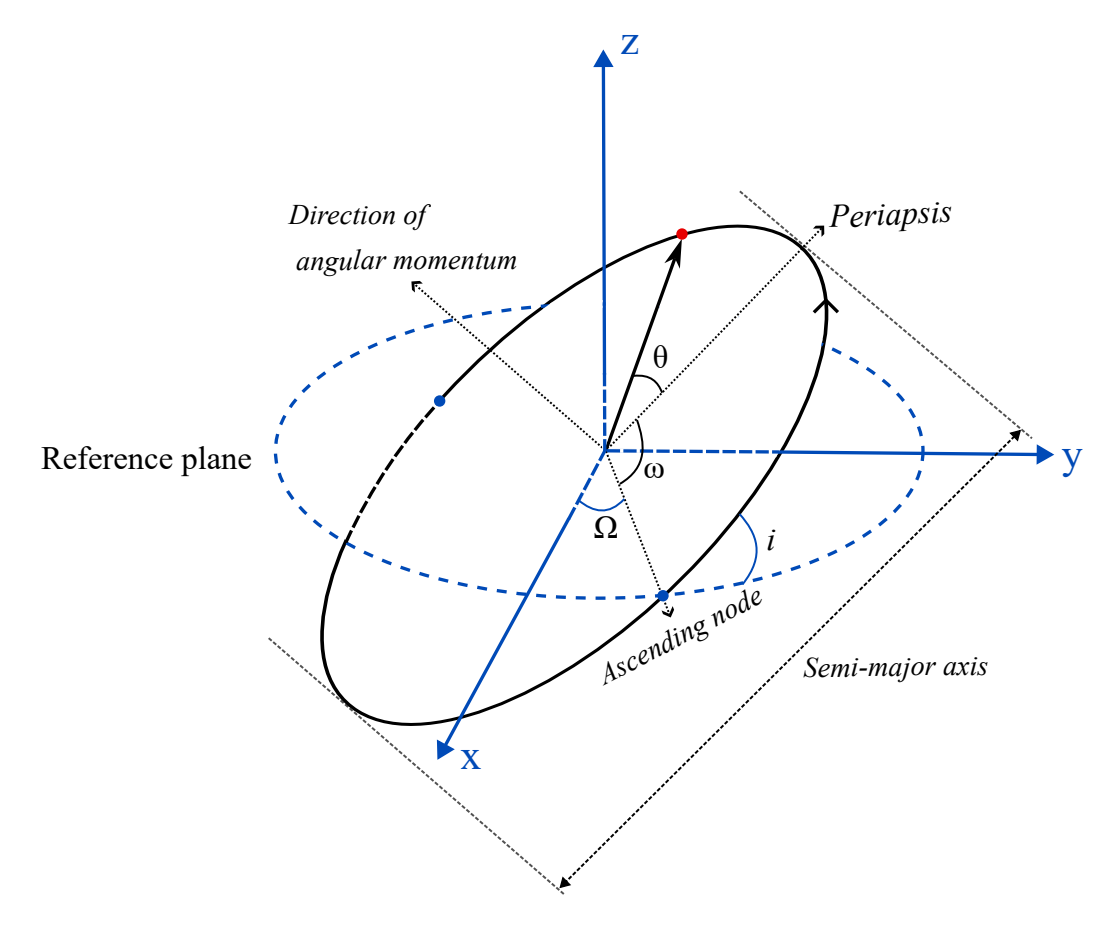


Figure 4.1: Representation of the classical Keplerian elements.

in LEO cannot be assumed to follow unperturbed trajectories. Various forces affect their motion, causing changes over timescales based on the perturbation's strength. If the satel-

lite uses a thruster, then the Keplerian orbit assumption is equally unsuitable. In an inertial Cartesian frame, the motion of an object orbiting the Earth with position  $\vec{r}_{sat}$  and velocity  $\vec{v}_{sat}$  experiencing a perturbation  $\vec{a}_p$  is described by

$$\ddot{\vec{r}}_{sat} = -\frac{\mu_E}{r_{sat}^3} \vec{r}_{sat} + \vec{a}_p \tag{4.1}$$

where  $\mu_E$  is the Earth's gravitational parameter and  $\vec{r}_{sat}$  is the satellite's orbital acceleration vector. Directly solving the Ordinary Differential Equation (ODE) through an integration scheme is typically called Cowell's Formulation, which falls within the domain of special perturbation techniques [106]. Although accurate and simple to implement, this method is computationally expensive, as the integration variable, the components of  $\ddot{\vec{r}}_{sat}$ , vary rapidly, because the vector rotates by 360 degrees over a single orbit.

Alternative representations have been developed to achieve faster computations. By assuming the orbital elements can vary in time, the Variation of Parameters can be employed [106]. One form of the Variation of Parameters is seen through the Gauss Planetary Equations, which are commonly expressed using Keplerian Elements. The Gauss Planetary Equations use osculating elements, representing the rate of change of the orbit's orbital elements. They typically change on a time scale much longer than a single orbit, allowing for more efficient computation. The Gauss Planetary Equations using Keplerian elements are [106]

$$\frac{da}{dt} = \frac{2}{n\sqrt{1 - e^2}} \left( e \sin(\theta_{TA}) a_r + \frac{p}{r_{sat}} a_s \right) \tag{4.2}$$

$$\frac{de}{dt} = \frac{\sqrt{1 - e^2}}{na} \left( \sin(\theta_{TA}) a_r + \left[ \cos(\theta_{TA}) + \frac{e + \cos(\theta_{TA})}{1 + e \cos(\theta_{TA})} \right] a_s \right)$$
(4.3)

$$\frac{di}{dt} = \frac{r_{sat}\cos(u)}{na^2\sqrt{1-e^2}}a_w \tag{4.4}$$

$$\frac{d\Omega}{dt} = \frac{r_{sat}\sin(u)}{na^2\sqrt{1 - e^2}\sin(i)}a_w \tag{4.5}$$

$$\frac{d\omega_p}{dt} = \frac{\sqrt{1 - e^2}}{nae} \left( -\cos(\theta_{TA})a_r + \sin(\theta_{TA}) \left[ 1 + \frac{r_{sat}}{p} \right] a_s \right) - \frac{r_{sat} \cot(i) \sin(u)}{h_{orb}} a_w$$
(4.6)

$$\frac{d\theta_{TA}}{dt} = \frac{h_{orb}}{r_{sat}^2} + \frac{1}{eh_{orb}} \left( p\cos(\theta_{TA})a_r - (p + r_{sat})\sin(\theta_{TA})a_s \right) \tag{4.7}$$

where  $a, e, b, \Omega, \omega_p$  and  $\theta_{TA}$  are the classical Keplerian elements with their standard symbols. The other parameters are n, p,  $h_{orb}$  and u which are the mean motion, the semi parameter, the orbital angular momentum and the argument of latitude respectively. The perturbing acceleration is represented through the  $a_r$ ,  $a_s$ , and  $a_w$  variables, which respectively represent the radial, tangential, and normal components of the total acceleration acting on the spacecraft, as shown in Figure 4.2.

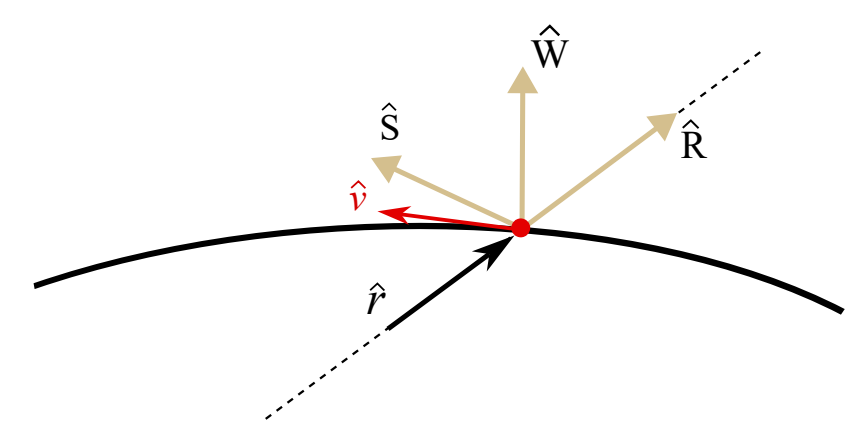


Figure 4.2: Sketch of the RSW frame.  $\hat{R}$  is along the radial direction,  $\hat{S}$  is along the orbital path and in the velocity direction, and  $\hat{W}$  completes the right-hand rule.

However, using Keplerian elements in the Gauss Planetary Equations presents singularities at circular, equatorial, and polar orbits. Unfortunately, these orbits experience high interest for both commercial and scientific applications. Other orbital element sets are sometimes used for propagation to address these limitations [106]. Whilst most of these orbital elements offer faster computation than Cowell's formulation, they still present singularities. However, the singularities are typically offset to less commonly encountered trajectories, such as retrograde orbits.

#### 4.2 Attitude motion

The  $\boxed{\text{D}\mu\text{PS}}$  presents a distributed architecture, which enables it to influence not only the orbital trajectory but also the attitude of satellites. The spacecraft's orientation, in turn, affects the orbital dynamics by changing the direction of the thrust and the effect of natural perturbations. Even in the absence of external torques, attitude motion can be complex. The satellite's mass distribution, represented by its inertia matrix determines rotational behaviour  $\boxed{3}$ ,  $\boxed{19}$ . If the mass distribution deviates from an ideal configuration, the resulting rotation is non-trivial. Additionally, both thruster-induced torques and environmental perturbations can influence the rotational dynamics. An appropriate simulation tool will, therefore, simulate a nanosatellite's attitude in high fidelity. This section reviews the fundamentals of attitude dynamics to inform on the tool selection.

Euler angles represent a common approach to describe a spacecraft's attitude, employing

three angles to define the orientation of a rigid body relative to an inertial frame. The angles represent a sequence of rotations performed in a specific order [3, 18]. Typically, Euler angle sequences use x-y-z rotations,

$$\mathbf{Q}_{xyz} = \mathbf{R}_x \mathbf{R}_y \mathbf{R}_z \tag{4.8}$$

or z-x-z,

$$\mathbf{Q}_{zxz} = \mathbf{R}_z \mathbf{R}_x \mathbf{R}_z \tag{4.9}$$

with the rotation matrices

$$\mathbf{R}_{x} = \begin{pmatrix} 1 & 0 & 0 \\ 0 & \cos \psi & \sin \psi \\ 0 & -\sin \psi & \cos \psi \end{pmatrix}, \tag{4.10}$$

$$\mathbf{R}_{y} = \begin{pmatrix} \cos \theta & 0 & -\sin \theta \\ 0 & 1 & 0 \\ \sin \theta & 0 & \cos \theta \end{pmatrix}, \tag{4.11}$$

$$\mathbf{R}_{z} = \begin{pmatrix} \cos \phi & \sin \phi & 0 \\ -\sin \phi & \cos \phi & 0 \\ 0 & 0 & 1 \end{pmatrix}. \tag{4.12}$$

$$\mathbf{R}_z = \begin{pmatrix} \cos \phi & \sin \phi & 0 \\ -\sin \phi & \cos \phi & 0 \\ 0 & 0 & 1 \end{pmatrix}. \tag{4.12}$$

However, Euler angles are singular when the rotation around the x-axis is zero. It leads to an attitude representation that is not unique, which can lead to a non-continuous solution [107]. Instead of Euler angles, quaternions, Rodrigues parameter and Modified Rodrigues parameters offer a more robust approach for attitude representation in spacecraft dynamics analysis [19].

Quaternions have been popular for attitude representation [19, 3, 106]. They offer a singularityfree representation and allow for efficient computation of successive rotations through simple expressions. A quaternion is a four-dimensional array that encodes the orientation of the body-fixed frame relative to the inertial frame through a single rotation around an imaginary axis. This imaginary axis is encoded within the quaternion, and to represent a rotation, the quaternion must be of unit length. However, during numerical integration, this norm can diverge from unity. Quaternions then require normalisation to maintain unit length, which can be computationally demanding. In astrodynamics, the notation typically encodes the

imaginary axis in the first three elements [3],

where  $e_1$ ,  $e_2$ , and  $e_3$  are the components of the rotation axis  $\vec{e}$ , and  $\beta$  is the rotation angle. The rotation axis must be a unit vector expressed in the inertial frame. Rodrigues parameters, sometimes called the Gibbs vector, use only three elements to represent attitude,

$$\vec{q}_{RP} = \tan\left(\frac{\beta}{2}\right) \begin{pmatrix} e_1 \\ e_2 \\ e_3 \end{pmatrix}. \tag{4.14}$$

While they provide a more compact representation than quaternions, they present a singularity for 180-degree rotations.

Modified Rodrigues Parameter (MRP) were developed to address some of the challenges of both quaternions and Rodrigues parameters [18]. Like Rodrigues parameters, MRPs use only three elements but are defined differently,

$$\vec{q}_{MPR} = \frac{\sin\left(\frac{\beta}{2}\right)}{1 + \cos\left(\frac{\beta}{2}\right)} \begin{pmatrix} e_1 \\ e_2 \\ e_3 \end{pmatrix}. \tag{4.15}$$

Their formulation allows MRPs to represent complete rotations without singularities. A unique feature of MRPs is a "shadow set" concept [19], [107]. Each set of MRPs has a corresponding shadow set that represents the same attitude. This property allows users to keep the magnitude of the MRP vector below unity by switching to the shadow set when needed, which can be computationally advantageous. However, when the norm of the MRP oscillates around one, fast switching between the two models can occur, causing discontinuities in the mathematical models and leading to numerical errors.

The orientation of the satellite at a given time depends on its angular velocity  $\overline{\omega}$ , which remains constant only if the mass distribution is considered ideal, even without external torques. An ideal mass distribution is characterised by an inertia matrix which is also a scalar matrix. To model the attitude in high fidelity, it is then essential to take into account

the satellite's inertia matrix  $\mathbf{I}$  and any disturbances  $\mathbf{r}_p$  by solving Euler's equation  $\mathbf{I}$   $\mathbf{I}$ ,

$$\dot{\vec{\omega}} = \mathbf{I}^{-1} \left( \vec{\tau}_p - \vec{\omega} \times \mathbf{I} \vec{\omega} \right). \tag{4.16}$$

An appropriate simulation tool should then use an orbit and attitude representation that balances computational efficiency with the singularities inherent to the model. As the attitude affects the orbital trajectory, the two dynamics must be coupled. The satellite's mass distribution should be taken into account for attitude propagation, and the tool should be able to include orbital and attitude disturbances. Accurate propagation of the satellite dynamics requires modelling the relevant environmental perturbations, which is the topic of the next Section.

#### 4.3 **Perturbations**

The perturbations that must be modelled for accurate satellite propagation and the level of detail involved depend on the orbital regime and the satellite geometry. We consider here the disturbances relevant to nanosatellites using the  $D\mu PS$  and orbiting in LEO, which is the topic of this work.

#### **Thrust**

Thrust, in the context of spacecraft dynamics, refers to the acceleration imparted by the onboard propulsion system. This force can significantly influence the orbital trajectory and the spacecraft's attitude. As discussed in Section 2.1, the principle of thrust generation relies on the expulsion of propellant, which results in an equal but opposite reaction applied to the spacecraft. The effect of thrust on the spacecraft's orbit is diverse and depends critically on the spacecraft's attitude at the time of firing [19]. Depending on the direction and magnitude of the thrust vector relative to the spacecraft's current orbital position and velocity, the resulting acceleration can manifest in various ways. These range from orbit-raising manoeuvres, which increase the orbit's altitude, to de-orbiting procedures that lower the spacecraft's trajectory. Thrust can also completely change the orbital trajectory, performing operations such as orbital plane changes or interplanetary transfers. A thruster can also control the spacecraft's attitude by applying external torques to spin a spacecraft or eliminate unwanted rotations. Given its impact on satellite motion, it is essential to accurately model thrust in spacecraft simulations.

#### **Aerodynamic forces**

Despite the low atmospheric density at high altitudes, air molecules are still in sufficient numbers to affect satellite motion, particularly in LEO [106]. As spacecraft travel at high velocities, they collide with these molecules, resulting in a loss of kinetic energy. This deceleration reduces the spacecraft's orbital energy, manifesting as a force known as atmospheric drag. For eccentric orbits, atmospheric drag circularises the trajectory over time [106] [3]. Circular orbits contract gradually due to drag while remaining quasi-circular. In addition to drag, if air molecules impact the satellite at an angle, a force perpendicular to the direction of motion can be experienced, called lift, as shown in Figure [4.3]. Aerodynamic forces significantly disturb spacecraft orbits, intensifying their influence as the spacecraft's altitude decreases. This creates a feedback loop as the drag force strengthens while the spacecraft decays, further accelerating the orbital decay process [107]. These atmospheric forces can also significantly perturb the spacecraft's attitude, potentially affecting its operational capabilities [19] [18]. Given the substantial impact of atmospheric drag and lift on orbital dynamics and attitude control, it is essential to accurately model these forces in spacecraft simulations.

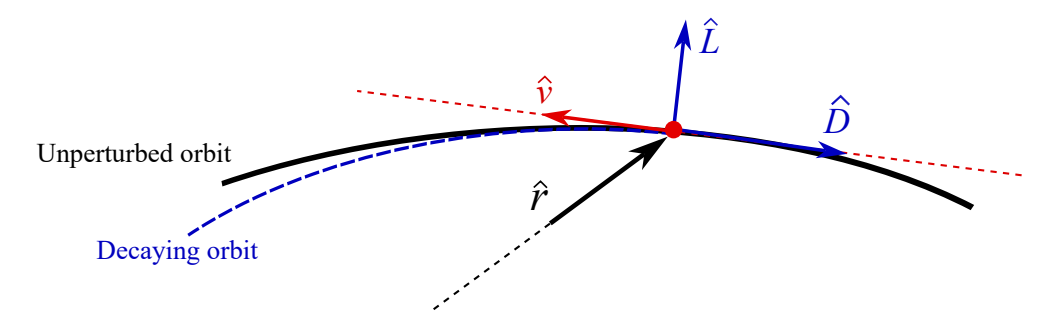


Figure 4.3: Aerodynamic forces acting on a satellite.

#### Solar radiation pressure

Similar to aerodynamic forces, radiation pressure arises from the impact of photons on the spacecraft, resulting in momentum transfer that affects both its orbit and attitude [106] 3]. The Sun, the dominant light source in the solar system, is the primary contributor to this perturbation, leading to the term Solar Radiation Pressure (SRP). The extent of momentum transfer is determined mainly by the reflective properties of the spacecraft's surface [107]. The influence of SRP on a spacecraft strongly depends on its shape, area-to-mass ratio, orbital height and eccentricity. Generally, this force acts to push the spacecraft away from the Sun, as seen from Figure 4.4. Over extended periods, SRP can induce significant

changes in various orbital elements, with particularly noticeable effects on the RAAN and eccentricity of the orbit. Regarding the attitude, asymmetrical shapes are more likely to experience more substantial perturbations. SRP can greatly alter a spacecraft's trajectory and attitude due to its cumulative impact over time. Accurate propagation of a satellite's orbit and attitude therefore requires the modelling of SRP.

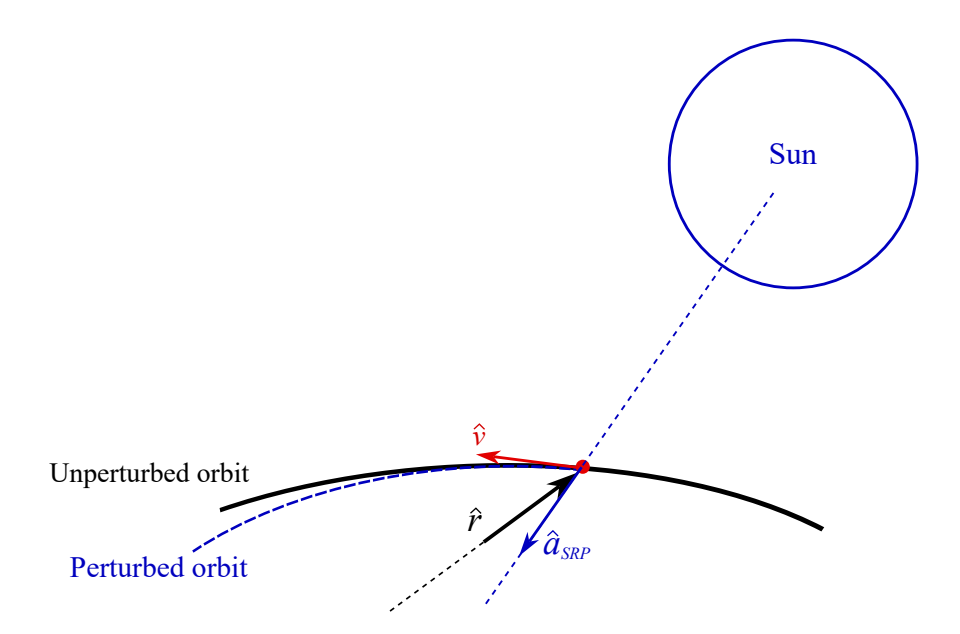


Figure 4.4: Solar radiation pressure forces acting on a satellite.

#### **Gravitational perturbations**

In this work, gravitational perturbations are defined as disturbances arising from the nonuniform mass distribution of the central body, in this case, the Earth. The Earth's surface has features, including valleys, mountain ranges, oceans with tides, and varying soil compositions at different locations, which contribute to this non-uniform mass distribution, resulting in a non-uniform gravity acceleration [106, 3]. As a spacecraft orbits the Earth, it experiences varying gravitational pulls as it passes over different surface features. These variations cause the gravitational force to deviate from the idealised point mass model, where gravity acts uniformly through the centre of mass. The resulting perturbations significantly affect the spacecraft's orbit. Over time, they cause a drift in the RAAN and the AOP, while the eccentricity and semi-major axis of the orbit experience periodic variations. These perturbations can accumulate to produce substantial deviations compared to the predicted orbit based on a Keplerian model. Given its impact on orbital dynamics, accurate modelling of gravitational perturbations is needed for precise orbit propagation [107].

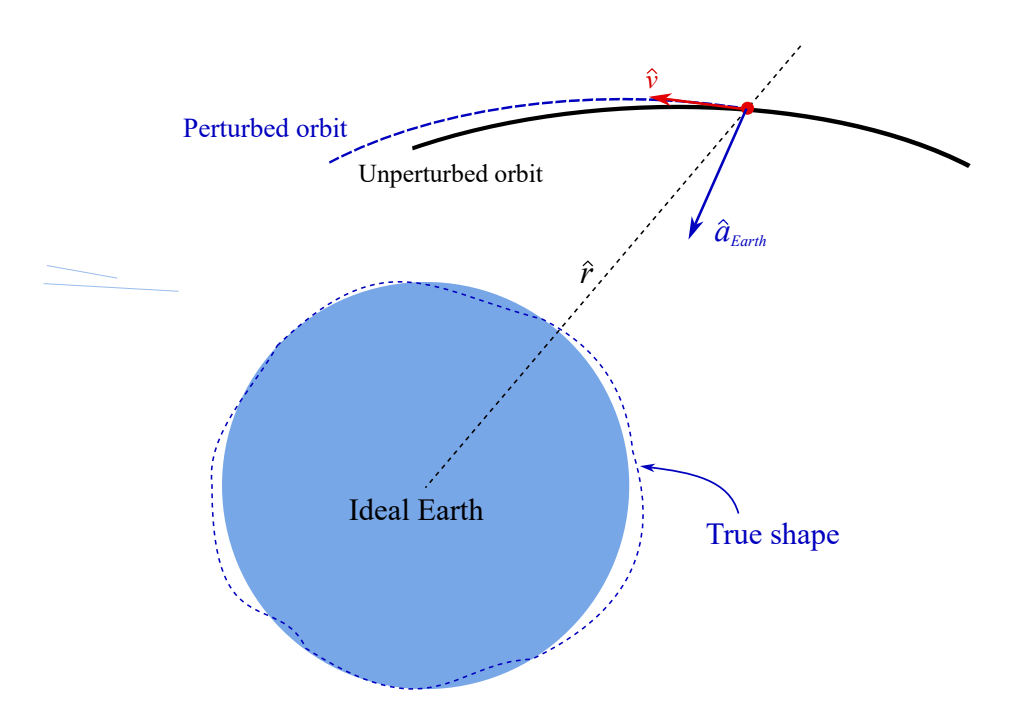


Figure 4.5: Geopotential forces acting on a satellite.

#### **N-body perturbations**

N-body perturbations refer to the gravitational influence exerted by celestial objects other than the primary body around which a spacecraft orbits [106]. While every object in the universe theoretically exerts a gravitational force on every other object, celestial bodies which are far away or have low mass are typically excluded [18]. In the context of spacecraft in LEO it is necessary to account for the gravitational acceleration induced by the Sun and the Moon [3]. Despite their considerable distance, these bodies have sufficient mass to noticeably affect orbital trajectories. The gravitational pull of these bodies induces secular and periodic changes in several orbital elements. They affect the RAAN the AOP and the inclination of the orbit. These perturbations can accumulate over time, leading to significant deviations from the Keplerian orbit. To accurately propagate nanosatellites in LEO it is then necessary to model the Sun and Moon's gravity.

#### Other perturbations

While increasing the number of perturbation models can theoretically enhance the realism of orbital simulations, it is essential to balance between simulation accuracy and computational efficiency. For nanosatellites operating in LEO, perturbations such as structural flexing, radiation pressure from distant stars, and Earth's albedo typically have negligible effects on the overall orbital dynamics. These perturbations often have a high computational cost

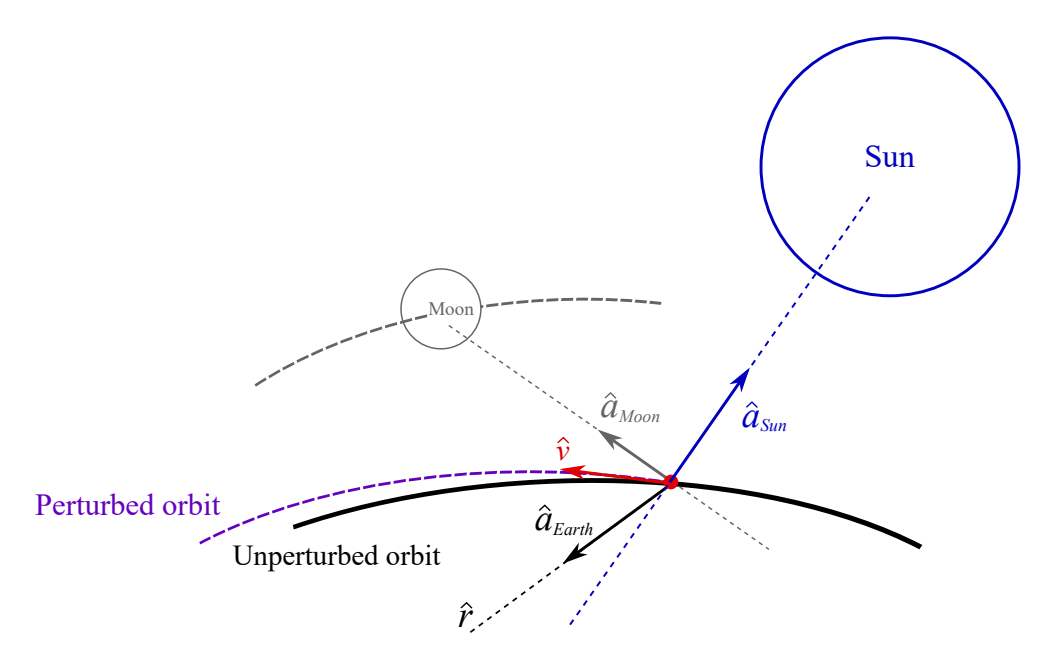


Figure 4.6: N-body acceleration acting on a satellite.

without significantly improving the simulation accuracy. Focusing on the dominant perturbations that significantly influence the spacecraft's motion is generally more efficient when modelling nanosatellite trajectories in LEO. This approach allows for the development of simulations that are computationally affordable and sufficiently accurate for practical orbit and attitude propagation.

#### **Existing software** 4.4

The comprehensive understanding of natural perturbations in LEO combined with the previous discussion on orbital and attitude dynamics, provides a solid foundation for selecting an appropriate simulation tool to model the behaviour of satellites equipped with the  $D\mu PS$ . An ideal simulation environment should be capable of coupling attitude and orbit dynamics. This is essential for capturing the effects of the micro-Newton thrust on the satellite's orbital trajectory and attitude dynamics. The chosen simulation tool should also balance computational efficiency and modelling accuracy. It must be capable of handling the primary perturbations that significantly influence nanosatellite motion in LEO, while also allowing for practical runtimes. In the following sections, I review standard software solutions and evaluate them with respect to these criteria.

#### **Analytical Graphics Incorporated System ToolKit**

Analytical Graphics Incorporated System Tool Kit (AGI STK) is a commercial software suite that offers a comprehensive range of astrodynamics packages for various applications [108] [109]. It has been used in planning several flagship missions, such as Double Asterbid Redirection Test (DART), the James Webb Space Telescope, and the Artemis program [110] [111] [112]. AGI STK includes the Astrogator module, which specialises in trajectory design and manoeuvre planning, and the High-Precision Orbital Propagator, which provides high-accuracy perturbation modelling. STK supports the propagation of Earth-orbiting spacecraft and offers attitude simulations through its dedicated Attitude Simulator module. The software can simulate various objects, provided their inertia matrices are known. However, AGI STK does not couple orbital and attitude dynamics, as each module is separate and self-contained. The simulator can accurately predict attitude but cannot communicate the state to the orbital propagator to reflect their impact on the spacecraft's trajectory. Additionally, its source code and implementation methods are inaccessible for debugging or manual enhancement as it is a commercial software. Therefore, AGI STK does not meet the requirement of providing a coupled attitude-orbit simulator.

#### **General Mission Analysis Tool**

General Mission Analysis Tool (GMAT) is free, open-source software used by NASA to design many missions, including the BepiColombo satellite, the OSIRIS-REx mission, and the Advanced Composition Explorer [113, [114]]. It offers functionalities similar to the AGI STK modules, including orbital perturbation modelling, manoeuvre planning, and trajectory optimisation. GMAT is a comprehensive tool with a significant heritage that is capable of designing complex missions. GMAT can model spacecraft attitude dynamics only to a limited extent. It can only propagate the attitude of objects with an ideal mass distribution. This limitation means that the results will not accurately represent the motion of actual spacecraft, which have non-ideal mass distributions. While GMAT is supported by extensive documentation for its use and implementation, its built-in scripting language lacks the flexibility other programming languages offer. This limitation makes incorporating a  $D\mu PS$  model, attitude control algorithms, and thrusting laws challenging. GMAT, therefore, does not meet the requirements as it does not provide high-fidelity attitude modelling, and including an accurate thruster model is not straightforward.

#### **Orbit Extrapolation Kit**

The Orbit Extrapolation Kit (Orekit) is an open-source Java toolbox used by companies such as Airbus, Thales Alenia Space, Centre National d'Études Spatiales (CNES), and ESA [III5]. It offers an extensive library, including orbit determination, reference frame computations, orbital perturbation modelling, and coupled orbit-attitude propagation [II6]. A significant advantage of Orekit is its ability to model coupled orbit-attitude dynamics, which is required for analysing the  $D\mu PS$ . This feature allows for more accurate simulations of complex spacecraft behaviour in orbit. However, Orekit has a limitation in that it does not simulate perturbations to the spacecraft's attitude. While custom force models can be incorporated into the orbital model, the attitude propagator does not include perturbations. Consequently, the effects of the  $D\mu PS$  torques cannot be modelled within Orekit, nor can the environmental perturbations affecting the attitude be accurately simulated. Given these constraints, Orekit is not suited for the specific requirements of this research.

#### **Smart Nanosatellite Attitude Propagator**

The Smart Nanosatellite Attitude Propagator (SNAP) is a MATLAB-Simulink-based simulation environment which couples attitude motion with Keplerian orbital propagation [75]. It is specifically designed to analyse the attitude dynamics of CubeSats. The propagator incorporates torque models that reflect perturbations commonly experienced by nanosatellites in Low Earth Orbit, such as aerodynamic and magnetic torques originating from magnetic stabilisation systems [74]. These features make SNAP particularly relevant for CubeSat attitude analysis when equipped with passive stabilisation systems. However, there are limitations to consider. As the orbit propagation does not consider environmental perturbations, accurate trajectory analysis cannot be performed. The validation process for the attitude also yielded ambiguous results, with SNAP fully recreating only one out of three test cases. No independent third-party validation of SNAP has been identified in the literature. Given these shortcomings, SNAP does not meet the requirements for this research project.

#### **Debris Spin/Orbit Simulation Environment**

D-SPOSE is an open-source orbit-attitude simulator designed for the long-term propagation of attitude dynamics for large space debris [117]. The propagator includes many environmental perturbations, such as non-uniform gravity and magnetic torques. However, its focus

on large debris makes many of its models less relevant for studying CubeSats. The simulator includes a comprehensive set of attitude and orbital perturbation models, including Earth albedo, infrared acceleration and torque, and Eddy-current torques [II8] [II9]. While these forces affect many spacecraft in orbit, their magnitude is generally negligible for nanosatellites. The  $\boxed{D\mu PS}$  represents a novel propulsion system architecture. Analysing its effects on CubeSats requires an interface to implement the exact propulsion system specifications and customised control laws. Given these considerations, D-SPOSE is not ideally suited for analysing the  $\boxed{D\mu PS}$  on nanosatellites.

#### 4.5 Review of tools used in literature

While many research efforts have incorporated combined dynamics for CubeSat modelling, very few have published their actual tools or code, instead focussing only on describing the core dynamics used [120, 121, 122]. As these fundamental dynamics are well-established, most literature focuses on specific mission applications rather than the detailed implementation [123] [124]. This means that the relevant aspects of these papers are primarily the basic dynamical equations, which are readily available in standard textbooks. This context is important when reviewing the various CubeSat modelling approaches that exist in the literature. Software frameworks like the NASA Operational Simulator for Small Satellites (NOS3) [125], which combines a dynamics simulator, core Flight System, and COSMOS command and control system, builds upon these standard orbital and attitude dynamics models, adding specialised layers for the modelling of on-board hardware and control systems. Similarly, Model Based Systems Engineering (MBSE) approaches use these same fundamental equations within their architectures, implementing them through known platforms like MATLAB and AGI STK [126]. Each of these approaches, while built on the same mathematical foundation, presents limitations when considering the integration of a distributed thruster architecture. Since the underlying code is not publicly available, any attempt to use these existing works would require complete re-implementation by the reader. In addition, as these papers focus primarily on their specific applications rather than detailing the implementation of equations of motion, recreating their work without their specialised layers would be equivalent to developing a custom simulator using standard textbook dynamical equations.

This review of existing tools shows that no available tools meet the requirements to perform the desired analysis. Software coupling orbit and attitude dynamics are not common and do not allow perturbations to both orbital and attitude motion. Additionally, the unconven-

tional architecture of the  $D\mu PS$  requires an interface that would allow modelling its unique characteristics. Therefore, a custom simulation tool has been developed for this thesis and is reviewed in the following chapter.

#### 4.6 **Conclusion**

This chapter has systematically examined the fundamental methods for representing and propagating attitude and orbital dynamics, establishing the theoretical framework essential for the development of the bespoke simulation environment required for the  $D\mu PS$ . While simple to implement, Cartesian formulations have been shown to be computationally costly for long-duration simulations. The analysis demonstrates that using Orbital Elements enables the application of Gauss Planetary Equations, significantly improving computational efficiency, an important consideration for the extensive simulation work in subsequent chapters. For attitude dynamics, quaternions, Rodrigues parameters and MRPs are identified as mathematically superior to Euler angles, which present problematic singularities that would compromise simulation robustness. The quaternion kinematics and Euler's equation established here provide the foundation for accurate attitude propagation throughout this thesis.

The chapter further establishes that in LEO, aerodynamic forces and SRP constitute the primary perturbations affecting both attitude and orbital trajectories of nanosatellites, with gravitational perturbations and third-body effects also requiring precise modelling. The review of existing software packages reveals that no available tool adequately addresses the specific requirements for accurately modelling the distributed nature of the D $\mu\mu$ PS, thus necessitating the development of the Comprehensive Attitude and Orbital Simulator (CHAOS) presented in the following chapter. This bespoke simulator will serve as the analytical platform for validating the novel applications of the  $D\mu PS$  explored in Chapters 5 and 6.

# 5

## Comprehensive High-fidelity Attitude and Orbit Simulator

This chapter details the development and validation of the Comprehensive High-fidelity Attitude and Orbit Simulator (CHAOS), a bespoke simulation environment specifically designed to model the unique distributed architecture of the  $D\mu PS$ . Building upon the theoretical foundations established in Chapter 4, this chapter presents the sophisticated mathematical models and equations of motion implemented to accurately propagate both orbital and attitude states simultaneously. The simulator incorporates transformation algorithms that convert mathematical elements into interpretable data. Following a critical evaluation of existing perturbation models, this chapter justifies the selection of specific modelling techniques for nanosatellite applications with distributed propulsion. Particular attention is given to the detailed geometric representation of the satellite within the simulator. The chapter concludes with a validation process that demonstrates CHAOS s high fidelity through direct comparison with industry-standard software, therefore establishing the reliability of the simulation results presented in Chapters 6 and 7 for novel  $D\mu PS$  applications in deorbiting and VLEO operations.

#### 5.1 Equations of motion

The core of any spacecraft simulator is a set of **ODE**s that must be integrated to predict orbital and attitude motion. These fundamental equations typically describe the satellite's

behaviour given a set of initial conditions. They also allow for the inclusion of disturbing accelerations, which can be derived from environmental perturbation models. The choice of ODEs is crucial, as it is critical in determining the accuracy of results and the speed of computations. The following sections outline the selected equations of motion for orbital and attitude dynamics in the CHAOS and present relevant associated expressions. In this thesis, the mathematical notation follows standard conventions. Vectors are denoted with an overhead arrow, e.g.,  $\vec{r}$ , indicating a quantity with both magnitude and direction in threedimensional space. Matrices are represented in bold uppercase letters e.g. A, signifying rectangular arrays of numerical values that typically describe linear transformations, rotations, or system properties.

#### **Attitude ODE**

As seen in Section [4.2], Euler angles and the Rodrigues parameter both present singularities in their modelling, while MRPs can present chattering due to the fast switching between the original and shadow set. Quaternions, on the other hand, are singularity-free. Although quaternions must have a unit length to represent rotation, CHAOS intentionally avoids normalising them. This approach transforms the error growth in the quaternion into a diagnostic tool: changes in the quaternion norm become indicators of error growth throughout the simulation. When CHAOS propagates the state, any non-linear growth in the quaternion suggests the simulation could be improved, while the magnitude of the growth itself indicates how trustworthy the simulation can be. Whilst regular quaternion normalisation was considered during development, this approach was rejected as it would reduce the quaternion's magnitude without ensuring the correctness of the associated rotation.

To propagate the spacecraft attitude, CHAOS uses quaternion kinematics, and standard expressions are used [3, 107],

$$\dot{\vec{q}} = \frac{1}{2}\Lambda\vec{q} \tag{5.1}$$

where the matrix  $\Lambda$  is composed of the components of the angular velocity vector  $\vec{\omega}$ 

$$\Lambda = \begin{pmatrix}
0 & \omega_z & -\omega_y & \omega_x \\
-\omega_z & 0 & \omega_x & \omega_y \\
\omega_y & -\omega_x & 0 & \omega_z \\
-\omega_x & -\omega_y & -\omega_z & 0
\end{pmatrix}.$$
(5.2)

The satellite's angular velocity is propagated using Euler's equation, as written in Equation (4.16). This allows the propagation of the angular velocity based on the satellite's mass distribution and external torques, which in turn will affect the spacecraft's orientation. This method involves updating both the angular velocity and the quaternion state at each integration time step, enabling the propagation of the satellite's attitude state.

While quaternions are computationally efficient, they are not the most intuitive representation for interpreting results. To address this, the angles between the rotated and inertial frames, both located at the satellite's centre of mass, are calculated. From a given quater-

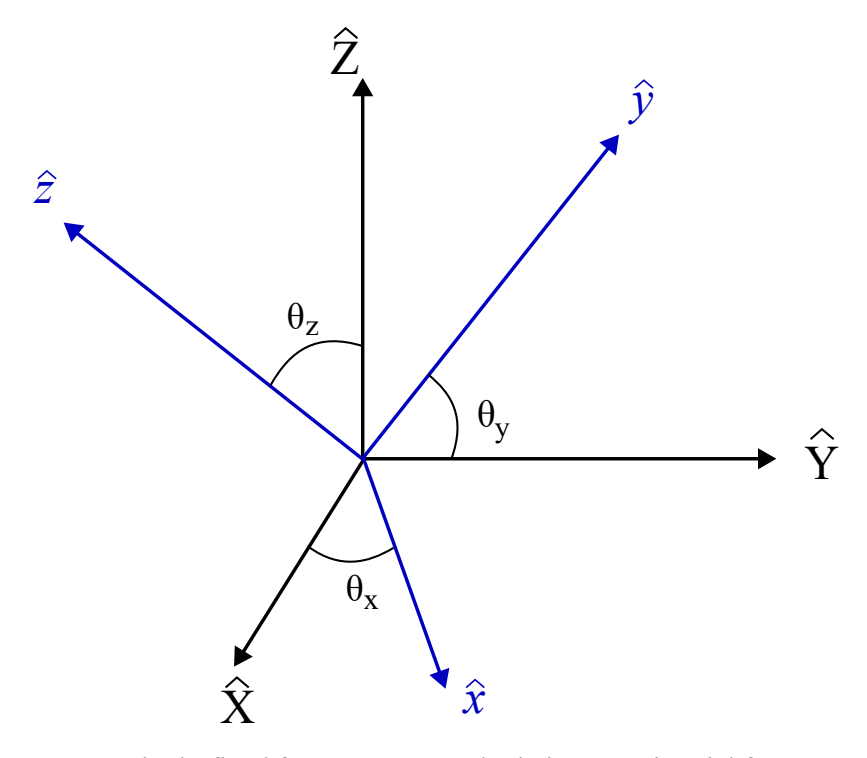


Figure 5.1: A body-fixed frame xyz rotated relative to an inertial frame XYZ.

nion  $\vec{q}$ , a direction cosine matrix  $\vec{A}$ , which rotates a vector  $\vec{p}$  in the inertial frame into the body-fixed frame, can be built as  $\vec{B}$ 

$$\mathbf{A} = \begin{pmatrix} q_1^2 - q_2^2 - q_3^2 + q_4^2 & 2(q_1q_2 + q_3q_4) & 2(q_1q_3 - q_2q_4) \\ 2(q_1q_2 - q_3q_4) & -q_1^2 + q_2^2 - q_3^2 + q_4^2 & 2(q_2q_3 + q_1q_4) \\ 2(q_1q_3 + q_2q_4) & 2(q_2q_3 - q_1q_4) & -q_1^2 - q_2^2 + q_3^2 + q_4^2 \end{pmatrix}$$
 (5.3)

such that

$$\vec{p}^{body-fixed} = \mathbf{A}\vec{p}^{in}.$$
 (5.4)

Note that the quaternion should be normalised,  $\|\vec{q}\| = 1$ , for the direction cosine matrix to represent a rotation. The angles between the axes of the body-fixed frame and the inertial

frame centred on the satellite can then be obtained with

$$\cos \theta_{\hat{x}} = \mathbf{A}^T \hat{x} \cdot \hat{X} \tag{5.5}$$

$$\cos \theta_{\hat{y}} = \mathbf{A}^T \hat{y} \cdot \hat{Y} \tag{5.6}$$

$$\cos \theta_{\hat{z}} = \mathbf{A}^T \hat{z} \cdot \hat{Z} \tag{5.7}$$

where  $\hat{x},~\hat{y},~\hat{z}$  are the axes of the body-fixed frame, and  $\hat{X},~\hat{Y},~\hat{Z}$  are the axes of the inertial frame, centred on the satellite. This conversion from quaternions to angular representations allows for easier interpretation of the satellite's orientation in space.

#### **Orbital ODE**

Section 4.1 has shown that using Keplerian Elements with the Gauss Planetary Equations leads to singularities at circular, equatorial, and polar orbits. To address these issues, the orbital elements must be redefined to shift the singularities to a rarely encountered point. For this purpose, the Modified Equinoctial Elements are used in CHAOS [127], [128]. These have their singularity at an inclination of 180 degrees, corresponding to retrograde orbits, a configuration that is virtually never used.

The relationship between Keplerian elements and Modified Equinoctial elements is provided below. Given a set of Keplerian Elements, the Modified Equinoctial Elements can be computed with [127, 128]

$$p = a(1 - e^2), (5.8)$$

$$f = e\cos(\omega_p + \Omega),\tag{5.9}$$

$$g = e\sin(\omega_p + \Omega),\tag{5.10}$$

$$h_{eq} = \tan\left(\frac{i}{2}\right)\cos(\Omega),\tag{5.11}$$

$$k = \tan\left(\frac{i}{2}\right)\sin(\Omega),\tag{5.12}$$

$$L = \Omega + \omega_p + \theta_{TA}. \tag{5.13}$$

Then, to propagate the orbit, CHAOS uses the Gauss Planetary Equations expressed in the

Modified Equinoctial form [129],

$$\frac{dp}{dt} = \frac{2p}{w_{eq}} \sqrt{\frac{p}{\mu_E}} a_{s}, \tag{5.14}$$

$$\frac{df}{dt} = \sqrt{\frac{p}{\mu_E}} \left( \underbrace{a_r \sin(L) + ((w_{eq} + 1)\cos(L) + f)}_{\underline{w_{eq}}} \frac{a_s}{w_{eq}} \right) - (h_{eq} \sin(L) - k \cos(L)) \frac{g}{w_{eq}} \underline{a_w} \right),$$
(5.15)

$$\frac{dg}{dt} = \sqrt{\frac{p}{\mu_E}} \left( -a_r \cos(L) + ((w_{eq} + 1)\sin(L) + g) \frac{a_s}{w_{eq}} + (h_{eq} \sin(L) - k\cos(L)) \frac{f}{w_{eq}} a_w \right),$$
(5.16)

$$\frac{dh_{eq}}{dt} = \sqrt{\frac{p}{\mu_E}} \frac{s_{eq}^2 a_w}{2w_{eq}} \cos(L),\tag{5.17}$$

$$\frac{dk}{dt} = \sqrt{\frac{p}{\mu_E}} \frac{s_{eq}^2 a_w}{2w_{eq}} \sin(L), \tag{5.18}$$

$$\frac{dL}{dt} = \sqrt{\mu_E p} \left(\frac{w_{eq}}{p}\right)^2 + \frac{1}{w_{eq}} \sqrt{\frac{p}{\mu_E}} (h_{eq} \sin(L) - k \cos(L)) a_w. \tag{5.19}$$

Additional variables are defined as

$$w_{eq} = 1 + f\cos(L) + g\sin(L),$$
 (5.20)

$$\alpha_{eq} = \sqrt{h_{eq}^2 - k^2},\tag{5.21}$$

$$s_{eq} = \sqrt{1 + h_{eq}^2 + k^2}. ag{5.22}$$

Despite the mathematical advantages of Modified Equinoctial Elements, they are not widely used to refer to orbits or interpret orbital analyses, as they are more challenging to visualise than Keplerian Elements. Despite their limitations, Keplerian Elements remain the preferred set for data visualisation, even if the propagation uses a different element set. Given a set of

Modified Equinoctial Elements, their Keplerian counterparts can be found using [127] [128]

$$a = \frac{p}{1 - f^2 - q^2},\tag{5.23}$$

$$e = \sqrt{f^2 + g^2}, (5.24)$$

$$i = \arctan 2\left(2\sqrt{h_{eq}^2 + k^2}, 1 - h_{eq}^2 - k^2\right),$$
 (5.25)

$$\omega_p = \arctan 2 \left( g h_{eq} - f k, f h_{eq} + g k \right), \tag{5.26}$$

$$\Omega = \arctan 2(k, h_{eq}), \tag{5.27}$$

$$\theta_{TA} = L - \arctan\left(\frac{g}{f}\right). \tag{5.28}$$

For many force models, the Cartesian state of the spacecraft must be provided. The Modified Equinoctial Elements must then be converted to Cartesian position and velocity vectors in the Earth Centred Inertial (ECI) frame. This can be done using the following expressions

$$\vec{r}_{sat} = \frac{p}{w_{eq} s_{eq}^2} \begin{pmatrix} \cos(L) + \alpha_{eq}^2 \cos(L) + 2h_{eq} k \sin(L) \\ \sin(L) - \alpha_{eq}^2 \sin(L) + 2h_{eq} k \cos(L) \\ h_{eq} \sin(L) - k \cos(L) \end{pmatrix}$$
(5.29)

$$\vec{v}_{sat} = \frac{1}{s_{eq}^2} \sqrt{\frac{\mu_E}{p}} \begin{pmatrix} -\left(\sin(L) + \alpha_{eq}^2 \sin(L) - 2h_{eq}k \cos(L) + g - 2fh_{eq}k + \alpha_{eq}^2 g\right) \\ -\left(-\cos(L) + \alpha_{eq}^2 \cos(L) + 2h_{eq}k \sin(L) - f + 2gh_{eq}k + \alpha_{eq} 2f\right) \\ 2\left(h_{eq} \cos(L) + k \sin(L) + fh_{eq} + gk\right) \end{pmatrix}.$$
(5.30)

#### 5.2 Geometry of the satellite

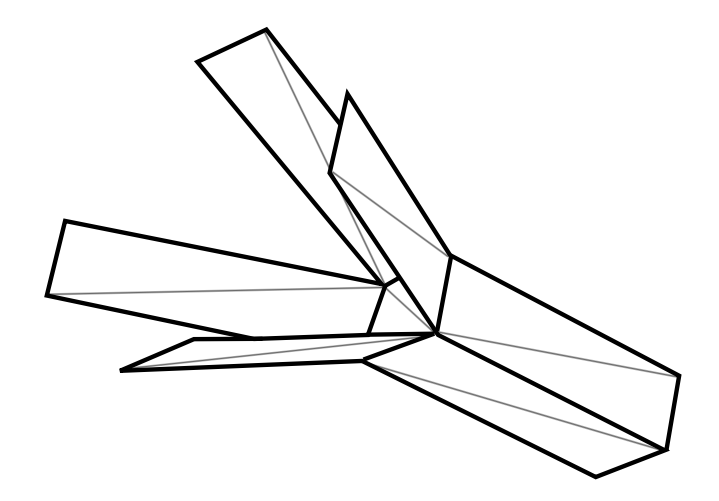


Figure 5.2: Visualisation of satellite facets.

A detailed representation of the satellite's geometry is included in CHAOS to improve the accuracy of modelling forces that depend on the satellite's shape and orientation. CHAOS uses Stereolithography (STL) to model the spacecraft's shape. This standard method represents 3D objects using many small triangles called facets [130]. Important information about each facet, such as its area, normal vector, and centre of mass, is calculated from the STL file data. CHAOS does not generate its own STL formatting, but instead uses the standard files format from Computer Aided-Design softwares. Each facet is assumed to have a uniform density to keep the computations simple. During the simulation, CHAOS updates the orientation of the STL model at each integration step by rotating each facet's normal vector  $\hat{n}_i$ .

$$\hat{n}_i^{in} = \mathbf{A}^T \hat{n}_i^{body-fixed}.$$
 (5.31)

Additionally, the perturbation models can be applied to each facet. Perturbations like SRP and aerodynamic forces are computed for each STL triangle, generating a force at its centre of mass. If the facet is at an angle, the projected area in any direction  $\hat{p}$  is [19]

$$\underline{A_{\vec{p}}} = A_i \left( \hat{n}_i^{in} \cdot \frac{\vec{p}^{in}}{\|\vec{p}\|} \right)_{\mathbb{R}>0}, \tag{5.32}$$

where  $A_i$  is the area of a facet i, and  $\mathbb{R} \geq 0$  indicates that only positive values of the dot product are considered. If the dot product is negative, the facet considered is "hidden" from the direction as it is on the other side of the spacecraft. By knowing the position of each facet's centre of mass  $\vec{r_i}$ , relative to the spacecraft's overall centre of mass, CHAOS can compute the total torque  $\vec{\tau}$  produced by forces  $\vec{F}$  acting on individual facets,

$$\vec{\tau} = \sum_{i=0}^{N_{facet}} \vec{r}_i \times \vec{F}_i. \tag{5.33}$$

This allows the perturbation models to also affect the spacecraft's attitude. This detailed approach provides more realistic results than simpler averaged-cross-section models.

For complex shapes, the accuracy of this method depends on the density of the STL mesh used to represent the spacecraft's geometry. While a denser mesh provides a more accurate representation of curved surfaces, it also increases the computational cost due to the larger number of triangular facets that must be processed. However, for simple geometric shapes such as cubes and rectangular prisms, e.g. CubeSats, a basic STL mesh using approximately 12 triangles is sufficient to define the geometry completely. It must be noted that this technique is only a geometric representation of the satellite affecting the compu-

tation of area-dependent natural perturbations. Models such as the thrust and gravitational perturbations do not use the STL model in CHAOS.

#### 5.3 **Perturbation modelling**

To simulate the motion of a spacecraft at high fidelity, it is important to include the perturbations that act upon it. This consideration becomes particularly significant for small satellites due to the fundamental relationship between spacecraft size and area-to-mass ratio. As an object's dimensions decrease, its surface area reduces with the square of its side length, while its mass decreases with the cube of its side length. Consequently, smaller spacecraft exhibit higher area-to-mass ratios, making them more susceptible to area-dependent perturbations. In CHAOS, this primarily affects two perturbation forces: solar radiation pressure and aerodynamic forces, which scale with the spacecraft's area-to-mass ratio. This section will discuss the modelling of the perturbations detailed in Section 4.3, and details the techniques used inside CHAOS...

# Solar radiation pressure

CHAOS models the SRP for increased fidelity in the simulations. The acceleration imparted by the solar pressure is applied to every facet and computed with [106]

$$\vec{a}_{srp} = \sigma P_{Sun} \frac{C_R A_{\hat{S}}}{m_{sat}} \frac{\vec{r}_{Sun-sat}}{r_{Sun-sat}}$$
(5.34)

where  $P_{Sun}$  is the solar radiation pressure at the satellite's position,  $C_R$  is the satellite's coefficient of reflectivity,  $A_{\hat{S}}$  is the projected area towards the sun,  $m_{sat}$  is the mass of the satellite, and  $\vec{r}_{Sun-sat}$  is the vector from the Sun to the satellite. The shadow function, which determines the fraction of the solar disk visible from the satellite's position, is denoted as  $\sigma$ . The solar pressure can be computed based on the solar flux SF at the location of the satellite, and the speed of light [106],

$$P_{Sun} = \frac{SF}{c} \tag{5.35}$$

with the solar flux being expressed as a function of the solar constant  $C_k$  and the radius of the Sun  $R_{Sun}$ ,

$$SF = \frac{C_k}{4\pi R_{Sun}^2}. ag{5.36}$$

CHAOS does not couple the SRP with the solar cycle. This choice aligns with industry-standard software such as NASA's GMAT and Ansys' STK HPOP, which similarly do not incorporate solar cycle effects in their SRP calculations [113] [108], [109]. Furthermore, for nanosatellite missions in LEO, which are the primary focus of CHAOS, solar radiation pressure typically plays a secondary role in both orbital and attitude dynamics [3], [18]. Therefore, the additional computational complexity and cost required to couple solar cycle effects with SRP calculations was not considered justified for the added accuracy gain.

The Sun's position relative to the spacecraft is computed with

$$\vec{r}_{Sun-sat} = \vec{r}_{sat} - \vec{r}_{Sun}. \tag{5.37}$$

Two main difficulties are encountered when modelling SRP Firstly, accurately determining the Sun's position as viewed from the spacecraft is complex. Several approaches are available for modelling the Sun's position relative to the spacecraft. Astronomical almanacs, which typically provide analytical expressions for the Sun's position as seen from Earth, offer one solution. The Astronomical Almanac 1992 computes the position of the Sun from the Earth as [131]

$$\vec{r}_{Sun} = r_{Sun} \begin{pmatrix} \cos(\lambda_{ecl}) \\ \cos\epsilon\sin(\lambda_{ecl}) \\ \sin(\epsilon)\sin(\lambda_{ecl}) \end{pmatrix}$$
(5.38)

with

$$r_{Sun} = 1.000\,140\,612 - 0.016\,708\,617\cos\left(M_{\odot}\right) - 0.000\,139\,589\cos\left(2M_{\odot}\right),\tag{5.39}$$

$$\lambda_{ecl} = \lambda_{M_{\odot}} + 1.914666471^{\circ} \sin(M_{\odot}) + 0.019994643 \sin(2M_{\odot}), \tag{5.40}$$

$$M_{\odot} = 357.529\,109\,2^{\circ} + 35,999.050\,34T_{C},\tag{5.41}$$

$$\lambda_{M_{\odot}} = 280.460^{\circ} + 36000.771T_{C}, \tag{5.42}$$

$$\epsilon = 23.439291^{\circ} - 0.0130042T_{C}. \tag{5.43}$$

The mean longitude  $\lambda_{M_{\odot}}$ , the mean anomaly  $M_{\odot}$  and the ecliptic longitude of the Sun  $\lambda_{ecl}$ 

depend on number of Julian centuries  $T_C$ , which is computed based on the Julian date JD,

$$T_C = \frac{JD - 2,451,545}{36,525}. (5.44)$$

While these are computationally efficient, their validity is limited to finite periods, and they typically present an accuracy of 0.01°, which would provide a performance below that of offthe-shelf tools [106] 3. A better method, similar to the Almanac, corresponds to using the precise ephemerides the Jet Propulsion Laboratory (JPL) provides [132], where each Keplerian element of the celestial objects in the Solar system are expressed as cubic polynomials. While similar to the Astronomical Almanacs, this method is of higher accuracy [106]. An even more accurate method involves directly incorporating the Earth's propagation around the Sun within CHAOS. This approach typically yields the most precise computation of the Sun's position relative to the Earth. To minimise the computational cost of evaluating the Sun's position, CHAOS uses the NAIF SPICE software [133] [134]. Developed by NASA, NAIF SPICE is a robust tool that provides accurate past, present and future ephemerides for celestial objects, and offers reliable coordinate transformations. By incorporating this package into CHAOS, the position of the Sun can be obtained with high accuracy. However, NAIF SPICE only provides the data for up-to roughly 250 years in the future. While this is typically more than enough, it is a limitation that must be noted. If the simulation length goes beyond the validity of this routine, then CHAOS automatically switches to the equations outlined by the Astronomical Almanac.

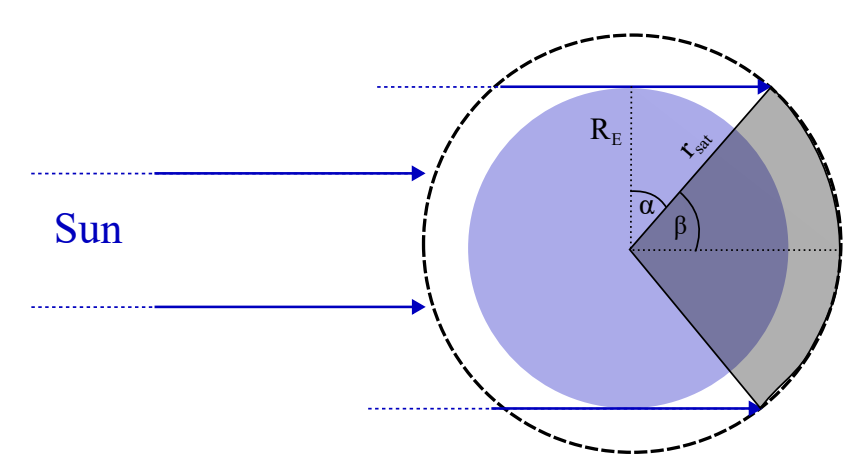


Figure 5.3: Ideal conical shadow model.

The second difficulty in modelling the SRP is accurately representing the Earth's shadow. The simplest models assume a perfectly spherical Earth and compute a conical shadow through basic geometry, as seen in Figure [5.3] [135]. In these models, the SRP is modelled up to the boundary where the spacecraft enters the shadow, where the force function is turned off ( $\sigma = 0$ ), creating a discontinuous model. A slightly different approach is the

Oblate Earth Conical Shadow Model (OECSM), which corrects the conical shadow model for the Earth's actual shape by including its oblateness [136]. While this offers improved accuracy, both the simple conical model and the OECSM suffer from discontinuities at the shadow boundary. These abrupt changes typically pose challenges for numerical integrators, potentially introducing errors in the propagation [137]. These simpler models also do not account for the Earth's penumbra, the region of partial shadow where the SRP acceleration gradually diminishes. To address these limitations, CHAOS implements a more accurate, continuous model: the Percent Shadow model [138].

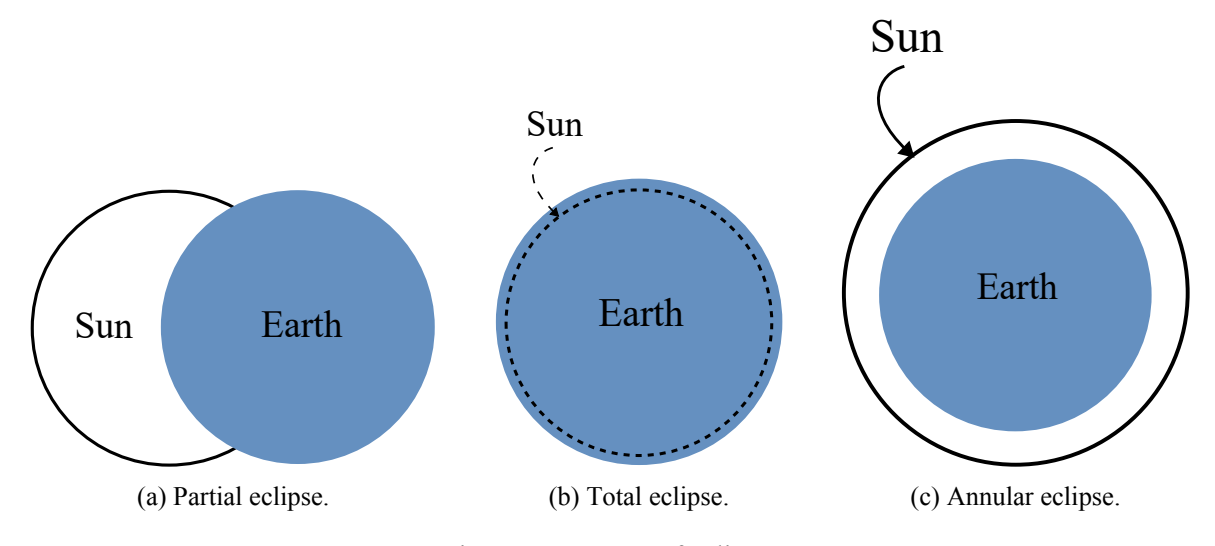


Figure 5.4: Types of eclipse.

The Percent Shadow model calculates the visible proportion of the solar disk as seen from the spacecraft's position. This approach allows for a mathematically smooth and continuous transition through the penumbra. It can also account for cases such as annular eclipses, as shown in Figure 5.4c. The Percent Shadow model starts by computing the apparent radius of the Sun and the Earth, with

$$R'_{Sun} = \sin^{-1} \left( \frac{R_{Sun}}{\|\vec{r}_{Sun} - \vec{r}_{sat}\|} \right)$$
 (5.45)

$$R_E' = \sin^{-1}\left(\frac{R_E}{\|\vec{r}_{sat}\|}\right) \tag{5.46}$$

where  $R_{Sun}$ ,  $R_{E}$  are the nominal radii of the Sun and Earth respectively,  $\vec{r}_{Sun}$ ,  $\vec{r}_{E}$  are their position vector, and  $R_{Sun}^{'},\ R_{E}^{'}$  are the apparent radii as seen by the spacecraft. The apparent separation between the two bodies is computed as

$$D' = \cos^{-1}\left(\frac{-\vec{r}_{sat}^T \cdot (\vec{r}_{Sun} - \vec{r}_{sat})}{r_{sat} \|\vec{r}_{sat} - \vec{r}_{Sun}\|}\right).$$
(5.47)

It is then possible to determine the proportion of the Sun disk concealed at the satellite's

position. The percent shadow p can be expressed as

$$\begin{cases} p = 0, & \text{if } D' \ge R'_{Sun} + R'_{E} \\ p = 1, & \text{if } D' \le R'_{E} - R'_{Sun}. \end{cases}$$
 (5.48)

If the Sun disk is only partially covered, with

$$|R_{E}^{'} - R_{Sun}^{'}| < D^{'} < |R_{Sun}^{'} + R_{E}^{'}|, \tag{5.49}$$

then  $A_{\odot}$ , the area of the Sun disk covered, is computed with

$$A_{\odot} = R_{Sun}^{'2} \cos^{-1} \left( \frac{c_1}{R_{Sun}^{'}} \right) + R_E^{'2} \cos^{-1} \left( \frac{D^{'} - c_1}{R_E^{'}} \right) - D^{'} c_2$$
 (5.50)

$$c_1 = \frac{D^{\prime 2} + R_{Sun}^{\prime 2} - R_E^{\prime 2}}{2D^{\prime}} \tag{5.51}$$

$$c_2 = \sqrt{R_{Sun}^{\prime 2} - c_1^2}. ag{5.52}$$

This allows CHAOS to compute the percent shadow with

$$p = \frac{A_{\odot}}{\pi R_{Sun}^{'2}}. (5.53)$$

If the condition  $|R_E^{'} - R_{Sun}^{'}| < D^{'} < |R_{Sun}^{'} + R_E^{'}|$  is not met, then the eclipse is annular, and the percent shadow is computed with

$$p = \frac{R_{Earth}^{'2}}{R_{Sun}^{'2}}. (5.54)$$

The shadow function  $\sigma$  then becomes

$$\sigma = 1 - p. \tag{5.55}$$

CHAOS therefore has a continuous shadow model that includes the modelling of the penumbra.

## **Aerodynamic forces**

Similarly to the SRP modelling, CHAOS applies aerodynamic forces to each facet of the spacecraft's geometry. The acceleration felt by a single facet is computed with [106] [19]

$$\vec{a}_{aero} = -\frac{1}{2} \frac{C_A A_{\hat{v}}}{m} \rho_{atm} v_{rel}^2 \frac{\vec{v}_{rel}}{\|\vec{v}_{rel}\|}$$
 (5.56)

where m is the satellite's mass,  $A_{\hat{v}}$  is the projected area towards the velocity direction, and  $v_{rel}$  is the relative velocity between the spacecraft's orbital velocity and the rotating atmosphere. The variables  $\rho_{atm}$  and  $C_A$  are the atmospheric density and the aerodynamic coefficient, respectively. The relative velocity is computed by accounting for the rotation of the atmosphere with [106]

$$\vec{v}_{rel} = \vec{v}_{sat} - \vec{\omega}_E \times \vec{r}_{sat} \tag{5.57}$$

where  $\vec{\omega}_E$  is the angular velocity vector of the Earth, which is taken to also be the angular velocity of the atmosphere. The mass is a known property of the satellite, leaving the density and aerodynamic coefficients as unknowns. However, determining the atmospheric density and the satellite's aerodynamic coefficients is more challenging. Accurately computing these variables requires complex modelling techniques, which are discussed in the following sections.

#### **Density model**

In recent years, atmospheric density modelling has seen significant advancements, with modern and accurate models such as CIRA12 and NRLMSISE00 becoming available [139, 140]. These models build upon earlier work, such as the Jacchia-Roberts model and the US Standard Atmosphere [141, 142]. However, while the newer models incorporate more accurate modelling of the physical and chemical processes of the upper atmosphere, they do not present significantly improved orbital trajectory predictions, especially over long time periods [143, 144]. Most standard models account for similar dynamics. They incorporate density variations over time, accounting for the interactions between varying levels of solar radiation and the Earth's magnetosphere. While the Sun emits radiation across the entire electromagnetic spectrum, the Earth's upper atmosphere is particularly sensitive to emissions at a wavelength of 10.7 cm, corresponding to infrared radiation [106, 144]. This radiation plays a crucial role in heating the upper atmosphere and changing its density. This density variation can be significant, up to two orders of magnitude, leading to severe

changes in the drag experienced by space objects. The activity of the Sun, especially at that wavelength, is thus tracked, and represented through the parameter  $F_{10.7}$ 

Vallado and Finkleman suggest that the parameters underlying an atmospheric model, such as satellite drag coefficient, satellite cross-sectional area and solar activity, are more important for accurate trajectory predictions than the choice of density model itself [144]. Then, correctly implementing the underlying parameters at high fidelity takes priority over implementing a newer model to predict orbital trajectories accurately. Atmospheric density modelling remains difficult due to challenges in predicting solar and geomagnetic activities. As a result, most astrodynamics software rely on mathematical methods to predict solar activity [145], 146]. Recorded historical data can be used to predict past solar activity. However, predicting future activity presents several options, each with its downside. A straightforward approach uses a sinusoidal curve representing the average 11-year solar cycle [106],

$$F_{10.7} = 145 + 75\cos(0.001696t + 0.35\sin(0.00001695t)) \tag{5.58}$$

where t is the number of days since the 1st of January 1989.

While simple, this method lacks accuracy as solar cycles are not an exact sine curve, but typically have varying periods and amplitudes. A more robust approach involves using predicted data from reputable organisations such as ESA, NASA or National Oceanic and Atmospheric Administration (NOAA) [147, 148, 149]. These organisations use weighted averaging techniques and specific indicators to extrapolate future activity based on past data. However, the accuracy of these predictions tends to decrease over time and is typically valid for up to one solar cycle ahead of time [144]. They are also rarely made for more than 30 to 40 years into the future.

Alternative methods have also been used in the literature. For instance, Oltrogge presents an approach where data from the past five solar cycles have been collected and mapped onto an average cycle [150]. For each simulated day, a solar flux value is randomly selected from one of the datasets at an equivalent point in its cycle. This method aims to capture the variability of solar activity while maintaining a realistic overall pattern. Unfortunately, this method is more computationally intensive and is a discontinuous model, which can lead to numerical errors. It is also purely based on statistics and ignores any potential indicators of an extended solar minimum or maximum. The choice of model and approach then depends on the application's specific requirements, typically balancing accuracy, computational cost, and available prediction data.

The Jacchia-77 atmospheric model was selected for implementation in CHAOS. Frey et al. presented a highly accurate interpolation of this model between 100 and 2500 km, achieving less than 1.5% error from the original tabular values while significantly improving computational speed – up to 60 times faster than the original implementation [I51]. This improvement allows for rapid density calculations without significantly sacrificing the accuracy of the results. The interpolation method employed by Frey et al. divides the atmosphere into partial regions, each fitted to an exponential model with its base density and scale height. These exponentials are then summed to create an analytical expression for density as a function of altitude. This method has been applied to a range of temperatures, allowing for a dynamic, temperature-dependent atmosphere model. CHAOS incorporates the temperature-dependent model and the required solar activity modelling to provide a comprehensive simulation environment. The nighttime global exospheric temperature  $T_n$  is computed using 100

$$T_n = 379 + 3.24\bar{F}_{10.7} + 1.3\left(F_{10.7} - \bar{F}_{10.7}\right) \tag{5.59}$$

where  $F_{10.7}$  is the solar flux index at 10.7 cm wavelength, and  $\overline{F_{10.7}}$  is its 81-day running average. This temperature corresponds to the average global temperature of the upper atmosphere based on solar activity. However, the part of the atmosphere in the sunlight will be warmer. This is taken into account by the uncorrected exospheric temperature of the atmosphere  $T_{unc}$  [106],

$$T_{unc} = T_n \left[ 1 + 0.3 \left( \sin^{2.2}(\theta) + \left[ \cos^{2.2}(\eta) - \sin^{2.2}(\theta) \right] \cos^3 \left( \frac{\tau^{deg}}{2} \right) \right) \right]$$
 (5.60)

$$\tau^{deg} = LHA_{Sun} - 37 + 6\sin\left(LHA_{Sun} + 43\right) \tag{5.61}$$

$$\theta = \frac{\|\phi_{gd} + \delta_{Sun}\|}{2} \tag{5.62}$$

$$\eta = \frac{\|\phi_{gd} - \delta_{Sun}\|}{2} \tag{5.63}$$

$$LHA_{Sun} = \frac{180}{\pi} \left[ \frac{r_x r_J - r_y r_I}{\|r_x r_J - r_y r_I\|} \arccos\left(\frac{r_x r_I + r_y r_J}{\sqrt{r_x^2 + r_y^2} \sqrt{r_I^2 + r_J^2}}\right) \right]$$
(5.64)

$$\phi_{gd} = \arctan\left(\frac{1}{(1 - f_E)^2} \left[\frac{r_K}{\sqrt{r_I^2 + r_K^2}}\right]\right) \tag{5.65}$$

$$\delta_{Sun} = \arcsin\left(\frac{r_z}{r_{Sun}}\right) \tag{5.66}$$

where  $f_E$  is the flattening of the Earth and  $r_x, r_y, r_z$  are the components of the Sun position vector  $\vec{r}_{Sun}$ , while  $r_I, r_J, r_K$  are the components of the satellite position vector  $\vec{r}_{sat}$ .

CHAOS uses predictions from NOAA for solar activity data. When simulations propagate beyond available predictions, the system switches to a sinusoidal model, as described in Equation 5.58. This switching allows CHAOS to propagate spacecraft beyond the NOAA predictions. To determine the Sun's position relative to Earth,  $\vec{r}_{Sun}$ , CHAOS calls the NAIF SPICE software. The result is a dynamic atmospheric density model within CHAOS, where solar activity, the Sun's position relative to the Earth, and the spacecraft's location all contribute to determining the local atmospheric density at the satellite's position.

#### Aerodynamic coefficients

The VLEO and LEO regimes are characterised by free molecular flow. In other words, the incoming-to-incoming molecule collisions are far less numerous than the surface-molecule collisions. The Knudsen number  $K_n$  indicates this, with

$$K_n = \frac{\lambda}{L} \tag{5.67}$$

where  $\lambda$  is the mean free path of the molecules, while L is the characteristic length of the system. If  $K_n \ge 10$ , then the regime is said to be in free molecular flow. Traditionally, satellites are assumed to have fixed aerodynamic coefficients [3, 19, 106]. However, these coefficients can be modelled more accurately using Gas-Surface Interaction (GSI) models in free molecular flow. Several GSI models exist, including classical analytical models such as the Sentman and Schaaf and Chambre models, which are widely used [152, 153]. Other models are also available, broadly categorised into scattering-kernel theory-based and physical GSI models [154].

Scattering-kernel models are kinetic models based on a statistical approach [155]. These models use a scattering kernel to represent the probability of a gas particle's velocity changing upon collision with a surface. The kernel models incident and reflected velocity distributions, allowing for modelling of gas-surface interactions without detailed knowledge of the underlying physics. This approach is advantageous in situations where the gas is too rarefied for continuum models to apply, but the full complexity of molecular dynamics simulations is unnecessary. Examples include the Maxwell model, the Nocilla-Hurlbut-Sherman model, and the Cercignani-Lampis-Lord model, one of the most successful kernel-based models [157, 158, 159].

Physical GSI models use experimental data to describe how surface thermal properties affect gas particle scattering. These models make assumptions about surface electric potential, morphological structure, and elasticity/stiffness characteristics. Simpler, quasi-onedimensional models are more common than complex two- and three-dimensional lattice models. While more complex models offer higher accuracy, their increased computational requirements usually limit their applicability in astrodynamics. Examples include the Hard Cube model, the Soft Cube model, and the Washboard model [160] [161] [162].

For LEO and VLEO applications, where many uncertainties affect the aerodynamic force and torque estimations, the added complexity of more advanced models is not justified, given the various sources of error present [154]. In the field of astrodynamics, the differences between existing Free Molecular Flow (FMF) models are typically smaller than the errors introduced by their fundamental assumptions and modelling requirements. Therefore, a computationally inexpensive model is chosen, even though it is not the most accurate. For this purpose, CHAOS implements the Sentman model, which is commonly used for astrodynamics applications. Despite being analytical, the Sentman model produces results comparable to more modern techniques that demand higher computational resources. It serves as the standard FMF model for orbital aerodynamics by providing an analytical approach that minimises computational costs while maintaining a physics-informed theory of gas-surface interactions.

The Sentman model provides analytical equations for aerodynamic coefficients of various shapes under free molecular flow conditions [152]. These equations are based on several critical assumptions about molecular behaviour. Primarily, Sentman assumed that the flow is free molecular, so the Knudsen number exceeds 10. In this scenario, the force experienced by an object results only from momentum transfer during molecule impacts and re-emissions. Another crucial assumption in Sentman's work is that molecules colliding with the surface are reflected diffusely, i.e., randomly re-emitted according to a Maxwellian velocity distribution. The Sentman model also ignores the interaction between the incoming molecules and the molecules that have been re-emitted after impact with a surface. Typically, this assumption is valid for convex shapes, but not concave geometries. Therefore, the model can only be used for convex objects.

Initially, the Sentman equations were challenging to apply accurately due to their reliance on variables with unknown precise values, particularly the re-emitted velocity of molecules. Moe later extended the formula, expressing the re-emitted velocity as a function of the satellite temperature [163]. Moe also made a convenient assumption for astrodynamics applications by approximating the incoming velocity of molecules to be equal to the spacecraft's velocity, which reportedly produces only negligible errors. CHAOS applies the Sentman equations for a one-sided flat plate to each facet of the spacecraft geometry. The equations are [164]

$$C_d = \left\{ \frac{P}{\sqrt{\pi}} + QZ\cos(\varphi) + \frac{\cos(\varphi)}{2} \frac{v_{re}}{v_{sat}} (\sqrt{\pi}\cos(\varphi) + P) \right\}$$
 (5.68)

$$C_{l} = \left\{ GZ \sin(\varphi) + \frac{\sin(\varphi)}{2} \frac{v_{re}}{v_{sat}} (\sqrt{\pi}Z \cos(\varphi) + P) \right\}$$
 (5.69)

$$P = \frac{1}{S}e^{-S^2\cos^2(\varphi)}$$
 (5.70)

$$G = \frac{1}{2S^2} \tag{5.71}$$

$$Q = 1 + G \tag{5.72}$$

$$Z = 1 + \operatorname{erf}(S\cos(\varphi)) \tag{5.73}$$

$$S = \frac{v_{sat}}{\sqrt{\frac{2RT_{unc}}{M_a}}} \tag{5.74}$$

$$\operatorname{erf}(x) = \frac{2}{\sqrt{\pi}} \int_0^x e^{-y^2} dy$$
 (5.75)

$$\frac{v_{re}}{v_{sat}} = \sqrt{\frac{2}{3} \left( 1 + \alpha \left( \frac{T_w}{T_i} - 1 \right) \right)} \tag{5.76}$$

$$T_i = \frac{v_{sat}^2}{3R} \tag{5.77}$$

where  $C_d$ ,  $C_l$  are the drag and lift coefficients of the spacecraft,  $\varphi$  is the angle between the velocity vector and the facet's normal vector, S is a dimensionless ratio between orbital velocity  $\vec{v}_{sat}$  and most probable random speed of the molecules, R is the ideal gas constant,  $M_a$  is the mean atomic mass of the molecules in the atmosphere, and  $T_i$  is the temperature of the incident molecules. The variable  $T_w$  is the temperature of the satellite's surface,  $T_{unc}$  is the temperature of the atmosphere, as expressed in Equation (5.60), and  $\alpha$  is the thermal accommodation coefficient. The function denoted as erf(x) corresponds to the error function.

In CHAOS, the Sentman model is applied for altitudes above 100 km, which is the limit of the interpolation of Jacchia-77 atmospheric model. At this altitude, calculations using the US Standard Atmosphere 1976 indicate a Knudsen number greater than 20, confirming free molecular flow conditions [165]. The simulator assumes invariant surface properties across the satellite and over time, with parameters such as  $\alpha$  and  $T_w$  remaining constant. This assumption is generally reasonable for nanosatellites, which have an operational lifetime too short for significant changes in the surface properties. CHAOS applies the Sentman equations for drag and lift coefficients to each triangular facet of the spacecraft geometry, treating each as a flat plate in free molecular flow. This approach is reasonable because aerodynamic edge effects are negligible in free molecular flow [154, 152]. As the Sentman model accounts only for momentum transfer between molecules and the surface, the shape of the flat plate is inconsequential, provided it is not curved. Then, the acceleration experienced by a plate depends on its total area. CHAOS therefore has an analytical drag and lift coefficient model which includes the dependency on the attitude of the spacecraft.

### **Gravitational perturbations**

The gravity potential is modelled with spherical harmonics to model the non-spherical shape of the Earth [106]. This approach is the most common formulation in astrodynamics because it can model the gravity potential in great detail [3] [106] [135]. Due to the inclusion of the attitude model, the time step required by the integrator is significantly smaller than the time step for the orbital models. Including orbital semi-analytical models would then not have improved the runtime, and thus, a fully numerical expression is used. The potential is expressed as

$$U = \frac{\overline{\mu_E}}{r_{sat}} \left[ 1 + \sum_{n=2}^{N_{max}} \left( \frac{\overline{R_E}}{r_{sat}} \right)^n \sum_{m=0}^n \left( C_{nm} \cos(m\lambda) + S_{nm} \sin(m\lambda) \right) P_{nm} \left( \cos(\phi) \right) \right]$$
(5.78)

where  $\phi, \lambda$  are the geocentric latitude and longitude respectively, and  $r_{sat}$  is the norm of the position vector. The parameters  $C_{nm}$ ,  $S_{mn}$  are the spherical harmonics coefficients provided by a model of choice, and  $P_{nm}(\cos(\phi))$  are the associated Legendre polynomials. From a gravity potential, the perturbing acceleration is obtained in the body-fixed frame with

$$\vec{a}_{qeo} = -\nabla U. \tag{5.79}$$

Expanding this leads to the following expressions [106],

$$a_{\hat{i}} = \left[ \frac{1}{r_{sat}} \frac{\partial U}{\partial r_{sat}} - \frac{r_z}{r_{sat}^2 \sqrt{r_x^2 + r_y^2}} \frac{\partial U}{\partial \phi} \right] r_x - \left[ \frac{1}{r_x^2 + r_y^2} \frac{\partial U}{\partial \lambda} \right] r_y - \frac{\mu_E r_x}{r_{sat}^3}, \tag{5.80}$$

$$a_{\hat{j}} = \left[ \frac{1}{r_{sat}} \frac{\partial U}{\partial r_{sat}} - \frac{r_z}{r_{sat}^2 \sqrt{r_x^2 + r_y^2}} \frac{\partial U}{\partial \phi} \right] r_y - \left[ \frac{1}{r_x^2 + r_y^2} \frac{\partial U}{\partial \lambda} \right] r_x - \frac{\mu_E r_y}{r_{sat}^3}, \tag{5.81}$$

$$a_{\hat{k}} = \frac{1}{r_{sat}} \frac{\partial U}{\partial r_{sat}} r_z + \frac{\sqrt{r_x^2 + r_y^2}}{r_{sat}^2} - \frac{\mu_E r_z}{r_{sat}^3},$$
(5.82)

where  $r_x, r_y, r_z$  are the components of the position vector  $\vec{r}_{sat}$  also expressed in the bodyfixed frame. The derivatives of the potential are taken with respect to the satellite's position

in spherical coordinates, and are

$$\frac{\partial U}{\partial r_{sat}} = \frac{-\mu_E}{r_{sat}^2} \sum_{n=2}^{\infty} \sum_{m=0}^{n} \left(\frac{R_E}{r_{sat}}\right)^n (n+1) P_{nm}(C_{nm}\cos(m\lambda) + S_{nm}\sin(m\lambda)), \tag{5.83}$$

$$\frac{\partial U}{\partial \phi} = \frac{\mu_E}{r_{sat}} \sum_{n=2}^{\infty} \sum_{m=0}^{n} \left(\frac{R_E}{r_{sat}}\right)^n \left(P_{n,m+1} - m\tan(\phi)P_{nm}\right) \left(C_{nm}\cos(m\lambda) + S_{nm}\sin(m\lambda)\right),\tag{5.84}$$

$$\frac{\partial U}{\partial \lambda} = \frac{\mu_E}{r_{sat}} \sum_{n=2}^{\infty} \sum_{m=0}^{n} \left(\frac{R_E}{r_{sat}}\right)^n m P_{nm}(S_{nm} \cos(m\lambda) - C_{nm} \sin(m\lambda)). \tag{5.85}$$

The associated Legendre polynomials  $P_{nm}$  can be calculated using the recursive formulae 106

$$\begin{cases} P_{n,0} = \frac{1}{n} \left( 2(n-1)\sin(\phi)P_{n-1,0} - (n-1)P_{n-2,0} \right) & n \ge 2 \\ P_{n,m} = P_{n-2,m} + (2n-1)\cos(\phi)P_{n-1,m-1}, \ m \ne 0 & m < n \\ P_{n,n} = (2n-1)\cos(\phi)P_{n-1,n-1} \end{cases}$$
 (5.86)

with initial values of

$$P_{0,0} = 1, (5.87)$$

$$P_{1.0} = \sin(\phi), \tag{5.88}$$

$$P_{1.1} = \cos(\phi). \tag{5.89}$$

While the theory for spherical harmonics is well-established, its application relies on the experimentally-determined coefficients  $C_{nm}$ ,  $S_{nm}$ . Several models have been developed to provide these coefficients. The GRACE Gravity Model (GGM) is based on data gathered over 14 months of the Gravity Recovery and Climate Experiment (GRACE) mission [166]. This model includes the Earth's gravitational field and incorporates oceanic currents and topography. The GGM provides coefficients for harmonic expansion up to degree and order 160, offering a comprehensive model of Earth's gravity field. The Earth Gravitational Model 2008 (EGM2008) is considered the most comprehensive gravity model to date 167 168 It provides coefficients up to a degree and order of 2156. EGM2008 combines GRACE mission data with altimetry, topological, and marine gravitational data, resulting in a highly detailed and accurate model of Earth's gravitational field. The GOCE (Gravity field and steady-state Ocean Circulation Explorer) model, which offers coefficients up to a degree and order of 200, is newer than EGM2008. It provides better resolution over parts of the Earth that are less frequently covered by other missions, such as South America, Africa, and Antarctica, although this improvement is only present at a high degree and order. However, the EGM2008 model remains the most precise model, even at low orders [168, 169]. Therefore, CHAOS implements spherical harmonics with the coefficients from the EGM2008 model. To obtain the orientation of the Earth at any given time, the NAIF SPICE software is used. The kernels used are summarised in Table 5.1

## N-body perturbations

CHAOS models the gravitational influence of the Sun and the Moon with [3] [106]

$$\vec{a}_{Luni-Solar} = Gm_L \left( \frac{\vec{r}_{L-sat}}{r_{L-sat}^3} - \frac{\vec{r}_{E-L}}{r_{E-L}^3} \right) + Gm_{Sun} \left( \frac{\vec{r}_{Sun-sat}}{r_{Sun-sat}^3} - \frac{\vec{r}_{E-Sun}}{r_{E-Sun}^3} \right)$$
(5.90)

where  $Gm_L$  and  $Gm_{Sun}$  are the gravitational parameters of the Moon and Sun, respectively. The vectors  $\vec{r}_{E-L}$  and  $\vec{r}_{E-Sun}$  are the positions of the Moon and the Sun relative to the Earth.

The main challenge lies in accurately computing the positions of the Sun and Moon. As discussed in Section 5.3, various methods exist for modelling the Sun's position. Similar approaches can be applied for the Moon. The Astronomical Almanac provides a low-accuracy, analytical option for obtaining the lunar position vector. The position of the Moon relative to the Earth is computed with [131]

$$\vec{r}_{E-L} = r_{Moon} \begin{pmatrix} \cos(\phi)\cos(\lambda) \\ \cos(\epsilon)\cos(\phi)\sin(\lambda) - \sin(\epsilon)\sin(\phi) \\ \sin(\epsilon)\cos(\phi)\sin(\lambda) + \cos(\epsilon)\sin(\phi) \end{pmatrix}$$
(5.91)

where

$$\lambda^{deg} = 218.32 + 481267.8813T_C + 6.29\sin(134.9 + 477198.85T_C) -1.27\sin(259.2 - 413335.38T_C) + 0.66\sin(235.7 + 890534.23T_C) + 0.21\sin(269.9 + 954397.7T_C) - 0.19\sin(357.5 + 35999.05T_C) -0.11\sin(186.6 + 966404.05T_C)$$
(5.92)

$$\phi^{deg} = 5.13\sin(93.3 + 483202.03T_C) + 0.28\sin(228.2 + 960400.87T_C) - 0.28\sin(318.3 + 6003.18T_C) - 0.17\sin(217.6 - 407332.20T_C)$$
(5.93)

$$\epsilon^{deg} = 23.439291 - 0.0130042T_C - 1.64 \times 10^{-7}T_C^2 + 5.04 \times 10^{-7}T_C^3.$$
 (5.94)

The variable  $T_C$  is the number of Julian centuries, computed with Equation (5.44) and allows the ecliptic latitude  $\phi^{deg}$  and ecliptic longitude  $\lambda^{deg}$  to be computed in degrees. The distance

to the moon is found with

$$r_{moon} = \frac{1}{\sin(P)},$$

$$P^{deg} = 0.9508 + 0.0518\cos(134.9 + 477198.85T_C)$$

$$+ 0.0095\cos(259.2 - 413335.38T_C) + 0.0078\cos(235.7 + 890534.23T_C)$$
 (5.96)
$$+ 0.0028\cos(269.9 + 954397.7T_C).$$

CHAOS provides higher accuracy by utilising the NAIF SPICE software using the DE440 kernel [170]. This tool offers highly precise ephemerides for celestial bodies, including the Moon and Sun. To ensure continuous simulation capabilities, CHAOS is designed to automatically switch to the Almanac calculations if the simulation period extends beyond NAIF SPICE's validity range.

### Thrust modelling

CHAOS provides a high-fidelity model which accounts for the pulsed nature of the  $D\mu PS$ thrusters and incorporates statistical variations to provide a more realistic representation of thruster performance. A pixel generates a thrust value at each pulse according to a Gaussian distribution centred on a nominal thrust  $T_{nominal}$  with a standard deviation  $\sigma_{std}$  of 10% [171] 172. This value might be validated or changed based on the results of the investigation of the concurrent team developing the  $D\mu PS$ . As their work progresses, the underlying physical principle used to model the thrust might also be updated. If the pixel fires for a firing time  $t_f$  at a high pulse frequency  $f_p$ , the average thrust generated will be close to the nominal value. Due to the Central Limit Theorem (CLT), the standard deviation  $\sigma_{CLT}$  of the average thrust calculated over a firing time  $t_f$  is computed with [173]

$$\sigma_{CLT} = \frac{\sigma_{std}}{\sqrt{n_p}} \tag{5.97}$$

where  $n_p$  is the number of pulses fired over  $t_f$ ,

$$n_n = f_n t_f. (5.98)$$

CHAOS uses this distribution of the thrust variation to model the average thrust generated when a pixel fires at a high frequency.

To accurately represent the  $D\mu PS$  grid, CHAOS accepts the coordinates of every pixel composing the thruster as an input. This approach ensures that the thrust vector is correctly associated with each ignited pixel and is used to compute the spacecraft's acceleration and torque. The thruster modelling is intentionally decoupled from the STL geometric modelling, reflecting the different requirements of these systems. Due to their simple shapes, most satellites can be adequately represented using a relatively small number of STL triangle facets. At the same time, a  $\boxed{D\mu PS}$  system typically comprises many individual thrusters distributed across the spacecraft. This decoupled approach also provides modularity, allowing for potential future modifications to the geometry modelling system without affecting the thruster representation. CHAOS uses the spacecraft's attitude to rotate the acceleration vector as it must be expressed into the inertial frame. This model also tracks fuel consumption for the individual pixels. Each pixel is assigned a fuel value, allowing CHAOS to monitor fuel usage across the entire thruster system. CHAOS assumes a constant fuel consumption rate throughout the simulation, governed by  $\boxed{101}$ 

$$\dot{m}_f = E_r \frac{P}{V_d}. ag{5.99}$$

The variable  $\dot{m}_f$  is the fuel mass erosion rate,  $E_r$  is a material-based erosion constant, P is the average operational power, and  $V_d$  is the plasma discharge voltage. As fuel is consumed, the spacecraft's mass is continuously updated to reflect this change.

Dynamics	Technique	Model	Note
Orbital motion	Gauss Planetary Equations (numerical)	Modified Equinoctial elements	-
Attitude motion	Euler's Equation, quaternion kinematics (numerical)	-	-
SRP	Facets modelling (numerical)	NAIF SPICE, Percent shadow, STL model	DE440 for ephemerides. Switches to Astronomical Almanac if epoch out of kernel scope
Drag/lift	Facets modelling (numerical)	Temperature-dependent Jacchia-77 interpolation, Sentman, STL model	-
Gravitational	Spherical harmonics (numerical)	EGM2008, NAIF SPICE	Kernels: earth_itrf93, earth_000101_230102_221009 earth_200101_990628_pre- dict
N-body	Point-mass gravity (numerical)	NAIF SPICE	Kernels: PCK00010, NAIF0012, DE440. Switches to Astronomical Almanac if epoch out of kernel scope.
Thrust	Attitude-coupled, attached to a pixel on satellite (numerical)	-	Thrust magnitude randomly generated according to a Gaussian distribution. Constant fuel consumption rate.

Table 5.1: Summary of the models and techniques used in CHAOS.

# 5.4 Validation

A multi-layered validation approach was employed to ensure the reliability of CHAOS. All models, including those for orbital and attitude dynamics, were validated in smaller portions. This approach allowed for the identification and correction of errors at the component level. At each step, smaller validation against either existing literature, expectations based on easier computations, such as simplified analytical solutions, or simple test cases to "sanity check" the code was performed. This iterative approach provided confidence in the accuracy and robustness of the individual components before they were integrated into CHAOS. However, for brevity, the thesis only presents the final validation comparing CHAOS to two industry-standard propagators. CHAOS is compared against NASA's GMAT and AGI STK's High-Precision Orbital Propagator (HPOP). This comparison allowed us to verify the accuracy of CHAOS in simulating orbital dynamics, including natural perturbations. STK's capabilities in modelling torque-free motion were also used to validate CHAOS's attitude dynamics simulations. The validation approach is indeed sufficient because CHAOS's additional capabilities primarily stem from combining established techniques rather than introducing fundamentally new models. While CHAOS does differ from the capabilities of individual packages like GMAT and HPOP, it does so by integrating standard orbital and attitude modelling techniques that are already well-validated. The main difference lies in how these techniques are coupled and in adding a customisable thrust modelling. Since the underlying physics and mathematical models remain consistent with industry standards, the comparison against established software packages, combined with the component-level validation strategy, provides adequate verification of CHAOS's implementation. The results were further compared to literature in the field to validate the attitude modelling under environmental perturbations. The following sections of this thesis present these validation efforts.

#### **Orbital validation**

The orbital validation uses a 1U CubeSat propagated over 400 days, corresponding to roughly 4800 revolutions, in a specific LEO orbit, as described in Table 5.2. This particular orbit was selected from Curtis [3], which provides a qualitative description of spacecraft behaviour under various perturbations in this orbit, offering an additional reference point for the validation. A 1U CubeSat was simulated in CHAOS, HPOP and GMAT using the data in Table 5.3. For the validation, CHAOS was configured to output data at time steps matching those of HPOP and GMAT, respectively. This approach allows for an accurate individual assess-

Orbit data	Value	
Semi-major axis	8059 km	
Eccentricity	0.17136	
Inclination	28°	
Right Ascension	45°	
Argument of perigee	30°	
True anomaly	$0^{\circ}$	
Start epoch	1st July 2007 (noon)	

Table 5.2: LEO orbit taken from Curtis for the validation of CHAOS [3].

ment of the performance of CHAOS against both GMAT and HPOP. Any deviations and error growth over time can be quantified by comparing the state vectors at each time step.

Plots of the error growth in each Keplerian element over the 400-day simulation period are now presented. This analysis quantifies CHAOS's accuracy and ability to accurately model various orbital perturbations over moderately long periods of time. The plots will present the percent error in the semi-major axis and eccentricity according to

$$\varepsilon_{\%} = \frac{|\bar{E}_{ref} - \bar{E}_{CHAOS}|}{|\bar{E}_{CHAOS}|} \times 100$$
 (5.100)

where  $\bar{E}_{ref}$  is the value of eccentricity or semi-major axis of the reference software, and  $\bar{E}_{CHAOS}$  is the corresponding value in CHAOS at a given time step. The remaining Keplerian elements represent angles, and thus, the smallest angle between two points is given in degrees, for each time step.

Property	Value
Mass	1.33 kg
Dimensions	$10 \times 10 \times 10$ cm
Fixed area (GMAT & HPOP only)	$0.015 \text{ m}^2$
Initial attitude quaternion (CHAOS only)	$\begin{pmatrix} 0.5 & 0.5 & 0.5 & 0.5 \end{pmatrix}^T$

Table 5.3: 1U CubeSat properties for validation.

#### **Keplerian motion**

The two-body problem in Keplerian motion allows for exact analytical solutions, providing an accurate starting point for the validation. The results from CHAOS, HPOP, and GMAT are compared against these analytical predictions. For additional perspective, the comparison also includes results from REBOUND, a high-accuracy planetary collision software [174]. Figure [5.5] shows the evolution of Keplerian elements over 400 days for all four

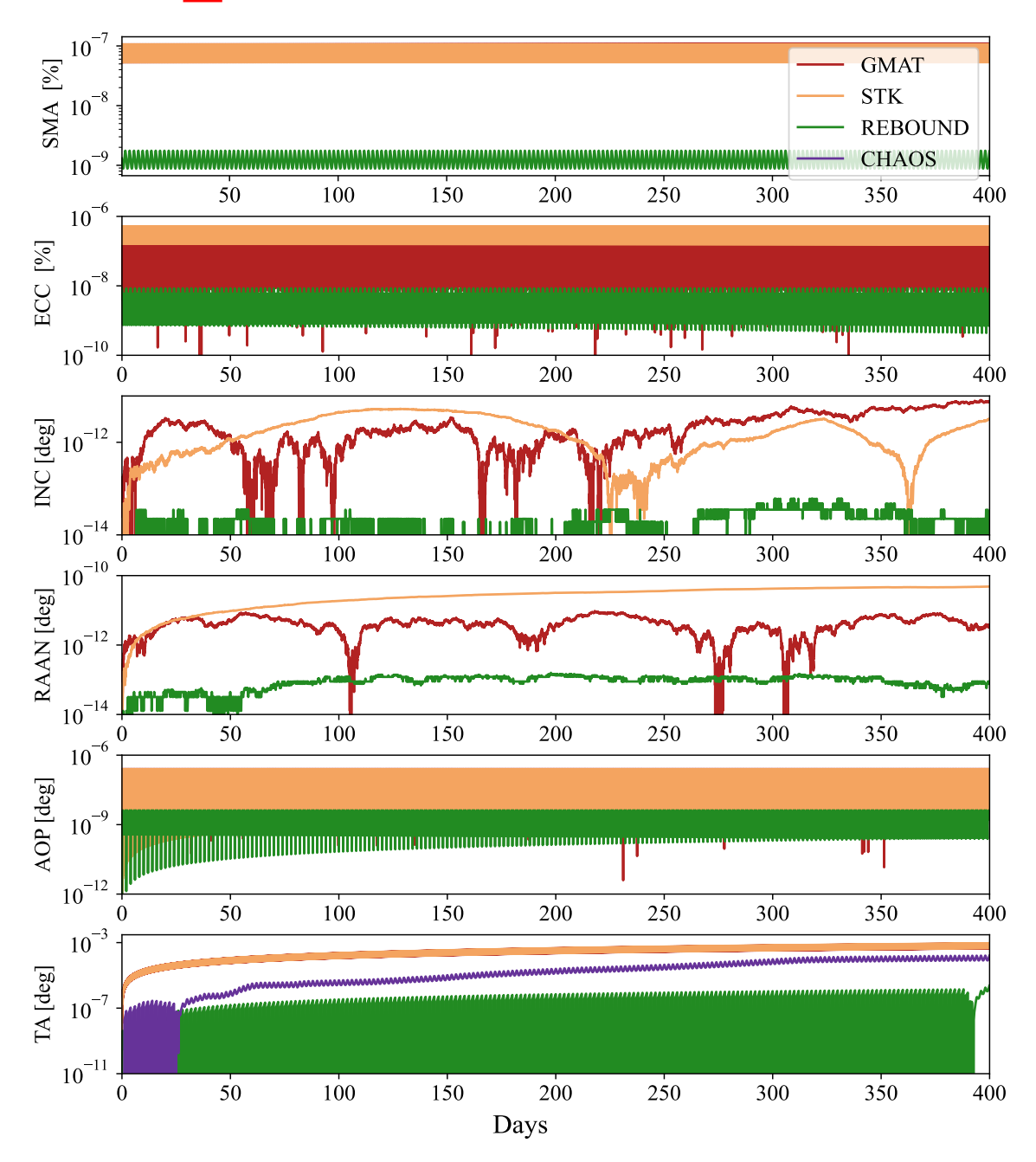


Figure 5.5: Error in keplerian elements variation over 400 days in a Keplerian orbit for CHAOS, HPOP, GMAT and REBOUND relative to the analytical solution. In the first five plots, CHAOS is not visible on the logarithmic scale as its error is too low. Due to fast oscillations, the lines can appear as solid blocks which are overlapping as the different propagators present similar behaviour.

software. CHAOS demonstrates high accuracy, with errors too low to appear on the logarithmic plot for the first five elements. REBOUND shows errors around  $10^{-9}$  for semimajor axis, eccentricity, and  $\overline{AOP}$  and  $10^{-14}$  for inclination and  $\overline{RAAN}$  CHAOS outperforms REBOUND in all elements except true anomaly, where its error grows secularly to  $10^{-5}$ . GMAT and HPOP's performances are close to each other, with errors around  $10^{-7}$  for semi-major axis, eccentricity, and AOP. The error for the inclination and RAAN approaches  $10^{-12}$ , while the True Anomaly error grows to  $10^{-3}$ . GMAT and HPOP show more substantial error growth across all elements compared to REBOUND and CHAOS, which maintain errors that are two orders of magnitude lower on average.

The GMAT and HPOP results for the semi-major axis, eccentricity, and argument of periapsis show an apparent offset. At the same time, errors in inclination, RAAN, and true anomaly exhibit secular growth. It was verified that the discrepancies did not come from an error in the initial conditions. Instead, GMAT and HPOP propagate orbital motion using the Cartesian formulation and internally convert the initial Keplerian elements to Cartesian state vectors, potentially losing accuracy. REBOUND, which uses Cartesian state vectors as initial conditions and integrates them directly, does not exhibit this issue. Figure 5.6 presents

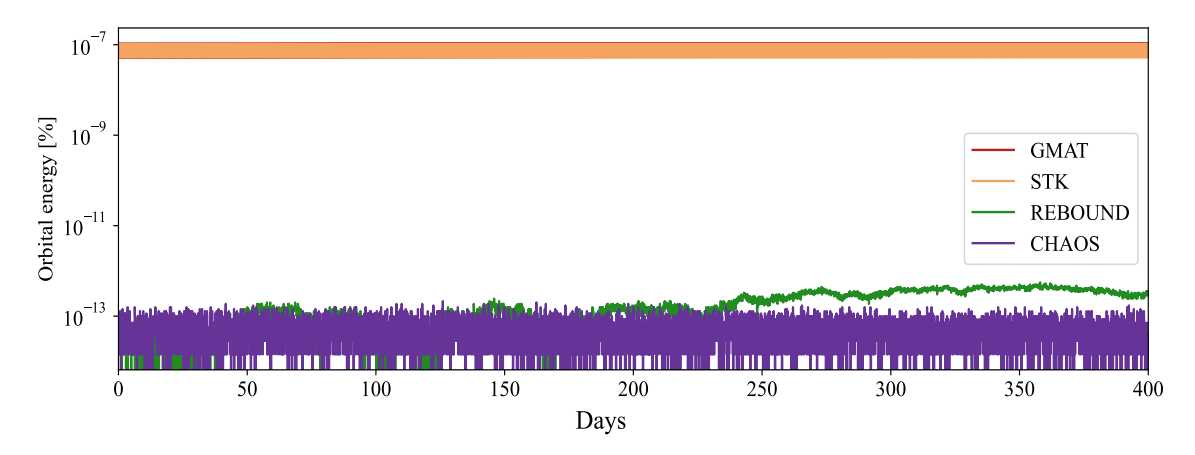


Figure 5.6: Orbital energy variation over 400 days in a Keplerian orbit for CHAOS, HPOP, GMAT and REBOUND.

the variation in orbital energy relative to the initial orbital energy, computed analytically. In a Keplerian orbit with no perturbations, the orbit remains fundamentally unchanged, with the only variable being the True Anomaly representing the satellite's position along its orbit. Using Modified Equinoctial elements in CHAOS, all derivatives (except True Anomaly) become zero during numerical integration. This approach ensures the numerical integration produces very low errors, which would grow extremely slowly—only over multiple years. The observed errors do not stem from the numerical integration scheme, but from computers' finite precision in representing real numbers. These finite precision errors are random and normally distributed around their nominal value. The plot again shows an offset for GMAT and HPOP, whose results are superimposed. Over the 400 days, CHAOS maintains a relatively constant error of  $10^{-13}$ , while REBOUND's error begins to grow. Although HPOP and GMAT show higher errors, they remain very close to the analytical solution, with deviations around  $10^{-7}$ . These results do not invalidate GMAT and HPOP as reference tools. Instead, they demonstrate that CHAOS and REBOUND outperform them in a Keplerian environment. This validation shows that the equations of motion are correctly implemented and accurately propagate Keplerian orbits.

### **Gravitational perturbations**

The orbit propagation under gravitational perturbations using GMAT and HPOP is compared to CHAOS. All three utilise the EGM2008 model, set to a degree and order of 36. Figure 5.7 plots the error between CHAOS and GMAT and between CHAOS and HPOP. It is important to note that GMAT employed older versions of NAIF SPICE kernels. For validation purposes, CHAOS matched the kernels used by GMAT. For planetary constants, GMAT uses the PCK0008 kernel. GMAT's Earth orientation binary kernel was renamed, making its version unclear. It was thus taken from GMAT's installation folder and used on CHAOS for the validation. Outside of the validation, CHAOS uses the most up-to-date available version of the kernels, employing the PCK00011 kernel for planetary constants. Although AGI STK includes NAIF SPICE within its packages, it remains uncertain whether HPOP uses it to obtain Earth orientation and planetary constant data. Relative to GMAT, CHAOS demonstrates an error of approximately  $10^{-4}$  for the semi-major axis, inclination, RAAN, and AOP. The eccentricity error grows to  $10^{-3}$ , while the True Anomaly error increases to  $10^{-1}$ . CHAOS matches the HPOP results more closely, showing errors around  $10^{-6}$  for the semi-major axis, inclination, RAAN, and AOP. The eccentricity error rises to  $10^{-5}$ , and the True Anomaly error reaches  $10^{-3}$ . Given that the semi-major axis and eccentricity errors are expressed as percentages, and the other elements are in degrees, these values indicate good agreement between CHAOS and the reference software. The error growth trend is predominantly linear, allowing for estimating errors in long-term simulations. The most significant percentage error is in the eccentricity, relative to GMAT, at  $10^{-3}$  after 400 days. Over 100 years, this error would reach approximately 0.09%. The largest angular error is in the true anomaly, relative to GMAT, at  $10^{-1}$ , which would result in an error of about 9.1 degrees after 100 years. Excluding the true anomaly, the most substantial angular error is in the AOP, at  $10^{-4}$ , leading to an error of roughly 0.009 degrees after 100 years. These results suggest that CHAOS propagates the orbit accurately, although the position along the trajectory is less precise. This discrepancy in the position is likely due to the difference in equations of motion and the specifics of the integration scheme chosen. However, the overall errors are relatively small. This analysis, therefore, shows that CHAOS models gravitational perturbations to a similar accuracy as the reference

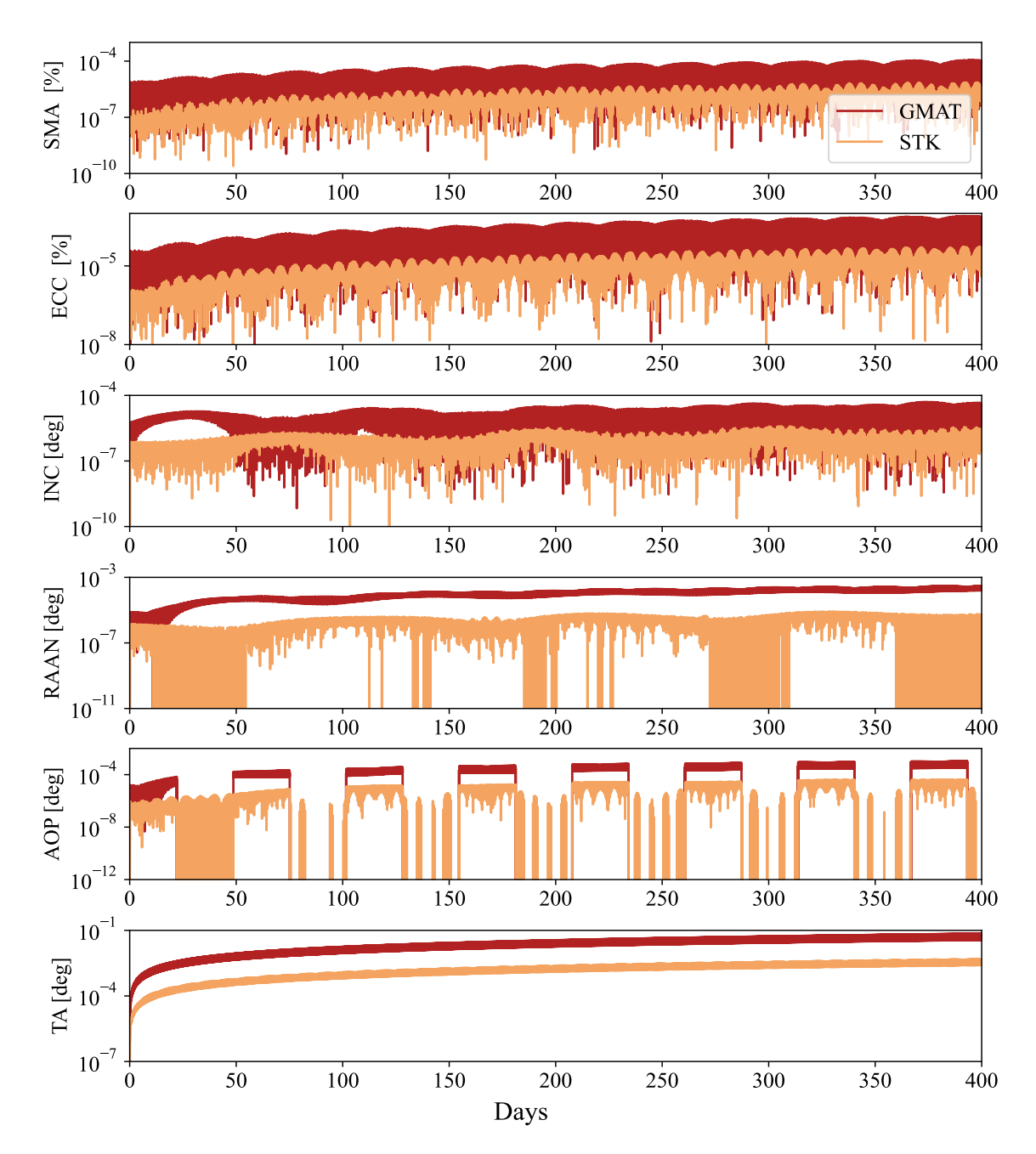


Figure 5.7: Keplerian elements error of CHAOS relative to HPOP and GMAT over 400 days under gravitational perturbations. Due to fast oscillations, the lines can appear as solid blocks which are overlapping as the different propagators present similar behaviour.

software and that their influence on orbital dynamics is correctly represented.

#### **Luni-solar perturbations**

The Luni-solar perturbations in CHAOS are validated against GMAT and HPOP. For validation purposes, CHAOS matched GMAT's use of the DE405 kernel for planetary ephemerides.

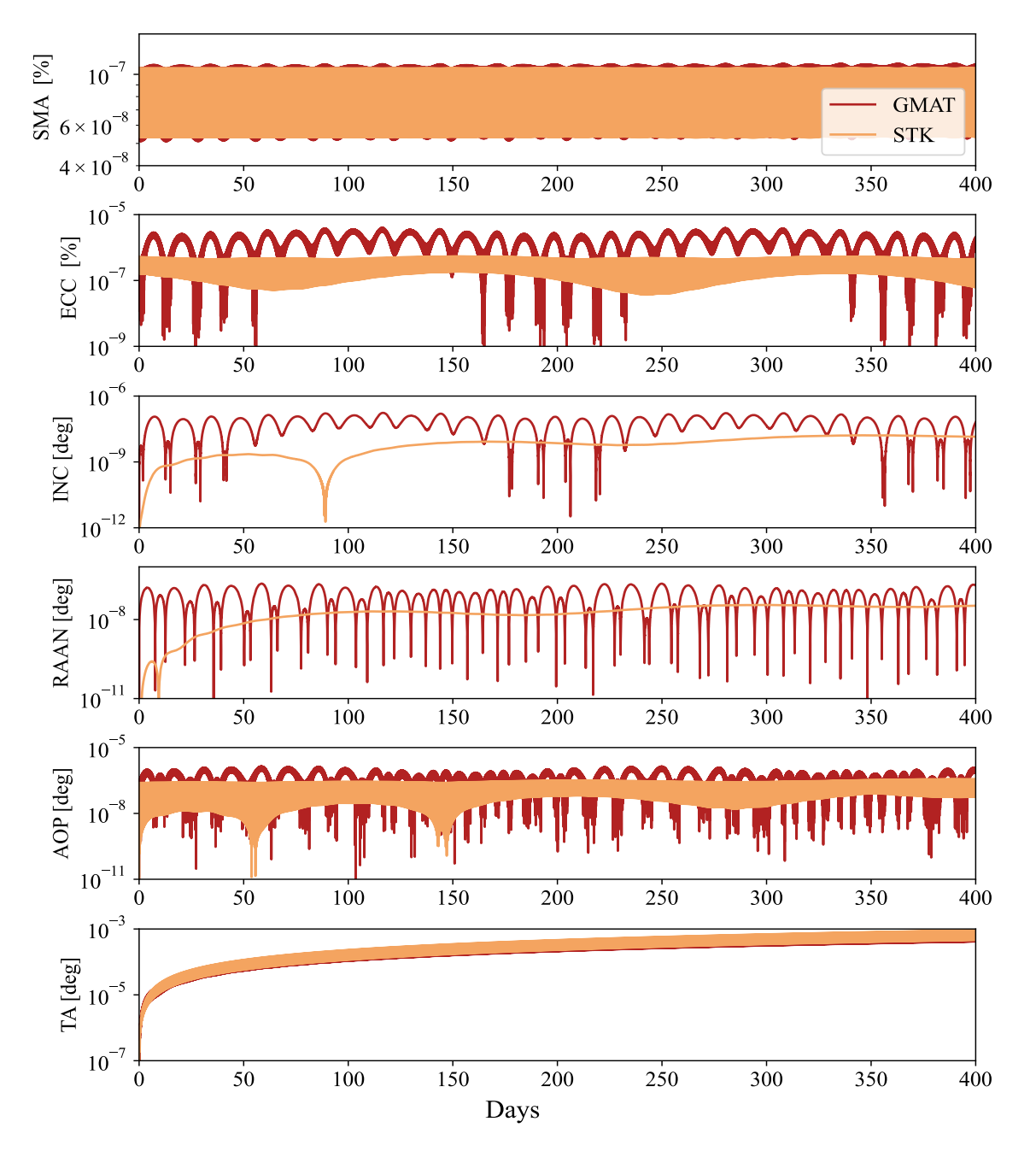


Figure 5.8: Keplerian elements error of CHAOS relative to HPOP and GMAT over 400 days under Luni-Solar perturbations. Due to fast oscillations, the lines can appear as solid blocks which are overlapping as the different propagators present similar behaviour.

Outside the validation, I updated CHAOS to utilise the most modern kernel, DE440. Again, although STK includes NAIF SPICE within its packages, whether HPOP employs it for planetary ephemerides is not explicitly stated. HPOP provides an option to include the time required for light to travel from the Sun to the satellite's position. This option changes the Sun's apparent direction, delaying it by 8 minutes from its actual position. This feature is not incorporated in CHAOS and thus was deactivated in HPOP for validation.

The performance of HPOP and GMAT relative to CHAOS, shown in Figure 5.8, is similar for Luni-solar perturbations. The error in the semi-major axis, inclination, RAAN, and AOP oscillates around  $10^{-7}$ . Equally, the True Anomaly error grows to  $10^{-3}$  after 400 days. Results differ slightly in eccentricity, where CHAOS aligns more closely with HPOP than GMAT, showing errors of approximately  $10^{-7}$  and  $10^{-6}$ , respectively. The oscillations relative to GMAT are due to the period of the Moon. These are less visible in STK, likely because the mathematical routine modelling the ephemeris is closer to the one used in CHAOS. The error growth shows a linear trend, allowing the approximation of the error for long-term simulations. The largest percentage of error is observed between CHAOS and GMAT in eccentricity at  $10^{-6}$ %. After 100 years, this error would reach about  $9 \times 10^{-5}$ %. The most significant angular error is in the True Anomaly, at  $10^{-3}$  after 400 days, which would result in an error of approximately 0.09 degrees after 100 years. Excluding the True Anomaly, the greatest angular error is  $10^{-7}$  for the AOP, leading to an error of roughly  $9 \times 10^{-6}$  degrees after 100 years. These results indicate that while the orbit is accurately propagated, the spacecraft's location along the trajectory is less precise. Again, this discrepancy can be attributed to slight variations in the models used and the integration scheme chosen. This validation shows that CHAOS correctly models the gravitational effects of the Sun and Moon and demonstrates good agreement with the chosen reference software.

#### Solar radiation pressure

The SRP modelling in CHAOS is compared with GMAT and HPOP. When compared to GMAT, CHAOS matched its NAIF SPICE kernel (DE405), although it uses the most upto-date version (DE440) otherwise. GMAT uses a fixed solar constant that differs from the one provided by Vallado, which was initially used in CHAOS. GMAT employs a  $C_k$  of  $3.844405613 \times 10^{26}$  W, while Vallado uses  $3.823 \times 10^{26}$  W. CHAOS was then updated to use the constant defined by GMAT permanently. GMAT also computes the direction of the SRP from the Sun to the central body, the Earth, meaning the vector  $\vec{r}_{Sun-sat}$  becomes  $\vec{r}_{Sun-E}$  and does not vary with the actual position of the spacecraft. These changes were implemented in CHAOS for validation purposes when compared to GMAT. Otherwise, CHAOS uses  $\vec{r}_{Sun-sat}$  which changes the direction of the SRP to account for the spacecraft's position. The equivalent information was not readily available for HPOP, so no changes were made for that comparison.

Figure 5.9 plots the error for all Keplerian elements. CHAOS computes the semi-major axis, inclination, and RAAN relative to HPOP with an error of  $10^{-6}$ . The eccentricity and AOP are computed with an error of  $10^{-5}$ , while the True Anomaly error grows to  $10^{-1}$  over 400

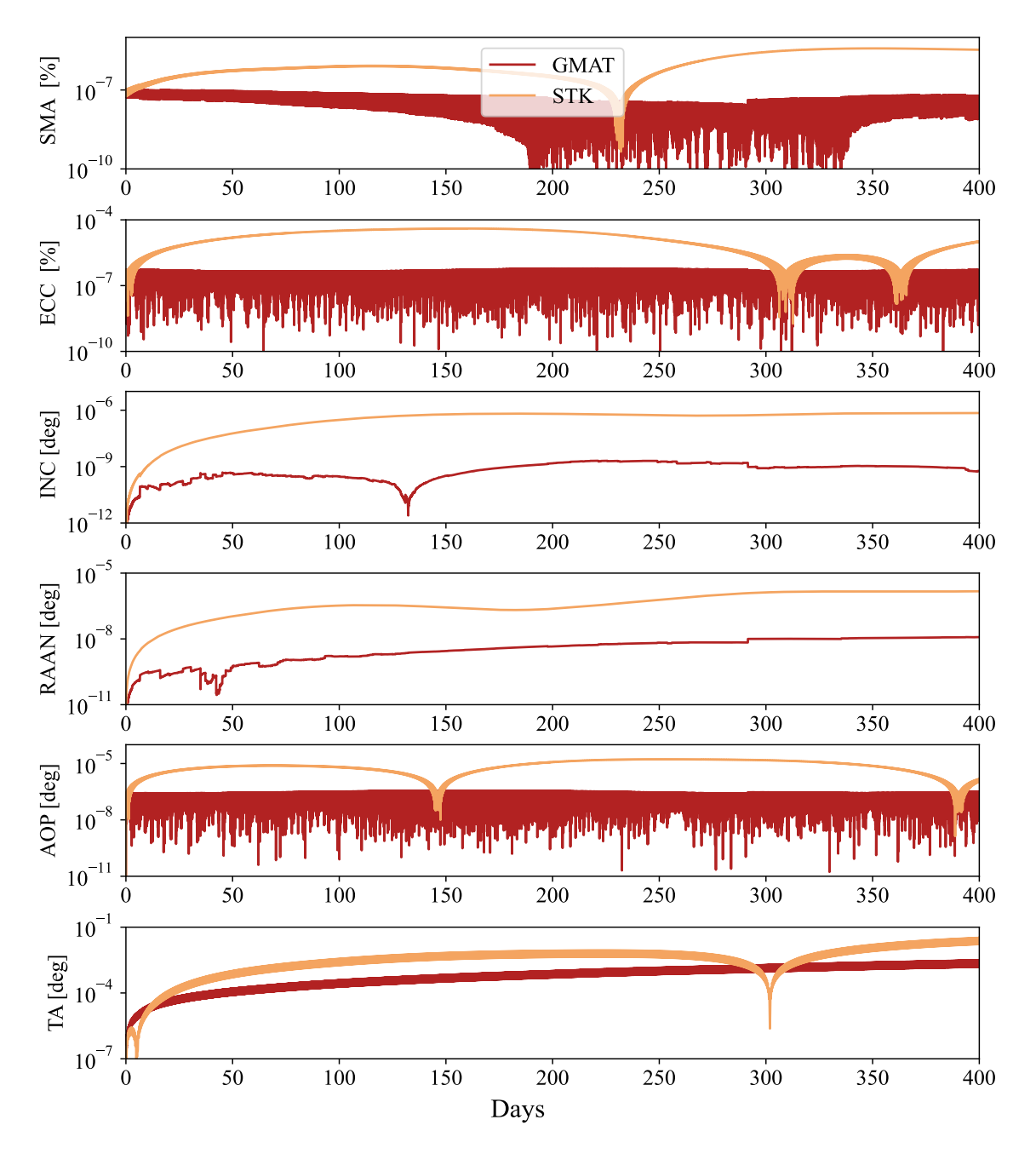


Figure 5.9: Keplerian elements error of CHAOS relative to HPOP and GMAT over 400 days under solar radiation pressure perturbations. Due to fast oscillations, the lines can appear as solid blocks which are overlapping as the different propagators present similar behaviour.

days. In this validation, CHAOS performs more closely to GMAT. The semi-major axis, eccentricity, and AOP have errors at  $10^{-7}$ , while the inclination and RAAN errors are around  $10^{-9}$ . The True Anomaly error grows to  $10^{-3}$ . Although the errors exhibit some periodic changes, they mostly grow linearly, allowing for estimating errors in long-term simulations. The largest percentage error is in the eccentricity, relative to HPOP, with an error of  $10^{-5}$ . This is due to the difference in the modelling of the SRP Additionally, GMAT and STK

were found to use different solar constant than given by standard textbooks [106, 113]. After 100 years, this error would become  $9 \times 10^{-4}$ %. The most significant angular error is in the true anomaly, measured against HPOP, reaching 10<sup>-1</sup>. After 100 years, this error would grow to 9.1 degrees. Excluding the true anomaly, the greatest angular error is in the AOP at  $10^{-5}$ , which would result in an error of  $9 \times 10^{-4}$  degrees after 100 years. As seen in previous comparisons, the error in True Anomaly grows rapidly and is poorly predictable, while the orbit itself is propagated much more accurately. This validation demonstrates that CHAOS's model of the SRP is in good agreement with both GMAT and HPOP.

### Aerodynamic drag

Aerodynamic drag modelling in CHAOS is compared to GMAT and HPOP. The analysis shows more significant errors due to differences in atmospheric models and underlying parameters. CHAOS does not model geomagnetic activity, while GMAT and HPOP do. GMAT and HPOP also employ the Jacchia-Roberts 1960 atmospheric model, whereas CHAOS utilises a fast interpolation over the Jacchia 1977 atmospheric model. Given the difficulty in predicting aerodynamic forces, significant differences between the models are expected, although the overall qualitative behaviour should remain similar.

Figure 5.10 shows the evolution of errors in all Keplerian elements. Relative to HPOP, the errors in the semi-major axis and eccentricity grow above  $10^{-1}$ . The inclination and AOP errors increase to  $10^{-2}$ , while the RAAN error reaches  $10^{-3}$ . The True Anomaly error grows significantly, exceeding 10<sup>1</sup>, with periodic oscillations indicating that CHAOS is many revolutions offset from the HPOP results. Compared to GMAT, the errors are lower. The semi-major axis, eccentricity, and  $\overline{AOP}$  errors grow to  $10^{-2}$ , while inclination and RAAN errors reach  $10^{-4}$  after 400 days. The True Anomaly error relative to GMAT also exceeds  $10^1$ . Again, these substantial differences are attributed to the varying underlying models. Given these discrepancies, a "point-by-point" comparison is less meaningful. Instead, the overall effect of CHAOS's atmospheric model is investigated by comparing the natural decay times of a 1U CubeSat between CHAOS, HPOP, and GMAT. The results, shown in Figure 5.11, demonstrate that CHAOS provides decay times close to GMAT's estimation. Notably, the error between the two reference software packages is more significant than between GMAT and CHAOS. This comparison indicates that the atmospheric model within CHAOS is correctly implemented and properly influences orbital dynamics.

Overall, the key finding is that the error between CHAOS and either reference software is consistently lower than the error observed between GMAT and HPOP, for all force models.

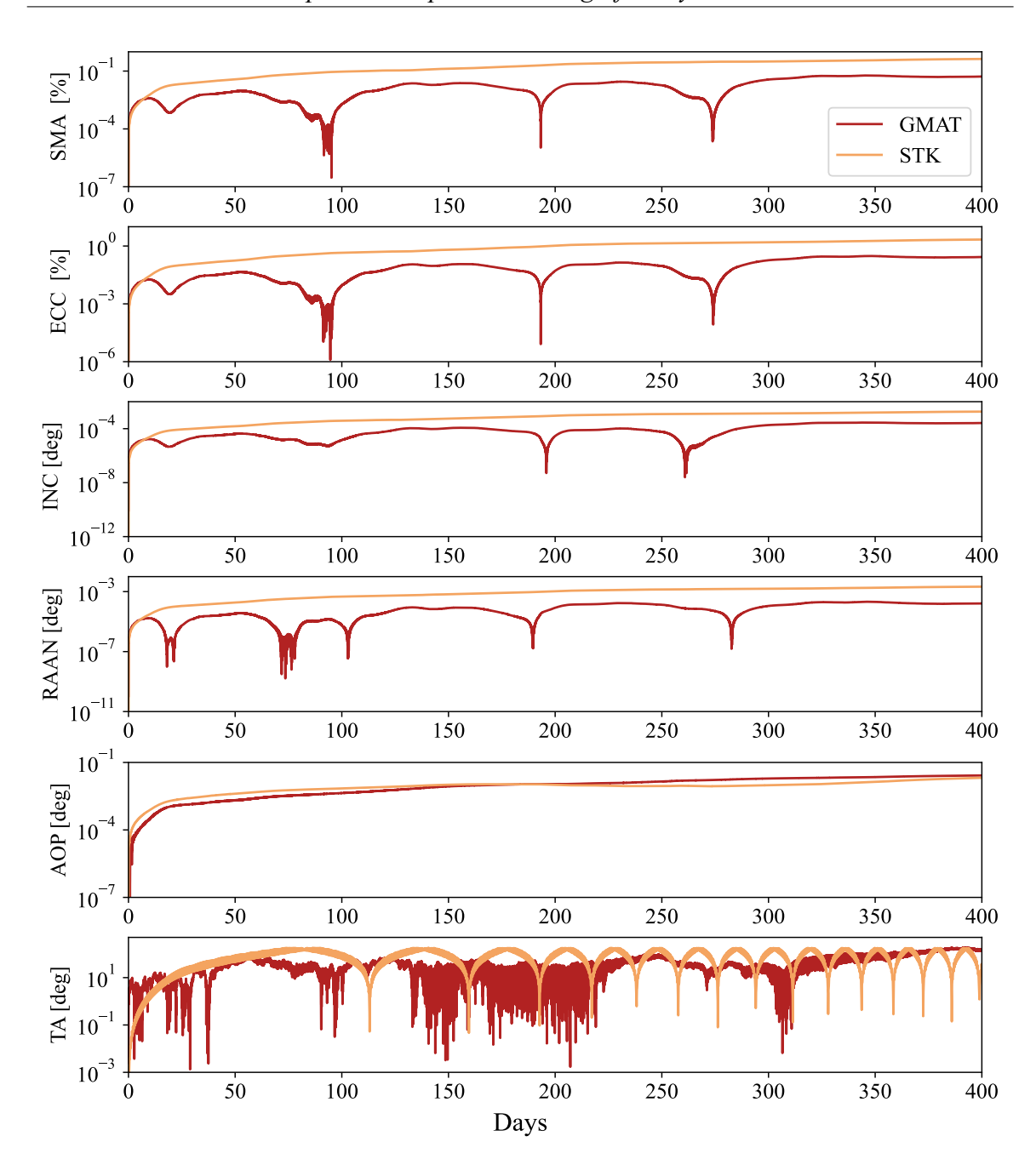


Figure 5.10: Keplerian elements error of CHAOS relative to HPOP and GMAT over 400 days under aerodynamic perturbations.

Given this result, the orbital equations of motion and force models implemented in CHAOS are successfully validated.

### **Attitude validation**

The attitude modelling of CHAOS is compared to STK's Attitude simulator for torque-free motion validation [175]. As the torques in CHAOS are derived from the same model as

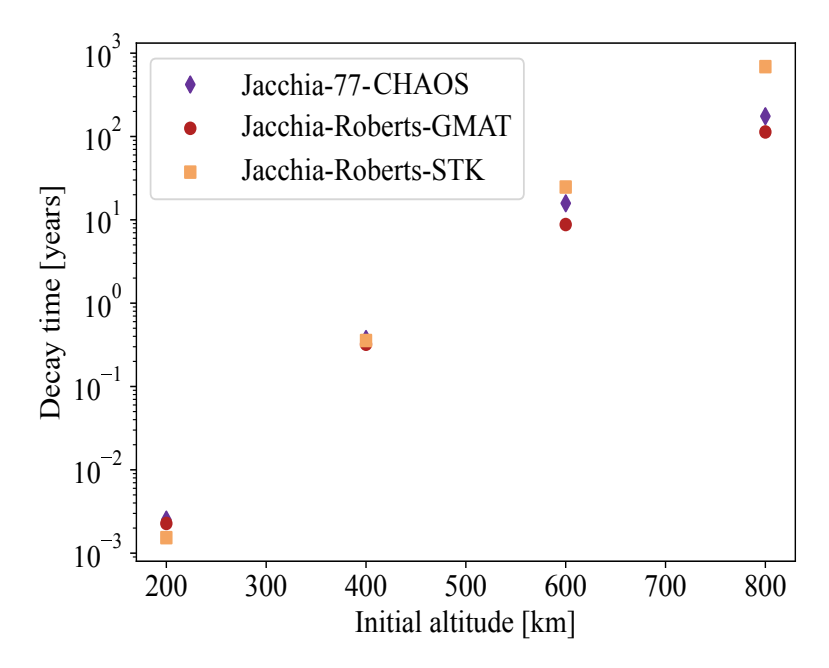


Figure 5.11: Decay times between simulators using the Jacchia-Roberts and Jacchia-77 atmospheric models.

the orbital perturbations, the orbital validation effectively demonstrates their correct implementation. To ensure thorough validation, the behaviour of a CubeSat under aerodynamic stabilisation was analysed. It is a practical, useful test case to evaluate CHAOS's ability to model more complex attitude dynamics scenarios.

#### **Torque-free motion**

Attitude data	Value
Initial attitude quaternion	$\begin{pmatrix} 0.5 & 0.5 & 0.5 & 0.5 \end{pmatrix}^T$
Initial angular velocity vector	$egin{pmatrix} \left(0.5 & 0.5 & 0.5 & 0.5 \right)^T \\ \left(0.01 & 0.1 & 0 \right)^T \text{ rad/s} \end{pmatrix}$
	(0.00182)
SLUCUBE-2 inertia matrix	$0.00185   kg \cdot m^2$
(frame centred on Cube- Sat's centre of mass)	0.00220

Table 5.4: Initial conditions for validation of torque-free motion.

CHAOS's attitude modelling capabilities are validated against STK using a realistic simulation of a 1U CubeSat, specifically the SLUCUBE-2 [77]. Table 5.4 presents the parameters used for this comparison. SLUCUBE-2 was selected due to its non-ideal inertia matrix, which provides a more complex and realistic test case. Nutations were introduced by adding a destabilising rotation around the unstable axis, which is defined as the axis with the intermediate value in the inertia matrix. The spacecraft was simulated for 25 hours with an initial angular velocity of  $\begin{pmatrix} 0.01 & 0.1 & 0 \end{pmatrix}^T$  rad/s, corresponding to 1375 rotations in a day. The primary metric for comparison is the quaternion error, which indicates the error in the

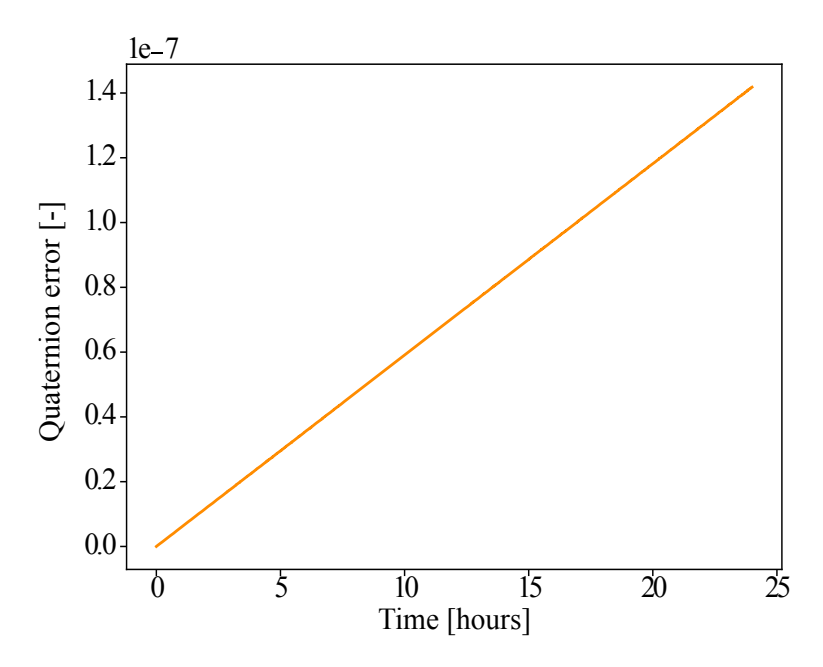


Figure 5.12: Error between CHAOS and STK quaternion in torque-free motion.

spacecraft's pointing. This error is computed using

$$\vec{q}_e = \|\vec{q}_{STK} - \vec{q}_{CHAOS}\|.$$
 (5.101)

Figure 5.12 shows the error evolution and reveals that the quaternion error grows linearly and remains low relative to STK, demonstrating the correct implementation of quaternion propagation in CHAOS relative to the reference software. Assuming the error growth remains linear, after 400 days, the error in the quaternion would reach  $10^{-5}$ , which remains low. The error in the angular velocity vector was also examined, with

$$\vec{\omega_e} = \|\vec{\omega}_{STK} - \vec{\omega}_{CHAOS}\|. \tag{5.102}$$

The error is shown in Figure 5.13. The difference between CHAOS and STK in this aspect also remains low and demonstrates a linear trend. Again, assuming the error growth remains linear, after 400 days, the error in the angular velocity would reach  $10^{-9}$  rad/s, which remains low. The low and predictable error growth in both quaternion and angular velocity calculations show the correct implementation of the attitude equations of motion in CHAOS relative to STK.

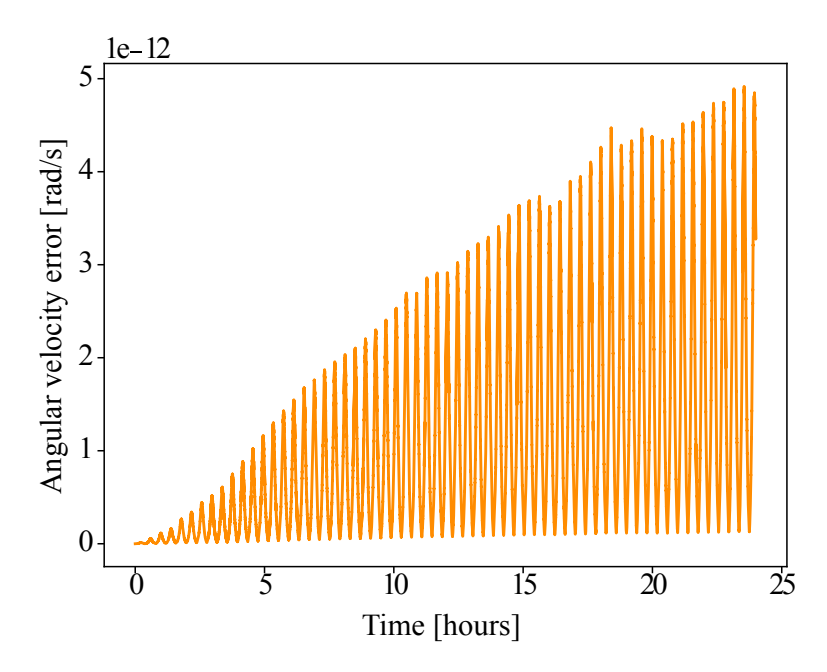


Figure 5.13: Error between CHAOS and STK angular velocity vector in torque-free motion.

#### Aerodynamic stabilisation

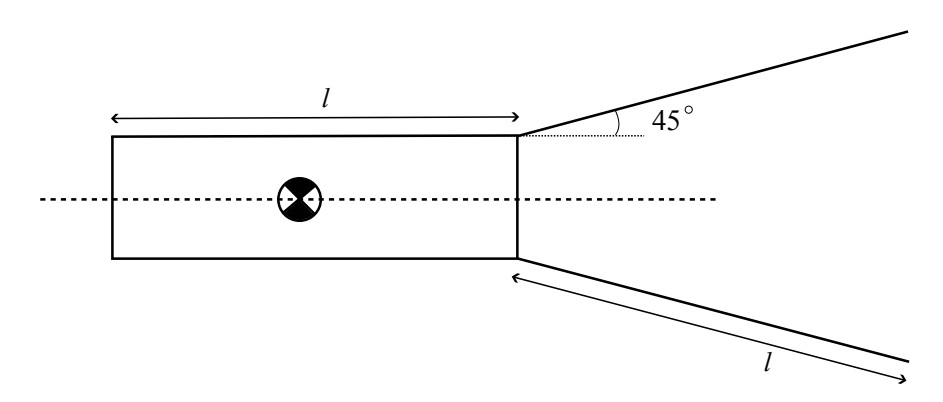


Figure 5.14: A 3U CubeSat with deployable panels arranged in a shuttlecock configuration for passive aerodynamic stabilisation.

The behaviour of attitude dynamics under complex torques in CHAOS is validated by testing the mechanics of passive aerodynamic stabilisation. The test uses a 3U CubeSat with deployable panels arranged in a shuttlecock configuration, as illustrated in Figure 5.15. These panels are set at a 45-degree angle relative to the CubeSat's centreline.

The 3U CubeSat was simulated at 250 km, 400 km, and 1000 km to examine stabilisation performance across varying atmospheric densities. This approach is supported by previous research [79, 80, 176], which suggests that the settling time should increase as altitude increases and drag forces decrease. At sufficiently high altitudes, where atmospheric drag becomes negligible, aerodynamic stabilisation should not be achieved. Figure 5.15 presents the angles between the body-fixed axes and the local velocity direction of the satellite. The plot shows the stabilisation process at different altitudes. At 250 km, the spacecraft achieves passive stabilisation within 10 hours and then successfully tracks the velocity direction, while at 500 km, stabilisation is achieved after approximately 40 hours. At 1000 km, no aerodynamic stabilisation is achieved. These outcomes demonstrate the correct implementation of torque modelling in CHAOS. The software captures spacecraft attitude and torque interactions and reproduces the expected passive aerodynamic stabilisation.

# 5.5 Code structure

CHAOS uses Object-Oriented Programming principles to create a robust and modular code. The architecture is designed to implement each physical component, including satellites, sensors, and thrusters, as a distinct class with its own specific properties. For instance, the satellite class maintains properties such as orbital and attitude states. Similarly, perturbation effects are implemented as separate instances, each containing relevant constants and holding functions to call dependent models, such as celestial object ephemeris or solar cycle activity. CHAOS coordinates the interactions between the classes and an integration scheme by gathering necessary data from various objects for integration purposes and invoking perturbation functions at each integration step, as shown in Figure 5.16. During this process, the system continuously updates the state of all objects, including parameters such as the satellite's orbital and attitude state, sensor bias values, and fuel distribution across pixels. The code is currently written in Python, and a 400 days simulation, with all perturbations on, takes approximately 100 minutes.

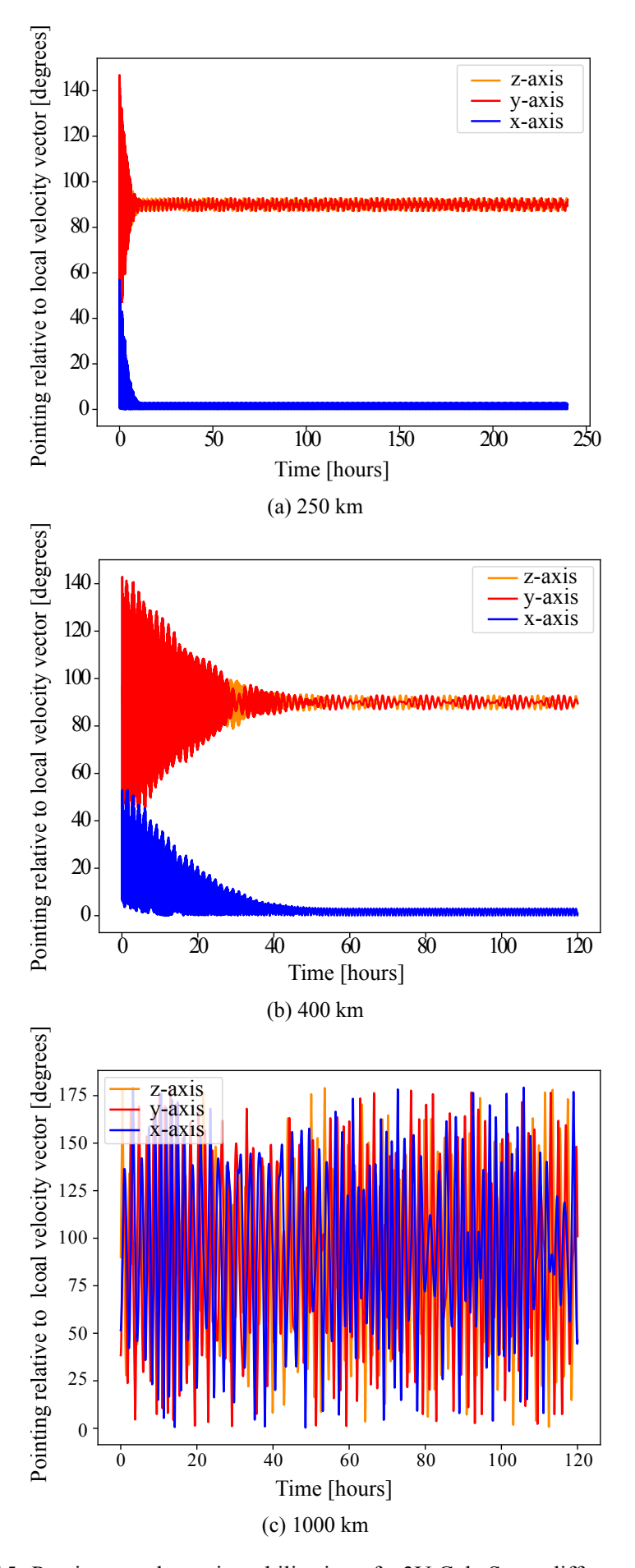


Figure 5.15: Passive aerodynamic stabilisation of a 3U CubeSat at different altitudes.

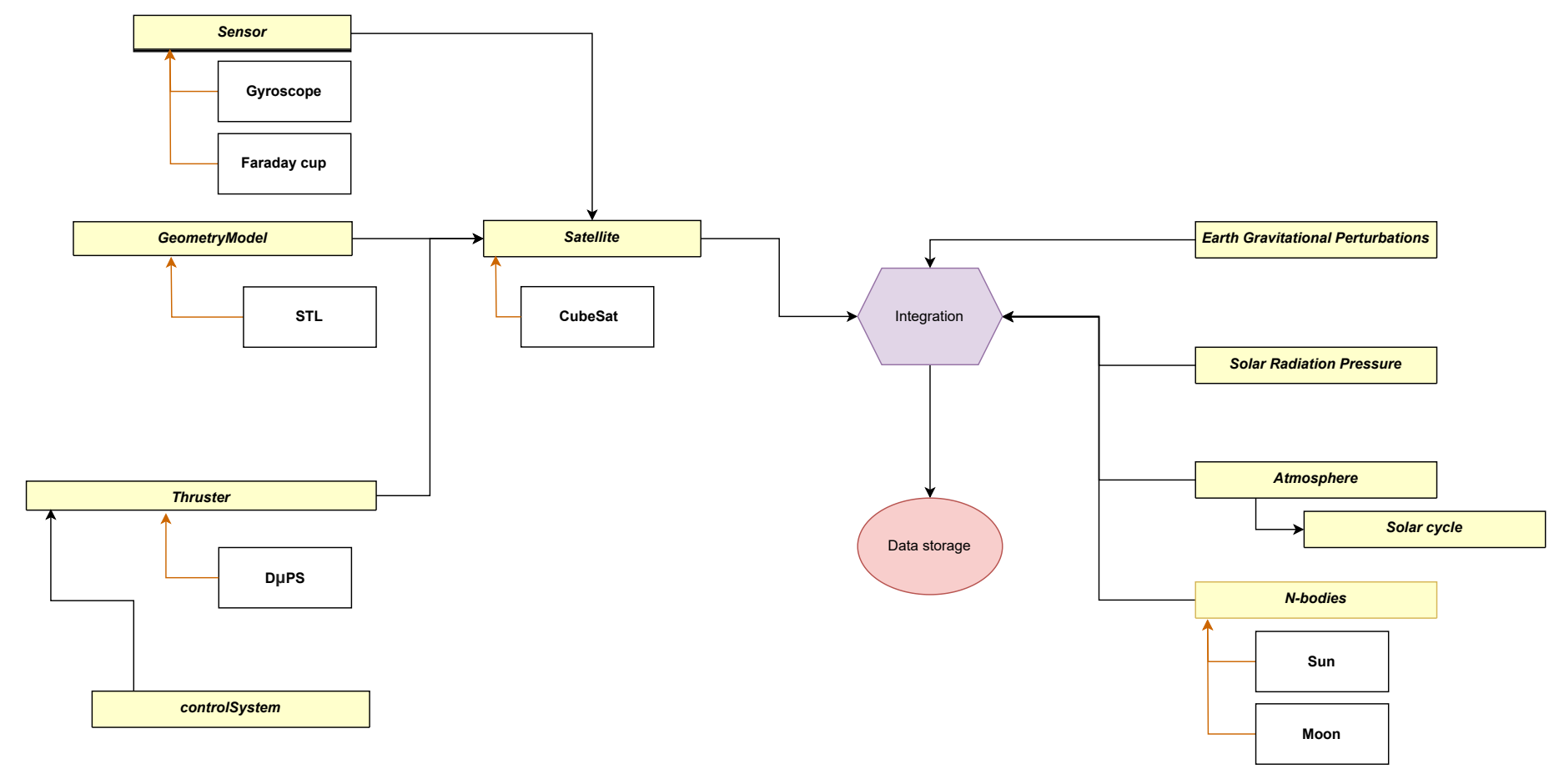


Figure 5.16: Visualisation of the code structure for CHAOS using standard Unified Modelling Language. For visualisation, the arrows denoting the inheritance relationship are coloured in brown.

#### **Conclusion** 5.6

This section has described the models used in CHAOS to provide 6-DOF spacecraft modelling. CHAOS utilises the Gauss Planetary Equations for orbital propagation using Modified Equinoctial elements, while attitude propagation is accomplished through Euler's equation and quaternion kinematics. CHAOS reads STL files to obtain detailed shape information of a spacecraft. A more accurate representation of how a spacecraft interacts with its environment is achieved by applying force models to each facet. The software models SRP and uses the NAIF SPICE software to determine the position of the Earth relative to the Sun. CHAOS includes the same shadow model as GMAT, the Percent Shadow model, which provides the visible fraction of the solar disk from the spacecraft's position. The simulation environment computes atmospheric density through an interpolation of the Jacchia-77 atmospheric model. A temperature-dependent atmosphere is represented using the uncorrected exospheric temperature to compute the density at a given position and time. This atmospheric density is then used in the Sentman model for Gas-Surface interactions, allowing CHAOS to compute the spacecraft's lift and drag coefficients based on its attitude. CHAOS employs spherical harmonics, using coefficients from the EGM2008 model to represent the Earth's non-spherical shape. The perturbing accelerations induced by the presence of the Moon and Sun are included, with NAIF SPICE used to determine their positions relative to the Earth. The exact attitude of the spacecraft determines the direction in which thrust acts. These models were validated by comparing CHAOS to two reference software packages, GMAT and HPOP. The validation was performed individually for each force model, and CHAOS demonstrated good overall agreement with the reference software. While it does not guarantee the lack of errors, it shows that CHAOS does not produce significant errors relative to our reference tools.

# 6

# Application: CubeSat post-mission disposal

The contents of this chapter have been published as Saddul et al in *Acta Astronautica* [177], presented at the *International Astronautical Congres 2022* [178], and form part of a group project delivered to ESA's Innovative Propulsion System for CubeSats and MicroSats scheme [36]. This chapter examines how the  $D\mu PS$  can be used to increase the operational ceiling of nanosatellites, as originally proposed by Min Kwan et al. [179]. I present the operation of the CubeSat De-orbiting All-Printed Propulsion System (Cube-de-ALPS), a specialised version of the  $D\mu PS$  which is being developed at the University of Southampton in collaboration with the European Space Agency to provide robust de-orbiting capability to sub-3U CubeSats. It comprises a flexible substrate on which coplanar arrays of vacuum arc micro-thrusters (micro-VAT) are printed alongside small supporting electronic subsystems. In particular, the focus is on the application of a Cube-de-ALPS End-Of-Life disposal to HUMSAT-D, an under-actuated 1U CubeSat with uncontrolled spin. In this scenario, a Faraday cup will provide coarse angle-of-attack estimates and trigger a single micro-VAT to ignite every time it points toward the forward velocity vector. Orbital lifetime estimates for different fuel materials, configurations, and operational modes are estimated using simplified dynamics and analytical thrust averaging. These results are compared to high-fidelity numerical simulations using CHAOS to confirm the viability of the concept and confirm that Cube-de-ALPS can de-orbit CubeSats from 1400 km. The analysis and results presented in this chapter are my own work, whilst the thruster itself is being developed by a concurrent team at the University of Southampton.

#### 6.1 **CubeSat de-orbiting All-Printed Propulsion System**

As part of ESA's Innovative Propulsion System for CubeSats and MicroSats, the  $D\mu PS$ concept has been specialised into a more detailed design at the University of Southampton [36]. The fully-printed, flat system can be placed on one or multiple sides of a 1U CubeSat and will provide thrusting capabilities. The thruster system still consists of multiple arrays of pixels that can generate, one at a time, a thrust level in the micro-Newtons with a 1.5 W power requirement on the bus. Nominally, it is arranged in a 10x10 grid to provide 100 micro-VATs, and its theoretical fuel capacity provides it with one year of firing time. The developed system is aimed to fit within a 0.2U volume and weighs up to 250 g including up to 100 g of propellant.

This specialised version of the  $D\mu PS$  is called the CubeSat De-orbiting All-printed Propulsion System (Cube-de-ALPS), a system designed to provide post-mission disposal capacities to sub-3U CubeSats. The system operates under the assumption that the host CubeSat is under-actuated and that Cube-de-ALPS does not control its pointing. Thus, Cube-de-ALPS will fire whenever its micro-thrusters point anywhere in the velocity direction, which relaxes the need for precise attitude determination and control. In addition to the VAT, Cube-de-ALPS includes all required attitude-sensing devices, as well as a control law for disposal and attitude maintenance.

A potential alternative approach to spacecraft de-orbiting uses orbital eccentricity to enhance exposure to atmospheric drag effects. By firing thrusters to increase the eccentricity, the spacecraft's perigee altitude is decreased, forcing it to pass through regions of higher atmospheric density during each orbit. This exposure to denser atmospheric layers subjects the spacecraft to increased drag forces, which gradually circularise the orbit at progressively lower altitudes. This process continues until the spacecraft encounters sufficient atmospheric density to cause re-entry. This technique was thoroughly investigated by Lucking et al. [103, 104, 105, 180], who examined its implementation through the Ikaros mission. Their research investigated a solar sail equipped with electrochromic control capabilities to achieve accelerated de-orbiting. The electrochromic control system, which is detailed in Chapter 3, allows for precise modulation of the solar radiation pressure effects on the spacecraft. However, while this approach demonstrates considerable promise for larger spacecraft, it faces significant implementation challenges for 1U CubeSats. The primary limitation stems from the CubeSat's inherent attitude control constraints - these miniature spacecraft typically cannot maintain the precise pointing accuracy needed to time and orient their thrusters for maximising orbital eccentricity changes.

# **Design of Cube-de-ALPS**

As of its use of distributed propulsion architecture, Cube-de-ALPS provides multiple microthrusters laid out in a co-planar fashion. Each micro-thruster, also called thruster pixel, is an individual micro-VAT capable of delivering thrust using the printed VAT micro-thrusters with a radius of 3 mm. To ensure total erosion of the fuel, the maximum distance between the anode and the cathode should be no greater than 4.7 mm, thus also limiting the pixel height to 3.6 mm, as shown in Figure 3.2b.

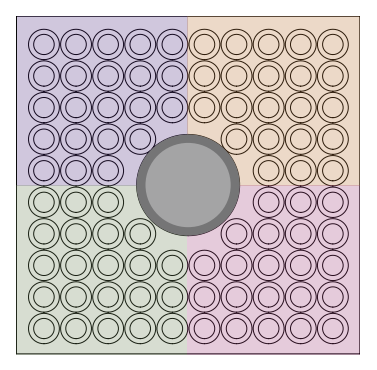


Figure 6.1: Drawing of the thruster pixels of Cube-de-ALPS, with a Faraday cup in the centre. The different colours correspond to the quadrant division.

The nature of the layout leads most pixels to generate a torque upon firing as they are not aligned with the centre of mass. To counter this effect, Cube-de-ALPS divides itself into four individually addressable quadrants, as shown in Figure [6.1]. The four zones were chosen over individual pixel control to provide essential attitude control while keeping the electronics design simple. Cube-de-ALPS based on its angular velocity, can decide in which quadrant a pixel will ignite, and based on the path of least electrical resistance within the quadrant's circuit, one of the micro-VATs will ignite. This selection process means Cube-de-ALPS has no control over which exact pixel will fire. Instead, it can only control in which quadrant a thruster pixel will turn on. Whenever a pixel ignites, it receives a pulsed electrical signal, and the thrust variation detailed in Chapter [3] still applies. However, with a pulse frequency of 100 Hz, the average thrust is still closely distributed around the nominal thrust level of each pulse, as per the Central Limit Theorem [173], leading to a very consistent average thrust delivered.

Due to its printed nature, Cube-de-ALPS has inherent flexibility in its pixel layout. In this chapter, two different layouts are studied: one Cube-de-ALPS system fitted on a single face (1-F) and another Cube-de-ALPS system split across two opposite faces (2-F) while retaining the same amount of fuel. As all faces equipped with Cube-de-ALPS also have their own Faraday cup, the 2-F layout is expected to fire more often and thus have improved

de-orbiting performance.

### **Onboard Attitude Determination**

Beyond the printed VAT, <u>Cube-de-ALPS</u> also includes sensors to estimate its angle-of-attack and angular velocity. This section introduces a MEMS gyroscope that can provide accurate angular velocity readings over a long operational time, and a Faraday cup that can provide coarse angle-of-attack estimates.

#### Gyroscopes for angular rates measurements

To correctly select which quadrant to fire, Cube-de-ALPS requires only knowledge of the CubeSat's angular velocity, as the quadrants only control the CubeSat's spin rate. The system utilises a gyroscope to provide angular rate readings. While many gyroscopes can provide accurate angular velocity measurements, the mass and volume restrictions on Cube-de-ALPS limit the range of options. As the sensor is expected to operate for at least the nominal lifetime of Cube-de-ALPS, the thruster requires a gyroscope that produces low noise over extended periods of time. Therefore, the STIM277H, an aerospace-grade 3-axis MEMS sensor manufactured by Safran, was selected for use on Cube-de-ALPS [181]. The sensor, measuring 21.5 x 38.6 x 35.9 mm, provides readings with a standard deviation of  $0.47 \frac{\text{deg}}{\text{s}}$  after one year, which is the nominal operational lifetime. In contrast, the MP6050 MEMS gyroscope, a typical consumer-grade sensor commonly used by hobbyists, will have readings with a standard deviation of  $6.7 \frac{\text{deg}}{\text{c}}$  after one year.

#### Angle-of-attack estimation with a Faraday cup

Cube-de-ALPS must know where its pixels are pointing to provide correct de-orbiting. While commercially available solutions for attitude determination exist, with typical packages using a combination of sensors to provide accurate pointing data, these systems also tend to be voluminous and heavy [15], making them unsuitable for the Cube-de-ALPS package.

Due to the opportunistic firing law, the system requires only knowledge of its angle relative to the velocity vector, referred to as the angle-of-attack. The work of Watanabe et al. [182] shows how a Faraday cup can estimate the CubeSat's orientation relative to the velocity vector by detecting the ions from the incoming flow direction. The EGG spacecraft, a 3U

CubeSat, has flown with a Faraday cup as an attitude sensor demonstrating its feasibility [183]. This method of estimating the attitude presents the advantage of being small and easy to fit on CubeSats, as the sensor is 30 mm in diameter and 10 mm in height, with an aperture of 7 mm.

The sensor detects the current generated by ions colliding with a collector plate placed behind the aperture of the Faraday cup. A series of charged grids, in-between the plate and the aperture, ensure that only ions with a high relative velocity, i.e., the spacecraft's orbital velocity, can enter the sensor. This gives confidence that a current will only be detected when facing the incoming flow. However, the detected current is proportional to the number of ions hitting the plate, given by

$$I = q_e \rho_{ions}(h) A_{fc}(\theta) v_{sat}$$
(6.1)

where  $q_e$ ,  $\rho_{ions}(h)$  and  $v_{sat}$  are the charge of an electron, the local density of positively charged ions as a function of altitude h, taken from [184], and the orbital velocity of the spacecraft, respectively. The angle-of-attack  $\theta$  is measured between the flow direction and the Faraday cup centerline, and the variable  $A_{fc}(\theta)$  denotes the area of the collector plate that ions can hit, shown in Figure [6.2] as the intersection area. As the spacecraft velocity

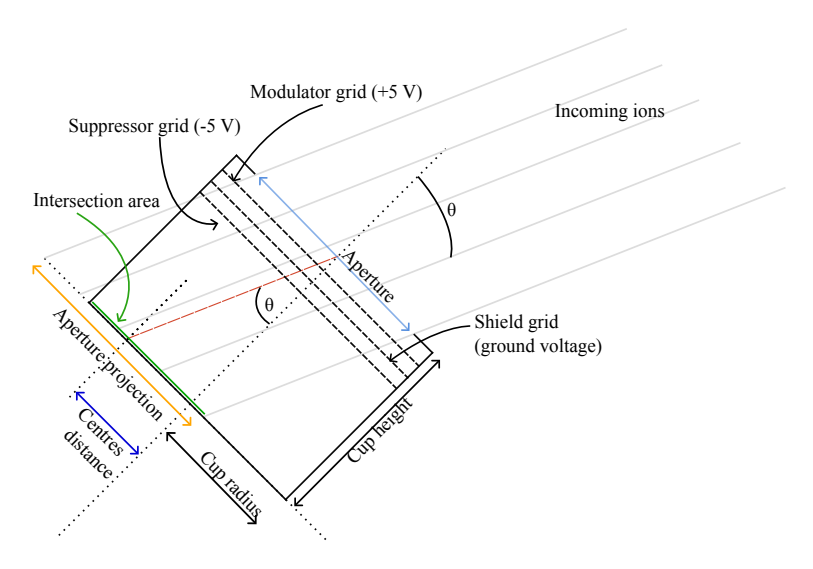


Figure 6.2: Sketch of the Faraday cup.

is significantly higher than the thermal velocity of the ions [152], the incoming flow is modelled as parallel rays that project the aperture on the collector plate plane at a distance d from the sensor centreline,

$$d(\theta) = h_{fc} \tan(\theta) \tag{6.2}$$

where  $h_{fc}$  is the height of the Faraday cup. The overlapping area between the sensor and the projected aperture corresponds to  $A_{fc}(\theta)$  and is computed as the intersection area between two circles of equal radius  $r_{fc}$  [185],

$$A_{fc} = 2r_{fc}^2 \arcsin\left(\frac{\sqrt{r_{fc}^2 - \frac{d^2(\theta)}{4}}}{r_{fc}}\right) - d(\theta)\sqrt{r_{fc}^2 - \frac{d^2(\theta)}{4}}.$$
 (6.3)

The Faraday cup on the EGG spacecraft has flown at altitudes lower than 500 km, where positive oxygen ions are present at a density of  $10^5$  ions  $\cdot$  cm<sup>-3</sup> [186]. The work of Nanan et al. ([184]) shows that while the density of positive Oxygen ions lowers above 500 km, the number of protons (H<sup>+</sup>) increases and stagnates at  $10^4$  ions  $\cdot$  cm<sup>-3</sup>, up to at least 2000 km. Operation at higher altitudes is then ensured by increasing the aperture of the Faraday cup to the collector plate diameter. As no other design parameters need to be changed, the sensor remains at the same dimensions, which leads to 12 pixels being removed from the Cube-de-ALPS grid, as shown in Figure 6.1. Due to the presence of thruster pixels in proximity to the Faraday cup, contamination from the plume is a potential concern. However, because the modulator grid is positively charged, which allows only ions with a high relative velocity to enter the Faraday cup, this is not an issue. Similarly, the presence of negatively charged ions could lead Cube-de-ALPS to detect a weaker signal, which would limit its firing opportunity. This is mitigated thanks to the presence of the negatively charged suppressor grid, which stops electrons and negatively charged ions from reaching the collector plate.

With the addition of the Faraday cup and the gyroscope, Cube-de-ALPS can now estimate its angle-of-attack and angular velocity. Table 6.1 provides a summary of the sensors, the characteristics and constraints of Cube-de-ALPS assumed for the simulations carried out in this chapter.

# **Onboard Firing Criterion**

Cube-de-ALPS is assumed to turn on at the end of the mission life of the host CubeSat or shortly after launcher separation if the spacecraft is dead-on-arrival.

To ensure de-orbiting, the system must thrust to slow down the orbital velocity of the host CubeSat, which can be achieved by firing against the velocity direction. As the measurements of the Faraday cup are electrical current readings, the exact angle-of-attack  $\theta$  of the spacecraft cannot be determined onboard. Indeed, solving Equation (6.1) for  $\theta$  would require knowledge of the spacecraft's velocity and altitude. However, Cube-de-ALPS cannot obtain real-time orbital height and velocity measurements. Fortunately, the exact angle is

Property	Value
Max. pixel height [mm]	3.6
Max. fuel mass [g]	100
Max. total system mass [g]	250
Max. system volume [U]	0.2
Operational power [W]	1.5
Pulse standard deviation [%]	10
Pulse frequency [Hz]	100
Number of pixels [-]	88
Number of quadrants [-]	4
Gyroscope	STIM277H
Faraday cup dimensions [mm]	30x10

Table 6.1: Summary of Cube-de-ALPS sensors and properties.

not required to determine whether the Faraday cup is facing forward. Instead, the system can decide to fire whenever it detects a signal above its expected noise  $\epsilon$ , which would imply that it is facing the incoming flow. This mode of operation consists of firing when the signal-to-noise ratio SN is equal to or above a given value. It can be expressed as

$$SN = \frac{q_e}{\epsilon} \rho_{ions}(h) A_{fc}(\theta) v_{sat}$$
 (6.4)

and the firing criterion is

$$SN \ge SN_{firing}$$
 (6.5)

where  $SN_{firing}$  is the desired minimal signal-to-noise ratio.

Equation (6.4) shows that the signal detected varies with the angle-of-attack, and a brief investigation of Figure 6.2 indicates that as  $\theta$  increases, the signal will decrease to zero. Therefore, there must exist an angle  $\alpha$  where the signal detected is equal to the firing criterion,

$$SN(\alpha) = SN_{firing}.$$
 (6.6)

The cone defined by the half-angle  $\alpha$  is called the thrusting cone, which is the region where  $SN \geq SN_{firing}$ . Due to the variation of ion density with altitude, the thrusting cone half-angle is a function of orbital height, which varies in time.

If the firing criterion in Equation (6.5) is true, by definition, the Faraday cup must be inside the thrusting cone, so Equation (6.5) is equivalent to

$$\theta \le \alpha(h(t), SN_{firing})$$
 (6.7)

where the value of  $SN_{firing}$  will determine the profile of  $\alpha$  with respect to altitude. This criterion is not usable onboard the CubeSat but is useful to understand the thrusting profile of Cube-de-ALPS. Generally, a higher  $SN_{firing}$  means the thrusting cone is smaller throughout all altitudes compared to a lower signal-to-noise ratio. Similarly, the thrusting cone  $\alpha$  is smaller at higher altitudes and combinations of high  $SN_{firing}$  and high altitudes can even make it disappear, in which case Cube-de-ALPS doesn't fire in any direction.

#### 6.2 Semi-analytical propagator

While accurate, CHAOS is computationally intensive for running simulations. During preliminary design phases and initial performance estimations, rapid simulations are often necessary, even at the cost of some accuracy. This section describes a semi-analytical propagator that uses the same orbital dynamics as CHAOS but without attitude propagation. Instead, an attitude-average technique is used to model the effect of thrust on the CubeSat. Section 6.3 then uses this semi-analytical propagator to provide preliminary performance estimates.

# Thrust averaging

Given a Cube-de-ALPS configuration with a fixed amount of fuel, or equivalently a total firing time  $t_{firing}$ , the thrust is modelled as a constant average thrust  $\hat{T}_{eff}$  along the velocity direction throughout the mission duration.

To obtain  $\widehat{T}_{eff}$ , the thrust delivered along the velocity direction throughout the entire mission is averaged analytically, while the effect of transversal thrust is ignored. This section assumes a random, uncontrolled tumbling of the spacecraft, making it equally likely to point in any direction relative to the orbital velocity vector. This assumption seems reasonable as CubeSats generally do not have actuation systems, and the randomness in the pixel selection leads to an unpredictable spin magnitude and direction [16], although passive stabilisation methods, such as hysteresis rods or deployables for aerodynamic stabilisation, could affect this assumption based on the CubeSat's altitude [74, 79].

I start by defining a coordinate system centred on the spacecraft with its  $\hat{z}$  axis aligned with the orbital velocity direction  $\hat{v}$ , as represented in Figure 6.3. The angle  $\alpha$  denotes the half-angle of the thrusting cone around the velocity direction. The highlighted sphere cap enclosed by the thrusting cone indicates all spacecraft orientations in which Cube-de-ALPS fires.

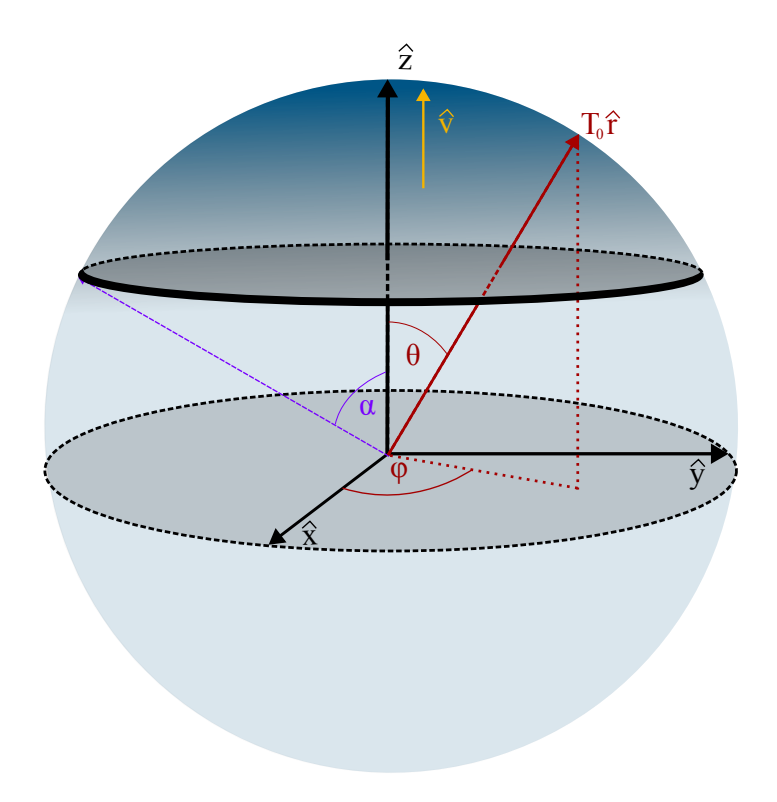


Figure 6.3: Unit sphere of all possible spacecraft orientations with the thrusting cone defined by  $\alpha$ . The highlighted sphere cap enclosed by the thrusting cone indicates all orientations in which Cube-de-ALPS fires.

Since all orientations are assumed to be equally likely over time, the fraction of time the system is thrusting,  $\tau_t$  is the same as the fraction of the surface of the full unit sphere covered by the sphere cap[187]:

$$\tau_t = \frac{A_{cap}}{A_{sphere}} = \frac{2\pi \left(1 - \cos(\alpha)\right)}{4\pi} = \frac{1 - \cos(\alpha)}{2}.$$
 (6.8)

Similarly, the average thrust delivered in the velocity direction can be calculated when the system is thrusting by averaging the projection of the thrust on  $\hat{v}$  over the sphere cap:

$$\widehat{T}_{\alpha} = \frac{T_0}{A_{cap}} \int_{cap} \widehat{r} \cdot \widehat{v} \, dA$$

$$= \frac{T_0}{2\pi \left(1 - \cos(\alpha)\right)} \int_0^{2\pi} \int_0^{\alpha} \cos(\theta) \, \sin(\theta) d\theta d\phi$$

$$= T_0 \left(\frac{1 + \cos(\alpha)}{2}\right)$$
(6.9)

where  $T_0\hat{r}$  is the thrust vector. Knowing the nominal firing time  $t_{firing}$  and  $\tau_t$ , one can

calculate the total mission duration throughout which Cube-de-ALPS is operational as

$$t_{mission} = \frac{t_{firing}}{\tau_t}. (6.10)$$

One can also obtain the total impulse imparted in the velocity direction throughout the mission as

$$I_{\hat{v}} = \widehat{T}_{\alpha} t_{firing}. \tag{6.11}$$

Finally, to obtain the equivalent average thrust  $\widehat{T}_{eff}$  constantly acting along the velocity direction throughout the entire mission duration  $t_{mission}$  and delivering the same total impulse  $I_{\hat{v}}$ , the following is defined,

$$\widehat{T}_{eff} = \frac{I_{\widehat{v}}}{t_{mission}} = \tau_t \widehat{T}_{\alpha} = T_0 \left( \frac{1 - \cos^2(\alpha)}{4} \right). \tag{6.12}$$

An important relationship between  $\alpha$ ,  $\widehat{T}_{eff}$ , and  $I_{\hat{v}}$  emerges out of Equations (6.11) and (6.12): An increased cone size  $\alpha$  also increases the effective thrust, but leads to a loss on the total impulse delivered against the velocity direction. This is because a bigger thrusting cone half-angle  $\alpha$  means Cube-de-ALPS can fire more often, but it will also thrust less accurately with a lower average component of thrust aligned in the desired direction.

If the case where Cube-de-ALPS is split across two opposite faces is considered, then the 2-F layout can fire twice as often as the 1-F setup, which leads Equation (6.8) to become

$$\tau_{t,2F} = 1 - \cos(\alpha). \tag{6.13}$$

Splitting the layout between two faces does not affect  $\widehat{T}_{\alpha}$ , and the new effective thrust can be computed using (6.12)

$$\widehat{T}_{eff,2F} = \tau_{t,2F} \widehat{T}_{\alpha} = 2\widehat{T}_{eff,1F}. \tag{6.14}$$

When using  $\widehat{T}_{eff}$  in the ODE integration of Equations (5.19), the thrusting cone half-angle  $\alpha$  is updated as a function of current orbital altitude by re-arranging Equation (6.4) for  $A_{fc}(\alpha)$ . Then, Equation (6.3) is inverted for d using a numerical root solver. Finally, the trivial relationship between d and  $\alpha$  is given by Equation (6.2).

As Equation (6.3) is not invertible, there is no analytical expression for  $\alpha$ . To avoid using a numerical root solver at every step of the integration, I pre-compute values  $\alpha$  for every 10 meters between 150 km and 2000 km. I then linearly interpolate between the data points to

update  $\widehat{T}_{eff}$  at every integrator step.

This change in  $\alpha$  over time influences the fraction of time the system is thrusting,  $\tau_t$ , which also affects the average fuel consumption rate. To accurately track the remaining fuel on board, the total impulse delivered is used to estimate the fuel consumption and fire as long as <u>Cube-de-ALPS</u> has not delivered all the onboard impulse. The ODE for the impulse delivered is expressed as

$$\dot{I}_{used}(t) = T_0 \tau_t(\alpha) \tag{6.15}$$

and is integrated alongside the modified equinoctial equations in (5.19). Therefore, the thrust value  $T_{ODE}$  turns off when all onboard fuel has been consumed,

$$T_{ODE} = \begin{cases} \widehat{T}_{eff}, & \text{if } \frac{I_{used}(t)}{I_0} \le 1\\ 0, & \text{otherwise} \end{cases}$$
 (6.16)

where  $I_0$  is the total onboard impulse.

# 6.3 System performance analysis

Using the semi-analytical propagator, the Cube-de-ALPS system parameters are systematically analysed, including fuel material, layout, and signal-to-noise ratio, and their impact on the de-orbiting performance. To that end, Cube-de-ALPS is integrated into HUMSAT-D, with satellite characteristics outlined in Table 6.2 This section assesses silver, aluminium, tungsten and copper as fuel materials by changing the thrust level and the firing time, which are both material-dependent quantities [4]. The layout analysis distributes the thruster system across opposing faces to increase thrusting time while maintaining the total amount of fuel. Varying the signal-to-noise ratio changes the thrusting cone size and its behaviour with altitude, which leads to a change in de-orbiting performance.

Property	Value
Orbit inclination	97.8°
Start date	1 Dec 2014
Fixed projected area	$0.015~\mathrm{m}^2$
Fixed drag coefficient	2.2
HUMSAT-D mass (no Cube-de-ALPS)	1 kg
Total mass (incl. Cube-de-ALPS)	1.2 kg

Table 6.2: HUMSAT-D satellite properties.

The semi-analytical propagator introduced in section 6.2 is used to limit the computational runtimes. The simulation stops when the spacecraft reaches 150 km. If the thruster stops firing at a higher altitude, atmospheric drag naturally decays the spacecraft. The satellite is given 90 simulated years to reach 150 km to avoid unnecessarily long computation times. If this time limit is reached, the simulation stops before re-entry occurs.

### **Cube-de-ALPS** Fuel Material

First, the best fuel material for Cube-de-ALPS s determined by simulating its de-orbiting time from different initial altitudes. The fuels selected for analysis are the materials used in the physical prototypes of Cube-de-ALPS. The thruster system has been tested with a printed polymer composed of 87% of silver by weight, machined copper, and machined aluminium, respectively, as the propellant [II]. For comparison, I also include tungsten in the comparison, as it is theoretically the propellant with the highest impulse that can be fitted on Cube-de-ALPS, although it could not be manufactured at the University of Southampton.

The thruster system has the maximum amount of each propellant while respecting the fuel mass and pixel size restrictions listed in Table 6.1 Table 6.3 summarizes the propellants selected for testing and their respective properties, with the firing time corresponding to the total cumulative firing time of all pixels. As Cube-de-ALPS has 88 pixels, each one will fire for  $1/88^{th}$  of the stated time, which, at the given pulse frequency of 100 Hz, yields a total number of pulses order of tens of millions. Although this is beyond the current state-of-the-art [172, 188, 17], current VAT technology can sustain a number pulse in the millions before failing to sustain the ignition. Therefore, it is reasonable to expect that this performance will likely be achievable in the future.

Fuel	Nominal	Firing	# of Pulses	Pixel	Fuel
	Thrust	Time	per Pixel	Height	Mass [g]
	$[\mu \mathbf{N}]$	[days]		[mm]	
Silver (Ag)	27.8	122.92	$12.06 \times 10^6$	3.6	94
Aluminium	11.5	152.18	$14.94 \times 10^6$	3.6	23
(Al)					
Copper	17.6	416	$40.86 \times 10^6$	3.6	80
(Cu)					
Tungsten	27.5	449.34	$44.11 \times 10^6$	2.08	100
(W)					

Table 6.3: Fuel materials for Cube-de-ALPS The nominal thrust and firing time are taken from [4] and scaled to the operational power of 1.5 W. The number of pulses correspond to firing at 100 Hz.

The de-orbiting time of the HUMSAT-D CubeSat is investigated between 150 km and 2000 km when equipped with Cube-de-ALPS. The results are shown in Figure 6.4, where the curve labelled "no Cube-de-ALPS" corresponds to the simulated natural decay of HUMSAT-D at different altitudes. The non-linearities in the curves are due to the atmospheric density variation with respect to time. The maximum altitude of Cube-de-ALPS is defined as the height above which the HUMSAT-D satellite would not de-orbit within 25 years. Therefore, the maximum altitude lies on the 25-year line.

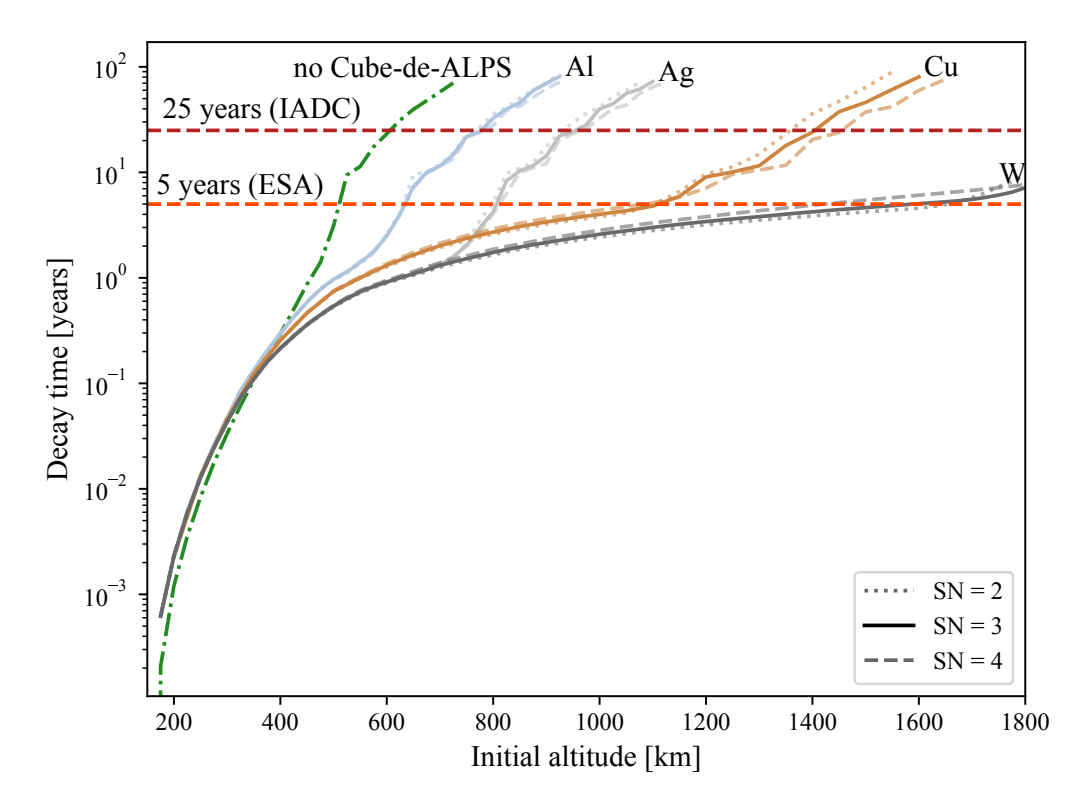


Figure 6.4: Decay time with respect to altitude for Copper (Cu), aluminium (Al), Tungsten (W), and printed silver (Ag). The plot presents the semi-analytical results and a baseline, corresponding to HUMSAT-D naturally decaying without Cube-de-ALPS.

At around 400 km, one can identify the point where the benefits of the thrust from Cubede-ALPS do not outweigh the drawback of the additional mass from the system. Therefore, the system is beneficial only for altitudes above this point until its maximum de-orbiting altitude. The results also show that the silver propellant de-orbits faster initially due to its higher thrust, but its limited total impulse, due to pixel size restrictions, means its maximum altitude is lower than copper.

The material that provides the best de-orbiting performance, and has also been used in a

prototype at the University of Southampton, is selected. Even though tungsten outperforms all the other materials, this section uses copper as fuel for the remainder of this work, as the simulations show it has the best de-orbiting performance of all the materials used in in-house prototypes. This section simulated the decay times for signal-to-noise ratios of 2, 3 and 4 and demonstrated that the mode of operation did not affect the decay times more than the choice of material.

# **Layout Comparison**

The 1-F and 2-F layouts are compared in this section by inspecting their de-orbiting performance. As shown through Equation (6.14), splitting Cube-de-ALPS across two faces doubles the effective thrust, although the total impulse remains the same since both layouts have the same amount of fuel.

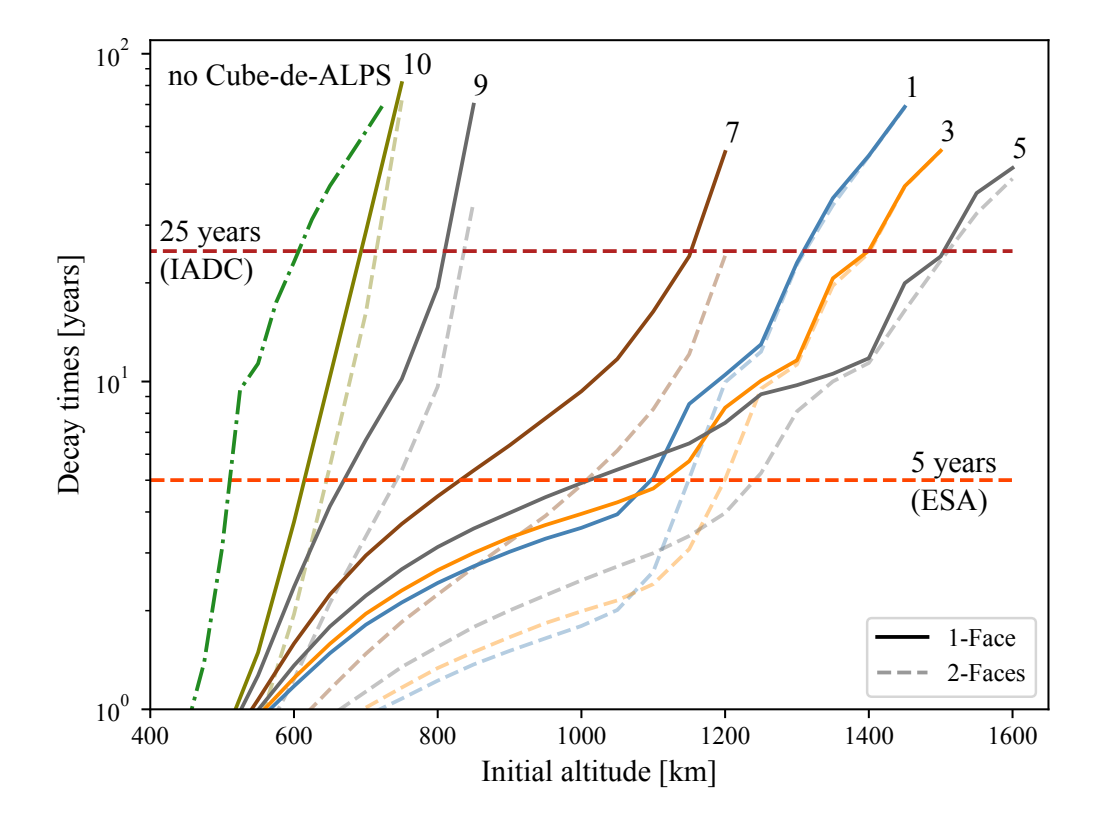


Figure 6.5: Decay time with respect to altitude for Copper (Cu), using signal-to-noise ratios of 10, 9, 7, 1, 3 and 5 for the 1-F and 2-F configurations.

Figure 6.5 shows the decay times for HUMSAT-D with the 1-F and 2-F configurations at different signal-to-noise ratios, which is discussed in Section 6.3. Due to its higher effective thrust, the 2-F layout performs better at lower altitudes, where the de-orbiting happens before the CubeSat has burnt out its fuel, i.e. it is still firing, and not all the impulse has been delivered. After the burnout point, represented on the graph as an inflection point, the curves for the 2-F layout rapidly converge towards their 1-F equivalent. At that point, both systems have delivered the same impulse against the velocity direction, and the high burnout altitude means the total de-orbiting time is dominated by natural decay, hence the similar de-orbiting performance. Figure 6.5 also shows that this behaviour does not change for different signal-to-noise ratios. Therefore, the preferred setup is the 2-F layout, which will provide faster de-orbiting for altitudes below its burnout point and similar performance to the 1-F beyond that height.

# Signal-to-noise Impact

Lastly, this section investigates the effect of the signal-to-noise ratio on the decay times by varying SN between 1 and 10. Figure 6.5 shows the de-orbiting times of HUMSAT-D, using Cube-de-ALPS with copper, at different signal-to-noise ratios. Interestingly, one can note that the signal-to-noise ratio that leads to the fastest de-orbiting is not constant but varies with altitude.

Low signal-to-noise ratios are favoured at lower orbital heights because they lead to a broader thrusting cone, which yields a higher effective thrust at the expense of total delivered impulse. As the initial altitude increases, the CubeSat requires more impulse to achieve de-orbiting, necessitating a smaller cone. Therefore, the signal-to-noise ratio leading to the quickest de-orbiting will be the lowest SN providing the required impulse. However, a higher SN also leads to less frequent firing, especially at higher altitudes, where strong signals are difficult to detect. As a result, Cube-de-ALPS practically never fires, leading the de-orbiting performance to worsen and approach the profile of natural decay. Such behaviour can be seen for the signal-to-noise ratios above 5, where the increased SN pushes the curves towards the natural decay baseline.

The results described in this section allow us to define an operational zone for Cube-de-ALPS, as shown in Figure 6.6. In the hatched region beyond the red line, Cube-de-ALPS will never thrust, and the CubeSat will experience natural decay until it reaches an altitude where the detected signal is strong enough to trigger firing. This behaviour never leads to de-orbiting within 25 years in the simulations.

The best signal-to-noise ratio will vary based on the host spacecraft's mission and altitude, but ideally, the SN that leads to the fastest decay should always be selected. If HUMSAT-D

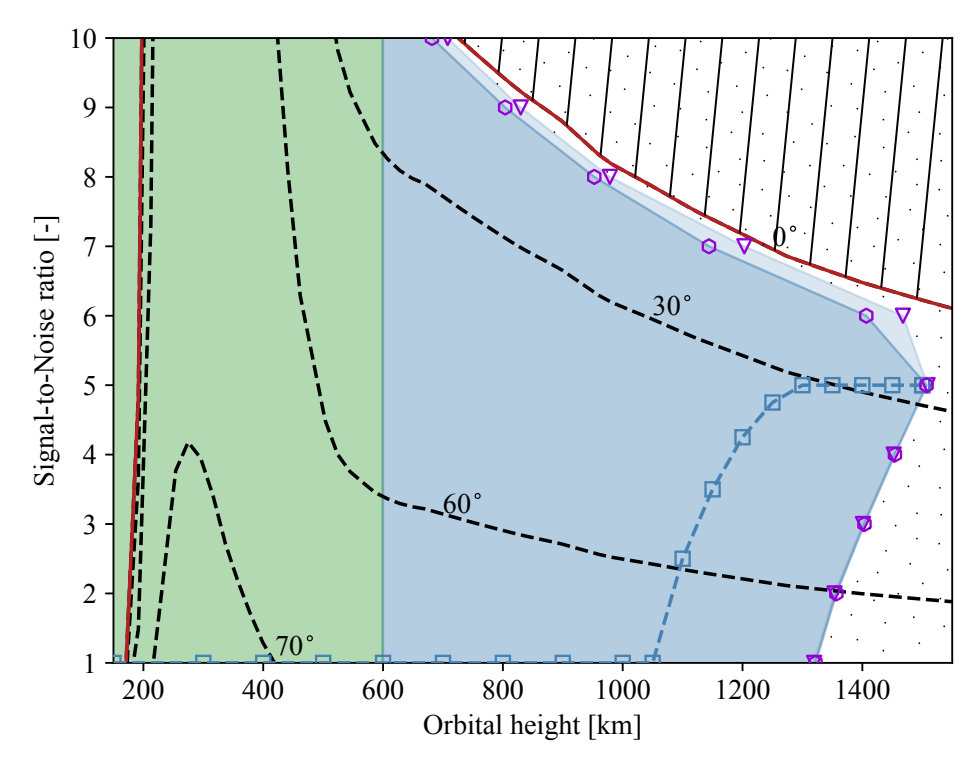


Figure 6.6: Operational zone of Cube-de-ALPS. The green area ( ) highlights the altitudes for which HUMSAT-D would naturally decay. The blue shades define the zones where the 1-F ( ) and the 2-F ( ) can provide de-orbiting. The maximum altitude from which Cube-de-ALPS can provide de-orbiting is marked for the 1-F ( $\bigcirc$ ) and the 2-F ( $\bigcirc$ ). For each initial altitude, the SN leading to the fastest de-orbiting is also shown (-=-). The dotted area defines the heights and SN where de-orbiting within 25 years is impossible, even with Cube-de-ALPS. Dashed contour lines (---) mark the maximum thrusting cone half-angle  $\alpha$  detectable, with the red line (—) bounding a region where no cone is perceived.

were equipped with Cube-de-ALPS, the recommended operational mode would be SN=1.

#### **Numerical results** 6.4

This section presents the high-fidelity numerical results, validating the prior semi-analytical analysis. To adequately compare the results, the experimental setup used here is the same as discussed in Section 6.3

Numerically propagating the attitude necessitates access to HUMSAT-D's inertia matrix. As this data was unavailable, I used the inertia matrix of SLUCUBE-2, a comparable 1U CubeSat [77]. The added mass from Cube-de-ALPS is represented by homogeneously increasing the inertia matrix by 20%,

$$\mathbf{I}_{HUMSAT-D} = \begin{pmatrix} 0.002184 & & \\ & 0.00222 & \\ & & 0.00264 \end{pmatrix} \quad \text{kg} \cdot \text{m}^2. \tag{6.17}$$

The Cube-de-ALPS is mounted so that its normal is aligned with the body-fixed x-axis of the HUMSAT-D CubeSat. Cube-de-ALPS can thus provide torque around the satellite's y-and z- axes. Therefore the angle-of-attack  $\theta$  is the angle between the body-fixed x-axis and the velocity direction,

$$\cos\left(\theta\right) = \hat{x} \cdot \hat{v}.\tag{6.18}$$

Due to the stochastic nature of quadrant selection and thrust generation, multiple realisations of each simulation are required. Preliminary trial runs indicate that 40 realizations per setup yield confidence intervals significantly smaller than the scale of the results, i.e. a decay time in years with a 95% confidence interval in weeks.

In the simulations, Cube-de-ALPS uses copper as fuel material and operates at a signal-to-noise ratio equal to 5. This section chooses SN=5 to validate the maximum altitude from which Cube-de-ALPS can provide de-orbiting within 25 years. A high initial angular velocity of 30 degrees per second is imposed on HUMSAT-D to simulate an out-of-control satellite. The complete numerical simulations continue until HUMSAT-D reaches 150 km, or Cube-de-ALPS has burnt out. In the latter case, should the CubeSat remain above the re-entry altitude of 150 km, the propagator deactivates the attitude propagation and only advances the orbit until 150 km is reached or 90 simulated years have elapsed. This transition allows for lower computational costs, as the complete numerical propagation involving attitude requires roughly 24 days for simulating approximately three years of active thrusting (mostly due to the non-optimized Python code).

The effect of the quadrant selection on HUMSAT-D was investigated and one can find that it successfully despins and maintains a low angular velocity throughout the simulations. Additionally, the numerical decay times and the semi-analytical predictions are compared, highlighting their resemblance and thus validating the work in sections [6.2] and [6.3]

# **Angular Velocity Control**

An example of the angular velocity profile with the closed-loop thrusting law is shown in Figure 6.7. The CubeSat is given 30 degrees per second as initial angular speed, which Cube-

de-ALPS successfully de-spins to simulate the recovery of an out-of-control satellite. The angular velocity remains below one rotation per minute, except at the end, where a velocity spike appears. This spike is due to the random pixel selection, which yields unequal fuel consumption across the grid and leaves pockets of pixels that do not balance each other out at the end, spinning up the satellite. As the spike appears only at the end of the firing time, operators can either ignore it, as Cube-de-ALPS will have de-orbited the spacecraft, or stop firing just before the angular velocity increases. On average, 97% of the fuel has been consumed before the velocity spike appears, which leads to minimal impact on the de-orbiting performance.

During the velocity spike, the control law will attempt to control the satellite's y- and z-axis, while the coupling effect of the non-uniform distribution of mass will build momentum around the x-axis. This induces spin stabilisation around the axis that Cube-de-ALPS cannot control, which in turn affects the thrust delivery. If the satellite is stabilised with its thruster pointing far outside the orbital plane, the thrust delivery is diminished due to reduced firing opportunities and a lower thrust component against the velocity vector. The opposite is true for a satellite that has stabilised with its thruster close to the orbital plane. Therefore, the satellite's spin rate influences the system's performance, reinforcing the need for a control law to manage the angular velocity.

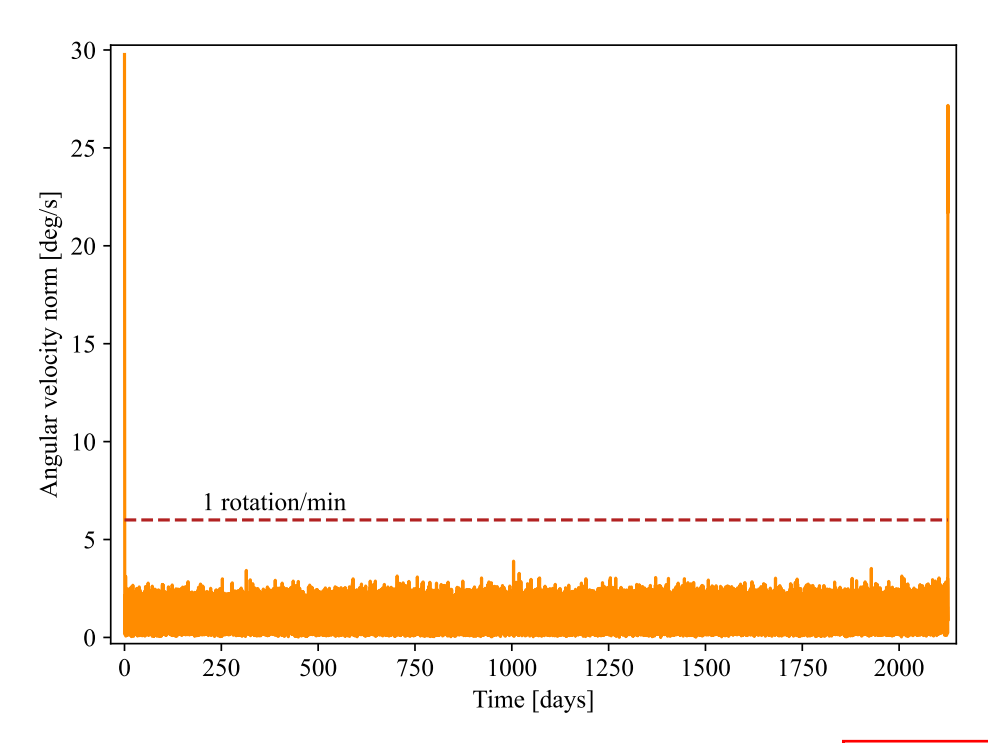


Figure 6.7: Example of the angular velocity of a 1U CubeSat equipped with Cube-de-ALPS using the closed-loop control law.

# **High-Fidelity Decommissioning Times**

Lastly, this section simulates HUMSAT-D de-orbiting from various initial altitudes, using the high-fidelity environment. Both the 1-Face (1-F) and 2-Faces (2-F) layouts are analysed at a signal-to-noise ratio of 5. For each initial altitude, 40 realisations are run, allowing the construction of a confidence interval of 95%. Figure 6.8 shows the high-fidelity decay times and compares them to the estimates obtained in Section 6.3, which match closely. Visible on the right of the graph, the convergence predicted by the estimates is confirmed by the high-fidelity results. The plot shows a clear trend for the high-fidelity results to be higher than the estimates, which is due to the varying cross-sectional area and the modelling of the lift force.

The consistency between the estimates and the predicted results shows that the assumptions made in the semi-analytical propagator in Section 6.2 are valid, and the subsequent results obtained in Section 6.3 are correct and Cube-de-ALPS will provide de-orbiting capacity from 1400 km within 25 years.

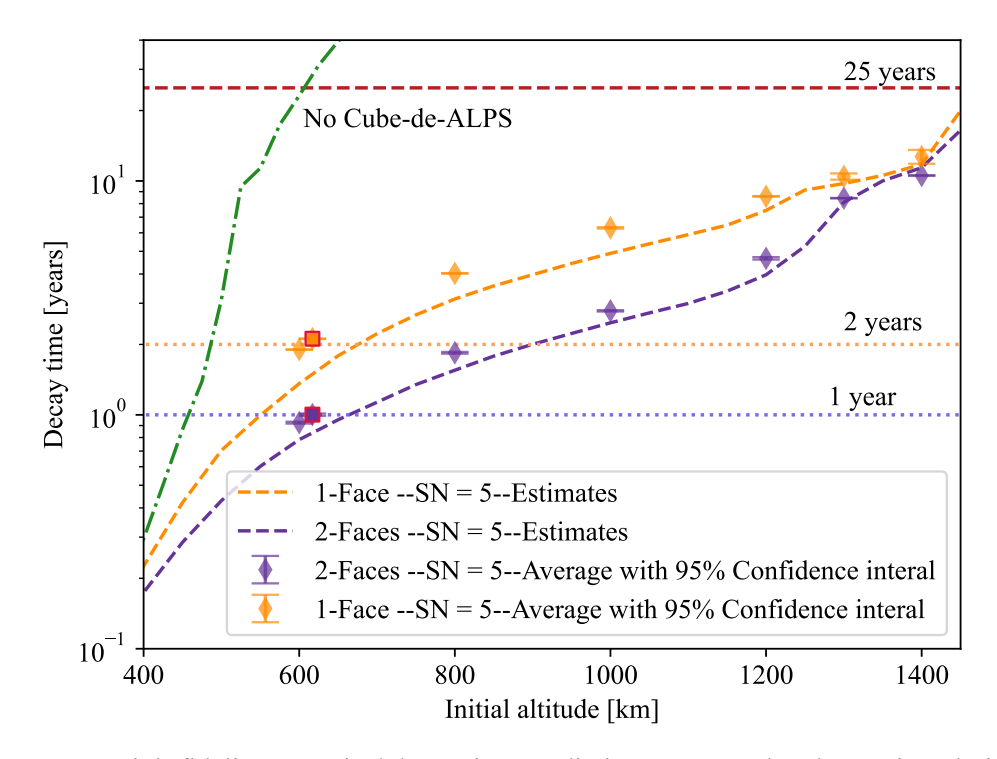


Figure 6.8: High-fidelity numerical decay time predictions compared to the semi-analytical estimation. The altitude of the HUMSAT-D satellite is marked for the 1-F (•) and the 2-F (•) configurations. Dotted lines mark the one and two year decay times, which corresponds to the lifetime of HumSat-D when equipped with Cube-de-ALPS.

It must be noted that the performance shown here is unique to the application to HUMSAT-D. In the case where the host satellite allows a greater amount of propellant, a different

performance can be expected. The reverse is similarly true, where the limit on the amount of propellant limits the de-orbiting performance.

For comparison, I include the deorbiting times of the two most prevalent deorbiting solutions for small nanosatellites: passive decay using drag sail and solar sail [189].

Both techniques aim to increase the satellite's area-to-mass ratio to enhance the effect of natural perturbations and gradually lower the satellite's orbit. Drag sails' operate by increasing the projected cross-sectional area of the satellite in the velocity direction, which results in increased atmospheric drag. This method is most effective in lower orbits, typically below 800 km [189, 190], where the atmospheric density is sufficient to cause orbital decay. For CubeSats, drag sails offer a conceptually simple solution. For example, a 1U CubeSat with a deployed sail achieving an area-to-mass ratio of 0.24 m<sup>2</sup>/kg in a circular orbit at 600 km can typically deorbit in 4 years [191], 79], while Cube-de-ALPS deorbits a 1U from the same altitude in less than 2 years. The deorbiting performance could be improved by increasing the area of the drag sail, although its size is likely limited by the small volume and mass budget of a 1U CubeSat. Additionally, the decay time assumes an ideal scenario where the drag acts orthogonally to the plane of the sail. Achieving this requires careful satellite design to achieve passive aerodynamic attitude stabilisation or an active system to control the spacecraft's orientation, none of which is trivial for CubeSat applications.

On the other hand, solar sails are generally considered for altitudes above 800 km, where atmospheric drag is insufficient for deorbiting within 25 years, even with a drag sail [189]. Solar sails can leverage the solar radiation pressure to increase the eccentricity of a satellite's orbit, which would lower the perigee into the dense part of the atmosphere [192]. Theoretically, a 1U CubeSat equipped with a solar sail to obtain an area-to-mass ratio of 10 m<sup>2</sup>/kg can re-enter the atmosphere in less than two years when deployed from a circular orbit at 1000 km [193]. However, this performance is dependent on the orbit inclination. At Sunsynchronous orbits, resonance effects between the SRP and gravitational perturbations act against the decay of the spacecraft by varying amounts, limiting the efficiency of solar sails deorbiting in one of the most popular orbital regimes [103]. Similarly to drag sails, solar sails require attentive design to provide precise pointing control, whether passive or active. To correctly modify the eccentricity, the pointing requirements will be even more stringent than with a drag sail, making this option more difficult for the smaller range of CubeSats. Additionally, to generate a significant perturbation, the solar sail requires a much larger area-to-mass ratio, leading to a sail which is unlikely to fit within the constrained volume and mass budget on a 1U CubeSat [84, 192].

# **Redundancy and Failure Analysis**

The distributed architecture of the Cube-de-ALPS system inherently has a degree of redundancy that provides mission robustness. However, failure modes must be carefully analysed to understand their impact on the thruster performance. When operating optimally with all pixels functional, the grid maintains perfect balance, facilitating straightforward attitude control as each pixel has an equivalent counterpart generating opposing torque. However, in-flight failures, an important consideration for nanosatellite operations, can manifest as either individual pixel failures or entire quadrant malfunctions, each with distinct consequences for orbital and attitude performance.

When isolated pixels fail within a single quadrant, orbital performance remains largely unaffected if the number remains low. With 88 total pixels distributed across the system, the failure of a small percentage does not significantly compromise de-orbiting capabilities. The primary challenge is attitude stability, as the formerly symmetric grid generates asymmetric torque distribution, inducing undesired spacecraft spin over extended operations. Adequate compensation requires the control system to deliberately disable the equivalent counterparts of failed pixels in opposing quadrants—effectively doubling the propellant penalty associated with each failure. Should the number of failed pixels within a single quadrant become excessive, both attitude control and orbital decay rates would deviate significantly from the above simulations.

Failures distributed across multiple quadrants present more nuanced scenarios with varying levels of impact. When failed pixels occur in diametrically opposite quadrants, active pixels are still roughly symmetrically distributed across the grid. Thus, attitude disturbances are naturally minimised through partial torque balancing, even when the affected pixels aren't perfect counterparts. On the other hand, failures concentrated in adjacent, non-opposite quadrants create acceptable balance along one axis but leave perpendicular axes vulnerable to cumulative torque imbalances, resulting in long-term attitude disturbances.

The most severe failure mode, complete quadrant malfunction, results in the loss of 25% propellant capacity per affected quadrant, significantly impacting the de-orbiting performance. Such failures induce a strong imbalance in the torque applied and can lead to a rapid multi-axis spin that could render the spacecraft inoperable for its intended de-orbiting mission. However, in the specific case where two opposite quadrants fail simultaneously, the distribution of active pixels is still balanced, enabling nominal attitude control.

# 6.5 Conclusion

This chapter has investigated how the  $\boxed{D\mu PS}$  can increase the operational ceiling of nanosatellites. it introduced Cube-de-ALPS, a specialisation of the  $\boxed{D\mu PS}$  that uses a gyroscope and a Faraday cup for attitude estimation. An operational mode was outlined, requiring only coarse angle-of-attack estimates and angular velocity readings. Cube-de-ALPS was equipped on HUMSAT-D, a 1U CubeSat that spent seven years in LEO as an untracked space debris and simulated de-orbiting missions. Using a semi-analytical model, the de-orbiting performance is investigated for different fuel materials, layouts, and signal-to-noise ratios. A high-fidelity numerical model was used, which includes full attitude propagation, to validate our results and show that Cube-de-ALPS would have decayed HUMSAT-D much faster than naturally possible. In conclusion, Cube-de-ALPS can provide de-orbiting capacity as intended and will allow 1U CubeSats to operate up to 1400 km, more than twice as high as naturally possible, while ensuring re-entry within 25 years, effectively raising the operational ceiling of 1U CubeSats.

# **Application: A hexagonal flat nanosatellite** in VLEO

The contents of this chapter are the sole work of the author and are published in Acta Astronautica as Saddul et al. [194]. After raising the operational ceiling with Cube-de-ALPS, this thesis develops a mission to decrease the lower boundary of the nanosatellite operational zone. This chapter introduces the concept of HexSats, a 2.5 cm thick flat hexagonal satellite architecture designed for efficient packing inside rocket fairings, which is based on the DiskSat, a concept created by the Aerospace Corporation [195]. For actuation, HexSats use the  $D\mu$ PS embedded in the satellite frame and produce thrust on the order of micro-Newtons. This work investigates the HexSats' capability to operate at 250 km altitude in VLEO with power requirements exceeding 100 W. Depending on the mission scenario, the HexSat can either constantly point in the Nadir direction or briefly track a target on the ground. The required angular acceleration and resulting drag profiles are analytically determined, along with the expected performance of the HexSats. These results are combined to examine the feasibility of the two mission profiles at different HexSat sizes and provide estimates of the power available to the payload at different VLEO altitudes. The results show that a HexSat at 250 km can actively track up to 8 ground targets per orbit and provide over 100 W of average payload power in these scenarios.

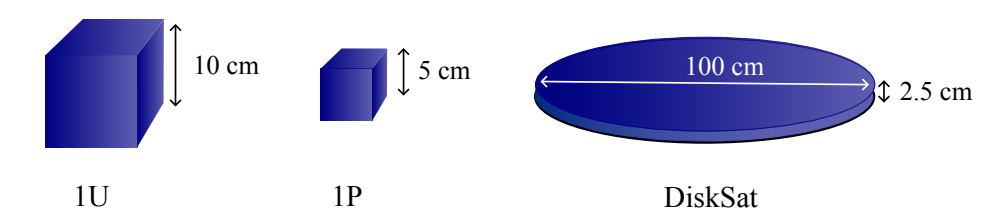


Figure 7.1: Comparison of base units for a CubeSat (1U), a PocketQube (1P), and a DiskSat (not to scale).

# 7.1 DiskSats

As explained in Chapter [1], the limitations of nanosatellites has created interest in a new form factor capable of providing a high power and surface area while adhering to a standardised architecture to minimise costs and design efforts. DiskSats are one such proposed form of spacecraft containerisation [196] [197]. They are a thin, circular satellite form factor, initially created by The Aerospace Corporation as an alternative to CubeSats for applications presenting high power and aperture requirements. Supported by NASA, they now aim to create a new standard to provide a high-power-to-mass ratio platform that can be easily stacked in a launcher fairing [198]. Composed of a 1-meter diameter graphite facesheet with a 2.5-centimetre thick aluminium honeycomb core, each DiskSat provides a volume equivalent to a 20U CubeSat. Figure 7.1 shows how a DiskSat compares to CubeSat and PocketQubes. A single unit provides a structural mass below 3 kg with enough surface area for over 200 W of peak power in ideal conditions, assuming the solar arrays fully cover one of the facesheets. The other facesheet would have the instruments mounted on it. The total launch mass of a DiskSat depends on the chosen launch vehicle's payload capacity. For instance, launching 20 DiskSats on RocketLab's Electron could allow individual DiskSats weighing up to 11 kg, including the payload. DiskSats sit on the boundary between two satellite class definitions, with a mass comparable to nanosatellites, and a size intuitively associated with microsats. Their theoretical peak power-to-mass ratio would be around 18 W/kg, while typical 3U CubeSats, without deployables, have a theoretical peak power-tomass ratio of 6 W/kg.

The Aerospace Corporation is preparing four DiskSats for in-orbit demonstration in 2024 to operate partly in Very Low Earth Orbit (VLEO) [199]. The proximity of the VLEO regime to the Earth's surface provides many benefits such as higher resolution and greater launch mass, as outlined in the work of Crisp et al. [30] [28]. Similarly to CubeSats and PocketCubes, the demonstration DiskSats take advantage of existing COTS components available in the nanosatellite supply chain. However, the current market was primarily aimed

at CubeSats, with their box-shaped form factor. Therefore, most COTS components are not made for the DiskSats' thin architecture. A notable example is the onboard electric propulsion (EP) system, Enpulsion's Nano-FEEP, a highly efficient Field Emission Electric Propulsion (FEEP) thruster that fits in the volume of a 1U CubeSat [200]. While DiskSats can easily cater to NanoFEEP's nominal power of 40 W, the dimensions of the thruster disrupt the thin, quasi-2D architecture of the satellite. The DiskSats will not only experience a higher drag, especially at lower altitudes, but their centres of mass will also be shifted, making attitude control more complex. The cube-like shape of the thruster also means that cut-outs are required in the disk, on the opposite side of the propulsion system, to allow for compact stacking in the launcher fairing.

The reason for this choice of propulsion system is the lack of a commercially available, flight-proven alternative on the market. While many electric propulsion systems can provide a similar thrust or power requirement, few existing architectures would have the dimensions required to maintain the thin form factor of the DiskSats. Of the 60 electric thrusters mentioned in NASA's report on small satellite technology, none have dimensions suitable for a thin form factor [10]. There is therefore a need for a miniature propulsion system capable of fitting in the thickness of the DiskSat while also providing meaningful manoeuvrability to the satellite.

This chapter proposes a DiskSat design with the  $D\mu PS$  distributed along its structure. The satellite can then be precisely controlled by keeping the pixels re-ignitable and the thrust level scalable. As shown in Figure [7.2], the pixels placed on the thickness of the DiskSat can provide thrust in the  $\hat{x}$  and  $\hat{y}$  axes, which are parallel to the facesheet. This thrust in the  $\hat{x}$  and  $\hat{y}$  directions can be used for orbital control. Meanwhile, the pixels arranged on the facesheet can deliver thrust in the  $\hat{z}$  direction, which is normal to the facesheet. This thrust in the  $\hat{z}$  direction can be used for attitude control.



Figure 7.2: Render of a DiskSat with the D $\mu$ PS concept.

# 7.2 Hexagons are the bestagons

The previous section has introduced the use of  $\boxed{D\mu PS}$  on a DiskSat. However, the current architecture presents limitations for constellation building, i.e. efficient mass deployment. This section introduces the HexSat concept, a thin platform similar to the DiskSat with a hexagonal profile. It uses the  $D\mu PS$  to provide complete orbit and attitude actuation. Transitioning from a circular to a hexagonal profile offers superior packing efficiency inside a rocket fairing, reducing total launch costs. An illustration of the HexSat concept is shown in Figure 7.3

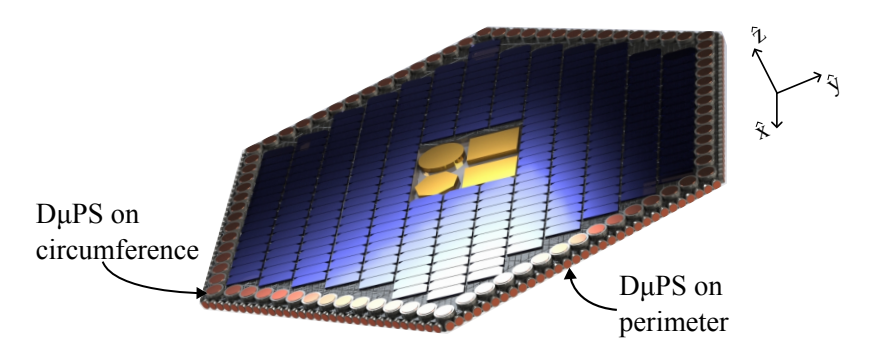


Figure 7.3: HexSat concept: A flat hexagonal satellite using the  $D\mu PS$  for orbital and attitude actuation.

The orbit and attitude control capabilities of DiskSats, SquareSats and HexSats are now analysed. Thanks to the non-circular profile, the pixels on the thickness are not all aligned with the centre of mass and can now also control the yaw motion. However, while providing complete 3-axis attitude control, a polygonal profile worsens misalignments between the pixels on the thickness and the thrust direction. For comparison, a SquareSat, using a square profile, is also analysed alongside the DiskSat and HexSat.

# Packing efficiency

The thin architecture of DiskSats, enabled by  $D\mu$ PS, allows for efficient vertical stacking within rocket fairings, as illustrated in Figure 7.4. However, when considering larger rockets, the fairing can accommodate multiple vertical columns of satellites. Unfortunately, the circular shape of the fairings results in inevitable gaps between these columns of satellites, effectively wasting costly space. By minimising the total area of the gaps and thus maximising the packing efficiency, operators can ensure a more effective use of the space provided by the launch vehicle.

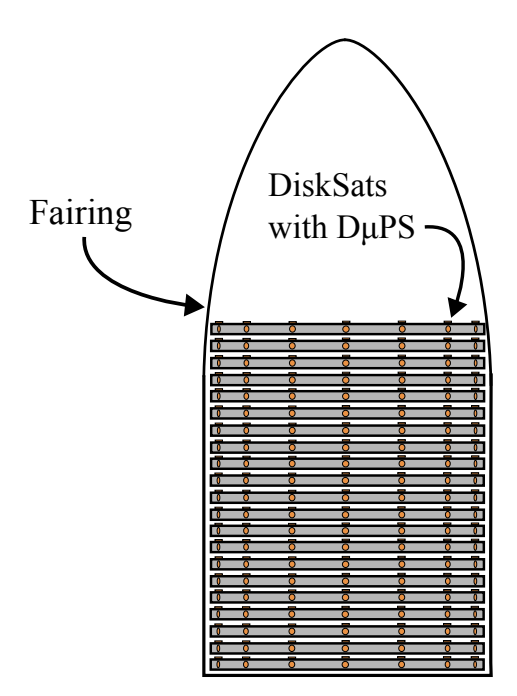


Figure 7.4: DiskSats stacked vertically inside a launch vehicle fairing.

Figure 7.5 presents the optimal or best-known layouts for packing discrete numbers of DiskSats, HexSats, and SquareSats inside a given rocket fairing.

To quantify the size of satellites allowed by these different configurations, Figure 7.6 shows the size of individual satellites for three popular launchers [13]: Falcon 9, Vega and Electron. The sizes of the graphical elements are proportional to their surface area, which are given inside the shapes. If the surface area of the satellite is equal or greater than that of the DiskSat demonstration mission, then the graphical element is highlighted in green. If not, then the shape is highlighted in red.

As expected, the larger the fairing size, the larger the surface area of each satellite. For up to three columns per fairing, the DiskSat geometry provides better packing efficiency and thus a larger satellite than a HexSat. However, for more columns, the HexSat architecture leads to a greater satellite size in a given fairing. The SquareSat profile always performs worse than the corresponding HexSat. Therefore, a HexSat yields the largest surface area when deploying many satellites at once.

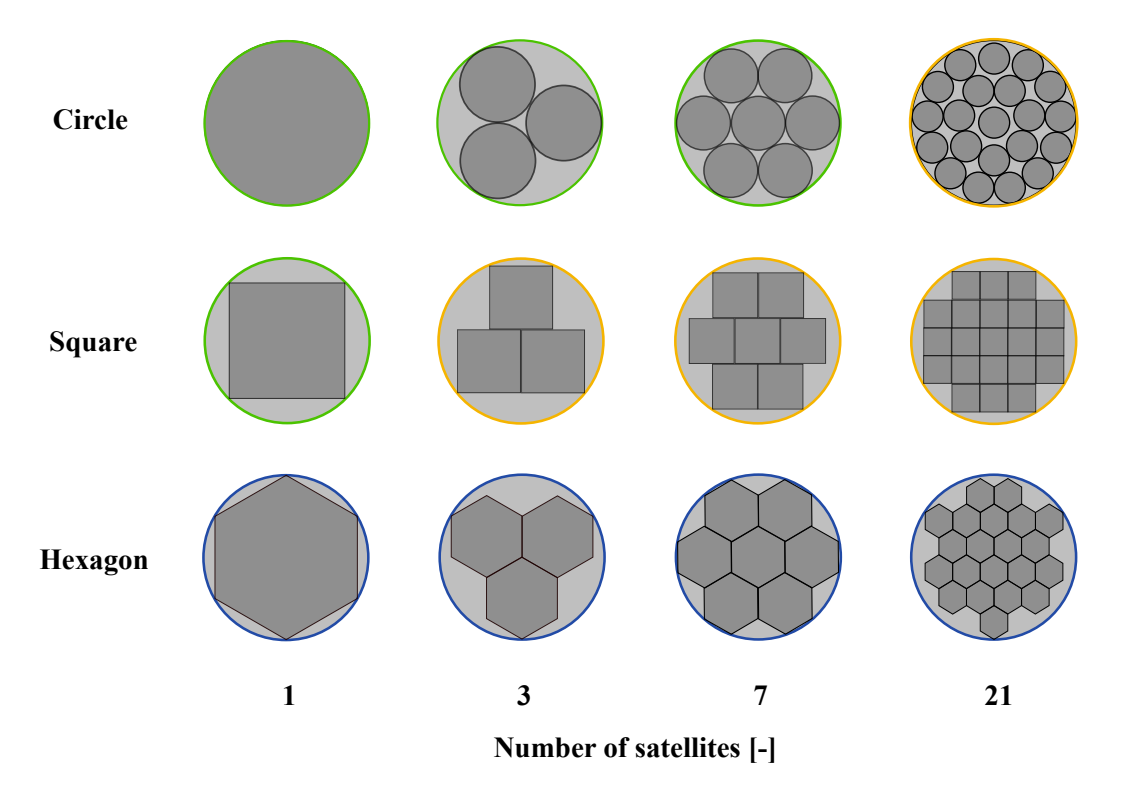


Figure 7.5: Packing configurations of DiskSats, SquareSats and HexSats inside a launcher fairing. The configurations proven to be optimal are highlighted in green while the best-known configurations are in orange. Configurations that are conjectured for this work are highlighted in blue.

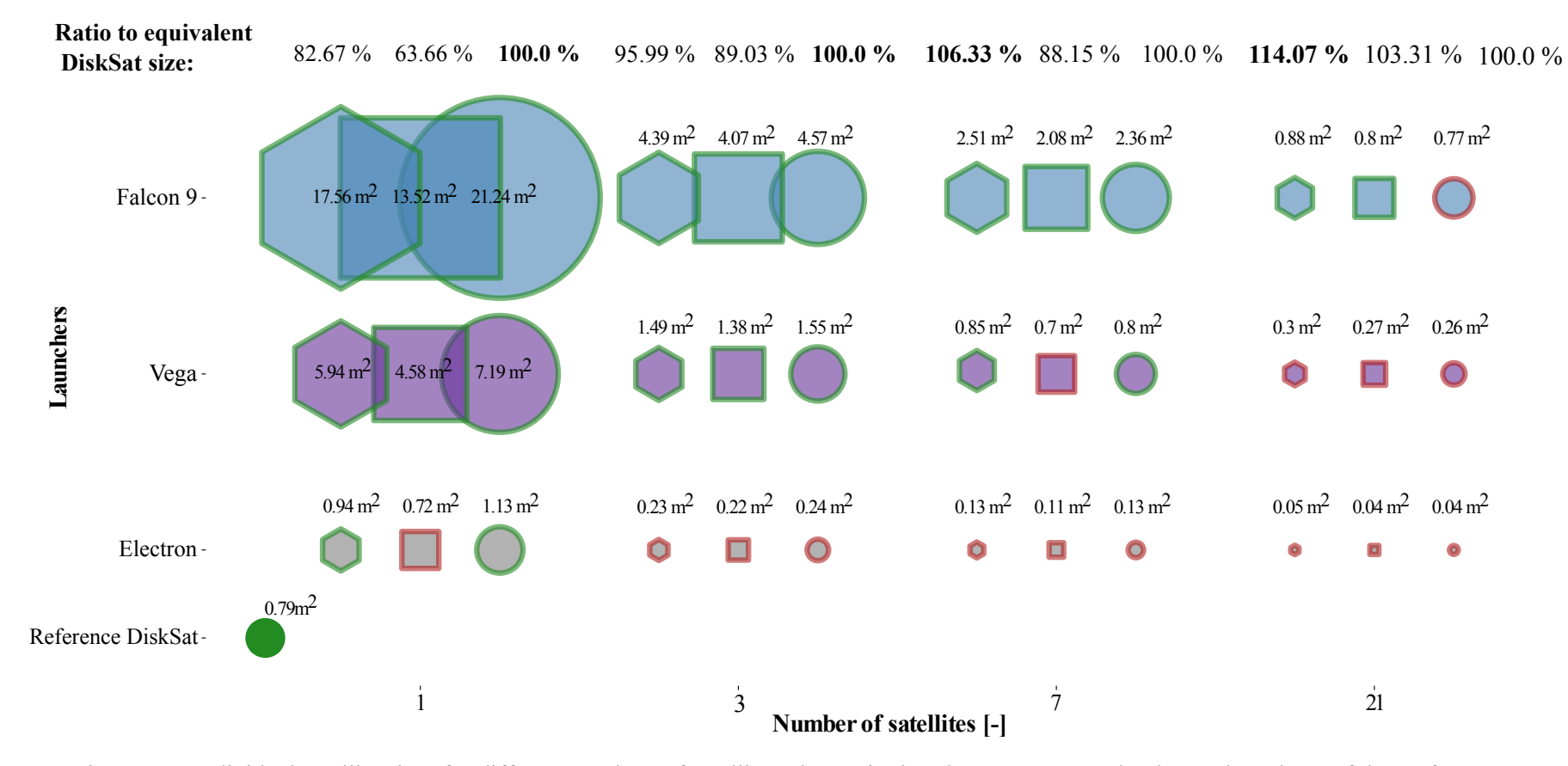


Figure 7.6: Individual satellite sizes for different numbers of satellite columns in the Electron, Vega and Falcon 9 launchers. If the surface area of is greater than the DiskSat demonstration mission, then it is highlighted in green. If not then the shape is highlighted in red.

# Orbit and attitude control capability

The DiskSat can control its attitude by firing the thrusters on its facesheet, and maintain its orbit by using the thrusters on its thickness. If the pixels on the thickness are not exactly aligned with the desired thrust direction  $\vec{u}$  but remains coplanar, the DiskSat can either first rotate around the  $\hat{z}$  axis or ignite two pixels whose thrust vectors will add up to the required thrust direction. If the direction  $\vec{u}$  is not coplanar with the pixels in the thickness, then the HexSat will need to fire pixels located on the facesheet to control its attitude. However,

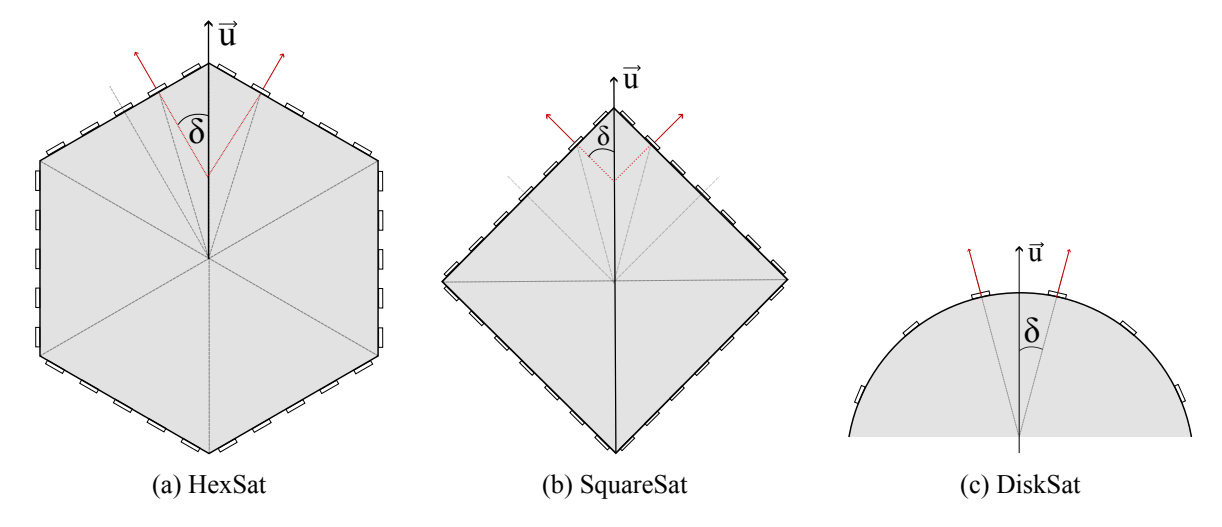


Figure 7.7: Maximum thrust misalignments for HexSats, SquareSats and DiskSats.

the thrust generated by the pixels on the thickness will act through the centre of mass. The DiskSat will therefore not produce any torque around the  $\hat{z}$  axis, which is normal to the facesheet, to control the yaw motion. Using a SquareSat or HexSat architecture, the  $D\mu PS$ can control the  $\hat{z}$  axis, providing complete 3-axis satellite control. The straight sides, however, mean that thrust can only be produced in four or six different directions for orbital manoeuvres. This means potentially larger misalignment relative to the desired thrust direction compared to the DiskSat architecture. Figure 7.7 illustrates each shape firing in a worst-case misalignment. The required thrust magnitude for a pixel  $T_{reg}$  will then need to be augmented to account for the sub-optimal thrust direction according to

$$T_{req} = \frac{T_u}{\cos(\delta)} \tag{7.1}$$

where  $T_u$  is the required thrust magnitude acting in the desired direction  $\vec{u}$ , and  $\delta$  is the angular misalignment.

For a DiskSat, the thrust misalignment is limited to half of the angular separation between each pixel. For example, with 100 pixels on the thickness, the maximum angular misalignment is  $\delta^{disk}_{max}=1.8^\circ$ . For HexSats and SquareSats, the maximum misalignment is half the angle formed by their respective diagonals, which leads to  $\delta^{hex}_{max}=30^\circ$  and  $\delta^{sq}_{max}=45^\circ$  respectively.

Table 7.1 specifies, for a worst-case misalignment, the required increase in thrust magnitude to deliver the desired acceleration in the direction  $\vec{u}$ . Using a HexSat allows complete 3-axis control while reducing thrust direction misalignment. Thus, compared to a SquareSat, a HexSat requires less increase in thrust to achieve the target acceleration in the desired direction  $\vec{u}$ . While the thrust misalignment can be corrected by rotating around the  $\hat{z}$  axis for HexSats and SquareSats, this analysis is important in scenarios where no time is allowed for an attitude manoeuvre (i.e. constant 'real-time' drag compensation) or if the D $\mu$ PS has burnt out many pixels and is unable to rotate the satellite.

Shape	Controlled axes	Max. misalignment	Thrust magnitude
DiskSat	$\hat{x},\hat{y}$	1.8°	$1.00049 \; T_u$
SquareSat	$\hat{x},\hat{y},\hat{z}$	45°	$\sqrt{2} T_u \approx 1.414 T_u$
HexSat	$\hat{x},\hat{y},\hat{z}$	$30^{\circ}$	$1.1547 T_u$

Table 7.1: Control characteristics of DiskSats, SquareSats, and HexSats. The controlled axes, worst-case thrust vector misalignment, and associated required thrust magnitude are illustrated for each satellite architecture. I assumed 100 pixels are mounted on the thickness of the DiskSat for this example.

To summarize, for launch configurations with more than three satellite columns HexSats provide the best packing efficiency and naturally allow 3-axis control with limited thrust misalignment. The HexSat geometry is also likely easier to manufacture due to its straight lines compared to the curved geometry of DiskSats.

# 7.3 HexSat performance

To better understand the capabilities of the HexSat concept, three key performance metrics are investigated for a HexSat in VLEO as a function of its size. These metrics are

- 1. the orbit-average power  $P_{avg}^{gen}$
- 2. the change in angular velocity  $\Delta\omega$  ("maneuverability")
- 3. the peak angular acceleration  $\dot{\omega}_{peak}$  ("agility")

Equations that express the performance metrics as functions of the HexSat's side-length and design parameters are presented. The analysis is based on specific values for the design parameters, which are provided in Table 7.2. Furthermore, the inertia matrix of a HexSat of assumed uniform density  $\rho_{Disk}$  with side-length s and thickness  $t_{hex}$  is given by

$$\mathbf{I}_{hex} = \frac{\sqrt{3}}{8} s^2 t_{hex} \rho_{Disk} \begin{pmatrix} \frac{5}{2} s^2 + t_{hex}^2 \\ \frac{5}{2} s^2 + t_{hex}^2 \\ 5s^2 \end{pmatrix}. \tag{7.2}$$

The density  $\rho_{Disk}$  and thickness t have been chosen to match the properties of the DiskSat demonstration missions. The side-length s remains a variable to analyse the scalability of the HexSat performance metrics.

Property	Symbol	Value
Pixel mass [mg]	$m_{pixel}$	0.912
Pixel radius [mm]	$R_{pixel}$	4.5
Thrust-to-power ratio [ $\mu$ N / W]	$T_{p}$	11.65
Mass flow rate [ $\mu$ g/s]	$\dot{m}_f$	1.4
DiskSat density [kg /m <sup>3</sup> ]	$ ho_{Disk}$	407.44
DiskSat thickness [cm]	$t_{hex}$	2.5
Solar array efficiency [-]	$\eta_{SA}$	15%
Solar flux at Earth [W / m <sup>2</sup> ]	$S_{flux}$	1400

Table 7.2: Summary of  $D\mu PS$  and HexSat properties.

# **Orbit-average power**

The instantaneous power generated along an orbit will vary based on the angle between the normal to the solar cells and the Sun vector. Assuming the HexSat maintains constant Nadir pointing, the normal to the solar cells can be approximated to the radial unit vector  $\hat{r}_{orb}$ ,

$$P_{gen} = \begin{cases} \sigma P_{peak} \left( \hat{r}_{Sun} \cdot \hat{r}_{orb} \right) & \text{if } \hat{r}_{Sun} \cdot \hat{r}_{orb} \ge 0\\ 0 & \text{else} \end{cases}$$
 (7.3)

where  $\hat{r}_{Sun}$  is the direction pointing towards the Sun from the HexSat and the shadow function  $\sigma$  denotes the fraction of the solar disk visible from the HexSat's position, and depends on the orbital parameters [135], 138]. The variable  $P_{peak}$  is the maximum power the solar array can generate in ideal conditions, which depends on the area of the HexSat and is given by

$$P_{peak} = \eta_{SA} \eta_p S_{flux} \frac{3\sqrt{3}}{2} s^2 \tag{7.4}$$

where the solar flux at the Earth is  $S_{flux}$ , the efficiency of the solar panels is  $\eta_{SA}$  and  $\eta_p$  is the packing efficiency of the solar panels. For this work, I used the peak power of the demonstration DiskSats and assumed the solar panels completely covered the facesheet, leading to  $\eta_{SA}=15\%$ .

Averaging the generated power over a full orbital period  $\tau_{orbit}$  yields the average power as

$$P_{avg}^{gen} = \frac{1}{\tau_{orbit}} \int_0^{\tau_{orbit}} P_{gen} dt.$$
 (7.5)

Depending on the orbital parameters, the HexSat will generate varying amounts of average power over an orbit, as shown on Figure [7.8]. For this plot, it is assumed the RAAN is measured from the direction of the Sun, as illustrated in Figure [7.9].

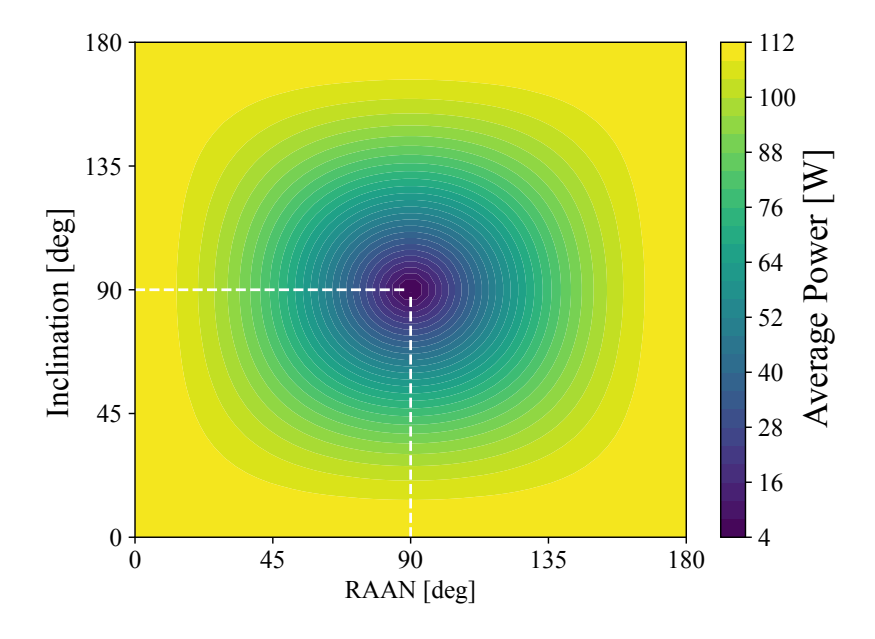


Figure 7.8: Orbit-average power as a function of inclination and RAAN, which change the orbit orientation relative to the Sun. Plot generated for an altitude of 250 km.

The results shown in Figure 7.10 are generated for a 250 km circular orbit where the Sun vector  $\hat{r}_{Sun}$  lies in the orbital plane. One can notice the orbit-average power grows with  $s^2$ , making a greater HexSat more desirable.

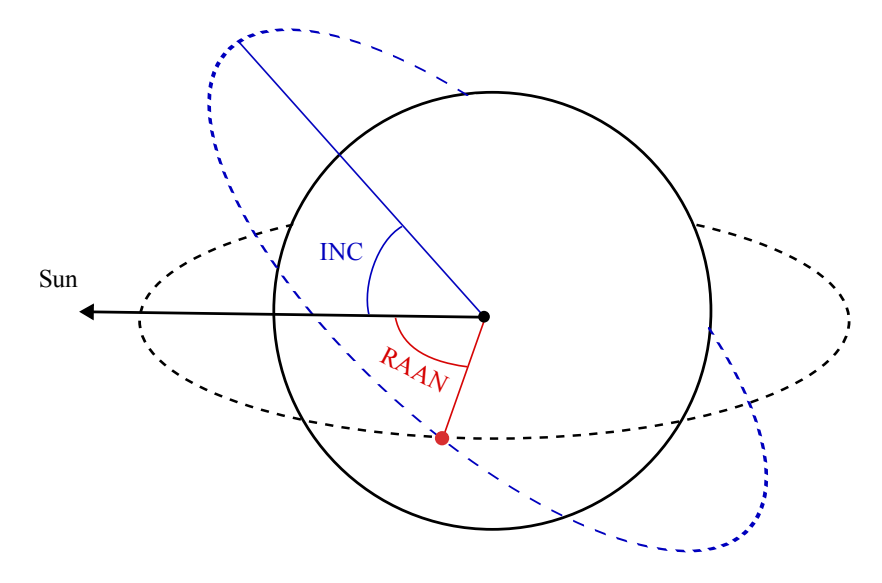


Figure 7.9: Measurement of inclination (INC) and RAAN relative to the Sun.

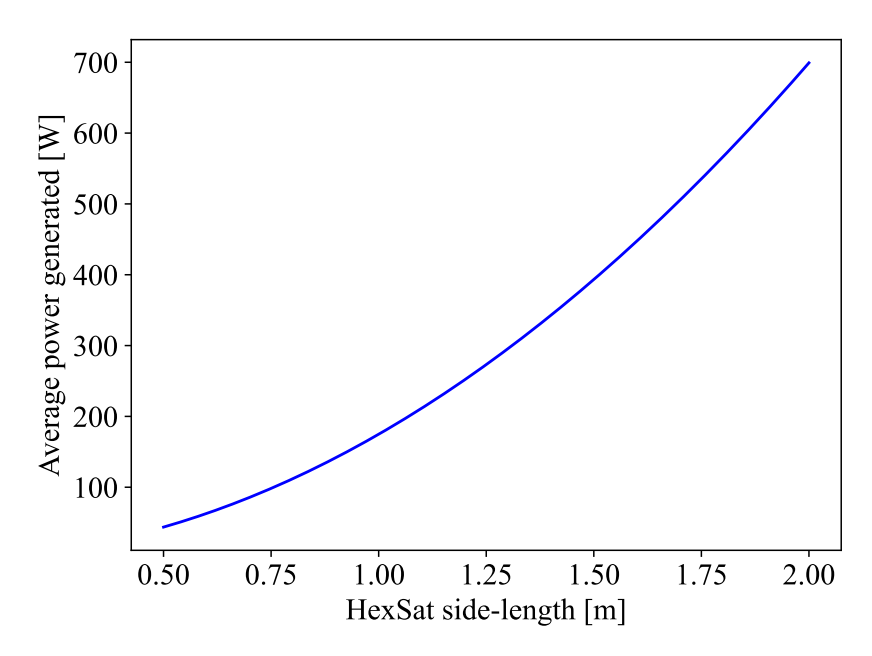


Figure 7.10: Orbit-average power of a HexSat as a function of side-length, assuming a circular orbit at 250 km with the Sun vector in the orbital plane.

# **Manoeuvrability**

To analytically estimate the total change in angular velocity that the HexSat can deliver, one must first compute the cumulative angular momentum change imparted by each pixel on the HexSat for each rotational axis. Then, the satellite's inertia is used to obtain the corresponding total change in angular velocity.

A given pixel i will produce a thrust  $\vec{T}_i$ , which depends on the power P used to operate the  $\mathrm{D}\mu\mathrm{PS}$ . For a constant thrust which is applied for a firing time  $\Delta t_i$ , the change in angular momentum  $\Delta \vec{h}_i$  is

$$\Delta \vec{h}_i = \left(\vec{r}_i \times \vec{T}_i\right) \Delta t_i = \vec{r}_i \times \left(T_p P \hat{T}_i\right) \Delta t_i \tag{7.6}$$

where  $\vec{r_i}$  is the position of the pixel, and  $T_p$  is the thrust-to-power ratio. Since the HexSat has many pixels, the total change in angular momentum it can deliver is the sum of the  $\Delta \vec{h_i}$  for all pixels. Vectorially, the sum of all  $\Delta \vec{h_i}$  is zero because every pixel has a counterpart placed symmetrically opposite, cancelling the net momentum change. However, the pixels will not all fire simultaneously but operate to provide a desired change in angular velocity. Therefore, the focus is placed on the magnitude of momentum around each axis,

$$\Delta h_{x,y,z} = \sum_{i=0}^{n_{pixel}} \left| \left( \Delta \vec{h}_i \right)_{x,y,z} \right|. \tag{7.7}$$

Due to the same symmetrical configuration, the maximum change in angular momentum is limited to half the value given by Equation (7.7).

Since the radius  $R_{pixel}$  of each pixel is small compared to the side-length of the HexSat, the pixels are modelled as uniformly distributed along a curve described by the continuous function  $\vec{r}(s)$ . Instead of considering discrete pixels i with a mass  $m_{pixel}$ , this analysis considers infinitesimally small pixels with a mass dm. The pixels have an infinitesimal firing time dt, which depends on the pixel mass  $dm = \rho_m \ dl$ , the mass flow rate, and the operational power.

As the total fuel mass is uniformly distributed between the pixels, the mass density  $\rho_m$  is obtained by dividing the total mass along  $\vec{r}(s)$  by its line length L. The total mass along  $\vec{r}(s)$  is approximated by multiplying the pixel mass  $m_{pixel}$  by the number of pixels  $n_{pixels}$ , which can be estimated by dividing L by the diameter of a pixel,

$$dt = \frac{\rho_m}{P\dot{m}_f} dl = \frac{m_{pixel}n_{pixel}}{LP\dot{m}_f} dl = \frac{m_{pixel}}{LP\dot{m}_f} \left| \frac{L}{2R_{pixel}} \right| dl$$
 (7.8)

where  $\dot{m}_f$  is the propellant mass flow rate at 1 W.

Combining Equations (7.6), (7.7) and (7.8), one can obtain the expression for the angular momentum change deliverable by the HexSat,

$$\Delta h_{x,y,z} = T_p \frac{m_{pixel}}{L\dot{m}_f} \left[ \frac{L}{2R_{pixel}} \right] \int \left| \left( \vec{r}(s) \times \hat{T} \right)_{x,y,z} \right| dl$$
 (7.9)

Since this analysis modelled the thrust generation as linearly dependent on P, and the firing time as inversely proportional to P, the angular momentum change is independent of the

power.

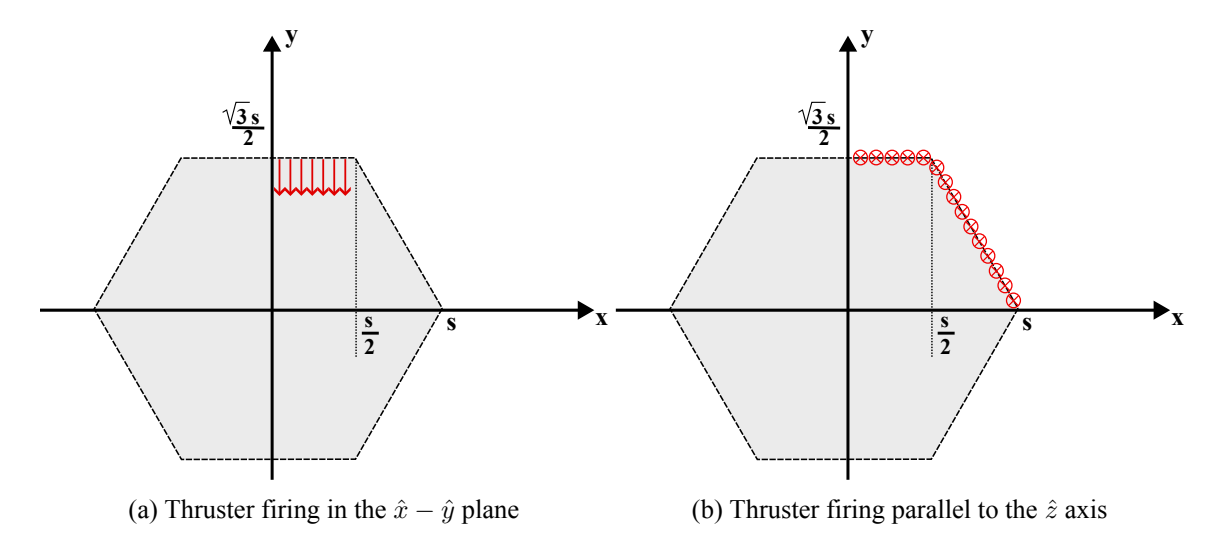


Figure 7.11: Forces generated by the  $D\mu PS$  on a HexSat. The red and orange arrows represent the forces generating torques around the  $\hat{z}$  axis, while torques around the  $\hat{x}$  and  $\hat{y}$ axes will be created by the forces illustrated with  $\otimes$ . The analysis is simplified thanks to the symmetry of the HexSat.

### Total $\Delta\omega_z$

This subsection now specialises Equation (7.9) for the pixel in the thickness. Due to the layout of the D $\mu$ PS on the HexSats, rotation around the  $\hat{z}$  axis, which is normal to the facesheet, can only be controlled by pixels in the thickness. Therefore, pixels on the facesheet are excluded when calculating  $\Delta\omega_z$ .

As shown in Figure 7.11a, all pixels along a single side-length of the HexSat produce thrust in the same direction. Additionally, the side-length exhibits symmetry around its midpoint. The change in angular momentum induced by pixels on one half of a side-length is equal in magnitude but opposite in direction to the contribution from the corresponding other half. This symmetry is present on all six sides of the HexSat, enabling us to restrict our analysis to a single half-side-length. The total change in angular momentum is then twelve times the  $\Delta h$  computed for half the side-length.

By inspecting Figure 7.11a, one can observe that the moment arm of a pixel increases linearly between the midpoint of the side-length and its corner. Equation (7.9) can therefore be simplified to

$$\Delta h_z = 24T_p \frac{m_{pixel}}{s\dot{m}_f} \left| \frac{\Box}{4R_{pixel}} \right| \int_0^{\frac{s}{2}} x \, dx. \tag{7.10}$$

The resulting expression for the total angular momentum change around the  $\hat{z}$  axis is

$$\Delta h_z = 3T_p \frac{m_{pixel}}{\dot{m}_f} \left[ \frac{s}{4R_{pixel}} \right] s. \tag{7.11}$$

Equation (7.11) shows that  $\Delta h_z$  grows with  $s^2$ . However, according to Equation (7.2), the inertia of a HexSat grows proportionally to  $s^4$ . The total *angular velocity* change  $\Delta \omega_z$ , computed with  $\Delta h_z/I_{hex}^{zz}$ , is thus inversely proportional to  $s^2$ .

### Total $\Delta\omega_{x,y}$

A similar approach is used to specialise Equation (7.9) for the pixels on the facesheet. Pixels on the thickness can be ignored, as they do not provide a torque around the  $\hat{x}$  or  $\hat{y}$  axes.

Some pixels on the facesheet will generate momentum around both the  $\hat{x}$  and  $\hat{y}$  axes, as shown in Figure 7.11b. This can be accounted for by summing the momentum components,

$$\Delta h_{x,y} = \sqrt{\Delta h_x^2 + \Delta h_y^2}. (7.12)$$

One can note from Figure 7.11b that the HexSat presents a mirror symmetry along the  $\hat{x}$  and  $\hat{y}$  axes, allowing us to restrict our analysis to a quarter of the satellite, as depicted. Again, the function for the moment arm is the curve delimiting the shape of the HexSat. Therefore, Equation (7.9) becomes

$$\Delta h_x = \Delta h_y = 8T_p \frac{m_{pixel}}{3s\dot{m}_f} \left[ \frac{3s}{4R_{pixel}} \right] \left( \int_0^{\frac{s}{2}} \frac{\sqrt{3}}{2} s \, dx + \int_{\frac{s}{2}}^s -\sqrt{3}x + \sqrt{3}s \, dx \right). \tag{7.13}$$

The final expression for the total  $\Delta h$  around the  $\hat{x}$  and  $\hat{y}$  axes is

$$\Delta h_{\hat{x},\hat{y}} = \sqrt{6}T_p \frac{m_{pixel}}{\dot{m}_f} \left[ \frac{3s}{4R_{pixel}} \right] s. \tag{7.14}$$

Equation 7.14 shows that the  $\Delta h$  around  $\hat{x}$  and  $\hat{y}$  increases with  $s^2$ , similarly to the  $\Delta h$  around  $\hat{z}$ . Again, because the inertia grows with  $s^4$ , this means the total deliverable change in *angular velocity* around each axis actually decreases with  $s^2$ , as shown in Figure 7.12.

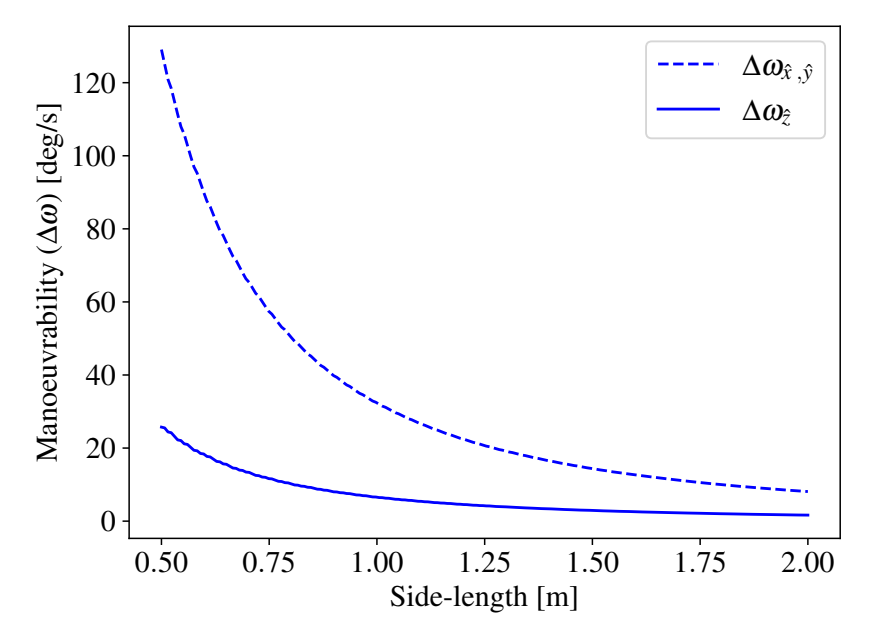


Figure 7.12: Deliverable angular velocity around the  $\hat{x}$ ,  $\hat{y}$  and  $\hat{z}$  axes, assuming a circular orbit at 250 km with the Sun vector in the orbital plane.

### **Agility**

To compute the agility  $\dot{\omega}_{peak}$ , a single pixel is fired, located on the corner of a HexSat, using the maximum power  $P_{peak}$  available to the HexSat. This produces a peak torque  $\vec{\tau}_{peak}$ , which can then be transformed into a peak acceleration thanks to the inertia of the satellite. The maximum power directly influences the peak torque  $\vec{\tau}_{peak}$  that the D $\mu$ PS can generate, which can be expressed as

$$\vec{\tau}_{peak} = \vec{r}_{corner} \times \boxed{T_p} P_{peak} \hat{T}$$
 (7.15)

where  $\vec{r}_{corner}$  is the position a pixel at a corner. The peak power  $P_{peak}$  is determined with Equation (7.4). Due to the layout of the D $\mu$ PS on the HexSat, only the pixels on the thickness will produce a torque around the  $\hat{z}$  axis. As depicted in Figure 7.11a, the moment arm around the  $\hat{z}$  axis of a pixel in the corner is half a side-length. The choice of corner will change the direction of the torque, but not its magnitude. Therefore, the magnitude of the peak torque around the  $\hat{z}$  axis is

$$\tau_{peak,z} = \frac{3\sqrt{3}}{4} \eta_{SA} \eta_p S_{flux} T_p s^3 \tag{7.16}$$

where the peak power  $P_{peak}$  is replaced with Equation (7.4).

The peak torque from the pixels on the facesheet is computed with a similar approach. Again, the choice of corner will change the direction of the peak torque, but not its magnitude. Thus, the pixel located on the  $\hat{x}$  axis at a distance s from the centre of mass is selected, as shown in Figure [7.11b]. The magnitude of the peak torque around the  $\hat{x}$  and  $\hat{y}$  axes is

$$\tau_{peak,xy} = \frac{3\sqrt{3}}{2} \eta_{SA} \eta_p S_{flux} T_p s^3. \tag{7.17}$$

Both the peak torques around the  $\hat{x} - \hat{y}$  and  $\hat{z}$  directions are proportional to  $s^3$ . However, the satellite's inertia grows with  $s^4$ , as shown in Equation (7.2). Therefore, the agility, computed with  $\tau_{peak}/I_{hex}$ , is inversely proportional to s.

In summary, while a greater HexSat size is desirable to generate more power, the increased inertia of the satellite will lead to reduced agility ( $\dot{\omega}_{peak}$ ) and less total manoeuvrability ( $\Delta\omega$ ). As the minimum agility required depends on the specific mission profile, this chapter explores the HexSat operational modes in Section 7.4.

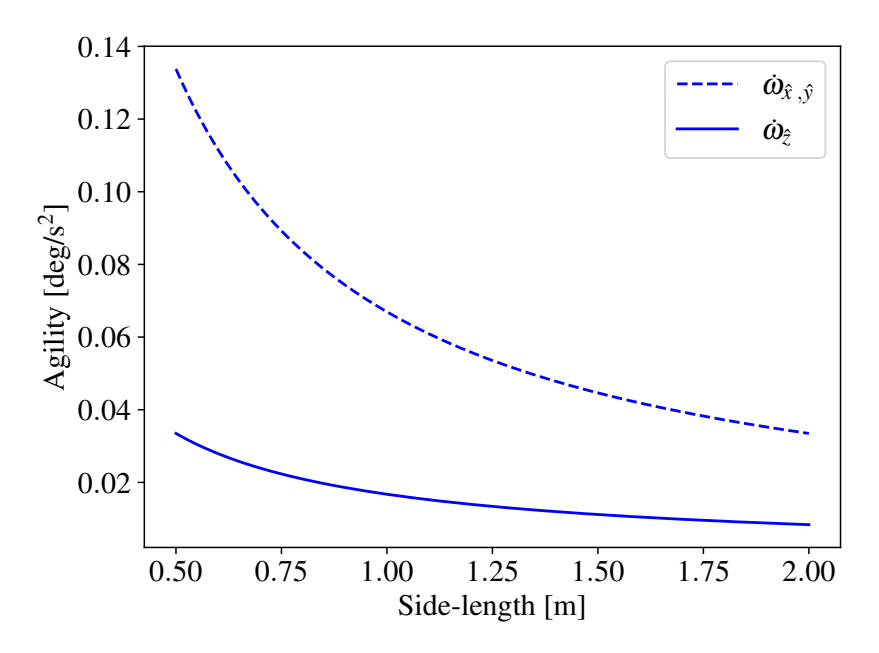


Figure 7.13: HexSat agility as a function of its side-length for the  $\hat{x}$ ,  $\hat{y}$  and  $\hat{z}$  axes, assuming a circular orbit at 250 km with the Sun vector in the orbital plane.

# 7.4 Operational mode & orbit geometries

The VLEO regime's advantages mainly apply to missions focusing on the Earth, such as remote sensing or communication constellations. Satellites are therefore likely to keep a Nadir-pointing orientation or briefly track a target on the ground. This section details the requirements for constant Nadir pointing and Active Ground Tracking operational modes.

Depending on the mode of operation, the satellite's projected frontal area will vary, changing the experienced drag. Expressions to compute the drag forces are provided, and the minimum acceleration profiles required to execute each operational mode are presented.

### **Drag compensation**

No matter the operational mode, due to the high atmospheric density of VLEO, most satellites will have to use their thrusters to prevent premature de-orbiting. The onboard propulsion can maintain the spacecraft's orbit by applying an equal and opposite force to the drag experienced. In this scenario, the thin form factor of the HexSats allows for a small frontal area to be produced, which yields a smaller drag and thus reduces the load on the propulsion system. However, this advantage only applies if a HexSat is flying in its minimal drag configuration. If the minimum drag direction, represented by  $\hat{d}$  in Figure 7.14, is not aligned with the velocity vector  $\vec{v}_{sat}$ , then the spacecraft will experience a greater drag. In this section, the minimum drag the  $D\mu PS$  must compensate based on the spacecraft's attitude is analysed.

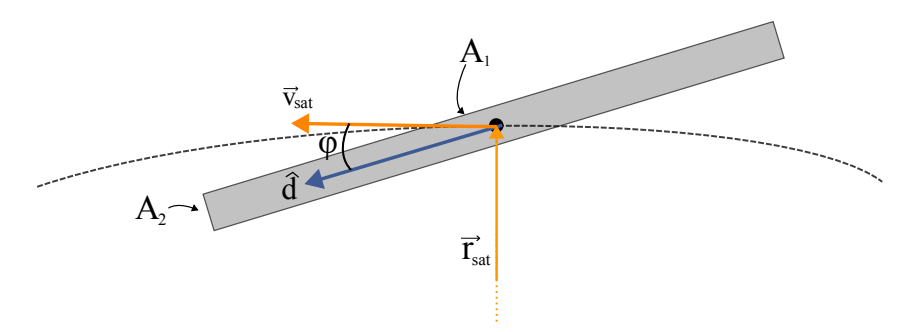


Figure 7.14: Geometry of the drag forces affecting a HexSat in VLEO.

The drag experienced by a spacecraft can be modelled using

$$D = \frac{1}{2} \rho_{atm} (\vec{r}_{sat}) v^2 (A_1 C_{D,1}(\varphi) + A_2 C_{D,2}(\varphi))$$
 (7.18)

where  $\rho_{atm}$  is the atmospheric density, a function of orbital position  $\vec{r}_{sat}$ ,  $\vec{v}_{sat}$  is the spacecraft's orbital velocity, and  $C_D$  is the drag coefficient and is a function of  $\varphi$ , the angle between the velocity vector and  $\hat{d}$ . The variable  $\varphi$  is called the angle of attack and is a function of time the model used here is the same as in CHAOS, and is detailed in Chapter 5. The drag coefficient  $C_D$  is computed using a free molecule theory model derived by Sentman, in the form presented by Sutton [152, 164]. The HexSat is represented using two thin plates: one for the facesheet denoted as  $A_1$ , and one for the thickness denoted as  $A_2$ . Their  $C_D$  are different as they have different dependencies on  $\varphi$ , i.e. the drag induced by

the thickness is maximum when the facesheet is parallel to  $\vec{v}_{sat}$ , which in turn experiences no drag in this configuration. The atmospheric density is modelled through an interpolation of the Jacchia-77 atmospheric model introduced in Frey and Colombo [151], which allows for both static and temperature-dependent models.

In Equation (7.18), the variables  $\vec{r}_{sat}$ ,  $\vec{v}_{sat}$ ,  $\rho_{atm}$  and the HexSat area can be determined from the chosen orbit and satellite geometry. However, computing the projected area and the drag coefficient requires knowledge of  $\varphi$ , which depends on the operational mode. The following subsections describe how a given operational mode can be maintained and its subsequent effect on the angle of attack profile.

### **Nadir pointing**

Maintaining a Nadir position allows the spacecraft to keep its instruments pointed directly at the Earth at all times. For this work, I use the geocentric Nadir direction which points directly towards the centre of the Earth from the spacecraft  $[\Pi 9]$ . Therefore, the satellite must rotate at the same angular speed as the position vector to keep its instruments aligned with the Nadir direction. The D $\mu$ PS must provide this precise acceleration profile to operate in this mode, unless the orbit is circular, in which case no angular acceleration is needed.

The angular velocity required for constant Nadir pointing is computed in a given orbit with [106]

$$\dot{\theta}_{TA} = \frac{na^2}{r_{sat}^2} \sqrt{1 - e^2} \tag{7.19}$$

where  $\overline{n}$  is the mean orbital motion, a is the semi-major axis, and e is the eccentricity. The function  $r_{orb}$  is the orbital radius, which depends on the true anomaly  $\overline{\theta_{TA}}$ 

$$r_{sat} = \frac{a(1 - e^2)}{1 + e\cos(\theta_{TA})}. (7.20)$$

The angular acceleration can then be obtained by taking the time derivative

$$\ddot{\theta}_{TA} = \frac{d\dot{\theta}_{TA}}{dt} = \frac{d\dot{\theta}_{TA}}{d\theta_{TA}} \frac{d\theta_{TA}}{dt} = \frac{d\dot{\theta}_{TA}}{d\theta_{TA}} \dot{\theta}_{TA}$$
(7.21)

which leads to the final expression of the angular acceleration

$$\ddot{\theta}_{TA} = -\frac{2n^2 e \sin(\theta_{TA}) \left(1 + e \cos(\theta_{TA})\right)^3}{\left(1 - e^2\right)^3}.$$
(7.22)

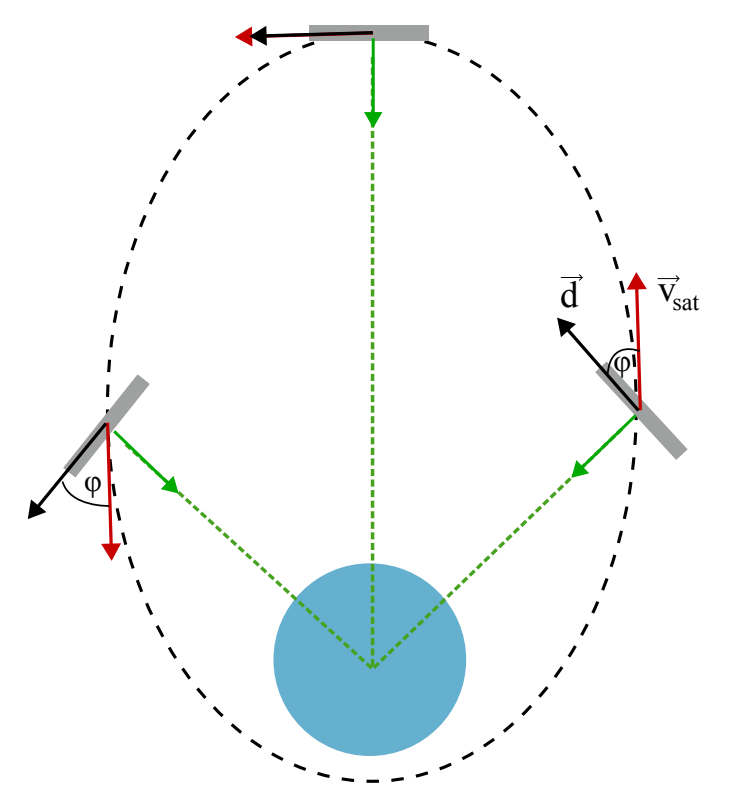


Figure 7.15: Constant Nadir-pointing mode: the spacecraft's instruments are always aligned towards the centre of the Earth.

The HexSat must be capable of providing the full range of angular accelerations determined by Equation (7.22) to correctly track the Nadir direction. If the HexSat follows this angular acceleration profile, its angle of attack profile can also be computed. As the HexSat must have its instruments aligned with the position vector in Nadir pointing, the vector  $\hat{d}$  is always perpendicular to the position vector. Therefore, the angle of attack  $\varphi$  becomes the angle between the velocity vector  $\vec{v}_{sat}$  and the normal to the position vector, or the flight path angle [106]. It is given by

$$\varphi = \arctan\left(\frac{\operatorname{esin}\theta_{TA}}{1 + e\cos\theta_{TA}}\right). \tag{7.23}$$

Figure 7.16a shows the acceleration profiles required to maintain Nadir pointing. The corresponding angles of attack along the orbit are shown in Figure 7.16b. Note that the angular acceleration required to maintain Nadir pointing in a circular orbit is zero as no variation in the angular velocity is needed. Similarly, for the non-circular orbits, the angle of attack remains small due to the low eccentricity.

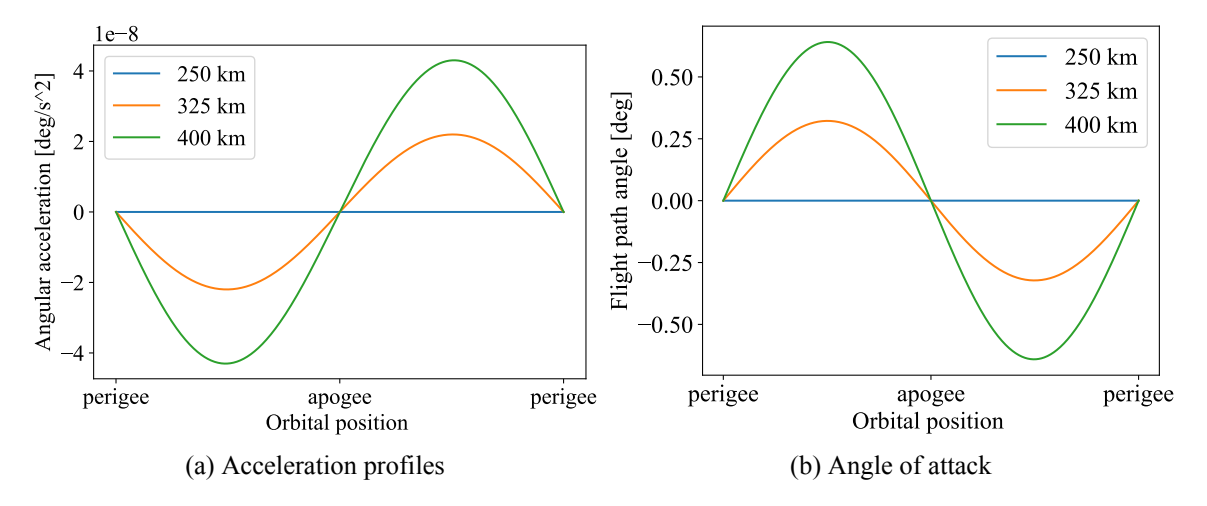


Figure 7.16: Required acceleration profile and flight path angle to perform Nadir pointing in low-eccentricity orbits with varying apogee altitudes. The perigee is fixed at 250 km for all orbits, and the legend represents the varying apogee altitudes.

# **Active Ground Tracking**

Active Ground Tracking (AGT) refers to the HexSat keeping the sensors pointed at a specific point on the ground, called the target, during a fly-over. It is achievable either by rotating the onboard sensors or by turning the spacecraft itself at a precise rate to keep the ground target aligned with the onboard instruments. This analysis assumes the HexSat is in a circular orbit and that the target lies on its ground track, specifically at  $\theta_{TA} = 0$ .

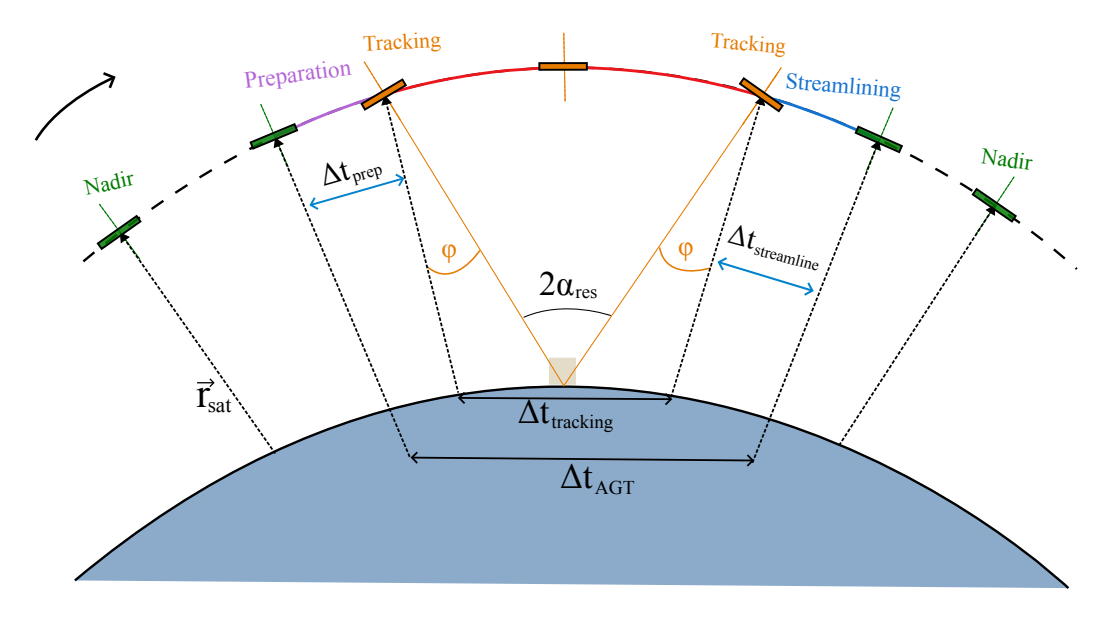


Figure 7.17: Sketch of a full Active Ground Tracking cycle, including preparation, tracking, and streamlining.

Unlike the continuous operation of the Nadir pointing mode, AGT requires a duty-cycled approach. The HexSat will track its target throughout the tracking window and then reorient

itself to coast in the minimum drag configuration until the next target is acquired.

As shown in Figure 7.17, a preparation phase, where the HexSat aligns itself with the target, is required to ensure correct tracking. Similarly, a streamlining manoeuvre, mirroring the preparation, is required to return the HexSat to the minimal drag configuration. The execution of the preparation and streamlining phases ultimately depends on the nature of the HexSat's mission and is therefore not specified. However, the angle between the Nadir direction and the target direction is the same at the end of the preparation phase and at the start of the streamlining phase. This angle is equal to half of the total angular change imparted during the tracking phase. Thus, it is assumed the preparation and streamlining phases will each require half the energy consumed during tracking.

To estimate the total AGT cycle time  $\Delta t_{AGT}$ , it is further assumed that both phases each take half the time of the tracking stage, such that

$$\Delta t_{AGT} = 2\Delta t_{tracking}. (7.24)$$

Then, the number of AGT cycles  $n_{cycles}$  performed during one orbit can be determined with

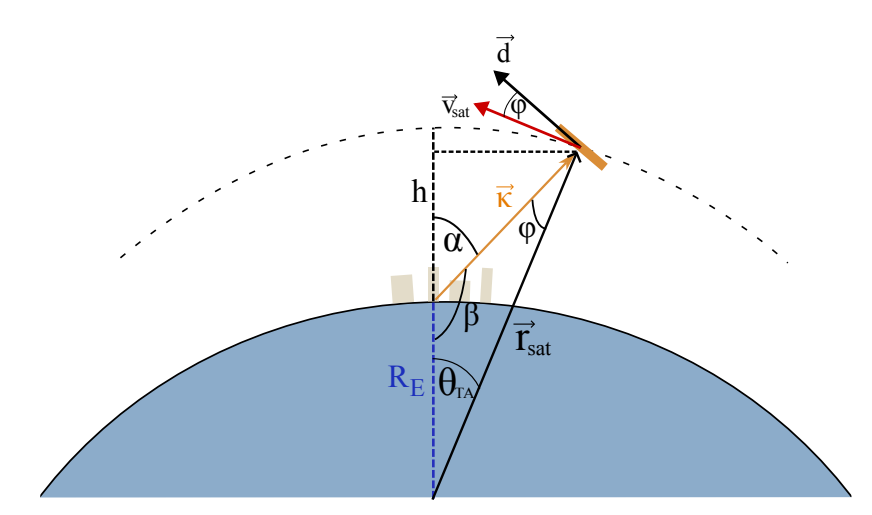


Figure 7.18: Active ground tracking mode: the spacecraft's instrument briefly point at a target on its ground track.

 $\Delta t_{AGT}$  and the duty cycle  $\zeta$ , the portion of the orbit dedicated to executing the AGT cycle which includes both preparation and streamlining phases,

$$n_{cycles} = \left\lfloor \frac{T_{orbit} \zeta}{2\Delta t_{tracking}} \right\rfloor \tag{7.25}$$

where the variable  $\tau_{orbit}$  is the orbital period.

During the tracking stage, the HexSat (or its instruments) must be aligned with and rotate

at the same angular speed as the relative position vector  $\vec{\kappa}$  to actively follow a target on the surface. The focus is on the angular acceleration  $\ddot{\alpha}$  required to track the target. Given the geometry shown in Figure 7.18, one can express  $\alpha$ , the relative angular position, as a function of the true anomaly  $\theta_{TA}$  through the sine projection of  $\vec{r}_{sat}$ ,

$$\alpha = \arcsin\left(\frac{r_{sat}}{\kappa}\sin\left(\theta_{TA}\right)\right) \tag{7.26}$$

where  $\kappa$  is the distance between the target and the satellite, called the slant range and  $\theta_{TA}$  is the true anomaly, measured from the target. The variables  $\kappa$  and  $r_{sat}$  are both dependent on the true anomaly  $\theta_{TA}$  but are written concisely for readability.

The variable  $\kappa$  is obtained by applying the cosine law

$$\kappa = \sqrt{R_E^2 + r_{sat}^2 - 2r_{sat}R_E\cos(\theta_{TA})}$$
 (7.27)

where  $R_E$  is the radius of the Earth. For a nominal circular orbit of 250 km, the magnitude of  $\kappa$  is greater than 350 km at values of  $\theta_{TA} \geq 2^{\circ}$ . At this distance, the satellite instruments are unlikely to provide a significant advantage compared to using instruments onboard the satellites at higher altitudes. Therefore, in this analysis AGT is limited to a useful tracking window  $\theta_{res}$  spanning about 2 degrees on each side of the target, as measured at the Earth's centre. It provides approximately one minute of tracking time, leading the total cycle to last around two minutes.

Taking the time derivative, the angular velocity is obtained,

$$\dot{\alpha} = \frac{d\alpha}{d\theta_{TA}} \dot{\theta}_{TA}.\tag{7.28}$$

Similarly, the angular acceleration is computed with the chain rule,

$$\ddot{\alpha} = \frac{d^2 \alpha}{d\theta_{TA}^2} \left( \dot{\theta}_{TA} \right)^2 + \frac{d\alpha}{d\theta_{TA}} \ddot{\theta}_{TA}. \tag{7.29}$$

Again, the HexSat must be capable of providing the full range of angular accelerations determined by Equation (7.29) to correctly track the ground target. Figure 7.19a shows an example acceleration profile. In this scenario, a circular orbit at 250 km is assumed and divided differences are used to compute the derivatives  $\frac{d\alpha}{d\theta_{TA}}$  and  $\frac{d^2\alpha}{d\theta_{TA}^2}$ . As this analysis only considered circular orbits, the vector  $\vec{r}_{sat}$  and  $\vec{v}_{sat}$  are orthogonal, which leads the angle between  $\vec{\kappa}$  and  $\vec{r}_{sat}$  to be the same as the angle of attack  $\varphi$ . The angle of attack is thus computed

$$\varphi = \alpha - \theta_{TA}.\tag{7.30}$$

The angle of attack profile is shown in Figure 7.19b for a circular orbit at 250 km. Compared

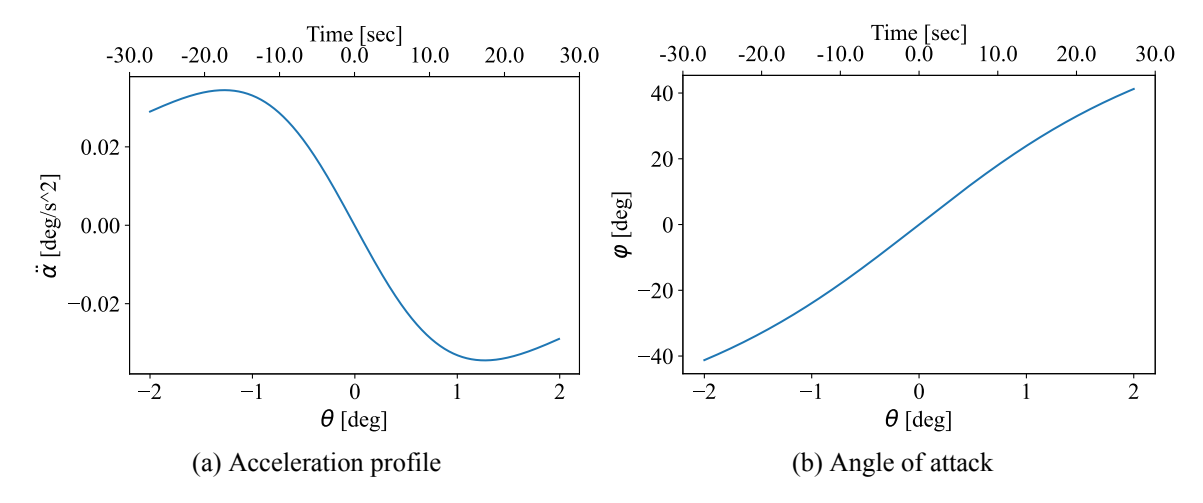


Figure 7.19: Angular acceleration profile and flight path angle to perform AGT in a 250 km circular orbit over a tracking window of two degrees of true anomaly.

to the Nadir pointing mode, the HexSat in AGT mode will deviate significantly more from the velocity direction.

# 7.5 HexSat power analysis

The impact of HexSat size on its ability to achieve the operational modes detailed in Section 7.4 is investigated. Specifically, HexSats that generate more power than they consume are of interest. This analysis uses the average excess power  $P_{avg}^{excess}$  as a measure, defined as

$$P_{avg}^{excess} = P_{avg}^{gen} - P_{avg}^{orbit} (7.31)$$

where  $P_{avg}^{orbit}$  is the average power consumption due to flight dynamics operations over one orbit. The excess power then becomes the power available for payload and bus operations. The average power consumption over one orbital period  $\tau_{orbit}$  consists of the drag compensation and the attitude manoeuvres,

$$P_{avg}^{orbit} = \frac{E_{orbit}^{drag} + E_{orbit}^{op}}{\tau_{orbit}},$$
(7.32)

where  $E_{orbit}^{drag}$  and  $E_{orbit}^{op}$  are the energy consumption due to drag compensation and operational mode respectively. The energy expenditure for drag compensation is calculated by integrating the instantaneous power required to generate a thrust that precisely counteracts the drag force at all times. The energy depends directly on the drag profile D experienced by the HexSat and thus, on the angle of attack profile,

$$E_{orbit}^{drag} = \frac{1}{T_p} \int_0^{\tau_{orbit}} D(\varphi) d\mathbf{E}$$
 (7.33)

Similarly, the energy required for operational manoeuvres depends on the HexSat inertia matrix  $\mathbf{I}_{hex}$  and the required angular acceleration profile  $\dot{\omega}$ . However, the rotation only acts around either the  $\hat{x}$  or  $\hat{y}$  axis. Depending on the pixel fired, the D $\mu$ PS will need to adjust its power level to produce the correct torque,

$$T_p Pr(s) = I_{xx}^{hex} \dot{\omega}. \tag{7.34}$$

To minimise the operating power level, one can fire the pixel with the greatest moment arm, which is located in the HexSat corner at a distance s from the centre of mass. Then write the energy required is written as

$$E_{orbit}^{op} = \frac{I_{xx}^{hex}}{T_n s} \int_0^{\tau_{orbit}} \dot{\omega} \, dt. \tag{7.35}$$

# **Nadir** pointing

The energy required to compensate for the drag in constant Nadir pointing mode is computed with Equations (7.18), (7.23) and (7.33). Similarly, Equations (7.22) and (7.35) are used to determine the energy required to maintain the Nadir pointing attitude profile. As shown in Figure 7.16a, the angular accelerations needed for Nadir pointing are minimal, resulting in an average power requirement in the order of  $10^{-5}$  W. It is drag compensation that dominates the  $D\mu PS$  power consumption in this pointing mode. Figure 7.20 presents the average excess power available to a HexSat of varying size as a function of apogee altitude, with a perigee fixed at 250 km. The results indicate that while a higher apogee offers a slight increase in available power, the improvement is negligible. Operating in low-eccentricity orbits thus provides no significant advantage over circular orbits. Compared to a circular orbit at 250 km, which uses 12 W of average power for drag compensation, an orbit with its apogee at 400 km will use an average of 8 W, assuming a HexSat of equivalent surface area to the demonstration DiskSats. The power required for the thrusters is not significantly reduced as the HexSat will have an increased speed at the perigee. The power saving is also negligible

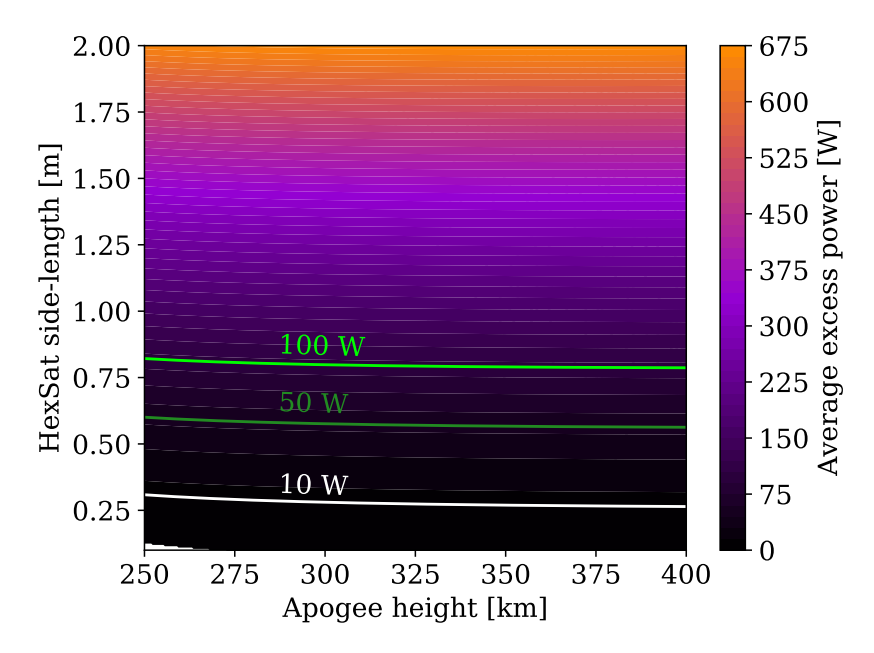


Figure 7.20: Excess power based on HexSat size and apogee height, with contour lines indicating 100 W, 50 W and 10 W levels. The perigee is fixed at 250 km.

compared to the power generated, which is above 100 W. Therefore, low eccentricity orbits have a negligible impact on the power available to the payload.

However, increasing the size of the HexSat significantly increases the excess power. Even in a circular orbit at 250 km, a HexSat with a side-length greater than 0.8 m can generate over 100 W of average excess power, making constant Nadir pointing a viable operational mode.

### **AGT**

As an AGT cycle occurs  $n_{cycles}$  times across an orbit, the analysis is restricted to a single flyover. As detailed in Section 7.4, both the preparation and streamlining manoeuvres need half the angular change required for the tracking stage. Consequently, the total energy required to perform the AGT cycle can be expressed as

$$E_{AGT} = E_{prep} + E_{tracking} + E_{streamline} = 2E_{tracking}$$
 (7.36)

where  $E_{tracking}$  is the energy required to follow a ground-based target actively, i.e. to follow the angular acceleration profile presented in Figure 7.19a. It is now possible to re-write the average power consumed as

$$P_{avg}^{orbit} = \frac{E_{orbit}^{drag} + 2E_{tracking}n_{cycles}}{\tau_{orbit}}$$
 (7.37)

where  $E_{orbit}^{drag}$  can be computed with Equations (7.18), (7.30) and (7.33), while  $E_{tracking}$  is determined with Equations (7.29) and

$$E_{tracking} = \frac{I_{xx}^{hex}}{T_p s} \int_0^{\Delta t_{tracking}} \ddot{\alpha}(t) dt.$$
 (7.38)

While similar to Equation (7.35), Equation (7.38) integrates only over the tracking time  $\Delta t_{tracking}$ , as no torques are needed to follow Nadir pointing in circular orbit.

Figure 7.21 presents, for a circular orbit at 250 km, the excess power for a HexSat of varying size as a function of the duty cycle  $\zeta$ . For simplicity, the power generation model is kept as detailed in Equation (7.5), which assumes the spacecraft is constantly in Nadir. While the HexSat's operational mode differs, it effectively spends a maximum of two minutes per target slewing before returning to a Nadir position. At most, the HexSat is  $40^{\circ}$  offset from the Nadir direction, which corresponds to a 24% decrease in power generation. It is therefore believed that this assumption is reasonable as long as the ratio of total AGT cycle time to orbit period, i.e.  $\zeta$ , remains relatively low.

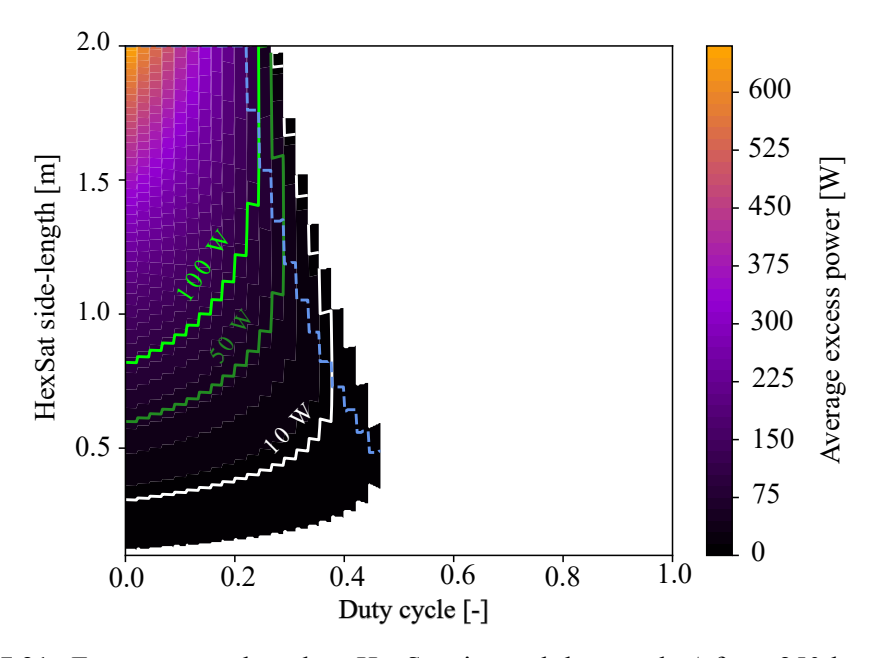


Figure 7.21: Excess power based on HexSat size and duty cycle  $\zeta$  for a 250 km circular orbit. The blue line represents the optimal HexSat size for maximum power at a given duty cycle.

The results show that if no AGT is performed ( $\zeta = 0$ ), a larger HexSat leads to greater

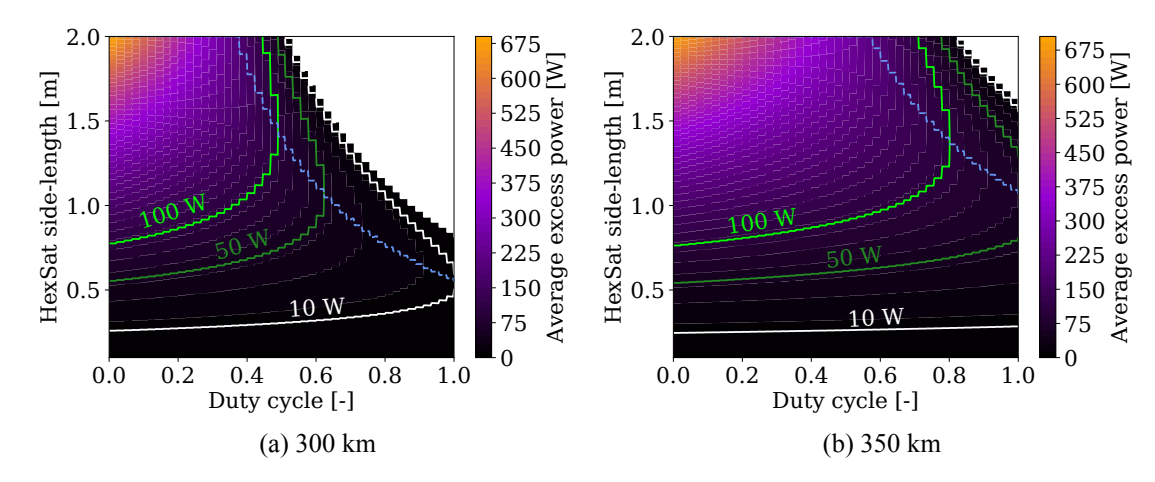


Figure 7.22: Excess power based on HexSat size, duty cycle  $\zeta$  and orbit height. The blue line represents the optimal HexSat size for maximum power at a given duty cycle.

available payload power. However, while the HexSat performs any amount of tracking  $(\zeta > 0)$ , there is an optimal HexSat size that maximises the excess power. This optimal size is marked by the dashed blue line in Figure 7.21 for each corresponding duty cycle. The optimum size decreases with increasing duty-cycle as the power consumption includes both the drag compensation and the rotation of the HexSat, which scales with  $s^3$ . For a HexSat with the equivalent surface area as the demonstration DiskSat, and a duty cycle of 0.3, the the HexSat will use 36 W for tracking and 68 W for drag compensation. However, the power for drag compensation is not always greater than the rotation. As the HexSat grows in size, the power required for rotation will increase with  $s^3$  compared to the power for drag compensation, which increases with  $s^2$ . Thus, for a larger HexSat with s=1with a duty-cycle of 0.3, 216 W will be used for the tracking, while 208 W will be used for drag compensation. The feasibility of the AGT is dependent on the HexSat side-length s. Small HexSats, with high agility, typically can perform tracking but have low excess power. Larger HexSats can provide high excess power while performing the AGT, although certain combinations of size, altitude and duty cycle are unfeasible, as their agility is not sufficient. These unfeasible combinations are shown by the white region, where the HexSat is too large and cannot generate enough power to sustain its operation. The step-like profile of the contour plot originates from Equation (7.25), where only integer values of  $n_{cycles}$  were considered.

The results presented are for circular orbits at 250 km in Figure 7.21, and 300 km and 350 km in Figure 7.22. One can observe that at higher altitudes, more combinations of s and  $\zeta$ are feasible as the drag is lower, and the overall angular acceleration required is reduced. However, to maximise the advantages of VLEO, orbits closer to the Earth are of primary interest. Focusing on the 250 km orbit, a HexSat with a 0.8 m side-length will provide more than 100 W of excess power for a relatively low duty cycle, approximately below 0.2. This translates to approximately 17 minutes of AGT time, or eight targets tracked across one orbit. Therefore, HexSats are capable of operating in AGT mode at 250 km.

An essential consideration in evaluating the DuPS system's operational feasibility is its stability under realistic conditions, accounting for manufacturing and operational imperfections. The DuPS thruster system operates at a high pulse frequency, resulting in a stable average thrust output with minimal magnitude variations. However, unavoidable physical imperfections - including manufacturing tolerances in thruster positioning, misalignments, and variations in thrust direction - will cause the HexSat's actual attitude and orbital parameters to deviate from their nominal values. These deviations necessitate the implementation of a dedicated control system. While such a system can effectively compensate for these real-world errors and maintain the desired spacecraft trajectory, this error correction requires additional fuel expenditure and places higher demands on the spacecraft's power system, although the associated analysis is beyond the scope of this work.

Estimates of orbital lifetime can also be obtained for different combinations of duty cycle and HexSat sizes. As HexSat size increases, the drag experienced by the HexSat increases with the surface area, proportional to  $s^2$ . In contrast, the available fuel mass increases with the perimeter length of the HexSat, proportional to s. This scaling indicates that larger HexSat will experience shorter lifetimes than smaller satellites, as shown on Figure 7.23 Similarly, the AGT operation induces a more substantial drag on the satellite, leading to a shortened orbital lifespan. Higher duty means the HexSat will experience a high drag multiple times per orbit, reducing the operational lifetime. Combined with the relatively high atmospheric density of VLEO, HexSats have an orbital lifetime of up to two years assuming a small size and low duty cycle. However, their lifetime is still higher than naturally possible without any thrust, demonstrating that the D $\mu$ PS can enable operation in VLEO.

### 7.6 Conclusion

This chapter has shown how the  $D\mu PS$  can extend nanosatellite operation below their current lower altitude bound. The HexSats, a novel concept of flat satellites using a Distributed micro ( $\mu$ )-Propulsion System for Very Low Earth Orbits introduced in this work, have significant advantages over traditional CubeSats regarding functional surface area and power generation. The hexagonal design enables complete 3-axis control and increases the usable surface area when multiple vertical stacks of HexSats fit within a launch vehicle fairing. Our investigation of the relationship between  $D\mu PS$  design parameters and the HexSats

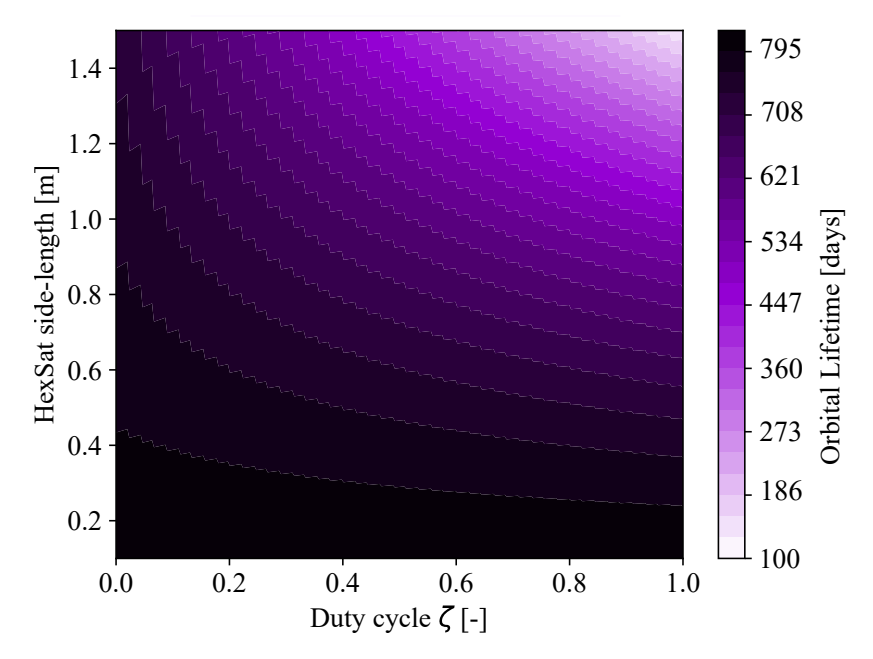


Figure 7.23: Orbital lifetime based on HexSat size and duty cycle  $\zeta$  for a 250 km circular orbit.

performance shows that while the orbit-average power increases with size, other performance parameters, such as agility, are inversely proportional to the HexSat size. The results demonstrate that HexSats can operate effectively in Nadir pointing mode in VLEO, although the feasibility of Active Ground Tracking is size-dependent. In a circular orbit at 250 km, a HexSat with a side-length of 0.8 m in Active Ground Tracking can track up to 8 targets per orbit while still delivering more than 100 W of average excess power to the payload.

# 8

# **Conclusion**

# **Summary of the thesis**

This thesis has demonstrated how nanosatellites can operate beyond their current operational range by using a novel propulsion system concept.

Chapter [I] explained that due to their small size and low-cost philosophy, nanosatellites, especially CubeSats, often struggle to include an actuation system. As a result, they are typically underactuated and constrained to a specific altitude range.

The challenges of miniaturisation in nanosatellite propulsion systems have been investigated in Chapter 2. Despite their high thrust capabilities, conventional chemical propulsion systems are impractical for nanosatellites due to the high mass and volume requirements of pressurised tanks, propellant delivery systems, and combustion chambers. Likewise, whilst highly efficient, Hall Effect Thrusters and Gridded Ion Thrusters face significant difficulties in downsizing and remain too power-intensive for nanosatellite applications. Reaction wheels, a common choice for attitude control, suffer from reduced angular momentum capacity when scaled down and require external means for momentum management. The chapter concludes that electrospray thrusters and Vacuum Arc Thrusters are the most promising actuation systems for further miniaturisation research.

This thesis then introduced, in Chapter 3 a novel propulsion system concept, the Distributed Micro ( $\mu$ )-Propulsion System (D $\mu$ PS), which originated from an ESA-funded project led by

Dr. Min Kwan Kim, and is the topic of research of another PhD student at the University of Southampton. It consists of many individual thrusters placed along the structure of a satellite.

As of its unique architecture, the effect of the  $\boxed{\text{D}\mu\text{PS}}$  on satellite dynamics is not trivial and cannot be simulated with off-the-shelf simulation tools. As a result, a high-fidelity numerical propagator is needed. Chapter  $\boxed{4}$  has thus examined the fundamental methods for representing and propagating attitude and orbital dynamics, including all relevant environmental perturbations, and reviewed popular propagators as potential simulators.

Chapter 5 then describes a bespoke high-fidelity numerical tool called the Comprehensive High-fidelity Attitude and Orbit Simulator (CHAOS), which couples orbit and attitude propagation with environmental perturbations. CHAOS utilises the Gauss Planetary Equations for orbital propagation using Modified Equinoctial elements, while attitude propagation is accomplished through Euler's equation and quaternion kinematics. It reads STL files to obtain detailed shape information of a spacecraft, applying force models to each facet for more accurate representation of environmental perturbations. The propagator models SRP, using the NAIF SPICE software for Earth-Sun positioning and includes a shadow model. CHAOS computes atmospheric density through an interpolation of the Jacchia-77 atmospheric model and uses the Sentman model for Gas-Surface interactions. It employs spherical harmonics using coefficients from the EGM2008 model to represent the Earth's non-spherical shape and includes perturbing accelerations induced by the Moon and Sun. CHAOS was compared to two reference software packages, GMAT and STK HPOP. The validation was performed individually for each force model, and CHAOS demonstrated good overall agreement with the reference software.

This thesis has then examined two nanosatellite missions enabled by the D $\mu$ PS. These missions demonstrate how nanosatellites can operate outside their current altitude range, and correspond to the novel contribution of this research.

Chapter 6 is published in Acta Astronautica and investigates a high-altitude deorbiting mission for a 1U CubeSat [I77]. It introduces Cube-de-ALPS, a fully printed standalone propulsion package that uses a gyroscope and a Faraday cup for attitude estimation. An operational mode was outlined, requiring only coarse angle-of-attack estimates and angular velocity readings. Cube-de-ALPS was installed on HUMSAT-D, a 1U CubeSat that spent seven years in Low Earth Orbit as untracked space debris. The de-orbiting performance was investigated using a semi-analytical model for various fuel materials, layouts, and signal-to-noise ratios. CHAOS was used to validate the results and demonstrate that Cube-de-ALPS would have significantly accelerated HUMSAT-D's de-orbiting compared to natural decay. Chap-

ter 6 demonstrated that the  $D\mu PS$  allow 1U CubeSats to operate up to 1,400 km, more than twice as high as naturally possible, whilst ensuring re-entry within 25 years. This effectively raises the operational ceiling of 1U CubeSats.

The thesis then investigated the operation of nanosatellites with the  $D\mu PS$  at the other end of the operational range, in Very Low Earth Orbit (VLEO). Chapter T published in Acta Astronautica T published in Acta Astrona

# Limitations and future work

The analysis presented in this thesis is entirely theoretical, based on the conceptual design of the  $\boxed{D\mu PS}$  As the  $D\mu PS$  progresses through development and testing, empirical data will provide a better understanding of its performance characteristics, potentially leading to revisions to the theoretical analysis presented in this thesis.

The central assumption made in this work is that a complete  $D\mu PS$  is achieved. However, the development path may deviate from its original characteristics, potentially influencing several factors. The final configuration of the  $D\mu PS$ , including the amount of fuel onboard and the total system mass, may differ from the estimates used in this thesis. The thrust produced at a given power level could also vary from the theoretical predictions. While the thesis assumed a linear relationship between thrust and power, i.e., the thrust-to-power ratio  $T_p$  is constant, empirical experiments may reveal a more complex relationship that could depend on different operational power ranges. Over time, the thrust produced by the  $D\mu PS$  might degrade, contrary to the assumption used in this thesis. This degradation could impact the nominal thrust level and distribution of thrust level at each pulse. Additionally,

constraints on the size of the pixels in the D $\mu$ PS could affect the analysis presented in Chapter [6], potentially changing the conclusions.

Therefore, one area of future work would be to either develop the  $\boxed{D\mu PS}$  to achieve the performance mentioned in this thesis or re-generate the data and the analysis performed with updated characteristics of the propulsion system once empirical data is available.

CHAOS, the custom tool for simulating the  $D\mu PS$ , has been validated and performs well. However, there is still room for improvement.

One area for additional development is the numerical integrator used for propagation. A more suitable algorithm could lead to enhanced runtimes and reduced numerical errors. CHAOS' runtime can also be improved, as the code is implemented in Python. The code could be translated into a low-level language, significantly improving the time efficiency of long-term simulations. To further optimise the runtime, CHAOS could parallelise the evaluation of the force models. In this approach, the force models would be evaluated in parallel on different cores at each function evaluation. However, this would involve a trade-off between the speedup achieved and the overhead from distributing the computation, and it is not clear yet if a net runtime improvement is guaranteed. Additional force models could be implemented, if deemed relevant, to refine the accuracy and realism of the simulations.

Therefore, future work could also focus on refining the high-fidelity tool developed for this thesis by enhancing the runtime and minimising the numerical errors.

# **Bibliography**

- [1] J. Saletes, M. Kim, K. Saddul, A. Wittig, K. Honda, and P. Katila, "Development of a novel CubeSat de-orbiting all printed propulsion system," Tech. Rep., 2022.
- [2] S. M. Spremo, A. R. Crocker, and T. L. Panontin, "Small Spacecraft Overview," Tech. Rep., 2017.
- [3] H. Curtis, Orbital Mechanics for Engineering students. Elsevier, 2005.
- [4] J. E. Polk, M. J. Sekerak, J. K. Ziemer, J. Schein, N. Qi, and A. Anders, "A theoretical analysis of vacuum arc thruster and vacuum arc ion thruster performance," *IEEE Trans. Plasma Sci.*, vol. 36, no. 5 PART 1, pp. 2167–2179, 2008.
- [5] Intel, "Intel's First Microprocessor," 2015.
- [6] Wikipedia, "Launch Vehicle Digital Computer," 2024.
- [7] I. Levchenko, K. Bazaka, Y. Ding, Y. Raitses, S. Mazouffre, T. Henning, P. J. Klar, S. Shinohara, J. Schein, L. Garrigues, M. Kim, D. Lev, F. Taccogna, R. W. Boswell, C. Charles, H. Koizumi, Y. Shen, C. Scharlemann, M. Keidar, and S. Xu, "Space micropropulsion systems for Cubesats and small satellites: From proximate targets to furthermost frontiers," *Appl. Phys. Rev.*, vol. 5, no. 1, 2018. [Online]. Available: <a href="http://dx.doi.org/10.1063/1.5007734">http://dx.doi.org/10.1063/1.5007734</a>
- [8] R. Smith, "Planet Labs Declares War on Global Warming," 10 2022.
- [9] G. Brown and W. Harris, "How Satellites Work," 2019.
- [10] S. S. Technology, "State of the Art report," Tech. Rep., 2021. [Online]. Available: http://www.sti.nasa.gov
- [11] J. Puig-Suari, J. Schoos, C. Turner, T. Wagner, R. Connolly, and R. P. Block, "Cube-Sat developments at Cal Poly: the standard deployer and PolySat," B. J. Horais and R. J. Twiggs, Eds., 11 2000, pp. 72–78.

Kash Saddul 150 BIBLIOGRAPHY

[12] R. Munakata, "Cubesat design specification rev. 13," *CubeSat Program, Calif. Polytech. State* ..., vol. 8651, p. 22, 2009.

- [13] E. Kulu, "Nanosat Database," 2014. [Online]. Available: https://www.nanosats.eu/
- [14] C. Clark, "Clark SSC10-III-5 Huge Power Demand...Itsy-Bitsy Satellite: Solving the CubeSat Power Paradox," Tech. Rep., 2010.
- [15] CubeSPACE, "CubeADCS The complete ADCS solution Interface Control Document," Tech. Rep., 2020.
- [16] H. C. Polat, J. Virgili-Llop, and M. Romano, "Survey, Statistical Analysis and Classifica-tion of Launched CubeSat Missions with Emphasis on the Attitude Control Method," *JoSS*, vol. 5, no. 3, pp. 513–530, 2016. [Online]. Available: www.jossonline.com
- [17] I. Kronhaus, K. Schilling, M. Pietzka, and J. Schein, "Simple orbit and attitude control using vacuum arc thrusters for Picosatellites," *Journal of Spacecraft and Rockets*, vol. 51, no. 6, pp. 2008–2015, 11 2014.
- [18] J. R. Wertz, Spacecraft Attitude Determination and Control, 1990.
- [19] F. Landis Markley and J. L. Crassidis, *Fundamentals of Spacecraft Attitude Determination and Control*, 2014. [Online]. Available: <a href="http://www.springer.com/series/6575">http://www.springer.com/series/6575</a>
- [20] N. M. Suhadis, *Statistical overview of cubesat mission*. Springer Singapore, 2020, no. March 2003. [Online]. Available: <a href="http://dx.doi.org/10.1007/978-981-15-4756-0">http://dx.doi.org/10.1007/978-981-15-4756-0</a> 50
- [21] (2024) BRITE. Accessed: 11 March 2024. [Online]. Available: https://en.wikipedia.org/wiki/BRITE
- [22] T. Greicius and N. Hartono. (2017) ASTERIA. Accessed: 08 March 2024. [Online]. Available: https://www.jpl.nasa.gov/missions/arcsecond-space-telescope-enabling-research-in-astrophysics-asteria/
- [23] J.-C. Liou, A. Anilkumar, B. Bastida Virgiili, T. Hanada, H. Krag, H. Lewis, M. Raj, M. Rao, A. Rossi, and R. Sharma, "Stability of the Future LEO Environment," in 6th European Conference on Space Debris, no. January, 2013, pp. 1–26.
- [24] Working Group 4, "IADC Space Debris Mitigation Guidelines," Tech. Rep., 2020.

[25] D. L. Oltrogge and K. Leveque, "An Evaluation of CubeSat Orbital Decay," 25th Annu. AIAA/USU Conf. Small Satell., no. August 2011, pp. 0–12, 2011. [Online]. Available: https://digitalcommons.usu.edu/cgi/viewcontent.cgi?article=

- [26] C. McGrath, C. Lowe, M. Macdonald, and S. Hancock, "Investigation of very low Earth orbits (VLEOs) for global spaceborne lidar," *CEAS Space Journal*, vol. 14, no. 4, pp. 625–636, 10 2022.
- [27] L. Berthoud, R. Hills, A. Bacon, M. Havouzaris-Waller, K. Hayward, J. D. Gayrard, F. Arnal, and L. Combelles, "Are Very Low Earth Orbit (VLEO) satellites a solution for tomorrow's telecommunication needs?" *CEAS Space Journal*, 2022.
- [28] N. H. Crisp, P. C. Roberts, F. Romano, K. L. Smith, V. T. Oiko, V. Sulliotti-Linner, V. Hanessian, G. H. Herdrich, D. García-Almiñana, D. Kataria, and S. Seminari, "System modelling of very low Earth orbit satellites for Earth observation," *Acta Astronautica*, vol. 187, pp. 475–491, 10 2021.
- [29] M. Leomanni, A. Garulli, A. Giannitrapani, and F. Scortecci, "Propulsion options for very low Earth orbit microsatellites," *Acta Astronautica*, vol. 133, pp. 444–454, 4 2017.
- [30] N. H. Crisp, P. C. Roberts, S. Livadiotti, V. T. Oiko, S. Edmondson, S. J. Haigh, C. Huyton, L. A. Sinpetru, K. L. Smith, S. D. Worrall, J. Becedas, R. M. Domínguez, D. González, V. Hanessian, A. Mølgaard, J. Nielsen, M. Bisgaard, Y. A. Chan, S. Fasoulas, G. H. Herdrich, F. Romano, C. Traub, D. García-Almiñana, S. Rodríguez-Donaire, M. Sureda, D. Kataria, R. Outlaw, B. Belkouchi, A. Conte, J. S. Perez, R. Villain, B. Heißerer, and A. Schwalber, "The benefits of very low earth orbit for earth observation missions," *Progress in Aerospace Sciences*, vol. 117, 8 2020.
- [31] European Space Agency. (2017) GOCE. Accessed: 12 February 2023. [Online]. Available: https://www.esa.int/Enabling\_Support/Operations/GOCE
- [32] A. Anselmi and S. Cesare, "Goce mission: Design phases and in-flight experiences Massimo Dumontel," Tech. Rep., 2010. [Online]. Available: <a href="https://www.researchgate.net/publication/260920187">https://www.researchgate.net/publication/260920187</a>
- [33] M. Albulet, "SpaceX V-Band Non-Geostationary Satellite System," Tech. Rep., 3 2017.

Kash Saddul 152 BIBLIOGRAPHY

[34] W. Zhang, X. Wang, W. Cui, Z. Zhao, and S. Chen, "Self-induced collision risk of the Starlink constellation based on long-term orbital evolution analysis," *Astrodynamics*, vol. 7, no. 4, pp. 445–453, 12 2023.

- [35] J. Saletes, K. Saddul, A. Wittig, and M. Kim, "Implementation of direct battery driven discharge in triggerless operation of vacuum arc thrusters," *Journal of Electric Propulsion*, vol. 3, no. 1, p. 4, 1 2024. [Online]. Available: https://link.springer.com/10.1007/s44205-023-00065-8
- [36] J. Saletes, K. Saddul, M. K. Kim, and A. Wittig, "Innovative propulsion systems for CubeSats and MicroSats-EXPRO+: CubeSat de-orbit ALI-printed Propulsion System Final Report," Tech. Rep., 2022.
- [37] K. Lemmer, "Propulsion for CubeSats," *Acta Astronaut.*, vol. 134, no. January, pp. 231–243, 2017. [Online]. Available: http://dx.doi.org/10.1016/j.actaastro.2017.01.
- [38] A. R. Tummala and A. Dutta, "An overview of Cube-Satellite propulsion technologies and trends," *Aerospace*, vol. 4, no. 4, pp. 1–30, 2017.
- [39] I. A. Spiegel, B. Zhou, R. Goodloe, B. Fox, and J. Dimatteo, "CubeSat Proximity Operations Demonstration (CPOD) Mission Results," in *Annual Small Satellite Conference*, 2023.
- [40] J. Bowen, J. Abel, and M. Vlla, "CubeSat Proximity Operations Demonstration (CPOD) Mission Update," in *IEEE*, 2015.
- [41] B. Yost and S. Weston, "State-of-the-Art: Small Spacecraft Technology," Ames Research Center, NASA, Tech. Rep., 2021.
- [42] Aerojet Rocketdyne, "MPS-120 data sheet-single sheet," Tech. Rep., 2020.
- [43] European Space Agency, "Considering hydrazine-free satellite propulsion," 2013. [Online]. Available: <a href="https://www.esa.int/Space\_Safety/Clean\_Space/Considering\_hydrazine-free satellite propulsion">https://www.esa.int/Space\_Safety/Clean\_Space/Considering\_hydrazine-free satellite propulsion</a>
- [44] G. Sutton and O. Biblarz, Rocket Propulsion Elements, 7th ed. Hoboken, 2001.
- [45] J. Hudson, S. Spangelo, A. Hine, D. Kolosa, and K. Lemmer, "Mission analysis for CubeSats with micropropulsion," *J. Spacecr. Rockets*, vol. 53, no. 5, pp. 836–846, 2016.

[46] R. Birkeland, "CubeSat propulsion: Expanding the affordable space platform," no. January, 2018.

- [47] D. Feili, B. Lotz, S. Bonnet, B. K. Meyer, H. W. L. Justus, and N. Puetmann, "µNRIT-2.5-A New Optimized Microthruster Of Giessen University," Tech. Rep., 2009.
- [48] P.-Y. C. R. Taunay, S. G. Bilén, and M. M. Micci, "Numerical Simulations of a Miniature Microwave Ion Thruster," Tech. Rep., 2013.
- [49] T. A. Trudel, S. G. Bilén, and M. M. Micci, "Design and Performance Testing of a 1-cm Miniature Radio-Frequency Ion Thruster," Tech. Rep., 2009.
- [50] SPACEMIND, "SM-SP Datasheet," Tech. Rep., 2020.
- [51] E. Dale, B. Jorns, and A. Gallimore, "Future directions for electric propulsion research," *Aerospace*, vol. 7, no. 9, 9 2020.
- [52] S. H. Yeo, H. Ogawa, D. Kahnfeld, and R. Schneider, "Miniaturization perspectives of electrostatic propulsion for small spacecraft platforms," 10 2021.
- [53] C. E. Pigeon, N. G. Orr, B. P. Larouche, V. Tarantini, G. Bonin, and R. E. Zee, "A Low Power Cylindrical Hall Thruster for Next Generation Microsatellites," Tech. Rep., 2015.
- [54] G. C. Potrivitu, Y. Sun, M. W. A. bin Rohaizat, O. Cherkun, L. Xu, S. Huang, and S. Xu, "A review of low-power electric propulsion research at the space propulsion centre Singapore," 6 2020.
- [55] T. Ikeda, K. Togawa, H. Tahara, and Y. Watanabe, "Performance characteristics of very low power cylindrical Hall thrusters for the nano-satellite "pROITERES-3"," *Vacuum*, vol. 88, no. 1, pp. 63–69, 2013.
- [56] A. Gurciullo, J. Jarrige, P. Lascombes, and D. Packan, "Experimental performance and plume characterisation of a miniaturised 50W Hall thruster," Tech. Rep., 2019. [Online]. Available: https://hal.science/hal-02422774
- [57] A. N. Manoudis, "Conceptual study of a low power electric propulsion system for LEO and VLEO microsatellite missions," Tech. Rep., 2022.
- [58] T. Andreussi, E. Ferrato, C. A. Paissoni, A. Kitaeva, V. Giannetti, A. Piragino, S. Schäff, K. Katsonis, C. Berenguer, Z. Kovacova, E. Neubauer, M. Tisaev, B. Karadag, A. Lucca Fabris, M. Smirnova, A. Mingo, D. Le Quang, Z. Alsalihi,

Kash Saddul 154 BIBLIOGRAPHY

F. Bariselli, P. Parodi, P. Jorge, and T. E. Magin, "The AETHER project: development of air-breathing electric propulsion for VLEO missions," *CEAS Space Journal*, vol. 14, no. 4, pp. 717–740, 10 2022.

- [59] P. Crandall and R. E. Wirz, "Air-breathing electric propulsion: mission characterization and design analysis," *Journal of Electric Propulsion*, vol. 1, no. 1, 9 2022.
- [60] V. P. Stanojkovska, S. Rodriguez, D. Daniel, and G. Almiñana, "Design of a Business Roadmap methodology: Application in Air-Breathing Electric Propul-sion (ABEP) systems for Very Low Earth Orbits (VLEO) missions," Tech. Rep., 2021.
- [61] R. S. Legge, P. Lozano, and M. Martinez-Sanchez, "Fabrication and Characterization of Porous Metal Emitters for Electrospray Thrusters," in *International Electric Propulsion Conference*, 2007.
- [62] B. Yost and S. Weston, "State-of-the-Art: Small Spacecraft Technology," Ames Research Center, NASA, Tech. Rep., 2024. [Online]. Available: <a href="http://www.sti.nasa.gov">http://www.sti.nasa.gov</a>
- [63] A. Kramer, P. Bangert, and K. Schilling, "UWE-4: First electric propulsion on a 1U cubesat-in-orbit experiments and characterization," *Aerospace*, vol. 7, no. 7, 7 2020.
- [64] M. R. Natisin, H. L. Zamora, W. A. McGehee, N. I. Arnold, Z. A. Holley, M. R. Holmes, and D. Eckhardt, "Fabrication and characterization of a fully conventionally machined, high-performance porous-media electrospray thruster," *Journal of Micromechanics and Microengineering*, vol. 30, no. 11, 11 2020.
- [65] D. Bock and M. Tajmar, "Highly miniaturized FEEP propulsion system (NanoFEEP) for attitude and orbit control of CubeSats," *Acta Astronautica*, vol. 144, pp. 422–428, 3 2018.
- [66] D. Bock, M. Tajmar, D. Bock, M. Bethge, and M. Tajmar, "Highly Miniaturized FEEP Thrusters for CubeSat Applications," Tech. Rep., 2014. [Online]. Available: https://www.researchgate.net/publication/280883495
- [67] D. B. Zolotukhin, S. Ram Prasad Bandaru, K. P. Daniels, I. I. Beilis, and M. Keidar, "Demonstration of electric micropropulsion multimodality," Tech. Rep., 2022. [Online]. Available: <a href="https://www.science.org">https://www.science.org</a>
- [68] S. Ciaralli, M. Coletti, and S. B. Gabriel, "Results of the qualification test campaign of a Pulsed Plasma Thruster for Cubesat Propulsion (PPTCUP)," *Acta Astronautica*, vol. 121, pp. 314–322, 4 2016.

[69] M. Coletti, F. Guarducci, and S. B. Gabriel, "A micro PPT for Cubesat application: Design and preliminary experimental results," *Acta Astronautica*, vol. 69, no. 3-4, pp. 200–208, 8 2011.

- [70] J. T. King, J. Kolbeck, J. S. Kang, M. Sanders, and M. Keidar, "Performance analysis of nano-sat scale μCAT electric propulsion for 3U CubeSat attitude control," *Acta Astronautica*, vol. 178, pp. 722–732, 1 2021.
- [71] S. Hurley, G. Teel, J. Lukas, S. Haque, M. Keidar, C. Dinelli, and J. Kang, "Thruster Subsystem for the United States Naval Academy's (USNA) Ballistically Reinforced Communication Satellite (BRICSat-P)," Tech. Rep. ists30, 2016.
- [72] F. Rysanek, J. W. Hartmann, J. Schein, and R. Binder, "SSC02-I-2 Micro-Vacuum Arc Thruster Design for a CubeSat Class Satellite," Tech. Rep., 2002.
- [73] G. Quinsac, B. Segret, C. Koppel, and B. Mosser, "Attitude control: A key factor during the design of low-thrust propulsion for CubeSats," *Acta Astronautica*, vol. 176, pp. 40–51, 11 2020.
- [74] D. T. Gerhardt and S. E. Palo, "Passive Magnetic Attitude Control for CubeSat Spacecraft," *Small Satell. Conf.*, p. 10, 2010. [Online]. Available: <a href="http://digitalcommons.usu.edu/cgi/viewcontent.cgi?article=1230&context=smallsat">http://digitalcommons.usu.edu/cgi/viewcontent.cgi?article=1230&context=smallsat</a>
- [75] S. A. Rawashdeh and J. E. Lumpp, "Nano-Satellite Passive Attitude Stabilization Systems Design by Orbital Environment Modeling and Simulation," Tech. Rep., 2010.
- [76] S. Jarmak, J. Brisset, J. Colwell, A. Dove, D. Maukonen, S. A. Rawashdeh, J. Blum, and L. Roe, "CubeSat Particle Aggregation Collision Experiment (Q-PACE): Design of a 3U CubeSat mission to investigate planetesimal formation," *Acta Astronautica*, vol. 155, pp. 131–142, 2 2019.
- [77] S. Jayaram and D. Pais, "Model-based Simulation of Passive Attitude Control of SLUCUBE-2 Using Nonlinear Hysteresis and Geomagnetic Models," *Int. J. Aerosp. Sci.*, vol. 1, no. 4, pp. 77–84, 2012.
- [78] J. Auret and W. H. Steyn, "Design of an Aerodynamic Attitude Control System for a CubeSat," Ph.D. dissertation, University of Stellenbosch, 2012. [Online]. Available: <a href="http://scholar.sun.ac.za">http://scholar.sun.ac.za</a>
- [79] M. Berthet and K. Suzuki, "Coupled Simulation of Passive Aerodynamic Stabilisation of a Nanosatellite During Orbital Decay," *Transactions of the Japan Society for Aeronautical and Space Sciences, Aerospace Technology Japan*, vol. 18, no. 6, pp. 384–390, 2020.

Kash Saddul 156 BIBLIOGRAPHY

[80] V. S. Aslanov and D. A. Sizov, "Chaos in flexible CubeSat attitude motion due to aerodynamic instability," *Acta Astronautica*, vol. 189, pp. 310–320, 12 2021.

- [81] C. R. McInnes, Solar Sailing: Technology, Dynamics and Mission Applications. Springer, 1999.
- [82] B. Wie, "Solar Sail Attitude Control and Dynamics, Part 1," *Journal of Guidance, Control, and Dynamics*, vol. 27, no. 4, pp. 526–535, 7 2004.
- [83] —, "Solar Sail Attitude Control and Dynamics, Part Two," *Journal of Guidance, Control, and Dynamics*, vol. 27, no. 4, pp. 536–544, 7 2004.
- [84] M. Berthet and K. Suzuki, "Sunflower mission concept for high-altitude earth observation in LEO via nanosatellite with pyramidal solar sail," *Acta Astronautica*, vol. 213, pp. 516–536, 12 2023.
- [85] R. Bauer, "Investigation of gain tuning and sensor noise for CubeSat B-dot detumbling and 3-axis PD magnetic attitude control," in *Proceedings of the Canadian Society for Mechanical Engineering International Congress*, 2020.
- [86] C. Pong, "High-Precision Pointing and Attitude Estimation and Control Algorithms for Hardware-Constrained Spacecraft," Ph.D. dissertation, Massachusetts Institute of Technology, 2014.
- [87] Blue Canyon Technologies, "Attitude Control Systems Datasheet," Tech. Rep., 2024.
- [88] S. Krishna, S. Gosavi, S. Sngh, N. Saxena, A. Kailaje, V. Datla, and P. Shah, "Design and Implementation of a Reaction Wheel System for CubeSats," in *IEEE*, 2014.
- [89] D. Zhang, Y. Zhang, K. Dong, and S. Wang, "Control allocation strategy for optimal digital microthruster arrays in orbit control applications," in *Journal of Spacecraft and Rockets*, vol. 56, no. 3. American Institute of Aeronautics and Astronautics Inc., 2019, pp. 836–843.
- [90] B. Yang, J. Miao, Z. Fan, J. Long, and X. Liu, "Allocation Optimization Strategy for High-Precision Control of Picosatellites and Nanosatellites," *International Journal* of Aerospace Engineering, vol. 2018, 2018.
- [91] P. A. Servidia and R. Sánchez Peña, "Spacecraft thruster control allocation problems," *IEEE Transactions on Automatic Control*, vol. 50, no. 2, pp. 245–249, 2 2005.
- [92] T. W. Lim, "Thruster attitude control system design and performance for Tactical Satellite 4 maneuvers," *Journal of Guidance, Control, and Dynamics*, vol. 37, no. 2, pp. 403–412, 2014.

[93] N. A. Gatsonis, Y. Lu, J. Blandino, M. A. Demetriou, and N. Paschalidis, "Micropulsed plasma thrusters for attitude control of a low-earth-orbiting cubesat," *Journal of Spacecraft and Rockets*, vol. 53, no. 1, pp. 57–73, 2016.

- [94] F. Mier-Hicks and P. C. Lozano, "Electrospray thrusters as precise attitude control actuators for small satellites," *Journal of Guidance, Control, and Dynamics*, vol. 40, no. 3, pp. 642–649, 2017.
- [95] X. Yao, G. Tao, Y. Ma, and R. Qi, "Adaptive actuator failure compensation design for spacecraft attitude control," *IEEE Transactions on Aerospace and Electronic Systems*, vol. 52, no. 3, pp. 1021–1034, 6 2016.
- [96] D. Selva and D. Krejci, "A survey and assessment of the capabilities of Cubesats for Earth observation," *Acta Astronaut.*, vol. 74, pp. 50–68, 2012. [Online]. Available: <a href="http://dx.doi.org/10.1016/j.actaastro.2011.12.014">http://dx.doi.org/10.1016/j.actaastro.2011.12.014</a>
- [97] J. D. Biggs, Y. Bai, and H. Henninger, "Attitude guidance and tracking for space-craft with two reaction wheels," *International Journal of Control*, vol. 91, no. 4, pp. 926–936, 4 2018.
- [98] J. D. Biggs and L. Colley, "Geometric Attitude Motion Planning for Spacecraft with Pointing and Actuator Constraints," *Journal of Guidance, Control, and Dynamics*, vol. 39, no. 7, pp. 1672–1677, 7 2016.
- [99] A. Mehrparwar Zinjanabi, H. Nejat Pishkenari, H. Salarieh, and T. Abdollahi, "Attitude control of an underactuated satellite in presence of disturbance torque with optimal motion planning," *Aerospace Science and Technology*, vol. 121, 2 2022.
- [100] N. M. Horri and P. Palmer, "Practical implementation of attitude-control algorithms for an underactuated satellite," *Journal of Guidance, Control, and Dynamics*, vol. 35, no. 1, pp. 40–50, 2012.
- [101] J. E. Polk, M. J. Sekerak, J. K. Ziemer, J. Schein, N. Qi, and A. Anders, "A theoretical analysis of vacuum arc thruster and vacuum arc ion thruster performance," *IEEE Transactions on Plasma Science*, vol. 36, no. 5 PART 1, pp. 2167–2179, 2008.
- [102] B. Osamu MORI, H. Sawada, R. Funase, M. Morimoto, T. Endo, T. Yamamoto, Y. Tsuda, Y. Kawakatsu, i. Kawaguchi, Y. Miyazaki, and Y. Shirasawa, "First Solar Power Sail Demonstration by IKAROS," Tech. Rep. ists27, 2010.
- [103] C. Lücking, C. Colombo, and C. R. McInnes, "A passive satellite deorbiting strategy for medium earth orbit using solar radiation pressure and the J 2 effect," *Acta Astronaut.*, vol. 77, pp. 197–206, 2012.

Kash Saddul 158 BIBLIOGRAPHY

[104] C. Lücking, C. Colombo, and C. Mcinnes, "Solar Radiation Pressure Augmented Deorbiting from High Altitude Sun-Synchronous Orbits," Tech. Rep.

- [105] C. M. Lücking, C. Colombo, and C. R. Mcinnes, "Orbit Control of High Area-to-Mass Ratio Spacecraft Using Electrochromic Coating," Tech. Rep.
- [106] D. A. Vallado, Fundamentals of Astrodynamics and Applications. Microcosm Press, 2013.
- [107] M. Sidi, Spacecraft Dynamics and Control, 1997.
- [108] P. Ghosh, "Revisiting Trajectory Design with STK Astrogator, Part 1," Tech. Rep., 2019. [Online]. Available: https://www.researchgate.net/publication/336074120
- [109] J. Carrico, "Revisiting Trajectory Design with STK Astrogator, Part 3," Tech. Rep., 2023. [Online]. Available: https://www.researchgate.net/publication/373329159
- [110] ANSYS, "How the Double Asteroid Redirection Test (DART) Hit a Bullseye," 2024. [Online]. Available: https://www.ansys.com/blog/dart-hits-a-bullseye
- [111] —, "Designing the James Webb Space Telescope with Simulation," 2024. [Online]. Available: <a href="https://www.ansys.com/blog/designing-the-james-webb-space-telescope-with-simulation">https://www.ansys.com/blog/designing-the-james-webb-space-telescope-with-simulation</a>
- [112] —, "Simulation Helps Artemis Keep in Touch and on Track to the Moon," 2024. [Online]. Available: <a href="https://www.ansys.com/blog/simulation-helps-artemis">https://www.ansys.com/blog/simulation-helps-artemis</a>
- [113] S. P. Hughes, R. H. Qureshi, D. S. Cooley, J. J. K. Parker, and T. G. Grubb, "Verification and validation of the general mission analysis tool (GMAT)," *AIAA/AAS Astrodyn. Spec. Conf. 2014*, no. August 2014, 2014.
- [114] R. H. Qureshi and S. P. Hughes, "Preparing General Mission Analysis Tool for Operational Maneuver Planning of the Advanced Composition Explorer Mission," Tech. Rep., 2014.
- [115] CS Group, "Orekit: An accurate and efficient core layer for space flight dynamics applications," 2024. [Online]. Available: <a href="https://www.orekit.org/">https://www.orekit.org/</a>
- [116] L. Maisonobe, V. Pommier-Maurussane, and P. Parraud, "Orekit: An Open Source Library for Operational Flight Dynamics Applications," Tech. Rep., 2010. [Online]. Available: <a href="https://www.researchgate.net/publication/310250345">https://www.researchgate.net/publication/310250345</a>
- [117] L. B. M Sagnières and I. Sharf, "Modeling and Simulation of Long-term Rotational Dynamics of Large Space Debris," Tech. Rep., 2019.

[118] L. B. Sagnières, I. Sharf, and F. Deleflie, "Simulation of long-term rotational dynamics of large space debris: A TOPEX/Poseidon case study," *Advances in Space Research*, vol. 65, no. 4, pp. 1182–1195, 2 2020.

- [119] L. B. Sagnières and I. Sharf, "Long-term rotational motion analysis and comparison to observations of the inoperative envisat," *Journal of Guidance, Control, and Dynamics*, vol. 42, no. 2, pp. 364–376, 2019.
- [120] D. Thomas, A. Wolosik, and J. Black, "CubeSat attitude control simulator design," in *AIAA Modeling and Simulation Technologies Conference*, 2018. American Institute of Aeronautics and Astronautics Inc, AIAA, 2018.
- [121] K. Vega, D. Auslander, and D. Pankow, "Design and Modeling of an Active Attitude Control System for CubeSat Class Satellites," in AIAA Modeling and Simulation Technologies Conference. Reston, Virigina: American Institute of Aeronautics and Astronautics, 8 2009.
- [122] K. Saulnier, D. Perez, G. Tilton, D. Gallardo, C. Shake, R. Huang, and R. Bevilacqua, "Operational Capabilities of a Six Degrees of Freedom Spacecraft Simulator," in *AIAA Guidance, Navigation, and Control (GNC) Conference*. Reston, Virginia: American Institute of Aeronautics and Astronautics, 8 2013.
- [123] E. M. Filho, L. O. Seman, C. A. Rigo, V. d. P. Nicolau, R. G. Ovejero, and V. R. Q. Leithardt, "Irradiation Flux Modelling for Thermal–Electrical Simulation of Cube-Sats: Orbit, Attitude and Radiation Integration," *Energies*, vol. 13, no. 24, p. 6691, 12 2020.
- [124] V. Carrara, R. B. Januzi, D. H. Makita, L. F. D. P. Santos, and L. S. Sato, "The ITASAT cubesat development and design," *J. Aerosp. Technol. Manag.*, vol. 9, no. 2, pp. 138–147, 2017.
- [125] D. M. Geletko, M. D. Grubb, J. P. Lucas, J. R. Morris, M. Spolaor, M. D. Suder, S. C. Yokum, and S. A. Zemerick, "NASA Operational Simulator for Small Satellites (NOS 3): the STF-1 CubeSat case study [Integration & Testing; Flight Software]," Tech. Rep., 2016. [Online]. Available: <a href="http://www.nos3.org">http://www.nos3.org</a>.
- [126] D. Kaslow, G. Soremkun, H. Kim, and S. Spangelo, *Integrated Model-Based Systems Engineering (MBSE) Applied to the Simulation of a CubeSat Mission*. [publisher not identified], 2014.
- [127] M. J. H. Walker and J. Owens, "A set of modified equinoctial orbit elements," Tech. Rep., 1985.

Kash Saddul 160 BIBLIOGRAPHY

- [128] M. Walker, "A Set of Modified Equinoctial Orbit Elements- Errata," 1986.
- [129] E. A. Roth, "The Gaussian Form of the Variation-Of-Parameter Equations Formulated in Equinoctial Elements-Applications: Air Drag and Radiation Pressure," *Acta Astronautica*, vol. 12, no. 10, pp. 719–730, 1985.
- [130] (2024) Stereolithography. Accessed: 01 March 2023. [Online]. Available: <a href="https://en.wikipedia.org/wiki/Stereolithography">https://en.wikipedia.org/wiki/Stereolithography</a>
- [131] Royal Greenwich Observatory, *Astronomical Almanac*. Cambridge University Press, 1992.
- [132] Jean Meeus, Astronomical Algorithms. Willmann-Bell Incorporated, 1 1991.
- [133] C. H. Acton, "Ancillary data services of NASA's Navigation and Ancillary Information Facility," Tech. Rep. 1, 1996.
- [134] C. Acton, N. Bachman, B. Semenov, and E. Wright, "A look towards the future in the handling of space science mission geometry," *Planetary and Space Science*, vol. 150, pp. 9–12, 1 2018.
- [135] O. Montenbruck and E. Gill, Satellite Orbits. Springer, 2000.
- [136] V. K. Srivastava, A. Ashutosh, M. V. Roopa, B. N. Ramakrishna, M. Pitchaimani, and B. S. Chandrasekhar, "Spherical and oblate Earth conical shadow models for LEO satellites: Applications and comparisons with real time data and STK to IRS satellites," *Aerospace Science and Technology*, vol. 33, no. 1, pp. 135–144, 2014.
- [137] J. Woodburn, "Effects of eclipse boundary crossings on the numerical integration of orbit trajectories," *Astrodyn. Spec. Conf.*, pp. 116–122, 2000.
- [138] NASA Goddard Space Flight Center, "General Mission Analysis Tool (GMAT) Mathematical Specifications," Tech. Rep., 2020.
- [139] Committee on Space Research, "COSPAR International Reference Atmosphere CIRA-2012 Models of the Earth's Upper Atmosphere," pp. 1–37, 2012.
- [140] J. M. Picone, A. E. Hedin, D. P. Drob, and A. C. Aikin, "NRLMSISE-00 empirical model of the atmosphere: Statistical comparisons and scientific issues," *J. Geophys. Res. Sp. Phys.*, vol. 107, no. A12, pp. 1–16, 2002.
- [141] C. E. Roberts, "An Analytical Model for Upper Atmosphere Densities based upon Jacchia's 1970 Models," *Celestial Mechanics*, 1971.

[142] NASA, "U.S. Standard Atmosphere," United States Air Force, Washington D.C., Tech. Rep., 1960.

- [143] K. A. Akins, L. M. Healy, S. L. Coffey, and J. M. Picone, "Comparison of MSIS and Jacchia atmospheric density models for orbit determination and propagation," *Adv. Astronaut. Sci.*, vol. 114, no. SUPPL., pp. 945–965, 2003.
- [144] D. A. Vallado and D. Finkleman, "A critical assessment of satellite drag and atmospheric density modeling," *Acta Astronautica*, vol. 95, no. 1, pp. 141–165, 2 2014.
- [145] D. Kerridge, T. Clark, and A. Thomson, "SOLMAG: An Operational System for Prediction of Solar and Geomagnetic Indices," in *Proceedings of the First European Conference on Space Debris*, Darmstadt, 1993.
- [146] V. M. Velasco Herrera, W. Soon, and D. R. Legates, "Does Machine Learning reconstruct missing sunspots and forecast a new solar minimum?" *Advances in Space Research*, vol. 68, no. 3, pp. 1485–1501, 8 2021.
- [147] European Space Agency, "ESA Space Weather," 2000. [Online]. Available: https://swe.ssa.esa.int/
- [148] National Aeronautics and Space Administration, "SOHO Space Weather," 2020. [Online]. Available: <a href="https://soho.nascom.nasa.gov/home.html">https://soho.nascom.nasa.gov/home.html</a>
- [149] National Oceanic and Atmospheric Administration, "Space Weather Prediction Centre," 2015. [Online]. Available: https://www.swpc.noaa.gov/
- [150] D. A. Vallado and D. L. Oltrogge, "Satellite Lifetime and Solar Cycle Predictions," in *Proceedings of the 8th Conference on Space Debris*, Darmstadt, 2021. [Online]. Available: <a href="http://www.sidc.be/silso/datafiles">http://www.sidc.be/silso/datafiles</a>
- [151] S. Frey, C. Colombo, and S. Lemmens, "Extension of the King-Hele orbit contraction method for accurate, semi-analytical propagation of non-circular orbits," *Adv. Sp. Res.*, vol. 64, no. 1, pp. 1–17, 2019. [Online]. Available: https://doi.org/10.1016/j.asr.2019.03.016
- [152] Lee H. Sentman, "Free molecule flow theory and its application to the determination of aerodynamic forces," *Lockheed Aircraft Corporation*, 1961.
- [153] S. A. Schaaf and P. L. Chambre, "H. Flow of Rarefied Gases," in *Fundamentals of Gas Dynamics*. Princeton University Press, 12 1958, pp. 687–740.

Kash Saddul 162 BIBLIOGRAPHY

[154] S. Livadiotti, N. H. Crisp, P. C. E. Roberts, S. D. Worrall, V. T. A. Oiko, S. Edmondson, S. J. Haigh, C. Huyton, K. L. Smith, L. A. Sinpetru, B. E. A. Holmes, J. Becedas, R. M. Domínguez, V. Cañas, S. Christensen, A. Mølgaard, J. Nielsen, M. Bisgaard, Y.-A. Chan, G. H. Herdrich, F. Romano, S. Fasoulas, C. Traub, D. Garcia-Almiñana, S. Rodriguez-Donaire, M. Sureda, D. Kataria, B. Belkouchi, A. Conte, J. S. Perez, R. Villain, and R. Outlaw, "A Review of Gas-Surface Interaction Models for Orbital Aerodynamics Applications," 10 2020. [Online]. Available: http://arxiv.org/abs/2010.00489http://dx.doi.org/10.1016/j.paerosci.2020.100675

- [155] C. Cercignani, *Rarefied Gas Dynamics: From Basic Concepts to Actual Calculations*. Cambridge University Press, 2000.
- [156] C. Cercignani and M. Lampis, "Kinetic models for gas-surface interactions," *Transport Theory and Statistical Physics*, vol. 1, no. 2, pp. 101–114, 1 1971.
- [157] J. Maxwell, "On stresses in rarefied gases arising from inequalities of temperature," *Proceedings of the Royal Society of London*, vol. 27, no. 185-189, pp. 304–308, 12 1878.
- [158] S. Nocilla, Basic Concepts in the Surface Interaction of Free-Molecular FLows or Molecular beams. Meccanica, 1967.
- [159] C. Cercignani, M. Lampis, and A. Lentati, "A new scattering kernel in kinetic theory of gases," *Transport Theory and Statistical Physics*, vol. 24, no. 9, pp. 1319–1336, 11 1995.
- [160] R. M. Logan and R. E. Stickney, "Simple Classical Model for the Scattering of Gas Atoms from a Solid Surface," *The Journal of Chemical Physics*, vol. 44, no. 1, pp. 195–201, 1 1966.
- [161] R. M. Logan and J. C. Keck, "Classical Theory for the Interaction of Gas Atoms with Solid Surfaces," *The Journal of Chemical Physics*, vol. 49, no. 2, pp. 860–876, 7 1968.
- [162] J. C. Tully, "Washboard model of gas-surface scattering," *The Journal of Chemical Physics*, vol. 92, no. 1, pp. 680–686, 1 1990.
- [163] K. Moe, M. M. Moe, and C. J. Rice, "Simultaneous analysis of multi-instrument satellite measurements of atmospheric density," *Journal of Spacecraft and Rockets*, vol. 41, no. 5, pp. 849–853, 2004.

[164] E. K. Sutton, "Effects of Solar Disturbances on the Thermosphere Densities and Winds from CHAMP and GRACE Satellite Accelerometer Data," Tech. Rep., 2008.

- [165] NASA, "U.S. Standard Atmosphere," United States Air Force, Washington D.C., Tech. Rep., 10 1976.
- [166] B. Tapley, J. Ries, S. Bettadpur, D. Chambers, M. Cheng, F. Condi, B. Gunter, Z. Kang, P. Nagel, R. Pastor, T. Pekker, S. Poole, and F. Wang, "GGM02 An improved Earth gravity field model from GRACE," *Journal of Geodesy*, vol. 79, no. 8, pp. 467–478, 11 2005.
- [167] N. K. Pavlis, S. A. Holmes, S. C. Kenyon, and J. K. Factor, "The development and evaluation of the Earth Gravitational Model 2008 (EGM2008)," *J. Geophys. Res. Solid Earth*, vol. 117, no. 4, pp. 1–38, 2012.
- [168] W. Yi and R. Rummel, "A comparison of GOCE gravitational models with EGM2008," *J. Geodyn.*, vol. 73, pp. 14–22, 2014. [Online]. Available: <a href="http://dx.doi.org/10.1016/j.jog.2013.10.004">http://dx.doi.org/10.1016/j.jog.2013.10.004</a>
- [169] T. D. Papanikolaou and D. Tsoulis, "Assessment of earth gravity field models in the medium to high frequency spectrum based on GRACE and GOCE dynamic orbit analysis," *Geosci.*, vol. 8, no. 12, pp. 1–18, 2018.
- [170] R. S. Park, W. M. Folkner, J. G. Williams, and D. H. Boggs, "The JPL Planetary and Lunar Ephemerides DE440 and DE441," *The Astronomical Journal*, vol. 161, no. 3, p. 105, 3 2021.
- [171] J. E. Polk, M. J. Sekerak, J. K. Ziemer, J. Schein, N. Qi, and A. Anders, "A theoretical analysis of vacuum arc thruster and vacuum arc ion thruster performance," *IEEE Transactions on Plasma Science*, vol. 36, no. 5 PART 1, pp. 2167–2179, 2008.
- [172] J. Schein, A. Gerhan, M. Au, K. Wilson, and M. Krishnan, "Long-term performance of Vacuum Arc Thrusters," Tech. Rep., 2004.
- [173] Peck Roxy, Olsen Chris, and Devore Jay, "Introduction to Statistics and Data Analysis," Tech. Rep., 2008.
- [174] H. Rein and S. Liu, "REBOUND: an open-source multi-purpose N-body code for collisional dynamics," *Astronomy & Astrophysics*, vol. 537, p. A128, 1 2012.
- [175] ANSYS, "Check your Attitude!" 2020. [Online]. Available: https://www.agi.com/blog/2020/10/check-your-attitude

Kash Saddul 164 BIBLIOGRAPHY

[176] S. A. Rawashdeh and J. E. Lumpp, "Aerodynamic Stability for CubeSats at ISS Orbit," Tech. Rep. [Online]. Available: www.JoSSonline.com

- [177] K. Saddul, J. Saletes, M. Kim, and A. Wittig, "Mission analysis of a 1U CubeSat post-mission disposal using a thin-film vacuum arc thruster," *Acta Astronautica*, vol. 219, pp. 318–328, 6 2024. [Online]. Available: https://linkinghub.elsevier.com/retrieve/pii/S0094576524001449
- [178] K. Saddul, A. Wittig, J. Saletes, and M. Kim, "End-Of-Life Disposal of Sub-3U CubeSat with a printed thin-film Vacuum Arc Thruster," in *Proceedings of the International Astronautical Congress*, 2022.
- [179] K. Minkwan, H. Lewis, Kim Minkwan, and H. Lewis, "Feasibility of Failsafe Deorbiting System using a Thin-layer Vacuum Arc Thruster," 2020.
- [180] C. Colombo, C. Lücking, and C. R. McInnes, "Orbit evolution, maintenance and disposal of SpaceChip swarms through electro-chromic control," *Acta Astronautica*, vol. 82, no. 1, pp. 25–37, 1 2013.
- [181] SAFRAN, "STIM277H Multi-axis Gyro Module," Tech. Rep., 2022.
- [182] Y. Watanabe, K. Suzuki, and K. Yamada, "Attitude Estimation of Nano-satellite with Deployable Aeroshell during Orbital Decay," Tech. Rep. ists30, 2016.
- [183] N. Enoki, Y. Takahashi, N. Oshima, K. Yamada, and K. Suzuki, "Aerodynamics of inflatable nano-satellite "eGG" in low earth orbit and reentry duration," in *AIP Conference Proceedings*, vol. 2132. American Institute of Physics Inc., 8 2019.
- [184] B. Nanan, C. Y. Chen, J. Y. Liu, N. Balan, C. Y. Chen, and G. J. Bailey, "Behaviour of the low-latitude ionosphere-plasmasphere system at long deep solar minimum An interdisciplinary approach for earthquake modelling and forecasting View project TCGA Network View project Behaviour of the low-latitude ionosphere-plasmasphere system at long deep solar minimum," Tech. Rep., 2012. [Online]. Available: <a href="https://www.researchgate.net/publication/267802546">https://www.researchgate.net/publication/267802546</a>
- [185] E. Weisstein, "Circle-Circle Intersection," 2014. [Online]. Available: https://mathworld.wolfram.com/Circle-CircleIntersection.html
- [186] W. R. Hoegy, J. M. Grebowsky, and L. H. Brace, "Ionospheric Ion Composition From Satellite Measurements made during 1970-1980: Altitude Profiles," Tech. Rep. 10, 1991.

[187] A. D. Polyanin and A. V. Manzhirov, *Handbook of Mathematics for Engineers and Scientists*. Chapman and Hall/CRC, 11 2006.

- [188] D. B. Zolotukhin and M. Keidar, "Optimization of discharge triggering in microcathode vacuum arc thruster for CubeSats," *Plasma Sources Science and Technology*, vol. 27, no. 7, 7 2018.
- [189] C. Palla and J. Kingston, "Forecast analysis on satellites that need de-orbit technologies: future scenarios for passive de-orbit devices," *CEAS Space Journal*, vol. 8, no. 3, pp. 191–200, 9 2016.
- [190] A. C. Long and D. A. Spencer, "A Scalable Drag Sail for the Deorbit of Small Satellites," Tech. Rep. 3, 2018. [Online]. Available: www.jossonline.com
- [191] M. Berthet, K. Yamada, Y. Nagata, and K. Suzuki, "Feasibility assessment of passive stabilisation for a nanosatellite with aeroshell deployed by orbit-attitude-aerodynamics simulation platform," *Acta Astronautica*, vol. 173, pp. 266–278, 8 2020.
- [192] R. Deienno, D. M. Sanchez, A. F. B. de Almeida Prado, and G. Smirnov, "Satellite deorbiting via controlled solar radiation pressure," *Celestial Mechanics and Dynamical Astronomy*, vol. 126, no. 4, pp. 433–459, 11 2016.
- [193] C. Lücking, C. R. Mcinnes, and C. Colombo, "A Passive High Altitude Deorbiting Strategy," Tech. Rep., 2011.
- [194] K. Saddul, J. Saletes, M. Kim, and A. Wittig, "HexSats: A novel flat hexagonal nanosatellite for high-power applications," *Acta Astronautica*, vol. 225, pp. 27–40, 12 2024.
- [195] "What is a DiskSat?" 2024. [Online]. Available: <a href="https://www.nasa.gov/smallspacecraft/disksat/">https://www.nasa.gov/smallspacecraft/disksat/</a>
- [196] NASA, "What is a DiskSat?" [Online]. Available: https://www.nasa.gov/smallspacecraft/disksat/
- [197] The Aerospace Corporation, "DiskSat: Think outside the box," 2020. [Online]. Available: https://aerospace.org/disksat
- [198] R. P. Welle, C. C. Venturini, D. A. Hinkley, and J. W. Gangestad, "The DiskSat: A Two-Dimensional Containerized Satellite," Tech. Rep., 2021.

Kash Saddul 166 BIBLIOGRAPHY

[199] R. Welle, C. Venturini, D. Hinkley, J. Gangestad, S. Grasso, A. Muszynski, R. Hunter, C. Frost, D. Mayer, and C. Baker, "DiskSat: Demonstration Mission for a Two-Dimensional Satellite Architecture," Tech. Rep., 2022.

[200] ENPULSION, "NanoFEEP Datasheet," Tech. Rep., 2018.